國立交通大學

電子工程學系電子研究所

博士論文

碳化矽基介電層與銅金屬整合之電性和阻障特性

Electrical and Barrier Properties of Silicon-Carbide-Based Dielectrics Integrated with Cu Metallization

研究生：蔣秋志

指導教授：陳茂傑

中華民國九十三年六月

碳化矽基介電層與銅金屬整合之電性和阻障特性

Electrical and Barrier Properties of Silicon-Carbide-Based Dielectrics Integrated with Cu Metallization

研究生：蔣秋志　　Student : Chiu-Chih Chiang

指導教授：陳茂傑　　Advisor : Mao-Chieh Chen

國立交通大學
電子工程學系電子研究所
博士論文

A Dissertation
Submitted to the Institute of Electronics
College of Electrical Engineering and Computer Science
National Chiao-Tung University
In Partial Fulfillment of the Requirements
for the Degree of
Doctor of Philosophy
in Electronic Engineering
2004
Hsinchu, Taiwan, Republic of China

中華民國九十三年六月

碳化矽基介電層與銅金屬整合之電性和阻障特性

學生：蔣秋志　　　　　　　　　教授：陳茂傑

國立交通大學　電機資訊學院　電子研究所

摘要

本論文探討多種碳化矽基（SiC-based）低介電常數介電阻障膜之基本特性以及使用這些介電膜作為銅帽阻障層和蝕刻停止層的銅梳狀電容（銅大馬士革結構）之電性表現。基本特性的探討包括各種三甲基矽烷基（3MS-based）非晶系 SiCN（介電常數小於 5.5）介電層、三甲基矽烷和四甲基矽烷基（3MS- and 4MS-based）非晶系 SiC（介電常數小於 5）介電層、三甲基矽烷基（3MS-based）非晶系 SiCO（介電常數小於 4.5）介電層，以及八甲基環狀四矽氧烷基（OMCTS-based）非晶系 SiCO 介電層之熱穩定性、物性和阻障特性。在銅大馬士革結構的電性表現方面，本論文針對以非晶系 SiCN、非晶系 SiC 或非晶系 SiCO 單層介電膜以及非晶系 SiCN/SiC 雙層介電膜作為銅帽阻障層的銅梳狀電容之時間相關介電崩潰（TDDB）壽命以及漏電和崩潰機制加以探討。

首先，三甲基矽烷基（3MS-based）非晶系 SiCN 膜的介電常數隨碳和氫含量的增加與氮含量的減少而從 5.4 減小至 3.5，而其熱穩定溫度（測試條件為氮氣環境退火 30 分鐘）則從 550 降低至 500°C。遞減的介電常數可歸因於碳原子具有較弱的雙極性和離子性偏極化以及氫原子具有較弱的電子性偏極化，而遞減的

熱穩定性則歸因於在高溫時有大量的碳氫分子團揮發。含有較大量碳與氫的非晶系 SiCN 膜展現較差的阻障特性和介電強度，此乃由於碳原子導致介電膜具有較為薄弱交叉結合的分子結構和孔洞度的增加，以及氫原子導致介電膜內含有大量氫相關缺陷，諸如 Si-H$^+$-Si 氫橋和 Si-H 弱鍵等。再者，鋁/非晶系 SiCN/銅（MIM）電容結構的銅表面在沉積三甲基矽烷基（3MS-based）非晶系 SiCN 膜之前，如果先經過氨氣或氮氣電漿處理，則該 MIM 電容會呈顯較大的漏電流和較低的崩潰電場，這是因為銅表面有不穩定態 Cu-O 氧化物和 Cu-N 氮化物的生成。

其次，四甲基矽烷基（4MS-based）非晶系 SiC 膜（介電常數為 4）比三甲基矽烷基（3MS-based）非晶系 SiC 膜（介電常數為 4.7）具有較高的碳含量，因而具有較低的介電常數和熱穩定溫度（500°C），而且這種較為多孔性的四甲基矽烷基（4MS-based）非晶系 SiC 膜的阻障特性和抗水能力也較差。利用三甲基矽烷基（3MS-based）非晶系 SiCN（介電常數為 5）與非晶系 SiC（介電常數為 4）的雙層介電膜（α-SiCN/α-SiC）取代三甲基矽烷基（3MS-based）非晶系 SiCN（介電常數為 5）單層膜作為銅梳狀電容的銅帽阻障層，可大幅改善銅梳狀電容結構的時間相關介電崩潰（TDDB）壽命；這是因為非晶系 SiC 的漏電流較小、與其接觸的銅表面不會有氮化現象，而且非晶系 SiC 對銅膜和金屬線間的有機矽玻璃介電層（OSG IMD）都具有較佳的附著力。銅梳狀電容結構的漏電流與非晶系 SiCN/SiC 雙層膜的厚度比率相關。以 SiCN(50 奈米)/SiC(2 奈米)雙層膜作為銅帽阻障層的銅梳狀電容結構，比起具有較厚非晶系 SiC 的雙層膜電容結構，諸如 SiCN(40 奈米)/SiC(10 奈米)或 SiCN(30 奈米)/SiC(20 奈米)，展現遠為優異的極低漏電流；較厚 SiC 膜電容結構的較大漏電流（屬於 Frenkel-Poole 激發機制）是因為較厚的非晶系 SiC 具有較大拉張力而易於產生較多界面缺陷，諸如在非晶系

SiC/有機矽玻璃（OSG）界面的裂痕、孔洞、陷阱或斷鍵等。另一方面，銅梳狀電容結構的崩潰電場和時間相關介電崩潰（TDDB）壽命與非晶系 SiCN/SiC 雙層膜的厚度比率沒有明顯的關連性，而所觀察到的銅梳狀電容結構的崩潰是由於有機矽玻璃（OSG）本體發生介電崩潰。

第三，三甲基矽烷基（3MS-based）非晶系 SiCO 介電膜的介電常數隨著介電膜沉積製程中二氧化碳流量的增加（0 至 1200 sccm）而從 4.4 逐漸降至 3.7；變小的介電常數可歸因於較大的氧含量導致介電膜具有較弱的電子性偏極化和較高的電負度。二氧化碳流量的增加也改善非晶系 SiCO 介電膜的熱穩定性、崩潰電場、漏電流、以及抗銅擴散能力；這是由於高流量二氧化碳沉積的三甲基矽烷基（3MS-based）非晶系 SiCO 介電膜具有較緻密和較少孔洞的結構。再者，以三甲基矽烷基（3MS-based）非晶系 SiCO（介電常數為 3.7）介電阻障膜作為介電層的銅金屬介電半導體（Cu-MIS）電容和作為銅帽阻障層的銅梳狀電容結構，都比用三甲基矽烷基（3MS-based）非晶系 SiC（介電常數為 4.4）介電膜製作的電容結構，展現大幅降低的漏電流和大幅提升的崩潰電場；此乃由於三甲基矽烷基（3MS-based）非晶系 SiCO 介電膜的結構密度較高、氧原子導致的薄膜特性改善、非半導體特徵、以及較低的邊緣或表面電場。八甲基環狀四矽氧烷基（OMCTS-based）非晶系 SiCO 膜的介電常數隨著介電膜沉積製程中的氧流量增加（0 至 300 sccm）而從 2.8 逐漸增至 6.3；變大的介電常數可歸因於過量的氧原子導致介電膜具有較強的雙極性和離子性偏極化。氧流量的增加也會導致八甲基環狀四矽氧烷基（OMCTS-based）非晶系 SiCO 介電膜的熱穩定性、抗水能力、以及銅阻障特性之劣化。值得注意者，三甲基矽烷基（3MS-based）非晶系 SiCO 介電阻障膜比八甲基環狀四矽氧烷基（OMCTS-based）非晶系 SiCO 膜展現較佳

的銅阻障特性；此乃由於三甲基矽烷基（3MS-based）非晶系 SiCO 介電膜具有碳化矽基（SiC-based）的分子結構，而八甲基環狀四矽氧烷基（OMCTS-based）非晶系 SiCO 介電膜的分子結構卻是氧化矽基（SiO-based）之故。

Electrical and Barrier Properties of Silicon-Carbide-Based Dielectrics Integrated with Cu Metallization

Student: Chiu-Chih Chiang **Advisor: Mao-Chieh Chen**

Institute of Electronics

College of Electrical Engineering and Computer Science

National Chiao-Tung University

Abstract

This thesis study includes the basic properties of various silicon-carbide-based (SiC-based) low-k dielectric barrier films as well as the electrical performance of Cu-comb capacitors (Cu damascene structure) using these dielectric films as the Cu cap-barrier and etching stop layer. The study of the basic properties includes the thermal stability and physical and barrier properties of various 3MS-based α-SiCN ($k<5.5$) dielectrics, 3MS- and 4MS-based α-SiC ($k<5$) dielectrics, 3MS-based α-SiCO ($k<4.5$) dielectrics, and OMCTS-based α-SiCO dielectric films. With regard to the electrical performance of the Cu damascene structure, the TDDB lifetime and the leakage and breakdown mechanisms are investigated using Cu-comb capacitors with a dielectric film of α-SiCN, α-SiC, or α-SiCO as well as with a bilayer dielectric stack of α-SiCN/α-SiC as a Cu cap-barrier layer.

First, the dielectric constant of the 3MS-based α-SiCN films decreases from 5.4 to 3.5 with increasing carbon and hydrogen contents and decreasing nitrogen content in

the dielectric films, and the thermally stable temperature of the α-SiCN films (annealed in N_2 ambient for 30 min) is also decreased from 550 to 500°C. The reduced dielectric constant is attributed to the lower dipolar and ionic polarizations of carbon atoms and the lower electronic polarization of hydrogen atoms, while the decreased thermal stability is due to massive outgassing of hydrocarbon groups at elevated temperatures. The α-SiCN films with abundant carbon and hydrogen contents exhibit degraded barrier property and dielectric strength. This can be attributed to the carbon-atom-induced poorly crosslinked molecular structure and porosity enrichment as well as the hydrogen-related defects, such as $\text{Si-H}^{+}\text{-Si}$ hydrogen bridges, and the numerous Si-H weak bonds arisen from the hydrogen atoms in the dielectric film. Moreover, the Al/α-SiCN/Cu MIM capacitors with the Cu-surface exposed to O_2- or N_2-plasma treatment prior to the deposition of the 3MS-based α-SiCN film exhibit higher leakage current and lower breakdown field. The increased leakage current and decreased breakdown field of the O_2- and N_2-plasma-treated samples are attributed, respectively, to the presence of metastable Cu-O oxide and Cu-N azide at the Cu-surface.

Second, the 4MS-based α-SiC (*k*=4) film contains a higher carbon content and thus has a lower dielectric constant and thermal stability temperature (500°C) than the 3MS-based α-SiC (*k*=4.7) film. The more porous 4MS-based α-SiC film also exhibits degraded barrier property and moisture resistance. The TDDB lifetime of Cu-comb capacitor is greatly improved by using a 3MS-based α-SiCN(*k*=5)/α-SiC(*k*=4) bilayer dielectric stack instead of the 3MS-based α-SiCN(*k*=5) single film as a Cu cap-barrier. This improvement is attributed to the lower leakage current of α-SiC, absence of nitridation on Cu surface, and better adhesion of α-SiC to Cu and OSG IMD. The leakage current between Cu lines in the Cu-comb capacitor is dependent on the thickness ratio of the α-SiCN/α-SiC bilayer barrier. The Cu-comb capacitor with an α-SiCN(50 nm)/α-SiC(2 nm) bilayer barrier exhibits a much smaller leakage current than that with a bilayer barrier of thicker α-SiC film, such as α-SiCN(40 nm)/α-SiC(10 nm) or α-SiCN(30 nm)/α-SiC(20 nm). The increased leakage (Frenkel-Poole emission) between Cu lines is attributed to the large number of interfacial defects, such as cracks, voids, traps or dangling bonds at the α-SiC/OSG interface, which are generated by the larger tensile force of the thicker α-SiC film. On the other hand, the breakdown field and TDDB lifetime of the Cu-comb capacitor reveal little dependence on the thickness ratio of the α-SiCN/α-SiC bilayer barrier, and the observed breakdown of the Cu-comb capacitor is due to dielectric breakdown of the bulk OSG layer.

Thirdly, the dielectric constant of the 3MS-based α-SiCO dielectric films decreases from 4.4 to 3.7 with increasing CO_2 flow rate (0~1200 sccm) during the dielectric deposition process. The decreased dielectric constant is attributed to the lower electronic polarization and higher electronegativity of oxygen atoms in the α-SiCO dielectric film. Increasing CO_2 flow rate also leads to an α-SiCO dielectric film of better thermal stability, higher breakdown field, lower leakage current, and superior resistance to Cu diffusion. The improved barrier property is attributed to the denser and less porous structure of the 3MS-based α-SiCO dielectric film deposited with a higher CO_2 flow rate. Moreover, the Cu-MIS and Cu-comb capacitors with a 3MS-based α-SiCO (k=3.7) dielectric barrier film exhibit much smaller leakage current and higher breakdown field than those with a 3MS-based α-SiC (k=4.4) dielectric film. This is attributed to the higher density, oxygen-improved film's property, non-semiconductor behavior, and lower fringe- or surface-electric field of the 3MS-based α-SiCO dielectric film. The dielectric constant of the OMCTS-based α-SiCO films increases from 2.8 to 6.3 with increasing O_2 flow rate (0~300 sccm) during the dielectric deposition process, presumably due to the increasing content of the higher dipolar and ionic polarized oxygen atoms in the dielectric film. Increasing O_2 flow rate also degrades the thermal stability, moisture resistance, and Cu barrier property of the OMCTS-based α-SiCO dielectric film. Notably, the 3MS-based α-SiCO dielectric barrier film is superior to the OMCTS-based α-SiCO film in the Cu barrier property. This is due to the fact that the 3MS-based α-SiCO films have a SiC-based molecular structure, while the molecular structure of the OMCTS-based α-SiCO films is SiO-based.

誌謝

「九層之台，起於累土。」

交大陪伴小鐵度過將近七年的時光，從電工系到電子所博士班順利畢業，小鐵點點滴滴的努力，卻不如許多貴人無怨無私的幫助。

「取之於人者太多，施之於人者太少，要感謝的人太多。」

陳茂傑老師，嚴肅謹慎而堅持不懈地追求真理，謙虛豁達而幽默風趣地善待眾人，無限感謝；沒有老師適時的指導與鼓勵，學生鐵定越不過許多生活障礙。

崔秉鉞老師，亦師亦友的感覺深植內心，對實驗數據有如鷹眼般敏銳仔細，對生活事務有如好友般關懷關心，真心感謝；沒有老師的挑剔，何來學生的完美？

台積電先進模組技術研發部門，鼎力幫助實驗樣品和材料分析；梁孟松協理、章勳明副處長、盧勇誠經理、吳振誠先生、李連忠先生和柯忠祈先生，特別感謝。

交大奈米中心和國家奈米元件實驗室，提供優良完善的實驗設備和協助；徐秀鑾小姐、黃月美小姐、范秀蘭小姐、林素珠小姐和彭兆光先生，由衷感謝。

陳老師和崔老師實驗室的各位學長姐弟妹，給予諸多指教和協助；王啟寧學姐、徐偉成、林成利、范慶麟、王超群、方國龍學長、黃誌鋒、張修維、賴祐生、吳偉豪、林信宏、楊宇國、王安志學弟、林巧茹和柯依秀學妹，超級感謝。

室友群，陪伴小鐵度過有苦有樂的生活；伍佑國，充滿歡樂、文藝和武學修養；常鼎國，擁有認真、踏實和刻苦特質；及其他如過客般的室友，誠心感謝。

最後，父母、家人和蛋仔的一路全力支持與支援，已不是隻字片語所能感謝；爸爸、媽媽，謝謝！

ps. 無限真心感謝各口試委員和系主任與所長，因為您的簽名是無限重要地。

______________蔣秋志@*June 2004*

Contents

Table Captions

Chapter 1

Chapter 2

Chapter 3

Chapter 5

Chapter 6

Chapter 7

Chapter 8

Chapter 9

Chapter 10

Chapter 11

Figure Captions

Chapter 1

Chapter 2

Chapter 3

Chapter 4

Chapter 5

Chapter 6

Chapter 7

Chapter 8

Chapter 9

Chapter 10

Chapter 1

Introduction

1-1 Interconnect RC Delay

The global wiring is becoming a fundamental roadblock to true scaling beyond the 0.25 μm node technology, as shown in Fig. 1-1 [1,2]. The variation disparity between the transistor gate delay and the global wiring (interconnect) delay is evident. However, the interconnect delay can be improved by repeaters, which have the effect of global buffering because of the loose pitch structure of back-end-of-line (BEOL) metallization [2] and interconnect length reduction [3]. For the high performance design, such as multi-GHz microprocessors, the interconnect delay is directly related to the resistance-capacitance (RC) time constant [2,3], which is defined in terms of the circuit response, as given by Eq. (1-1):

$$V_{out}(t) = V_{out}(\text{maximum}) \times \left[1 - \exp\left(\frac{-t}{RC}\right)\right] \qquad (1\text{-}1)$$

where $V_{out}(t)$ is the output voltage of the circuit, t is the time, and R and C are lumped total of resistances (except that of load transistor resistance) and capacitances associated with the dielectric of the circuit, respectively [3]. Thus, RC delay is the time when $V_{out}(t = RC)$ attains a value of 63.2% of V_{out}(maximum). One can approximate the RC delay by multiplying R with a simple parallel metal-line capacitance, as illustrated in Fig. 1-2, leading to an expression of Eq. (1-2):

$$RC = \frac{\rho \cdot L}{W_M \cdot t} \times \frac{\varepsilon \cdot L \cdot t}{W_{ILD}} = \frac{\rho \cdot \varepsilon \cdot L^2}{W_M \cdot W_{ILD}} \qquad (1\text{-}2)$$

where ρ, ε, L, t, W_M, and W_{ILD} are the metal resistivity, interlayer dielectric (ILD) permittivity, interconnect length, interconnect thickness, metal width, and ILD width, respectively. Note that $\varepsilon = k\varepsilon_0$, where k is the dielectric constant (k-value) of ILD and ε_0 is the permittivity of free space [3]. Thus, besides using a lower resistivity metal for interconnect wiring and a lower dielectric constant material for the ILD, one can also reduce the RC delay by designing the circuit to accommodate shorter interconnects and wider wires. However, a longer interconnect becomes inevitable because larger chip size and multilevel interconnection are both needed to meet the requirements of the increased functional complexity and packing density of the integrated circuits (ICs) [4]. Moreover, wider wires are short-term solution for reducing the RC delay because of the concerns of smaller IC area and higher IC throughput. Therefore, using a lower resistivity metal for the interconnect wiring and a lower dielectric constant material for the ILD becomes a feasible approach for reducing the interconnect RC delay.

1-2 Cu Metallization

Copper (Cu) has been widely used as an interconnect wiring in ultra-large scale integrated (ULSI) circuits. Compared with the conventional aluminum-based (Al-based) wires, Cu metal reduces the electrical resistance of interconnect lines because of its lower electrical resistivity; moreover, Cu line also sustains a higher current density because of its higher thermal conductivity and higher melting point, as shown in Table 1-1. Furthermore, Cu exhibits excellent resistance to electromigration, stress-migration, and hillock formation. However, there are a number of integration and reliability issues needed to be solved before the Cu metallization can be successfully used in the silicon-based (Si-based) ULSI circuits. Cu readily drifts into SiO_2 and ILDs deposited by spin-on or plasma-enhanced chemical vapor deposition (PECVD) with an applied electric filed of 1 MV/cm at temperatures as low as 100°C [5-9], resulting in poor dielectric breakdown lifetime. Cu also has a very high temperature-independent diffusion coefficient (D_o) of 0.04 cm^2/sec in Si [10]. In addition, Cu is a deep-level dopant in Si and forms a number of acceptor and donor type generation-recombination centers within the forbidden band gap, leading to induce a large leakage current [4,11]. Since it is inevitable to use metallic and/or dielectric barriers to encapsulate the Cu metallization in order to suppress the diffusion/drift of Cu into the active region of the electronic devices, a number of issues regarding the encapsulation scheme must be addressed, such as the Cu/barrier interface-diffusion arisen from electromigration, Cu/barrier interface-reaction during the deposition of the barrier layer, and poor breakdown lifetime of dielectric barrier resulting from the Cu diffusion [12,13]. Notably, the dielectric breakdown lifetime can be improved by using an ammonia-plasma (NH_3-plasma) treatment on the Cu-surface prior to the cap α-SiN (amorphous silicon-nitride) deposition on a Cu-comb capacitor [13]. Before making a successful integration of the barrier film and the Cu metal with a plasma-treated surface, fundamental properties, such as plasma induced Cu-surface roughness and chemical bonding of the plasma-treated Cu-surface, must be first explored. In this thesis, we investigate the effects of oxygen-plasma (O_2-plasma) and nitrogen-plasma (N_2-plasma) treatments on the Cu-surface.

1-3 Dielectric Barriers

The metallic and dielectric barrier layers are necessary in the Cu metallization scheme, as shown in Fig. 1-3 [1]. Many metallic barrier materials have been studied, such as titanium-based (Ti-based), tantalum-based (Ta-based), chromium-based

(Cr-based), and molybdenum-based (Mo-based) metallic barriers [14-27]. However, the conventional α-SiN film (k~7) is still the primary dielectric material used for cap-barrier and etch stop layer (ESL) in the Cu metallization of production-chip [28]. Although a modified α-SiN film (k~5.4) was developed by low-pressure chemical vapor deposition (LPCVD) using hexachlorodisilane (HCD) [29], it is still desirable to replace α-SiN with dielectric materials of lower k-value (k<5) in order to further reduce the effective dielectric constant of the Cu interconnection line. In recent years, a number of studies have been reported regarding the thermally stable and Cu-diffusion restrained low-k silicon-carbide-based (SiC-based) films deposited by PECVD using organosilicate gases [30-39]. The PECVD amorphous silicon-carbide (α-SiC), amorphous silicon-nitricarbide (α-SiCN), and amorphous silicon-oxycarbide (α-SiCO) have received extensive attention for applications as Cu cap-barrier and ESL in Cu metallization because of their lower k-value, better etching selectivity with organosilicate glass (OSG), robust chemical mechanical polishing (CMP) strength, good photoresist poisoning resistance, higher anti-reflective ability, and superior properties as a Cu barrier/passivation layer in terms of Cu-restraint, electromigration resistance, and Cu-hillock density [35,38-42].

For the study of the SiC-based dielectric barrier films in this thesis, we investigated the thermal stability, physical property, barrier characteristic, and electrical performances (leakage current, leakage mechanism, breakdown field, and breakdown mechanism) of the PECVD α-SiCN, α-SiC, and α-SiCO films deposited using trimethylsilane [$(CH_3)_3SiH$, 3MS], tetramethylsilane [$(CH_3)_4Si$, 4MS], or octamethylcyclotetrasiloxane {[$(CH_3)_2SiO]_4$, OMCTS} organosilicate gases. Table 1-2 summarizes the α-SiCN, α-SiC, and α-SiCO dielectric barrier films studied in this thesis.

1-4 Thesis Organization

This thesis study consists of three major topics as follows. The first topic studies the electrical and barrier properties of various PECVD α-SiCN dielectric films on Cu surfaces with and without a plasma treatment (chapters 2, 3, and 4). The second topic deals with the electrical and barrier properties of various PECVD α-SiC dielectrics and α-SiCN/α-SiC bilayer-structured films (chapters 5, 6, and 7). The third topic explores the electrical and barrier properties of various PECVD α-SiCO dielectric films (chapters 8, 9, and 10).

In chapter 2, we investigate the thermal stability and physical and barrier properties of three 3MS-based α-SiCN films with different carbon and nitrogen concentrations and with dielectric constants of less than a value of 5.5; for a comparison, an α-SiN film with a *k*-value of 7.2 is also studied. Chapter 3 investigates the thermal stability and physical and barrier properties of two 3MS-based α-SiCN films with different hydrogen concentrations and with dielectric constants of less than a value of 5. Chapter 4 investigates the effects of O_2-plasma and N_2-plasma treatments on the Cu-surface with respect to the leakage current and breakdown field of the Al/α-SiCN/Cu metal-insulator-metal (MIM) capacitor.

In chapter 5, we investigate the thermal stability and physical and barrier properties of two α-SiC films (with *k*-values less than 5) deposited using 3MS and 4MS organosilicate gases. Chapter 6 investigates in the first place, the thermal stability and physical and barrier properties of two species of 3MS-based dielectric films: the nitrogen containing α-SiCN film with a dielectric constant of 4.9 and the nitrogen free α-SiC film with a dielectric constant of 3.8. This is followed by investigating the time-dependent dielectric breakdown (TDDB) lifetime for a Cu-comb capacitor having a bilayer-structured cap-barrier made up of these two species of films.

Chapter 7 investigates the leakage and breakdown mechanisms of the Cu-comb capacitor with a carbon-doped low-*k* PECVD OSG (k=3) as the intermetal dielectric (IMD) and an α-SiCN (k=5)/α-SiC (k=4) bilayer-structured dielectric film as the cap-barrier.

In chapter 8, we investigate the thermal stability and physical and barrier properties of α-SiC and α-SiCO dielectric barrier films using 3MS precursor and He carrier gas without and with various CO_2 flow rates. Chapter 9 investigates in the first place, the improvement of leakage current and breakdown field of the Cu metal-insulator-semiconductor (Cu-MIS) capacitor with an α-SiCO (k=3.7) dielectric barrier. This is followed by investigating the improvement of leakage current and breakdown field of the Cu-comb capacitor with a carbon-doped low-*k* PECVD OSG (k=3) as the IMD and an α-SiCO dielectric film as the cap-barrier. Chapter 10 investigates the thermal stability and physical and barrier properties for three α-SiCO dielectric barrier films deposited using OMCTS precursor and He carrier gas with and without O_2 reaction gas.

Finally, chapter 11 presents the conclusions of this thesis study and the suggestions for the future work.

References

[1] International Technology Roadmap for Semiconductor, *ITRS Conference* (Hsinchu, Taiwan, 2003) interconnect section.

[2] Héctor Sánchez, *IEEE IITC Technol. Dig.* (2003) p. 3.

[3] S. P. Murarka, I. V. Verner and R. J. Gutmann, *Copper-Fundamental Mechanisms for Microelectronic Applications* (John Wiley & Sons, New York, 2000) chap. 1.

[4] Z. C. Wu, *Electrical Reliability of Integrating Low-K Dielectrics with Cu Metallization and Passivation Study of Cu Films* (Ph.D. Thesis, National Chiao-Tung University, Hsinchu, Taiwan, 2001) chap. 1.

[5] J. D. McBrayer, R. M. Swanson, and T. W. Sigmon, *J. Electrochem. Soc.*, **133** (1986) p. 1242.

[6] Y. S. Diamond, A. Dedhia, D. Hoffstetter, and W. G. Oldham, *J. Electrochem. Soc.*, **140** (1993) p. 2427.

[7] A. L. S. Loke, J. T. Wetzel, P. H. Townsend, T. Tanabe, R. N. Vrtis, M. P. Zussman, D. Kumar, C. Ryu, and S. S. Wong, *IEEE Trans. Electron Devices*, **46** (1999) p. 2178.

[8] A. L. S. Loke, C. Ryu, C. P. Yue, J. S. H. Cho, and S. S. Wong, *IEEE Electron Devices Lett.*, **17** (1996) p. 549.

[9] A. L. S. Loke, J. T. Wetzel, C. Ryu, W. J. Lee, and S. S. Wong, *IEEE VLSI Technol. Dig.* (1998) p. 26.

[10] S. Wolf and R. N. Tauber, *Silicon Processing for the VLSI Era, Volume 1: Process Technology* (Lattice Press, California, 1986) p. 252.

[11] M. Vogt and K. Drescher, *Appl. Surface Science*, **91** (1995) p. 303.

[12] G. P. Beyer, M. Baklanov, T. Conard and K. Maex, *Mat. Res. Soc. Symp. Proc.*, **612**

(2000) p. D9.17.1.

[13] J. Noguchi, N. Ohashi, T. Jimbo, H. Yamaguchi, K. I. Takeda and K. Hinode, *IEEE Trans. Electron Devices*, **48** (2001) p. 1340.

[14] C. A. Chang, *J. Appl. Phys.*, **67** (1990) p. 6184.

[15] J. Noguchi, T. Saito, N. Ohashi, H. Ashihara, H. Maruyama, M. Kubo, H. Yamaguchi, D. Ryuzaki, K. I. Takeda, and K. Hinode, *IEEE IRPS Technol. Dig.* (2001) p. 355.

[16] W. F. McArthur, K. M. Ring, and K. L. Kavanagh, *Mat. Res. Soc. Symp. Proc.*, **514** (1998) p. 321.

[17] J. S. Pan, A. T. S. Wee, C. H. A. Huan, J. W. Chai, and J. H. Zhang, *Mat. Res. Soc. Symp. Proc.*, **612** (2000) p. D9.18.1.

[18] S. Li, Z. L. Dong, K. M. Latt, and H. S. Park, *Appl. Phys. Lett.*, **80** (2002) p. 2296.

[19] G. W. Book, K. Pfeifer, and S. Smith, *Microelectronic Engineering*, 64 (2002) p. 255.

[20] G. S. Chen and S. C. Huang, *J. Electrochem. Soc.*, **148** (2001) p. G424.

[21] K. L. Ou, W. F. Wu, C. P. Chou, S. Y. Chiou, and C. C. Wu, *J. Vac. Sci. Tecnol. B*, **20** (2002) p. 2154.

[22] T. Heiser, C. Brochard, and M. Swaanen, *Mat. Res. Soc. Symp. Proc.*, **612** (2000) p. D7.3.1.

[23] S. J. Im, S. H. Kim, K. C. Park, S. L. Cho, and K. B. Kim, *Mat. Res. Soc. Symp. Proc.*, **612** (2000) p. D6.7.1.

[24] S. I. Nakao, M. Numata, and T. Ohmi, *Jpn. J. Appl. Phys.*, **38** (1999) p. 2401.

[25] C. L. Lin, *Copper Chemical Vapor Deposition and Its Application to Deep Sub-Micron Via-Filling* (Ph.D. Thesis, National Chiao-Tung University, Hsinchu,

Taiwan, 2002) chap. 8.

[26] T. Laurila, K. Zeng, J. K. Kivilahti, J. Molarius, and I. Suni, *J. Appl. Phys.*, **91** (2002) p. 5391.

[27] J. C. Chuang, *Reliability Issues of Passivation Layers against Copper Oxidation and Barrier Layers against Copper Diffusion in Copper Metallization for ULSI Application* (Ph.D. Thesis, National Chiao-Tung University, Hsinchu, Taiwan, 1999) chap. 6-7.

[28] H. Aoki, K. Torii, T. Oshima, J. Noguchi, U. Tanaka, H. Yamaguchi, T. Saito, N. Miura, T. Tamaru, N. Konishi, S. Uno, S. Morita, T. Fujii, and K. Hinode, *IEEE IEDM Technol. Dig.* (2001) p. 76.

[29] M. Tanaka, S. Saida, and Y. Tsunashima, *J. Electrochem. Soc.*, **147** (2000) p. 2284.

[30] P. Xu, K. Huang, A. Patel, S. Rathi, B. Tang, J. Ferguson, J. Huang, C. Ngai, and M. Loboda, *IEEE IITC Technol. Dig.* (1999) p. 109.

[31] M. J. Loboda, *Microelectronic Engineering*, **50** (2000) p. 15.

[32] M. J. Loboda, J. A. Seifferly, and F. C. Dall, *J. Vac. Sci. Technol. A*, **12** (1994) p. 90.

[33] C. C. Chiang, M. C. Chen, Z. C. Wu, L. J. Li, S. M. Jang, C. H. Yu, and M. S. Liang, *IEEE IITC Technol. Dig.* (2002) p. 200.

[34] K. Higashi, N. Nakamura, H. Miyajima, S. Satoh, A. Kojima, J. Abe, K. Nagahata, T. Tatsumi, K. Tabuchi, T. Hasegawa, H. Kawashima, S. Arakawa, N. Matsunaga, and H. Shibata, *IEEE IITC Technol. Dig.* (2002) p. 15.

[35] J. Martin, S. Filipiak, T. Stephens, F. Huang, M. Aminpur, J. Mueller, E. Demircan, L. Zhao, J. Werking, C. Goldberg, S. Park, T. Sparks, and C. Esber, *IEEE IITC Technol. Dig.* (2002) p. 42.

[36] S. G. Lee, Y. J. Kim, S. P. Lee, H. S. Oh, S. J. Lee, M. Kim, I. G. Kim, J. H. Kim, H. J. Shin, J. G. Hong, H. D. Lee, and H. K. Kang, *Jpn. J. Appl. Phys.*, **40** (2001) p. 2663.

[37] K. L Fang, B. Y. Tsui, C. C. Yang, and S. D. Lee, *IEEE IITC Technol. Dig.* (2001) p. 250.

[38] K. I. Takeda, D. Ryuzaki, T. Mine, and K. Hinode, *IEEE IITC Technol. Dig.* (2001) p. 244.

[39] T. Ishimaru, Y. Shioya, H. Ikakura, M. Nozawa, Y. Nishimoto, S. Ohgawara, and K. Maeda, *IEEE IITC Technol. Dig.* (2001) p. 36.

[40] F. Lanckmans, W. D. Gray, B. Brijs, and K. Maex, *Microelectronic Engineering*, **55** (2001) p. 329.

[41] K. Goto, H. Yuasa, A. Andatsu, and M. Matsuura, *IEEE IITC Technol. Dig.* (2003) p. 6.

[42] M. Fayolle, J. Torres, G. Passemard, F. Fusalba, G. Fanget, D. Louis, L. Arnaud, V. Girault, J. Cluzel, H. Feldis, M. Rivoire, O. Louveau, T. Mourier, and L. Broussous, *IEEE IITC Technol. Dig.* (2002) p. 39.

Table 1-1 Basic properties of Cu and Al metals.

Property	**Cu**	**Al**
Resistivity (μΩ-cm)	**1.67**	**2.66**
Thermal conductivity (W/cm)	**3.98**	**2.38**
Melting point (^{o}C)	**1085**	**660**
Delay (ps/mm)	**2.3**	**3.7**
Adhesion to SiO_2	**Poor**	**Good**
Corrosion in air	**Yes**	**No**
Dry etching	**No**	**Yes**
Wet etching	**Yes**	**Yes**

Table 1-2 The α-SiCN, α-SiC, and α-SiCO dielectric barrier films studied in this thesis.

Dielectrics	**α-SiCN**	**α-SiC**	**α-SiCO**
Precursor	**3MS**	**3MS, 4MS**	**3MS, OMCTS**
Carrier gas	**with/without He**	**with/without He**	**He**
Reaction gas	NH_3	**--**	CO_2, O_2

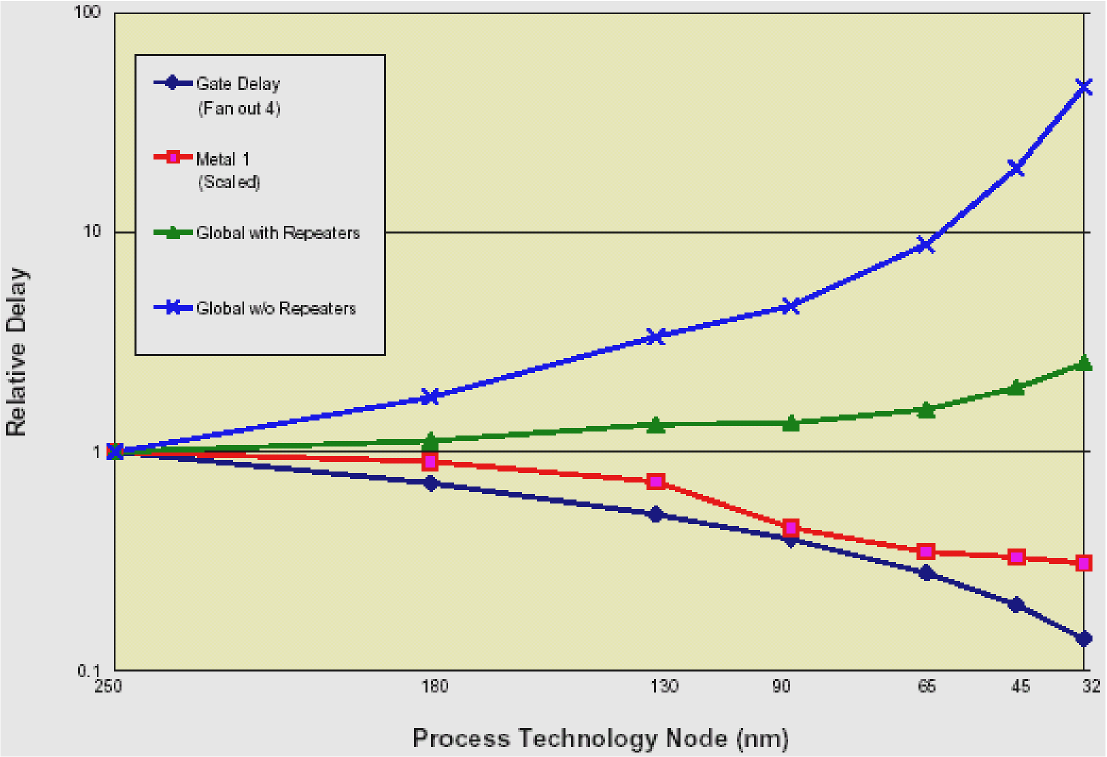

Fig. 1-1 Relative delay for gate, metal 1, and global wiring vs. process technology node.

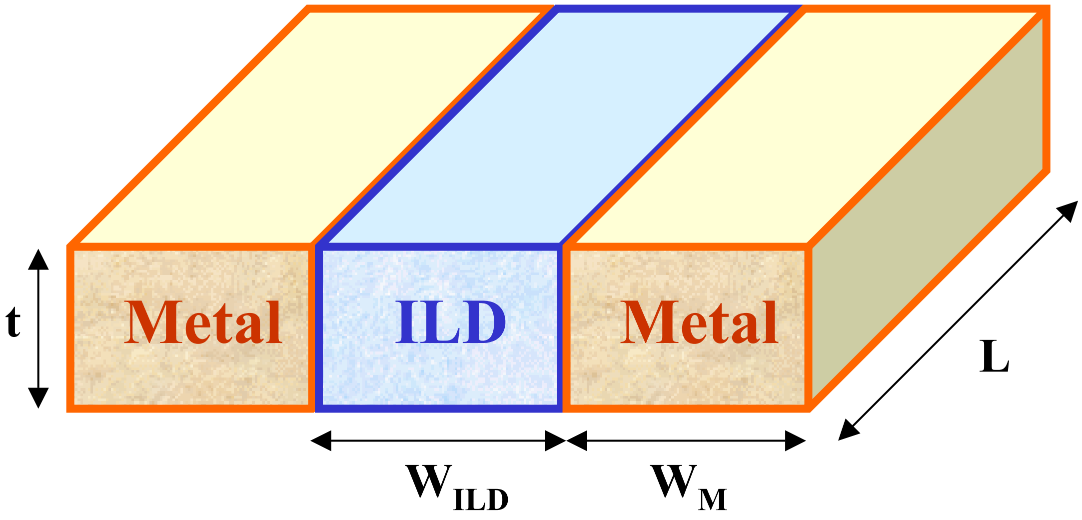

Fig. 1-2 An ILD sandwiched between two parallel metal-lines illustrates a simple paradigm of interconnect.

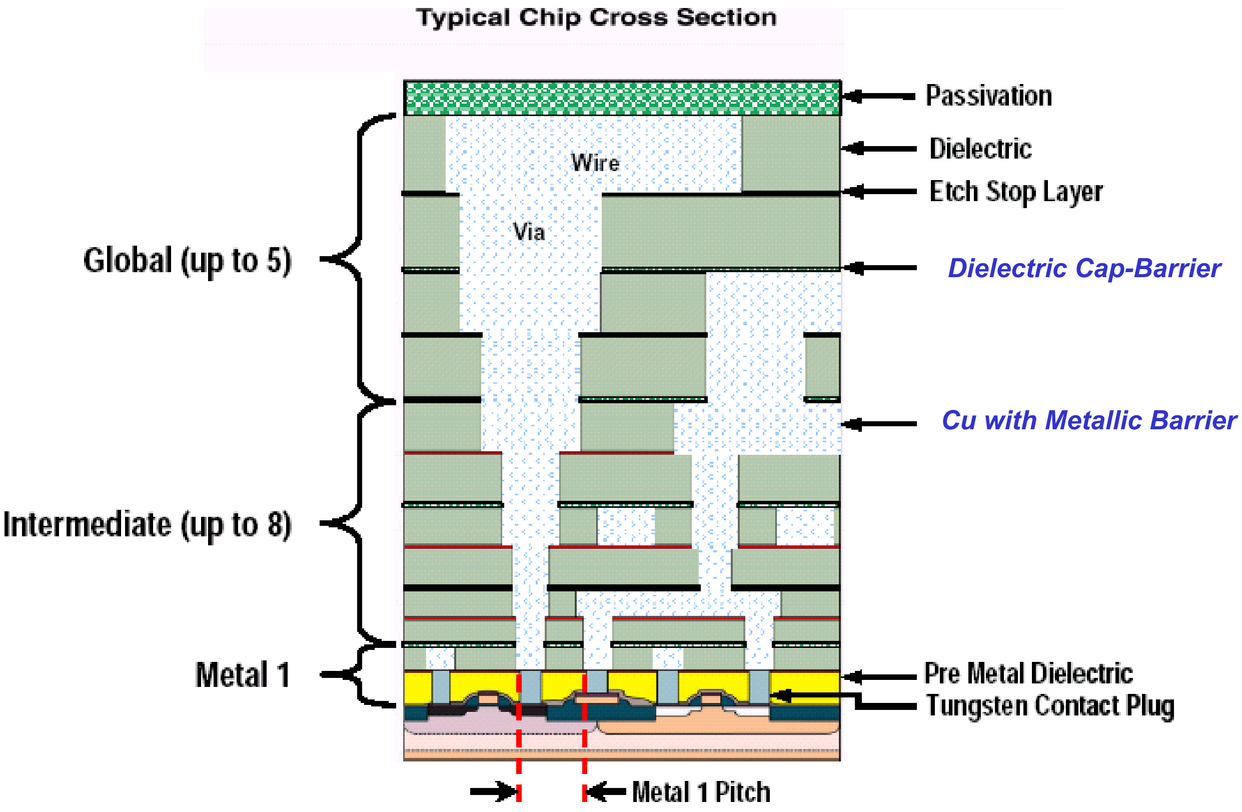

Fig. 1-3 Schematic cross-sectional view of a typical chip with the Cu metallization.

Part 1

Chapter 2

Amorphous Silicon-Nitricarbide (α-SiCN) Dielectric Barrier

2-1 Introduction

As device dimensions continuously shrink, one of the key limitations of integrated circuits performance is the RC time delay of the interconnect system. In order to minimize the delay of signal propagation, it is necessary to use low dielectric constant (low-*k*) materials as the ILDs. While many low-*k* (k<3) materials have been used as ILDs, the high-dielectric-constant (k>7) α-SiN is still the primary candidate, providing the cap-barrier and ESL required in Cu damascene structures. Thus, it is desirable to replace α-SiN with lower dielectric constant materials to further reduce the effective dielectric constant of the Cu interconnect system [1]. In recent years, there have been reports on the study of low stress and thermally stable low-*k* SiC-based films deposited by PECVD using organosilicate gases [2-6]. In this chapter, we investigate the physical and barrier properties of three low-*k* α-SiCN dielectric films with dielectric constants less than a value of 5.5; for a comparison, an α-SiN film with a *k*-value of 7.2 is also studied.

2-2 Experimental Details

Three α-SiCN dielectric barrier films with different carbon (C) and nitrogen (N) concentrations and an α-SiN film, for a comparison, were investigated. All films were deposited to a thickness of 50 nm on p-type, (100)-oriented Si wafers using a parallel-plate PECVD system operated at 13.56 MHz. The α-SiCN films were deposited at temperatures of 350 and 400°C using NH_3 and $(CH_3)_3SiH$ (3MS) gases with various flow ratios ranging from 0.5 to 4.0, which resulted in three α-SiCN films with different compositions. The α-SiN film, which is the primary cap-barrier and ESL in the present multilevel interconnect system, was deposited at 400°C using SiH_4 and NH_3 gases with a SiH_4/NH_3 flow ratio of 1/8. All deposited films were annealed at 400°C for 30 min in N_2 ambient to remove moisture possibly absorbed in the dielectrics prior to the investigation of the film's physical property or the deposition of electrode (TaN/Cu or Al) used to construct the MIS capacitor structure. The TaN/Cu-gated MIS capacitors were constructed by first sputter-depositing a 200-nm-thick Cu layer on the α-SiCN and the α-SiN films, followed by a reactive sputter deposition of a 50-nm-thick TaN layer on the Cu surface in the same sputtering system without breaking the vacuum. The TaN film served as a passivation layer to prevent the Cu metal from oxidizing during the subsequent high-temperature processes. For a comparison, Al-electrode control samples were also prepared by depositing a 500-nm-thick Al layer directly on the α-SiCN and the α-SiN dielectric surfaces. All metal electrodes were defined by a lift-off process in order to avoid unexpected deterioration of the dielectrics due to chemical wet etching. For better electrical measurements, a 500-nm-thick Al layer was also deposited on the backside of the Si substrate for all samples. Some of the completed MIS samples were thermally annealed at 400°C for 30 min in N_2 ambient. This annealing step eliminates the plasma-induced damage that may have occurred during the sputter deposition of TaN/Cu electrodes and also provides the driving force for Cu diffusion.

Rutherford backscattering spectroscopy (RBS) with $^4He^+$ ions at 2.0 MeV was used to determine the compositions of the dielectric films. Thermal desorption spectroscopy (TDS) was used to analyze the outgassing behavior of the dielectrics during the thermal annealing process. The film thickness and refractive index were measured by an n&k analyzer at 633 nm wavelength, and the *k*-value of the dielectrics was determined by the maximum capacitance of the Al-gated MIS capacitors measured at 1 MHz using a Keithley 82 system. An HP4145B semiconductor parameter analyzer was used to measure the dielectric leakage current and provide the bias for the bias-temperature-stress (BTS) test. Secondary ion mass spectrometry (SIMS) was used to detect the penetration of Cu in the dielectrics.

2-3 Physical Property and Thermal Stability

The compositions, dielectric constants, refractive indices, and deposition temperatures of the α-SiCN and α-SiN films studied in this chapter are summarized in Table 2-1. It is found that the dielectric constant of the α-SiCN films decreases with increasing carbon (C) and decreasing nitrogen (N) contents in the dielectric. The SC3 film has a low dielectric constant of 3.5 due to its high carbon content (C/Si atomic ratio of 0.875) because carbon is less ionic polarizable and has no orientational (dipolar) contribution to the *k*-value [7,8]. Moreover, carbon in the silicon matrix generates atomic-scale nanopores and results in the enhancement of pre-existing nanoporosity or microvoids in the films after annealing [7,9]. The SC2 film has a lower dielectric constant at 1 MHz and a higher refractive index at 633 nm (~5×10^{14} Hz) than the SC1 film presumably because the SC2 film is more reflective than the SC1 film at the optical high frequency [10]. In fact, many insulators have lower dielectric constants but higher refractive indices than SiO_2 (*k*=4.0, n=1.47), such as low-*k* materials BCB^{TM} (*k*=2.65, n=1.55) and SiLK^{TM} (*k*=2.65, n=1.63) [11], or a dielectric barrier SiOCH (*k*=3.85, n=1.77) [12]. Figure 2-1 shows the thickness shrinkage of the dielectrics thermally annealed at various temperatures for 30 min in N_2 ambient. The thickness of all films remained nearly constant at temperatures up to 500°C. Upon annealing at 600°C, the percentage of shrinkage of SC1 and SN films remained below 5%, whereas SC3 and SC2 films shrank drastically, presumably due to massive outgassing of CH_4 observed by TDS, as shown in Fig. 2-2. This implies that the thickness shrinkage is closely related to the changes of chemical bonding and microstructure of the dielectric films, which result in the variation of refractive index and dielectric constant. Figures 2-3 and 2-4 show, respectively, the refractive indices and dielectric constants versus temperature during a 30 min annealing in N_2 ambient. The refractive indices of SC3 and SC2 films increased markedly at temperatures above 500°C, particularly that of the SC2 film. The dielectric constants of SC3 and SC2 films remained constant at temperatures up to 500°C but increased drastically at temperatures above 500°C, whereas the *k*-values of SC1 and SN films remained constant at temperatures up to 550°C.

2-4 Electrical and Barrier Properties

Figure 2-5 shows the room-temperature leakage current density for the as-fabricated as well as 400°C-annealed Al-gated and TaN/Cu-gated MIS capacitors of various α-SiCN and α-SiN dielectric films. The measurements were carried out with the MIS capacitors biased in the accumulation region. For each dielectric film, very little difference in leakage current was observed between the Al-gated and TaN/Cu-gated MIS capacitors, whether as-fabricated or 400°C-annealed. This implies that all the dielectrics were capable of preventing Cu permeation at temperatures up to 400°C. The BTS test was used to further explore the barrier property of the TaN/Cu-gated MIS capacitors. Prior to the BTS test, all MIS capacitors were thermally annealed at 400°C for 30 min in N_2 ambient to repair the plasma-induced damage that occurred during the metal electrode sputtering and also to provide the driving force for Cu diffusion. The BTS test was performed in N_2 ambient to prevent the Cu electrode from oxidizing at elevated temperatures as well as moisture uptake into the dielectric films. Figure 2-6 shows the leakage current density versus stress time for various TaN/Cu-gated and Al-gated MIS capacitors under BTS at 200°C with an applied electric field of 1 MV/cm. It can be seen that the TaN/Cu-gated SC3 sample failed after being subjected to the BTS for 30 min, whereas all other samples remained stable under the BTS up to at least 15 h. The breakdown of the TaN/Cu-gated SC3 sample is presumably due to the penetration of Cu into the SC3 dielectric rather than due to wear out of the SC3 film from the BTS. Figure 2-7 illustrates the leakage current density versus electric field for various MIS capacitors measured at 200°C before and immediately after the BTS test. There is a significant increase in leakage current for the TaN/Cu-gated SC3 sample after application of the BTS for 1 h, while all other samples show no obvious change in leakage current after application of the BTS. Figure 2-8 shows the SIMS depth profiles of Cu in the TaN/Cu-gated SC3, SC2, and SC1 samples after removal of the TaN/Cu electrode. The depth profile of Cu clearly indicates the permeation of Cu into only the SC3 dielectric for the TaN/Cu-gated SC3 sample after one hour of BTS. Thus, we may conclude that the spiking in the leakage current of the TaN/Cu-gated SC3 sample during the BTS test (Fig. 2-6a) and the significant increase of leakage current in the TaN/Cu-gated SC3 sample after application of BTS for one hour (Fig. 2-7a), resulted from the penetration of Cu into the SC3 dielectric.

The poor barrier property of the SC3 film against Cu penetration might be attributed to the film's rich carbon content. The rich carbon content makes the molecular structure of α-SiCN film more polymeric and poorly crosslinked [13]. Figure 2-9 illustrates schematic molecular structures of α-SiCN film with different C/Si ratios. The better crosslinked molecular structure contains fewer methyl groups, and thus the film will preserve a better barrier property against Cu permeation. Moreover, the concentrated carbon atoms also enhance the porosity of α-SiCN films [7,9], resulting in easier penetration of Cu into the film. Figure 2-10 illustrates a schematic microstructure of a porous α-SiCN film. The open pore is a cavity or a channel that can communicate with the surface of the dielectric film, while the closed pore is a cavity not communicating with the surface [14]. A highly porous film will lead to more adsorption of moisture into the film. After the α-SiCN films were immersed in boiling water for 1 h, the signal of H_2O was observed in the TDS spectrum for the SC3 sample, as shown in Fig. 2-11. It is obvious that the SC3 film stored the most amount of moisture (H_2O) with a major mass peak at 18. Moisture in the dielectric will enhance the drift of Cu ions in the dielectric film during the BTS test [15]. Thus, the penetration of Cu into the SC3 film in the TaN/Cu/SC3/Si MIS capacitor during the BTS test is presumably due to the porosity enrichment caused by an abundant amount of carbon atoms in the SC3 dielectric.

2-5 Summary

Three α-SiCN films with different carbon and nitrogen concentrations and dielectric constants of less than 5.5 were investigated with respect to the thermal stability and physical and barrier properties. For a comparison, an α-SiN film with a *k*-value of 7.2 was also studied. It is found that the dielectric constant of α-SiCN films decreases with increasing content of carbon and decreasing content of nitrogen in the films. All of the dielectrics, including the three α-SiCN and the one α-SiN films, are thermally stable up to 500°C (for 30 min in N_2 ambient). However, degraded barrier capability and moisture resistance were observed for the α-SiCN film with a *k*-value of 3.5, which has a C/Si atomic ratio of 0.875. This is presumably due to the poorly crosslinked molecular structure and the porosity enrichment caused by the abundant amount of carbon atoms in the α-SiCN film.

References

[1] L. Peters, *Semicond. Int.* (June 2000) p. 122.

[2] P. Xu, K. Huang, A. Patel, S. Rathi, B. Tang, J. Ferguson, J. Huang, C. Ngai, and M. Loboda, *IEEE IITC Technol. Dig.* (1999) p. 109.

[3] M. J. Loboda, *Microelectronic Engineering*, **50** (2000) p. 15.

[4] M. J. Loboda, J. A. Seifferly, and F. C. Dall, *J. Vac. Sci. Technol. A*, **12** (1994) p. 90.

[5] M. J. Loboda, J. A. Seifferly, C. M. Grove, and R. F. Schneider, *Mat. Res. Soc. Symp. Proc.*, **447** (1997) p. 145.

[6] S. G. Lee, Y. J. Kim, S. P. Lee, H. S. Oh, S. J. Lee, M. Kim, I. G. Kim, J. H. Kim, H. J. Shin, J. G. Hong, H. D. Lee, and H. K. Kang, *Jpn. J. Appl. Phys.*, **40** (2001) p. 2663.

[7] B. K. Hwang, M. J. Loboda, G. A. Cerny, R. F. Schneider, J. A. Seifferly, and T. Washer, *IEEE IITC Technol. Dig.* (2000) p. 52.

[8] S. K. Pangrle, S. Nitta, and J. Pellerin, *Symp. VMIC Technol. Dig.* (1999) p. 161.

[9] A. Grill, L. Perraud, V. Patel, C. Jahnes, and S. Cohen, *Mat. Res. Soc. Symp. Proc.*, **565** (1999) p. 107.

[10] C. Kittel, *Introduction to Solid State Physics*, 7th ed. (John Wiley & Sons, New York, 1996) p. 307.

[11] M. Morgen, J. H. Zhao, M. Hay, T. Cho, and P. S. Ho, *Mat. Res. Soc. Symp. Proc.*, **565** (1999) p. 69.

[12] T. Ishimaru, Y. Shioya, H. Ikakura, M. Nozawa, Y. Nishimoto, S. Ohgawara, and K. Maeda, *IEEE IITC Technol. Dig.* (2001) p. 36.

[13] S. W. Rynders, A. Scheeline, and P. W. Bohn, *J. Appl. Phys.*, **69** (1991) p. 2951.

[14] S. J. Gregg and K. S. W. Sing, *Adsorption, Surface Area and Porosity*, 2nd ed. (Academic Press, London, 1982) p. 38.

[15] J. D. McBrayer, R. M. Swanson, and T. W. Sigmon, *J. Electrochem. Soc.*, **133** (1986) p. 1242.

Table 2-1 Compositions, dielectric constants, refractive indices, and deposition temperatures of α-SiCN and α-SiN films.

Sample identification	α-SiCN			α-SiN
	SC3	SC2	SC1	SN
C/Si ratio	0.875	0.718	0.513	0.040
N/Si ratio	0.111	0.333	0.467	1.111
Dielectric constant @ 1 MHz	3.5	4.5	5.4	7.2
Refractive index @ 633 nm	1.65	1.93	1.83	1.95
Deposition temperature (^{o}C)	350	350	400	400

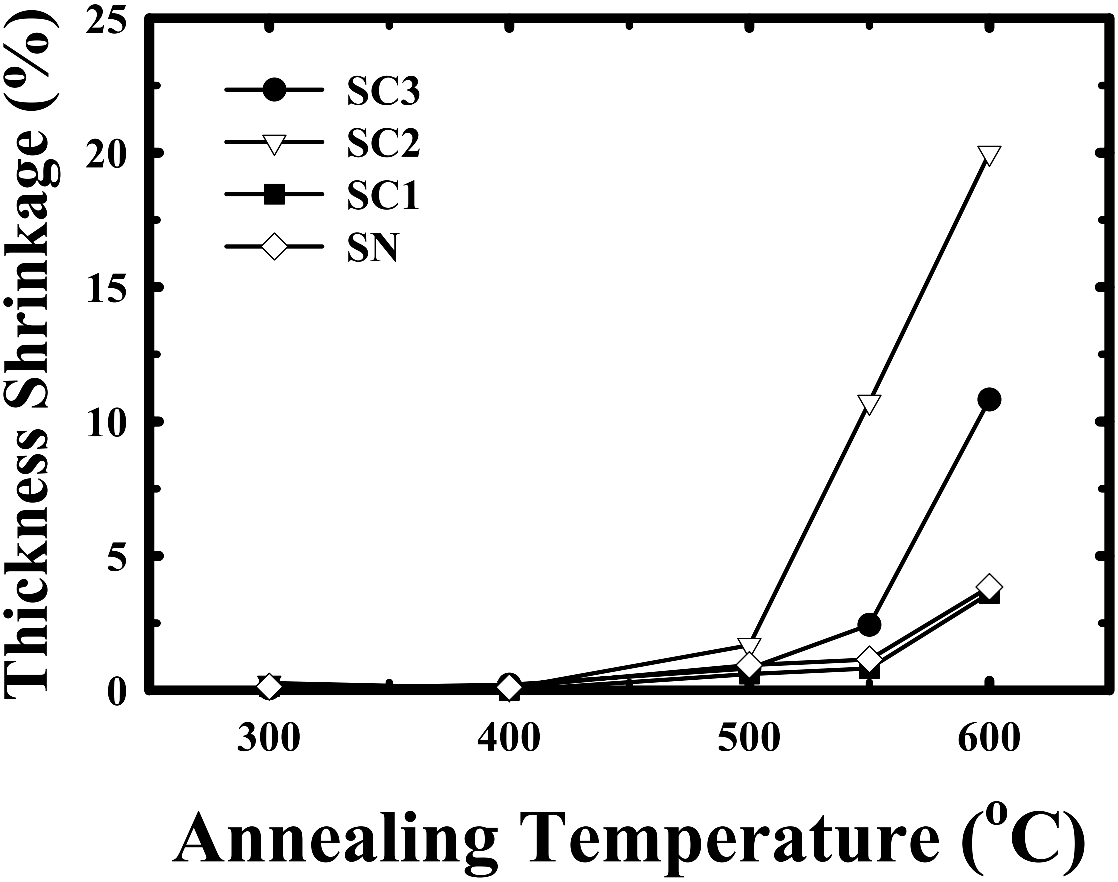

Fig. 2-1 Thickness shrinkage of α-SiCN and α-SiN films vs. annealing temperature.

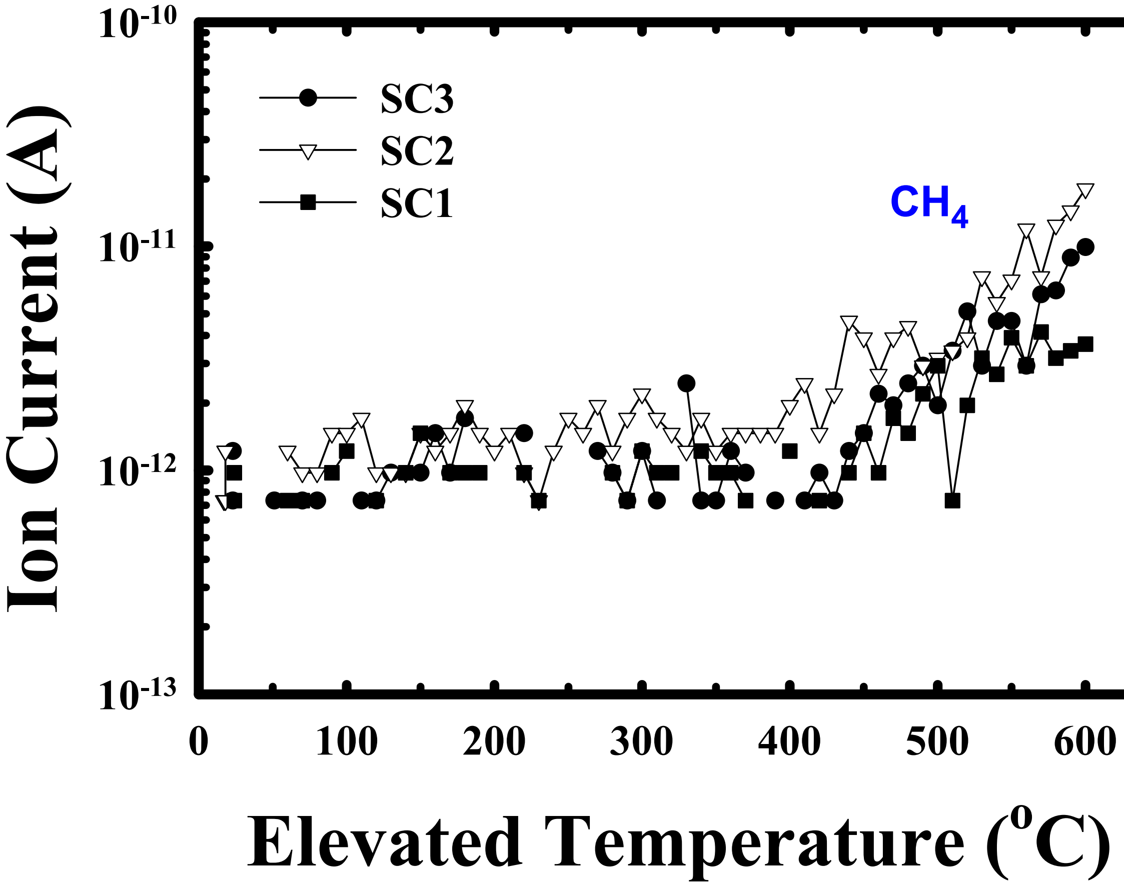

Fig. 2-2 TDS spetra of CH_4 obtained from SC3, SC2, and SC1 films.

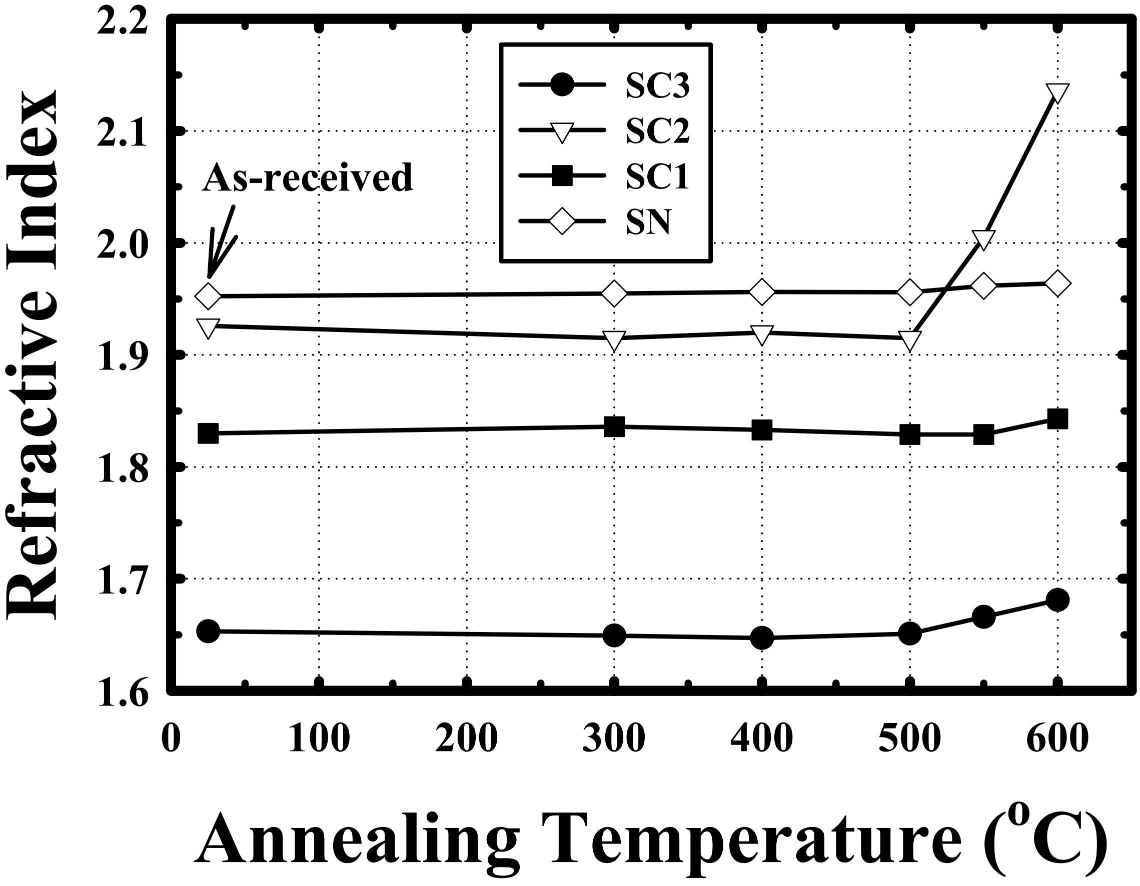

Fig. 2-3 Refractive index of α-SiCN and α-SiN films vs. annealing temperature.

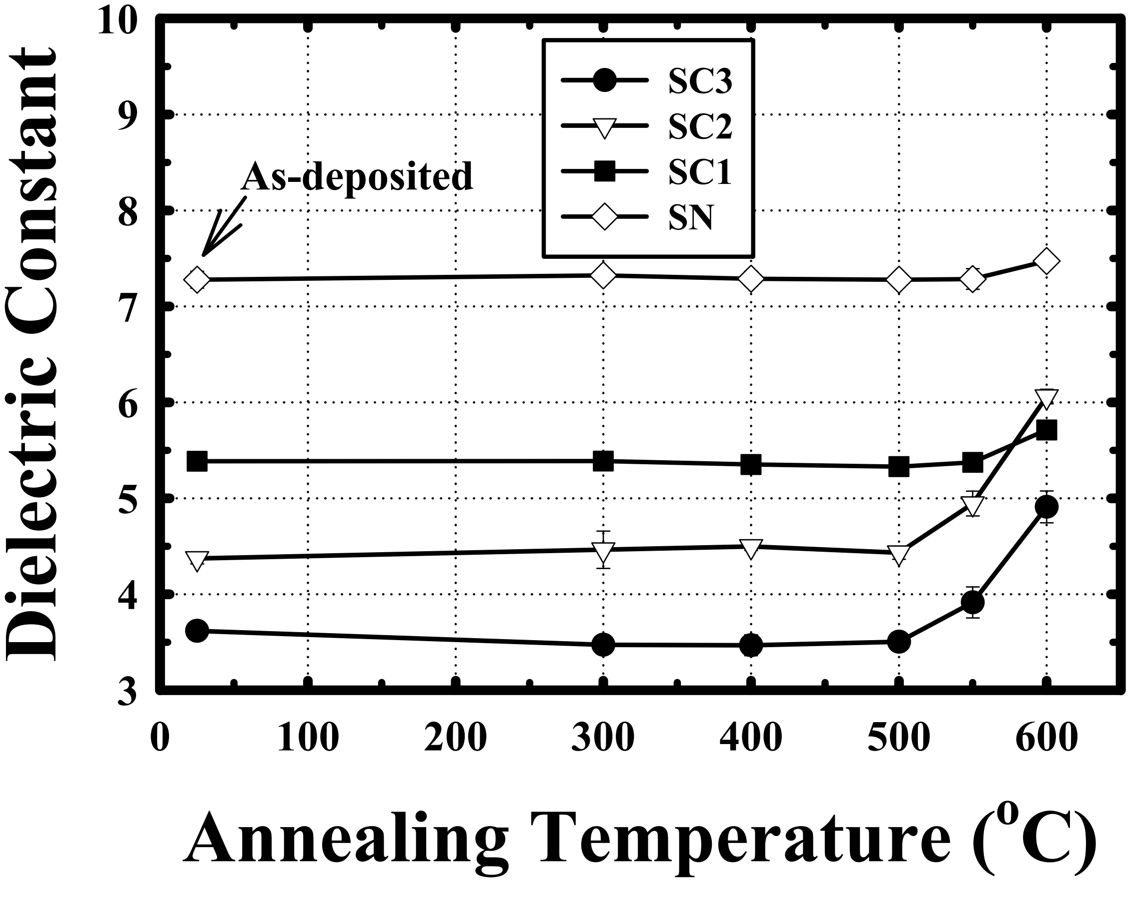

Fig. 2-4 Dielectric constant of α-SiCN and α-SiN films vs. annealing temperature.

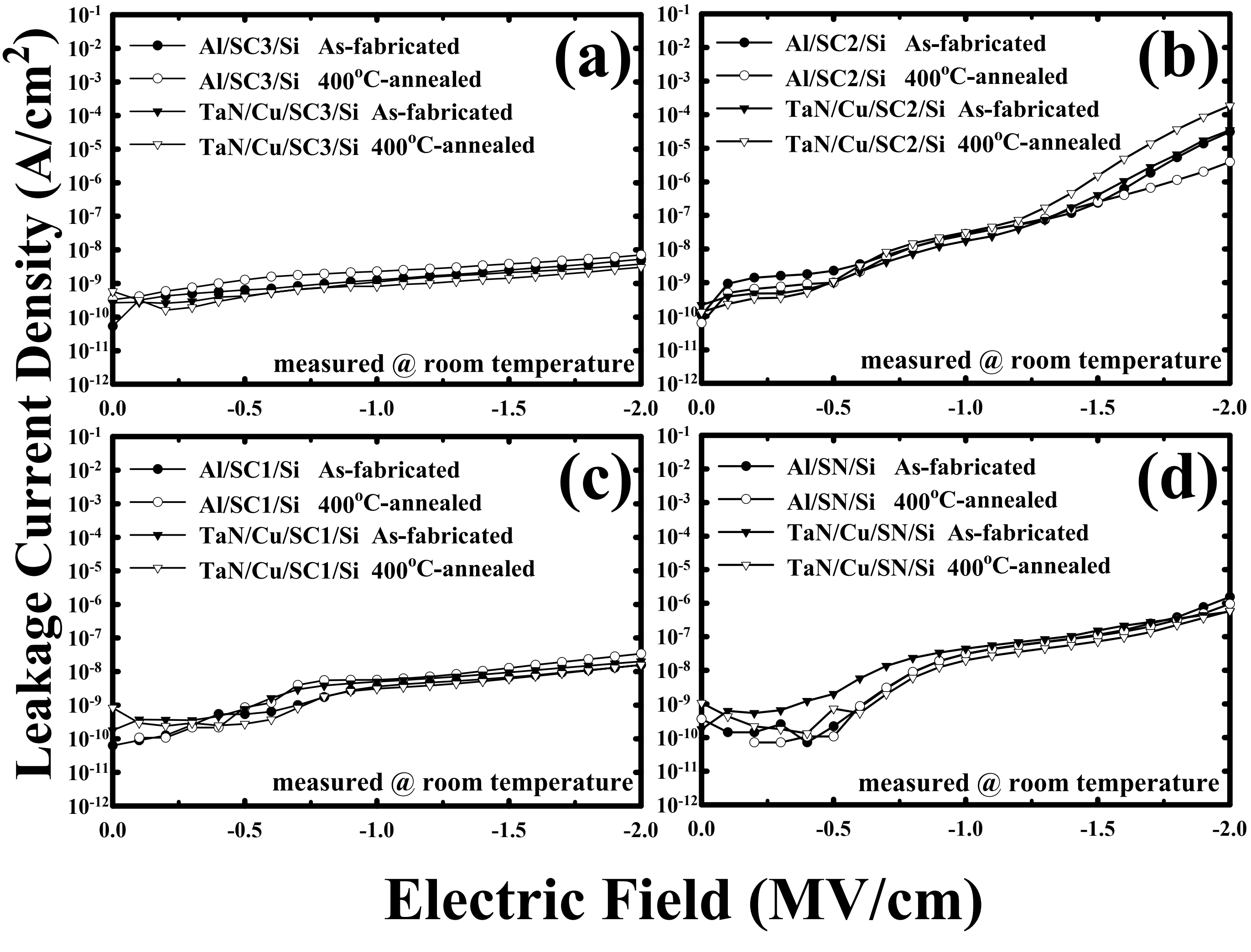

Fig. 2-5 Leakage current density vs. electric field measured at room temperature for the as-fabricated and 400°C-annealed Al- and TaN/Cu-gated MIS capacitors of (a) SC3, (b) SC2, (c) SC1, and (d) SN dielectric films.

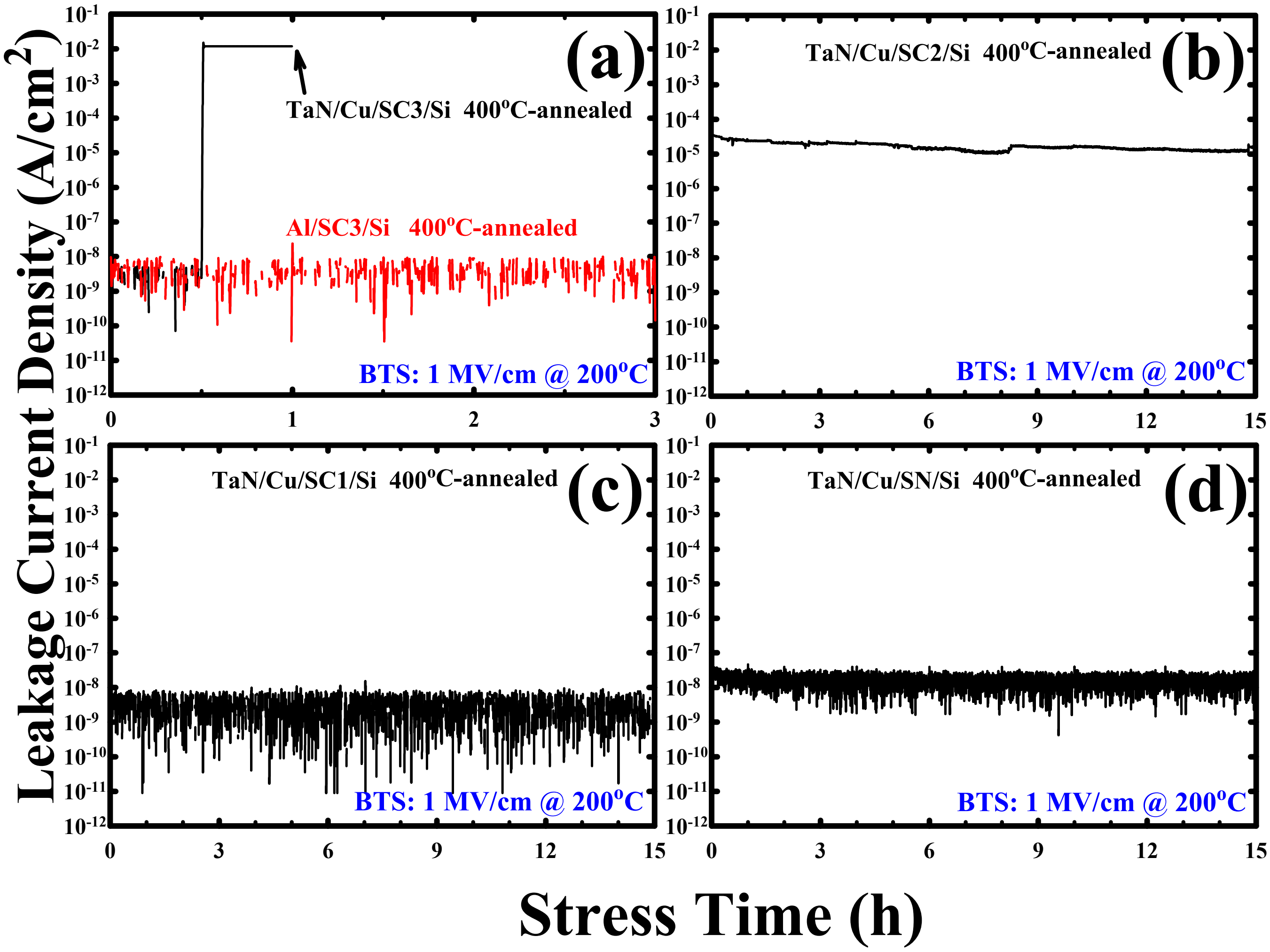

Fig. 2-6 Time-dependent dielectric breakdown (TDDB) of Al- and TaN/Cu-gated MIS capacitors of (a) SC3, (b) SC2, (c) SC1, and (d) SN dielectric films under BTS at 200^{o}C with an electric field of 1 MV/cm.

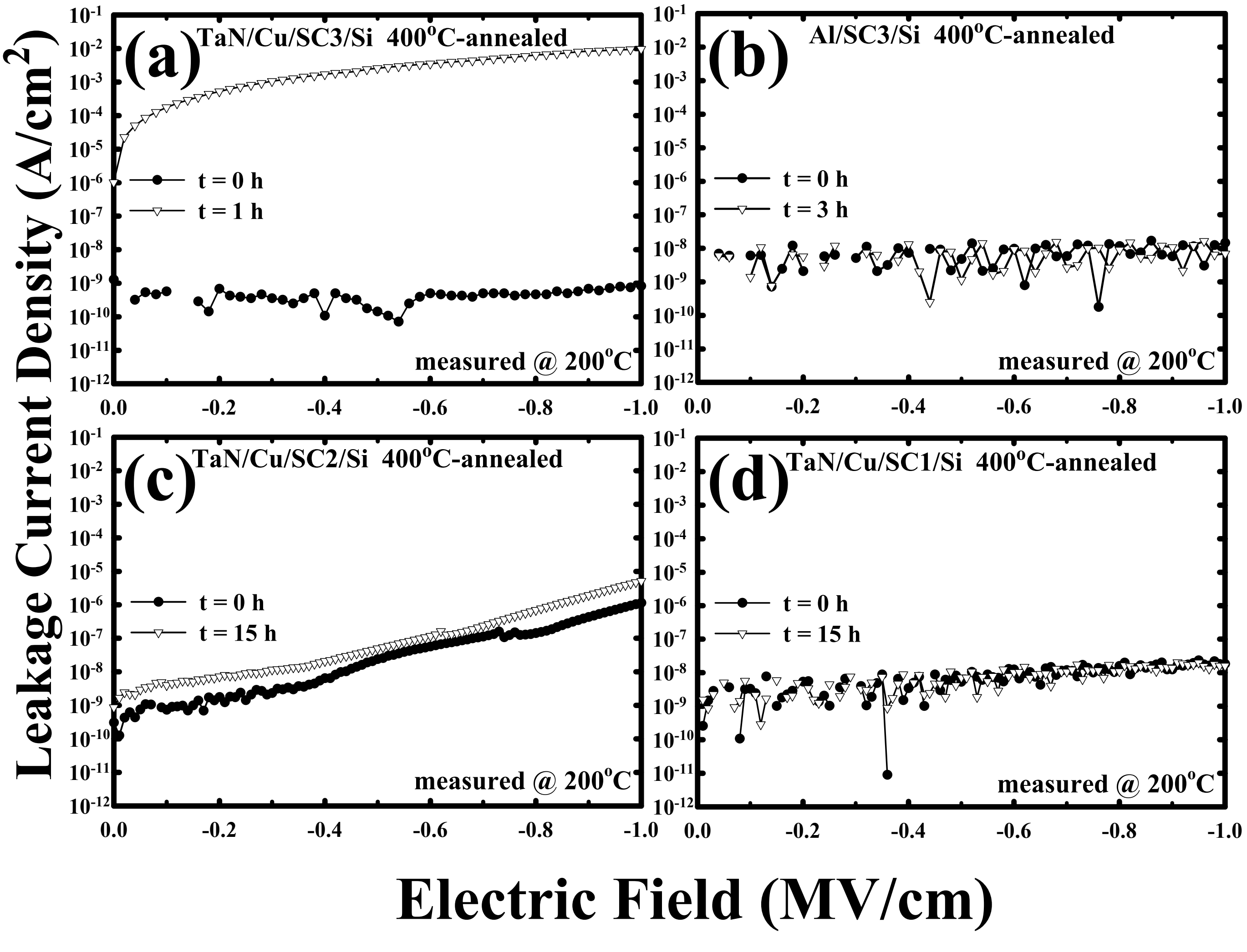

Fig. 2-7 Leakage current density vs. electric field measured at 200°C for (a) TaN/Cu/SC3/Si, (b) Al/SC3/Si, (c) TaN/Cu/SC2/Si, and (d) TaN/Cu/SC1/Si samples before and immediately after a BTS test at 200°C with an electric field of 1 MV/cm.

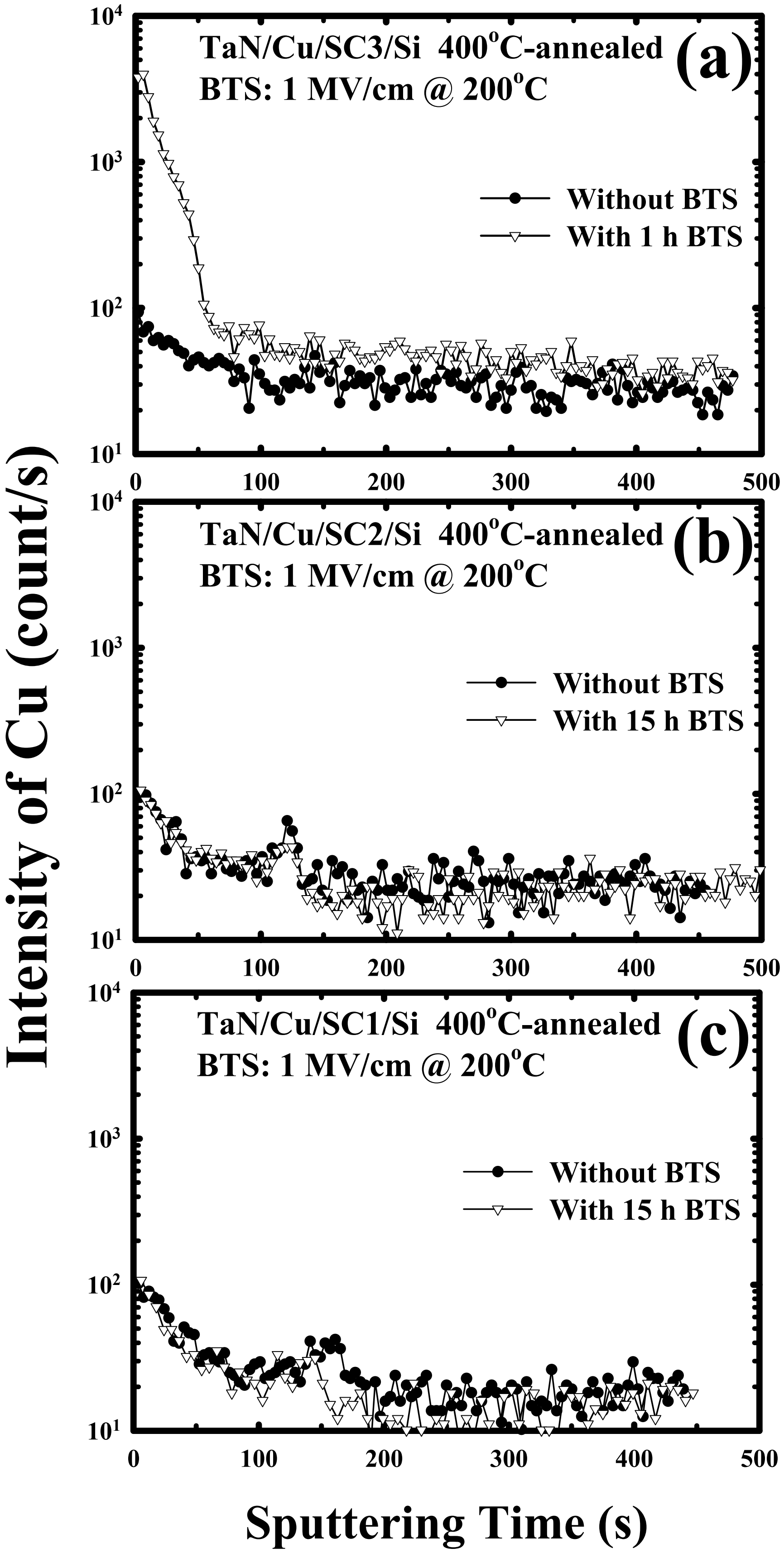

Fig. 2-8 SIMS depth profiles of Cu in (a) SC3 film of TaN/Cu/SC3/Si, (b) SC2 film of TaN/Cu/SC2/Si, (c) SC1 film of TaN/Cu/SC1/Si capacitors before and after a BTS test at 200°C with an electric field of 1 MV/cm. The TaN/Cu electrodes were removed before the measurements of SIMS profiles.

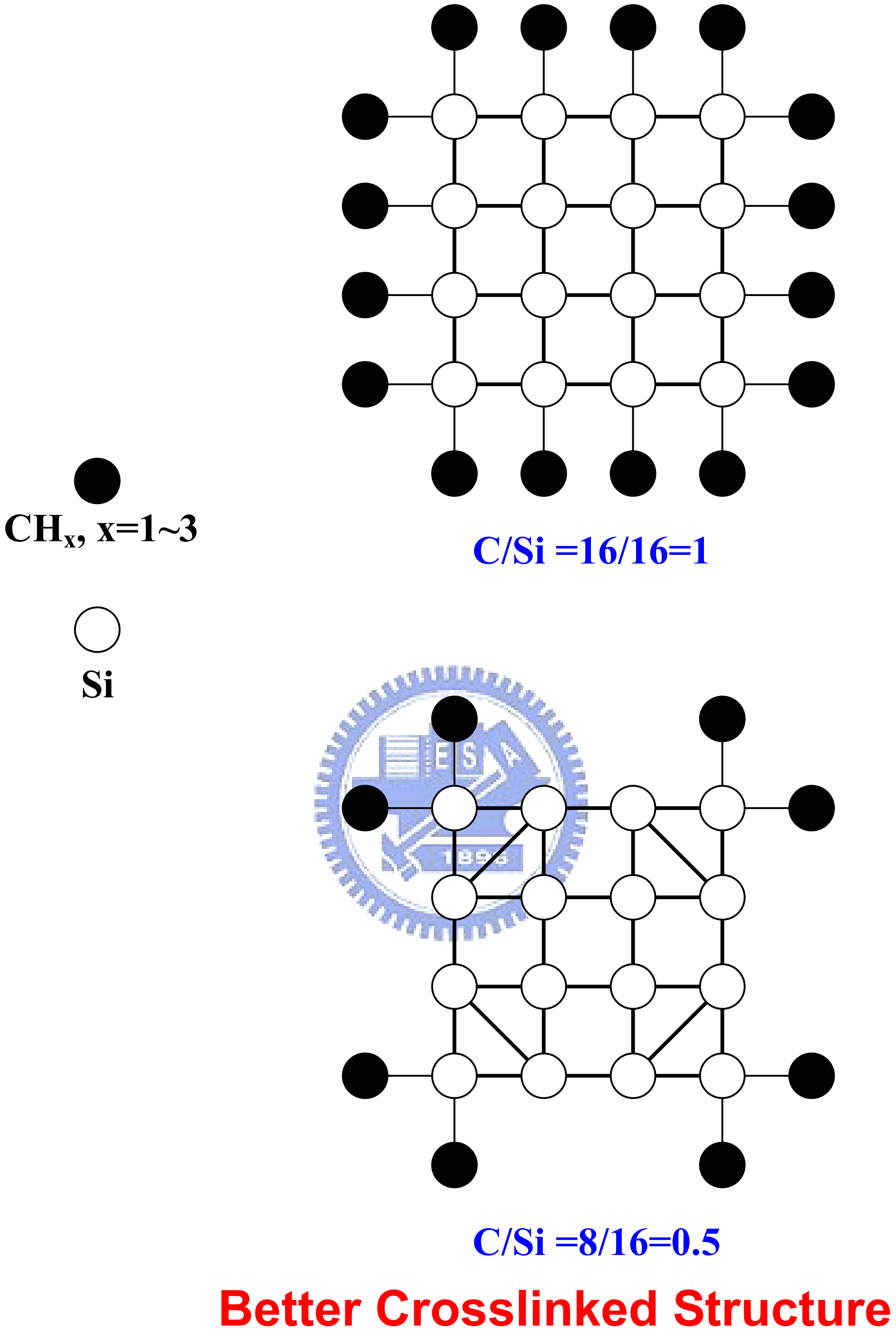

Fig. 2-9 Schematic diagram showing molecular structures of α-SiCN films with different C/Si ratios. This is a simple two-dimensional sketch; the actual structure should be three-dimensional.

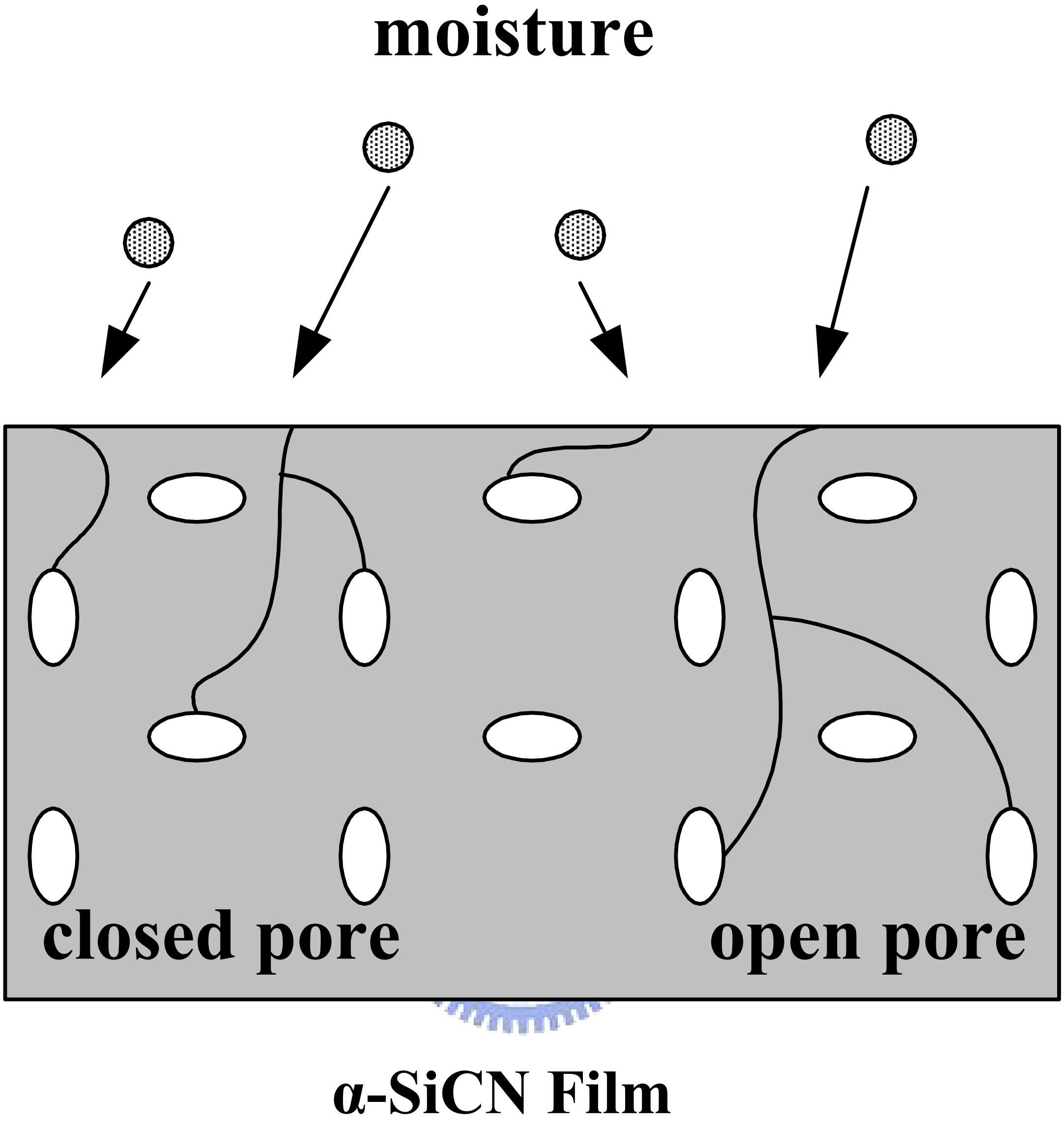

Fig. 2-10 Schematic diagram showing microstructure of a porous α-SiCN film.

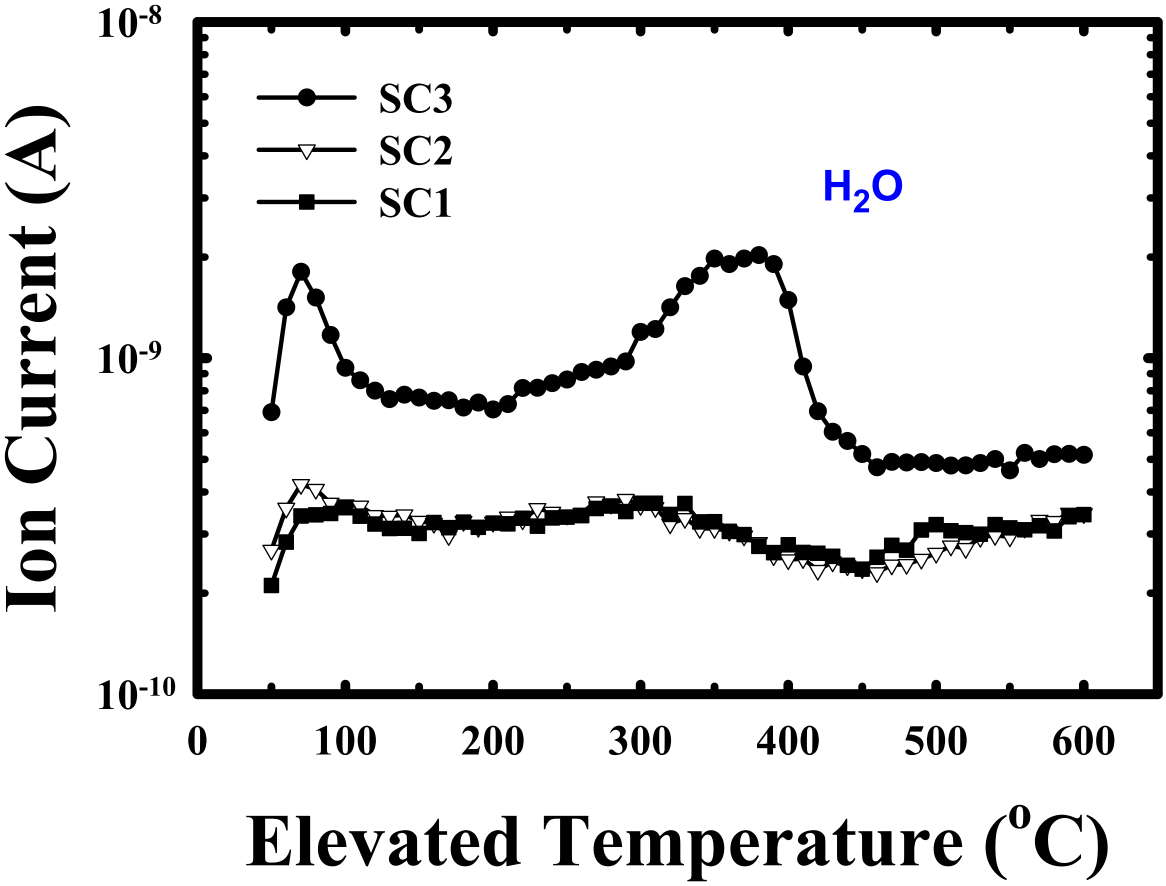

Fig. 2-11 TDS spectra of H_2O obtained from SC3, SC2, and SC1 films after immersion in boiling water for 1 h.

Chapter 3

α-SiCN Dielectric Barrier with Different Hydrogen Concentration

3-1 Introduction

Many low-stress and thermally stable low-*k* SiC-based films deposited by PECVD using organosilicate gases have been investigated [1-5], like the α-SiCN films discussed in chapter 2. The thermal stability and physical and barrier properties of α-SiCN films are dependent on the carbon (C) and nitrogen (N) concentrations. However, the α-SiCN films deposited using $(CH_3)_3SiH$ (3MS) organosilicate gas usually contains a rich content of hydrogen (H). In this chapter, we investigate the physical and barrier properties of two low-*k* (k<5) α-SiCN dielectric films with nearly the same carbon and nitrogen contents but fairly different hydrogen concentrations.

3-2 Experimental Details

Two α-SiCN dielectric films with different hydrogen concentrations are investigated in this chapter. They are both deposited to a thickness of 50 nm on p-type, (100)-oriented Si wafers using a parallel-plate PECVD system operated at 13.56 MHz. The α-SiCN films were deposited at a temperature of 350°C using $NH_3/SiH(CH_3)_3$ gases with the flow ratios of 0.5 to 2.0, a total gas pressure of 3-5 Torr, and a plasma power of 150-350 W, resulting in the two α-SiCN films with different compositions. Both films were annealed at 400°C for 30 min in N_2 ambient to remove moisture possibly absorbed in the dielectrics prior to the investigation of the physical properties or the deposition of electrode (TaN/Cu or Al) to construct the MIS capacitor structure. The

TaN/Cu-gated MIS capacitors were constructed by first sputter-depositing a 200-nm-thick Cu layer on the α-SiCN films, followed by a reactive sputter deposition of a 50-nm-thick TaN layer on the Cu surface in the same sputtering system without breaking the vacuum. The TaN film served as a passivation layer to prevent Cu metal from oxidizing in the subsequent high-temperature processes. For a comparison, Al-electrode control samples were also prepared by depositing a 500-nm-thick Al layer directly on the α-SiCN dielectric surfaces. All metal electrodes were defined by a lift-off process in order to prevent unexpected deterioration of the dielectrics by chemical wet etching. For better electrical measurements, a 500-nm-thick Al layer was also deposited on the back surface of the Si substrate for all samples. Some of the prepared MIS samples were thermally annealed at 400°C for 30 min in N_2 ambient. This annealing step eliminates the plasma-induced damage during the sputter deposition of the TaN/Cu electrodes and also provides the driving force for Cu diffusion.

Secondary ion mass spectrometry (SIMS) was used to detect the compositions of the α-SiCN films and the penetration of Cu or Al in the dielectrics. Thermal desorption spectroscopy (TDS) was used to analyze the outgassing behavior of the dielectrics during the thermal annealing process. Fourier transform infrared spectroscopy (FTIR) was used to analyze the chemical bonding of the dielectrics. The film thickness and refractive index were measured by an n&k analyzer at 633 nm wavelength, and the *k*-value of the dielectrics was determined by the maximum capacitance of the Al-gated MIS capacitors measured at 1 MHz using a Keithley 82 C-V measurement system. An HP4145B semiconductor parameter analyzer was used to measure the dielectric leakage current and provide the bias for the bias-temperature stress (BTS).

3-3 Physical Property and Thermal Stability

Table 3-1 shows the $NH_3/SiH(CH_3)_3$ flow ratios, compositions, refractive indices, and dielectric constants for the two PECVD α-SiCN dielectric films studied in this chapter. The SCH1 film has a higher content of hydrogen than the SCH0 film. As a result, the SCH1 film has a lower refractive index, and thus a smaller electronic polarization and a lower dielectric constant [6], similar to the well-known hydrogen silsesquioxane [HSQ, $(HSiO_{1.5})_{2n}$, n=3 to 8] low-*k* material [7]. Figure 3-1 shows the TDS spectra of these PECVD α-SiCN dielectric films. The outgassing of the CH_4 molecule from the α-SiCN dielectric films started at a temperature of about 450°C. Figure 3-2 shows the thickness shrinkage of the dielectrics thermally annealed at various temperatures for 30 min in N_2 ambient. Both films remained nearly unchanged in thickness at temperatures up to 400°C but slightly shrunk at 500°C. Upon annealing at 600°C, the thickness shrinkage exceeded 5% for both films, presumably due to the massive outgassing of CH_4. This implies that the thickness shrinkage is closely related to the changes in the chemical bonding and microstructure of the dielectric films, which also result in the variation of the refractive indices and dielectric constants of the dielectrics, as shown in Figs. 3-3 and 3-4, respectively. The refractive indices and dielectric constants of the two α-SiCN dielectrics remained nearly constant at temperatures up to 500°C but increased drastically at temperatures above 550°C, in particular the SCH1 film.

3-4 Electrical and Barrier Properties

Figure 3-5 shows the room-temperature leakage current density for the as-fabricated as well as 400°C-annealed (30 min in N_2 ambient) Al-gated and TaN/Cu-gated MIS capacitors of the α-SiCN dielectric films. The measurements were performed with the MIS capacitors biased in the accumulation region. For each dielectric film, a negligible difference in leakage current was observed between the Al-gated and TaN/Cu-gated MIS capacitors, whether as-fabricated or 400°C-annealed. This implies that both SCH0 and SCH1 dielectric films were capable of preventing Cu penetration at temperatures up to 400°C. The BTS test was used to further explore the barrier property of the dielectric films. The BTS test was performed at 200°C with an applied electric field of 1 MV/cm on the MIS capacitors that had been annealed at 400°C for 30 min. N_2 purging was used to prevent the oxidation of the Cu electrode and moisture uptake in the dielectric films during the BTS test. Figure 3-6 shows the leakage current density versus stress time for the TaN/Cu-gated and Al-gated MIS capacitors under the BTS. It can be seen that the TaN/Cu- and Al-gated SCH1 samples failed after approximately 30 min BTS, whereas the SCH0 sample remained stable under the BTS up to at least 15 h. The breakdown of the TaN/Cu- and Al-gated SCH1 samples is presumably due to the wear-out of the SCH1 film resulting from the BTS rather than the penetration of Cu into the SCH1 dielectric. The wear-out of dielectrics is defined as the dielectric breakdown resulting from prolonged thermal and/or electrical stress. Figure 3-7 illustrates the leakage current density versus electric field for various MIS capacitors measured at 200°C before and immediately after the BTS. There are significant increases in leakage current for the TaN/Cu- and Al-gated SCH1 samples after 1 h BTS because of the dielectric breakdown, while the SCH0 sample shows a negligible change in leakage current even after 15 h BTS. Figure 3-8 shows the SIMS depth profiles of Cu and Al in the TaN/Cu- and Al-gated SCH1 films after removal of the TaN/Cu and Al electrodes, respectively. No apparent penetration of Cu and Al into the SCH1 dielectric was detected for the TaN/Cu- and Al-gated SCH1 samples after 1 h BTS. Thus, we may conclude that the spiking in the leakage current of the TaN/Cu- and Al-gated SCH1 samples during the BTS test (Fig. 3-6a) and the significant increase of leakage current in the TaN/Cu- and Al-gated SCH1 samples after 1 h BTS (Figs. 3-7a and 3-7b), resulted from the wear-out of the SCH1 film during the BTS test.

The poor dielectric strength of the SCH1 film during the BTS might be attributed to its large hydrogen content. A large hydrogen content tends to create a large number of hydrogen-related defects, such as Si-H^+-Si hydrogen bridges [8,9], resulting in the degradation of the dielectric strength. Moreover, the large hydrogen content in the SCH1 film may also produce numerous Si-H weak bonds (320 kJ/mol) [10], as illustrated by the stronger Si-H peak associated with the SCH1 film in the FTIR spectra shown in Fig. 3-9. Presumably due to numerous hydrogen-related defects and Si-H weak bonds, the SCH1 dielectric film exhibited a lower dielectric breakdown field than the SCH0 film, as shown in Fig. 3-10. We may also conclude that the wear-out of the SCH1 film in the TaN/Cu/SCH1/Si and Al/SCH1/Si MIS capacitors during the BTS is attributed to the hydrogen-related defects and the Si-H weak bonds arisen from the large hydrogen content in the film.

3-5 Summary

Two α-SiCN films with different hydrogen concentrations and dielectric constants of less than 5 were investigated with respect to their thermal stability and physical and barrier properties. It is found that the α-SiCN film with a larger hydrogen content has a lower dielectric constant. Both α-SiCN films are thermally stable at temperatures up to 500^{o}C (for 30 min in N_2 ambient). However, a degraded dielectric strength was observed for the α-SiCN film with a lower k-value of 4, which has a much larger hydrogen content. This may be attributed to the hydrogen-related defects, such as Si-H^+-Si hydrogen bridges, and numerous Si-H weak bonds arisen from the large hydrogen content in the α-SiCN film.

References

[1] P. Xu, K. Huang, A. Patel, S. Rathi, B. Tang, J. Ferguson, J. Huang, C. Ngai, and M. Loboda, *IEEE IITC Technol. Dig.* (1999) p. 109.

[2] M. J. Loboda, *Microelectronic Engineering*, **50** (2000) p. 15.

[3] M. J. Loboda, J. A. Seifferly, and F. C. Dall, *J. Vac. Sci. Technol. A*, **12** (1994) p. 90.

[4] C. C. Chiang, M. C. Chen, Z. C. Wu, L. J. Li, S. M. Jang, C. H. Yu, and M. S. Liang, *IEEE IITC Technol. Dig.* (2002) p. 200.

[5] S. G. Lee, Y. J. Kim, S. P. Lee, H. S. Oh, S. J. Lee, M. Kim, I. G. Kim, J. H. Kim, H. J. Shin, J. G. Hong, H. D. Lee, and H. K. Kang, *Jpn. J. Appl. Phys.*, **40** (2001) p. 2663.

[6] C. Kittel, *Introduction to Solid State Physics*, 7th ed. (John Wiley & Sons, New York, 1996) p. 390.

[7] S. P. Jeng, K. Taylor, T. Seha, M. C. Chang, J. Fattaruso, and R. H. Havemann, *IEEE VLSI Technol. Dig.* (1995) p. 61.

[8] P. E. Blöchl and J. H. Stathis, *Physical Rev. Lett.*, **83** (1999) p. 372.

[9] J. Suñé and E. Wu, *IEEE VLSI Technol. Dig.* (2001) p. 97.

[10] J. R. Bowser, *Inorganic Chemistry* (Brooks/Cole Publishing Co., California, 1993) p. 401.

Table 3-1 Compositions and some basic data of α-SiCN dielectrics. The compositions of the dielectrics are detected by SIMS analysis.

Sample designation	**SCH1**	**SCH0**
$NH_3/SiH(CH_3)_3$ flow ratio	**0.5-1**	**1.5-2**
H ($\times 10^4$ count/s)	**10.71**	**3.57**
N ($\times 10^4$ count/s)	**0.342**	**0.281**
C ($\times 10^4$ count/s)	**2.77**	**2.84**
Si ($\times 10^4$ count/s)	**24.2**	**23.5**
Refractive index @ 633 nm	**1.64**	**1.81**
Dielectric constant @ 1 MHz	**4.0**	**4.8**

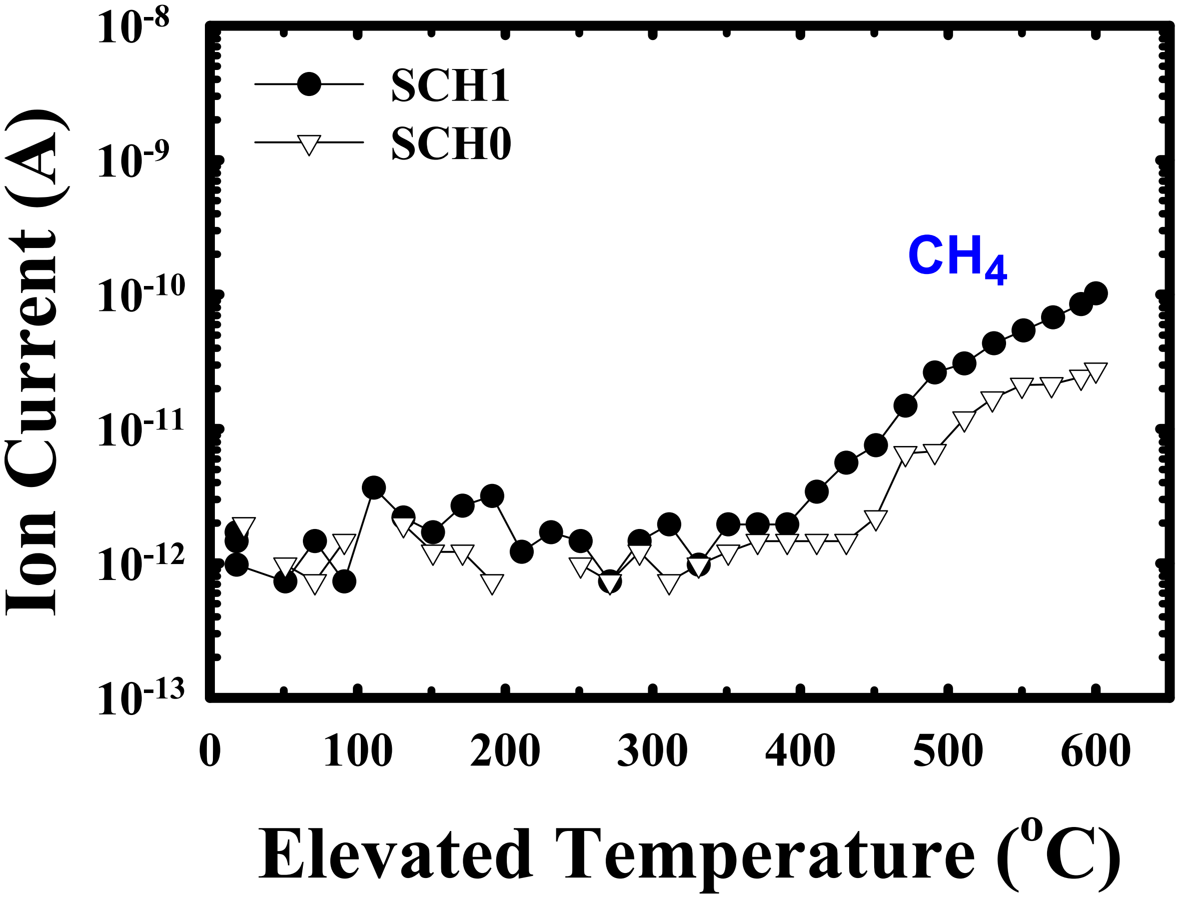

Fig. 3-1 TDS spectra of CH_4 obtained from two PECVD α-SiCN dielectrics.

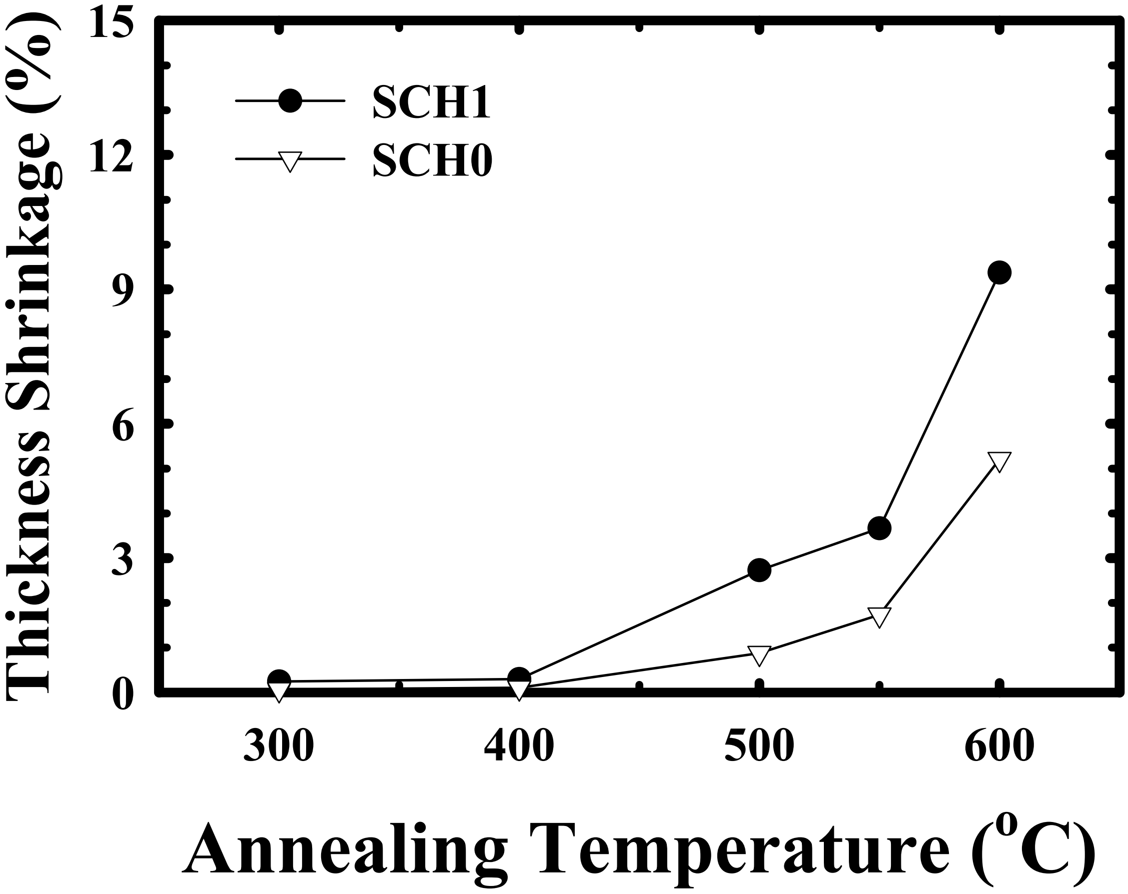

Fig. 3-2 Thickness shrinkage vs. annealing temperature for two PECVD α-SiCN dielectrics.

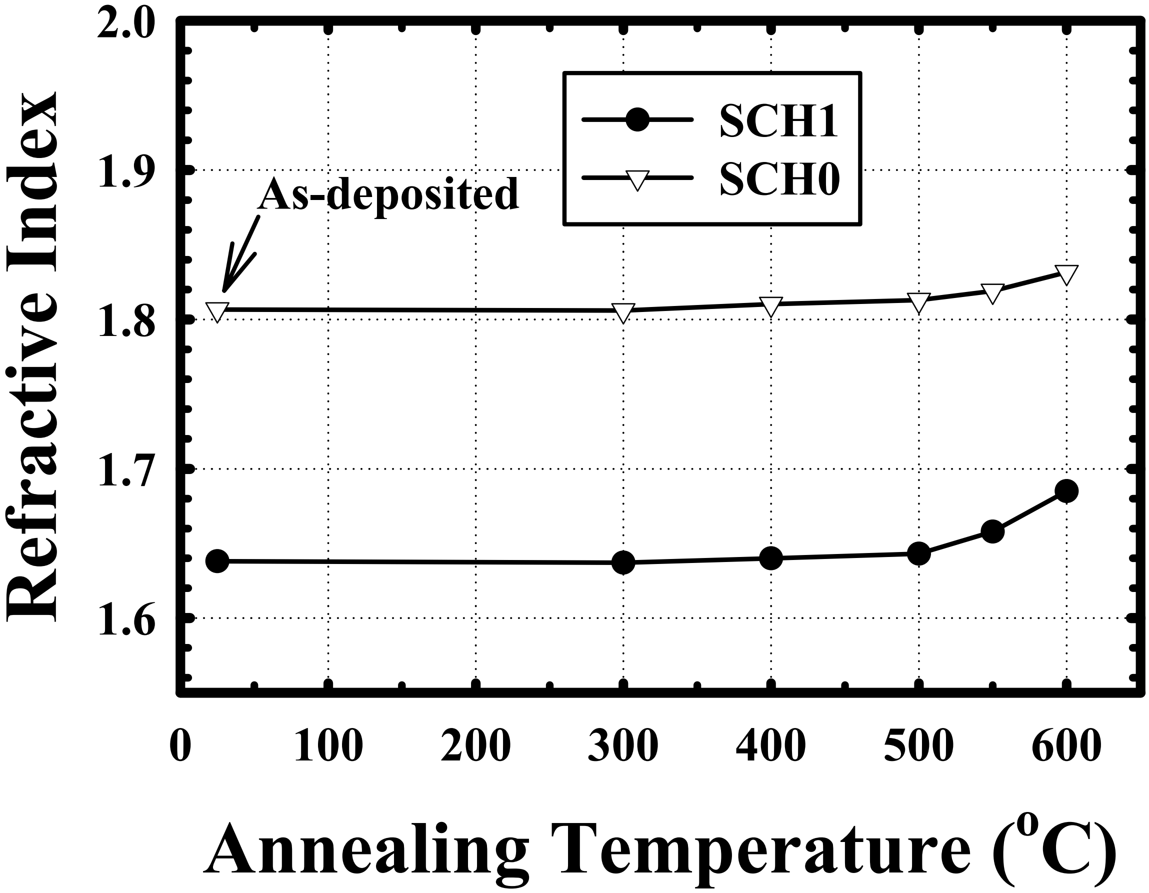

Fig. 3-3 Refractive index vs. annealing temperature for two PECVD α-SiCN dielectrics.

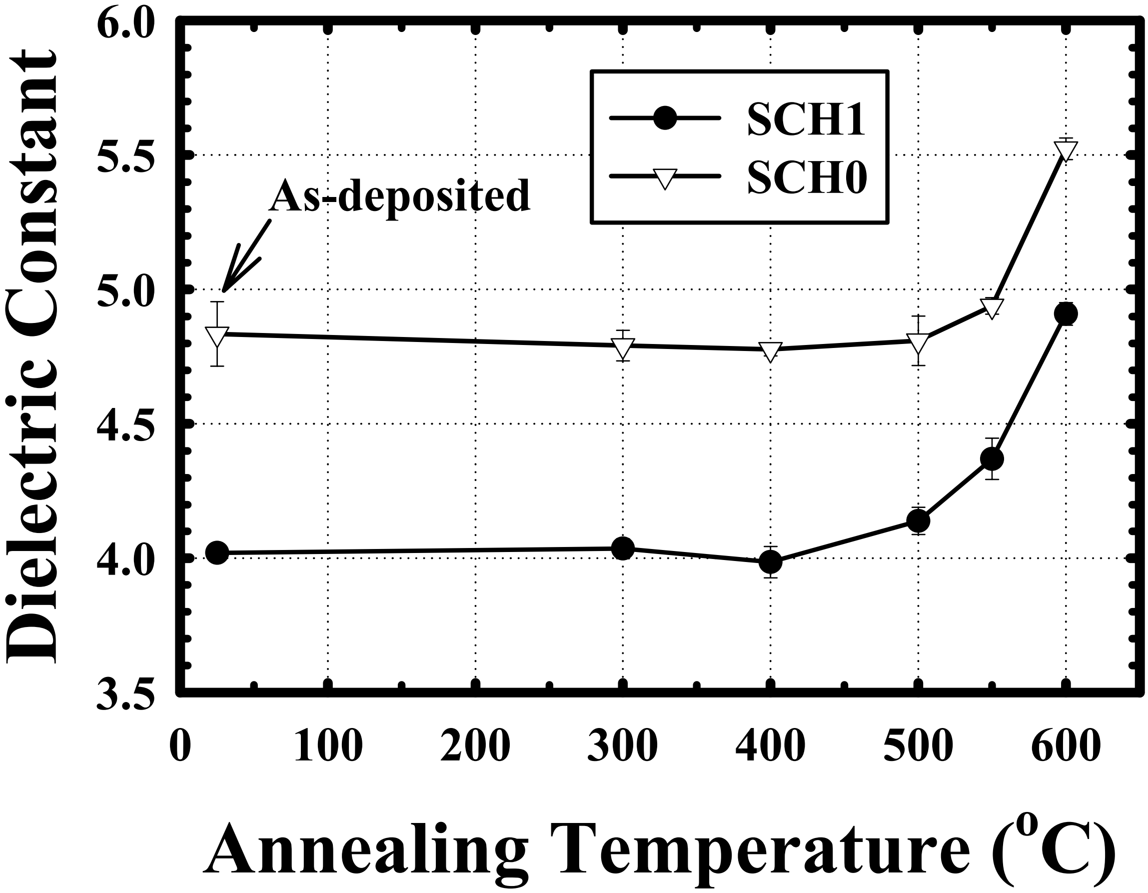

Fig. 3-4 Dielectric constant vs. annealing temperature for two PECVD α-SiCN dielectrics.

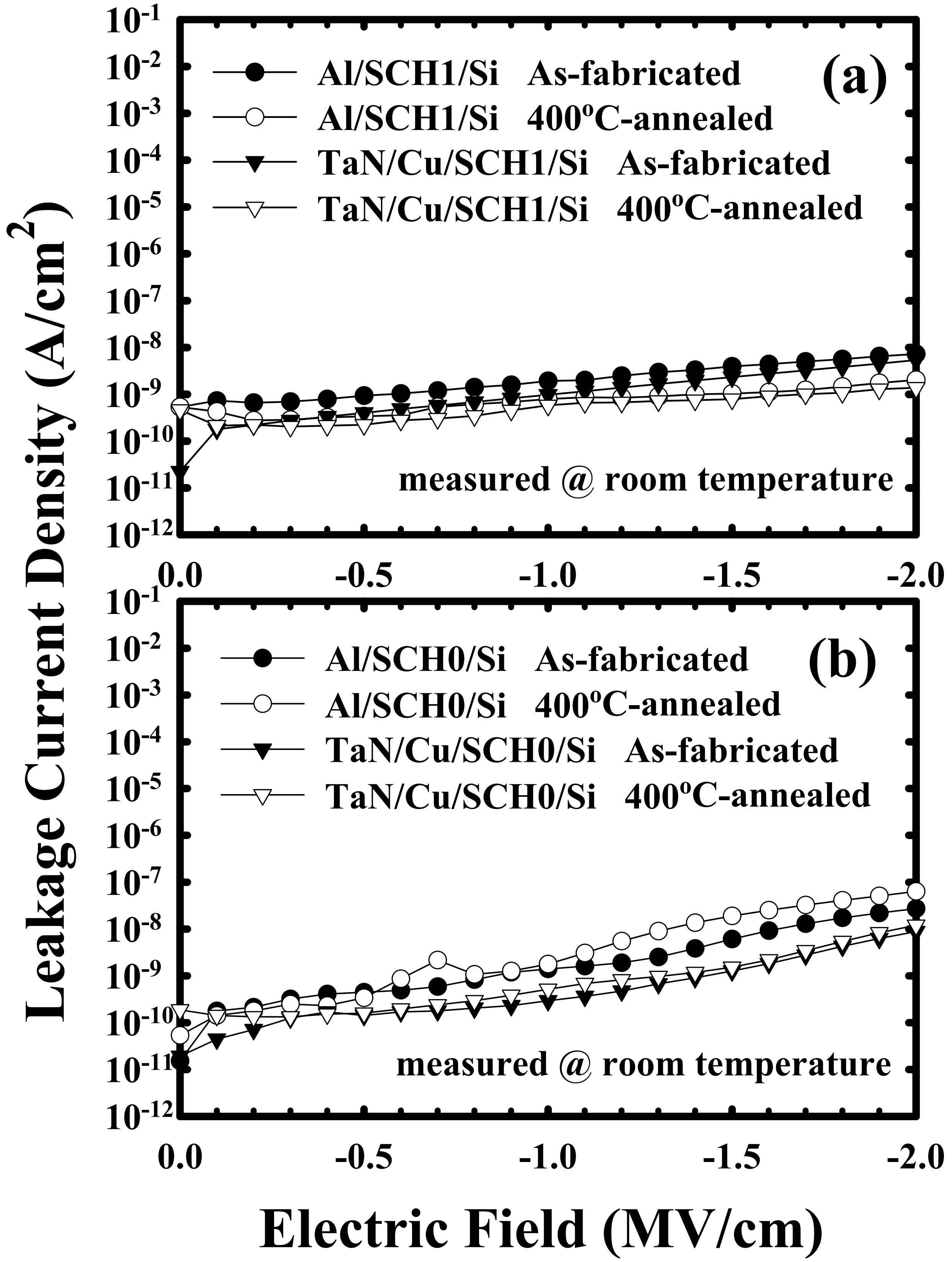

Fig. 3-5 Leakage current density vs. electric field measured at room temperature for the as-fabricated and 400°C annealed Al- and TaN/Cu-gated MIS capacitors of (a) SCH1 and (b) SCH0 dielectric films.

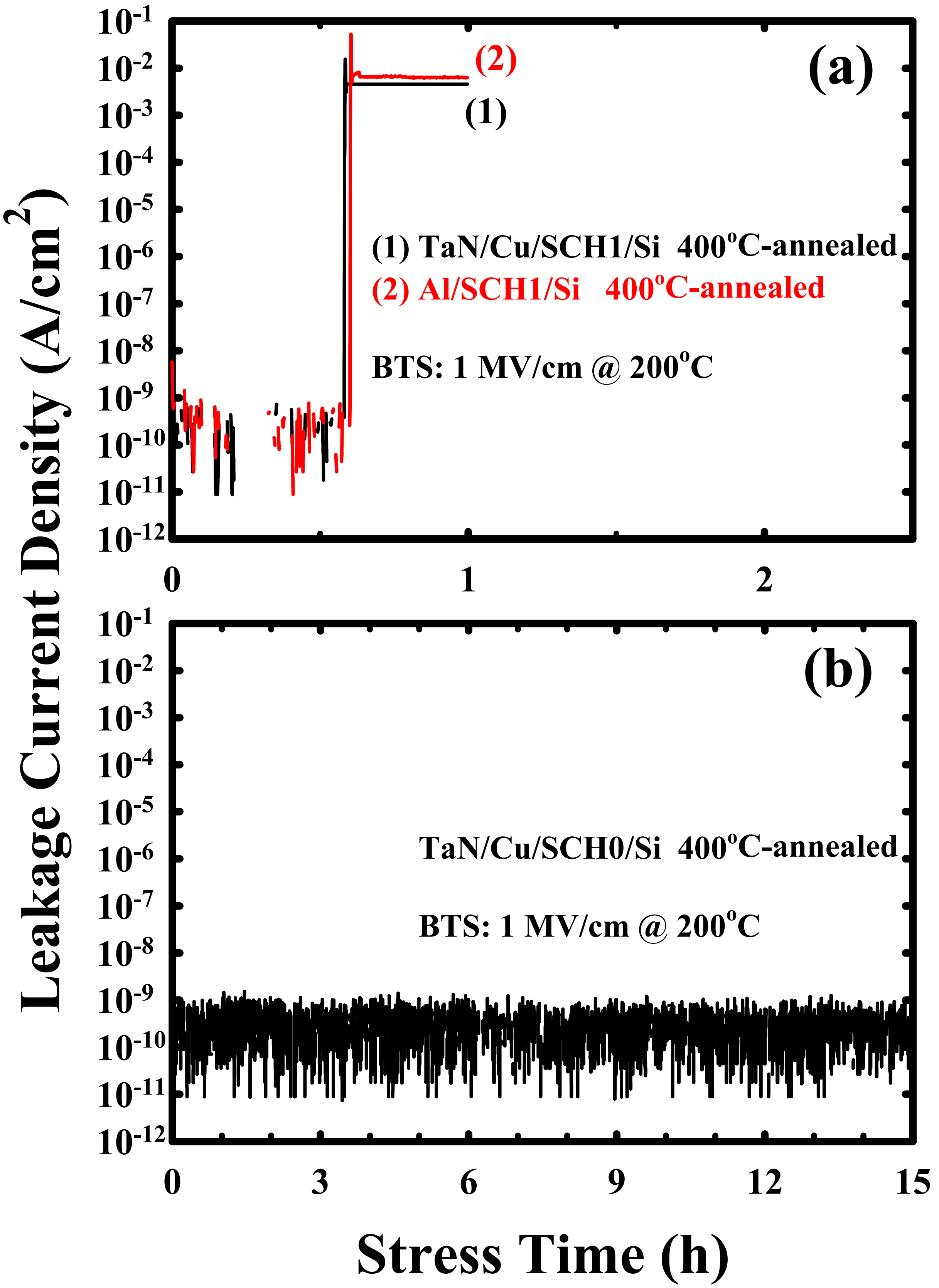

Fig. 3-6 Time-dependent dielectric breakdown (TDDB) for the Al- and TaN/Cu-gated MIS capacitors of (a) SCH1 and (b) SCH0 dielectric films under BTS at 200°C with an electric field of 1 MV/cm.

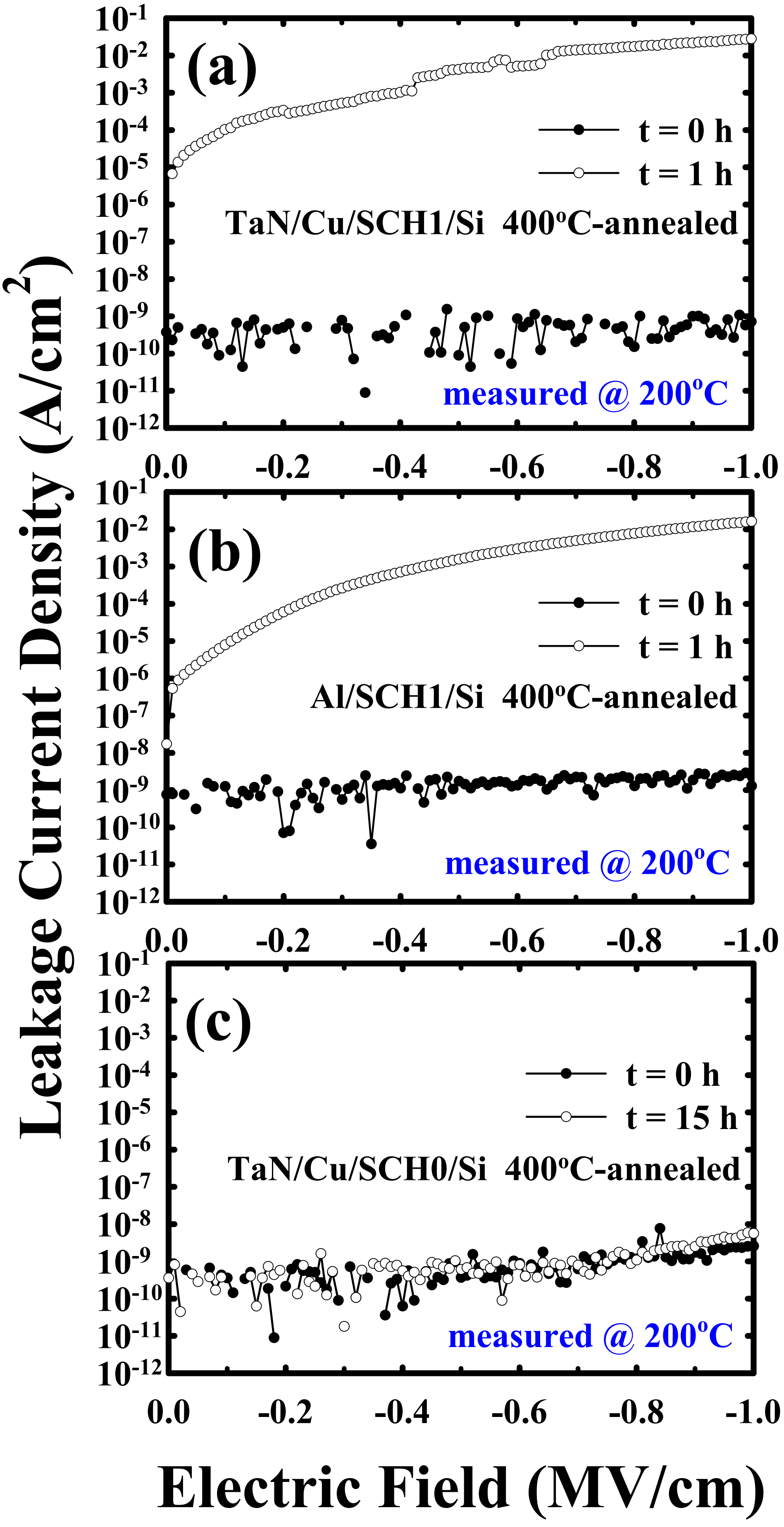

Fig. 3-7 Leakage current density vs. electric field measured at 200°C for (a) TaN/Cu/SCH1/Si, (b) Al/SCH1/Si, and (c) TaN/Cu/SCH0/Si samples before and immediately after 1 h or 15 h BTS at 200°C with an electric field of 1 MV/cm.

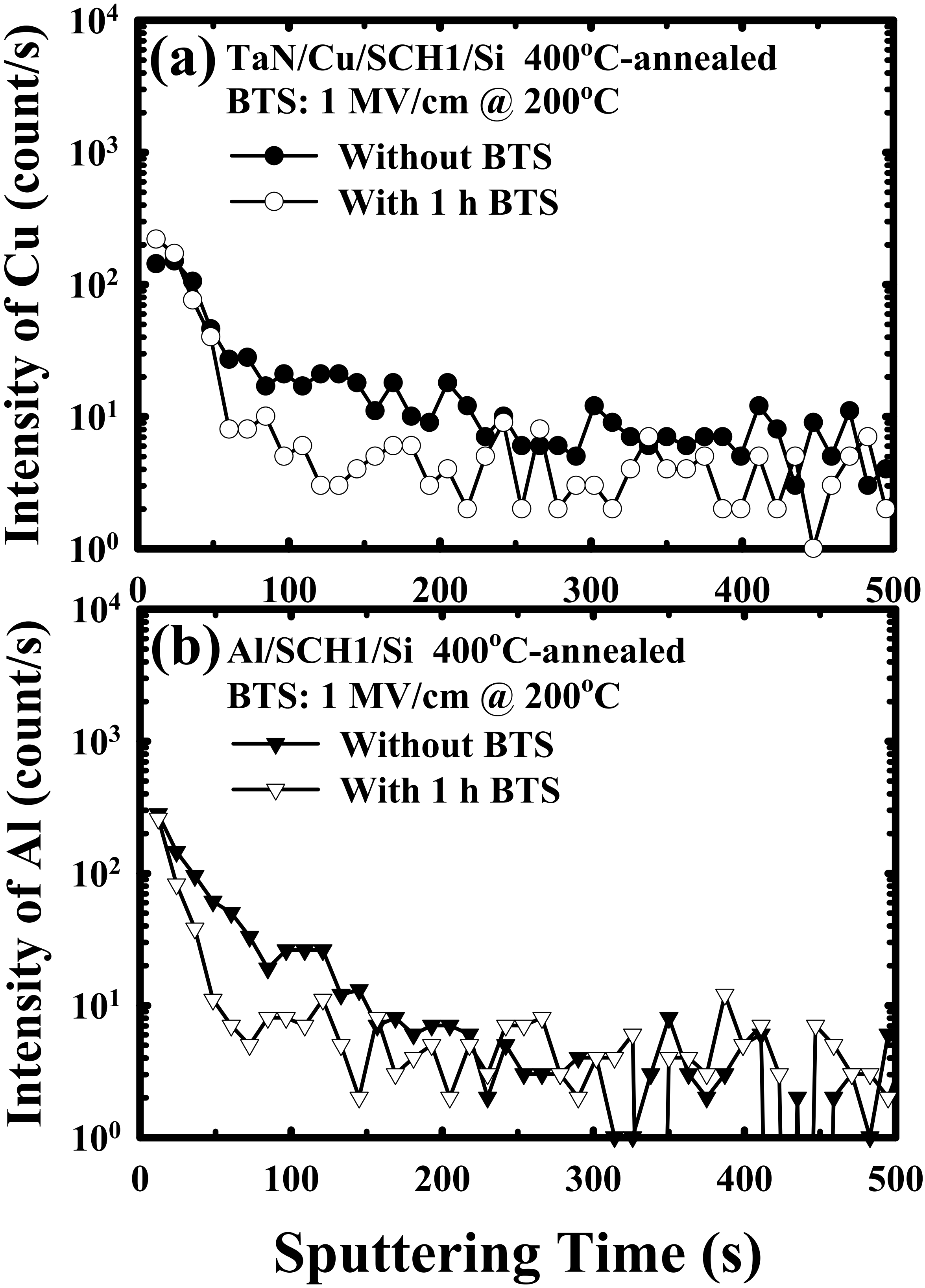

Fig. 3-8 SIMS depth profiles of (a) Cu in SCH1 film of TaN/Cu/SCH1/Si capacitor and (b) Al in SCH1 film of Al/SCH1/Si capacitor before and after 1 h BTS at 200°C with an electric field of 1 MV/cm. The TaN/Cu and Al electrodes were removed before the SIMS analysis.

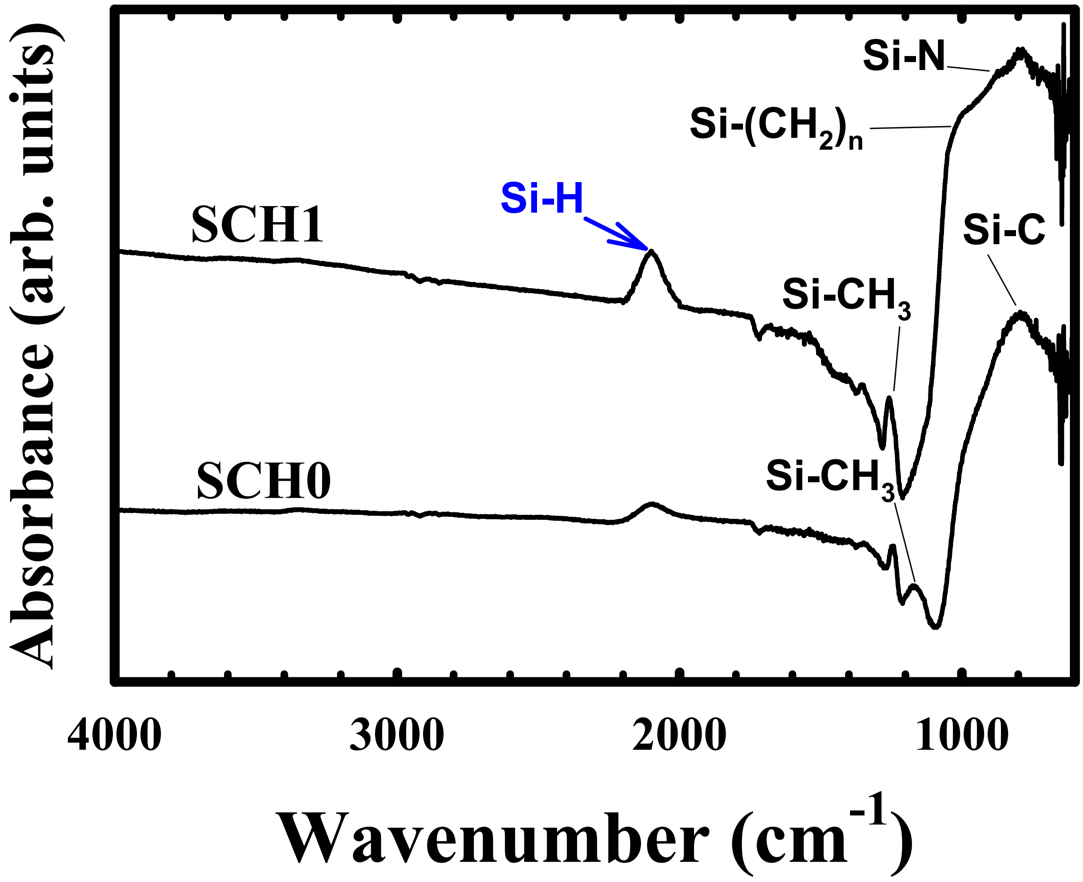

Fig. 3-9 FTIR spectra for two PECVD α-SiCN dielectrics.

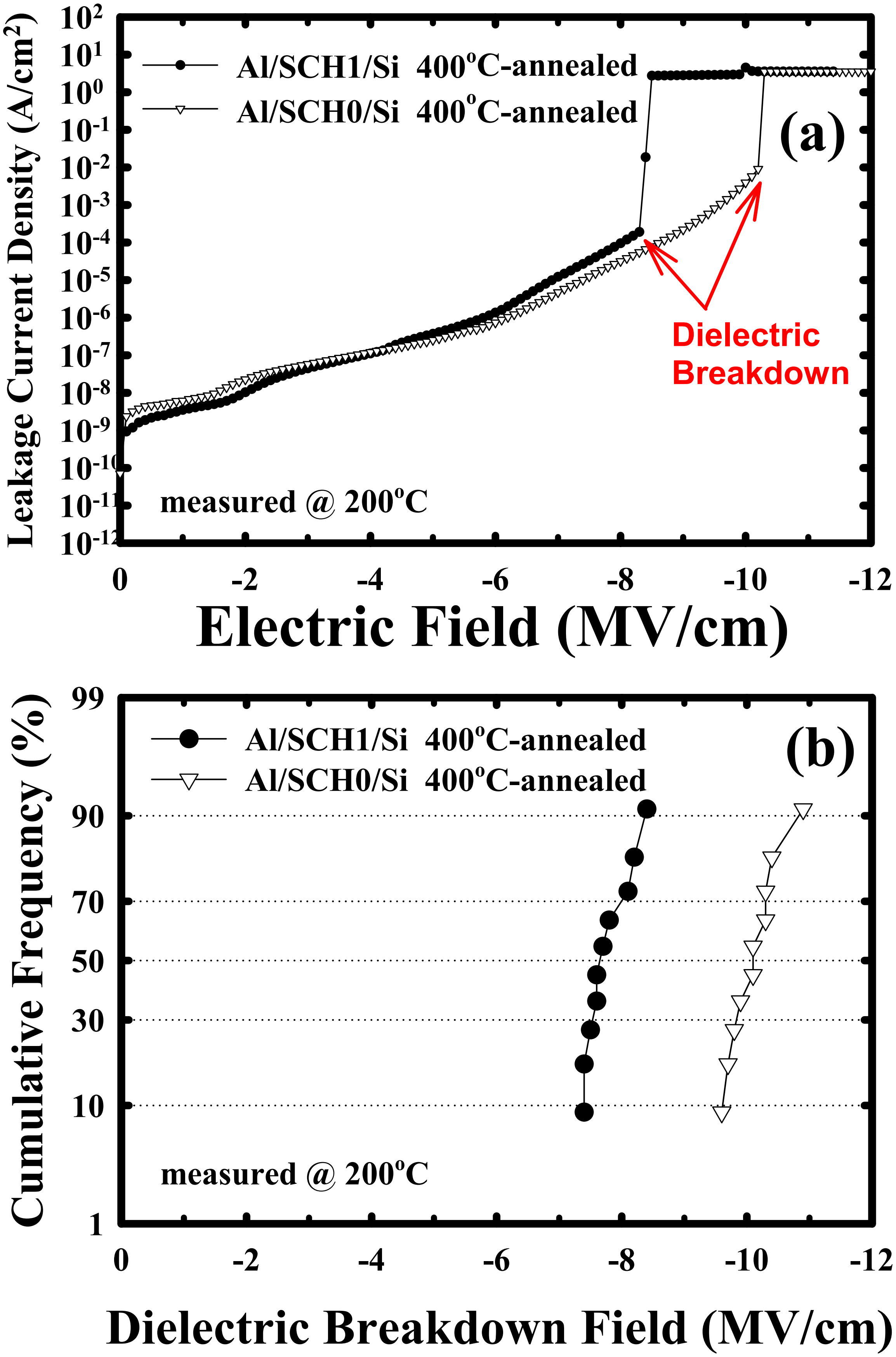

Fig. 3-10 (a) Leakage current density vs. electric field and (b) statistical distribution of dielectric breakdown field for the 400°C-annealed Al/SCH1/Si and Al/SCH0/Si MIS capacitors measured at 200°C.

Chapter 4

α-SiCN Dielectric Barrier on Plasma-Treated Cu-Surface

4-1 Introduction

The film quality of the α-SiCN dielectric barrier films was found to be dependent on the carbon, nitrogen, and hydrogen concentrations as well as the condition of the Cu-surface, as discussed in chapters 2 and 3, because the α-SiCN dielectric cap-barriers are usually deposited directly on the Cu-surface in the typical production-chip, as shown in Fig. 1-3. However, Cu-surface easily oxidizes at low temperatures (<200°C) in the common process-environment, and unlike Al-alloys, Cu cannot form a stable self-limiting surface oxide layer; the Cu-oxides are chemically and mechanically unstable, and their presence can adversely affect the adhesion of Cu to the adjacent passivation, barrier, and protective cladding layers [1]. A number of receipts are useful to remove the Cu-oxides, such as a sulfuric acid wet etching, a thermal treatment in vacuum at 350°C, or a hydrogen-plasma (H_2-plasma) treatment [1,2]. Since it is inevitable to use metallic and/or dielectric barriers to encapsulate the Cu metallization in order to suppress the diffusion/drift of Cu into the active region of electronic devices, a number of issues regarding the encapsulation scheme must be addressed, such as the Cu/barrier interface-diffusion arisen from electromigration, Cu/barrier interface-reaction during the deposition of the barrier layer, and poor breakdown lifetime of dielectric barrier resulting from the Cu diffusion [2,3]. Notably, the dielectric breakdown lifetime can be improved by using an NH_3-plasma treatment on the Cu-surface prior to the cap α-SiN dielectric deposition on a Cu-comb capacitor [3]. Before making a successful integration of the barrier film and the Cu metal with a plasma-treated surface, fundamental properties, such as plasma induced Cu-surface roughness and chemical bonding of the plasma-treated Cu-surface, must be first explored. This chapter investigates the effects of O_2- and N_2-plasma treatments on the Cu-surface with respect to the leakage current and breakdown field of the Al/α-SiCN/Cu MIM capacitor.

4-2 Experimental Details

The Al/α-SiCN/Cu MIM capacitors without and with O_2- or N_2-plasma treatment on the Cu-surface, as shown in Fig. 4-1, are investigated in this study. First, a 200 nm physical vapor deposited (PVD) TaN metallic film was deposited on the substrate of p-type, (100)-oriented Si wafer. The TaN film served as a barrier layer to prevent the Cu metal, to be deposited on the TaN film, from diffusion into the Si substrate in the subsequent high-temperature processes. After sputter-depositing a Cu layer of 400 nm thickness on the TaN film, the Cu-surface was exposed to O_2- or N_2-plasma treatment. The O_2-plasma treatment was performed at 200 W power for 5 s under the conditions: O_2 flow rate 700 sccm, gas pressure 4 Torr, and substrate temperature 350°C. The N_2-plasma treatment was performed at 300 W power for 20 s under the conditions: N_2 flow rate 800 sccm, gas pressure 3.5 Torr, and substrate temperature 350°C. After the plasma treatment, a 50 nm PECVD 3MS-based [$(CH_3)_3SiH$] α-SiCN (k~3.5) dielectric barrier film was deposited on the Cu layer at 350°C. The Al metal-electrode with a circular area of 0.84 mm diameter was prepared by thermally evaporating a 500-nm-thick Al layer on the α-SiCN dielectric surface followed by photolithography and chemical wet etching. The O_2- and N_2-plasma-treated samples are designated as O_2-sample and N_2-sample, respectively. For a comparison, control samples of the Al/α-SiCN/Cu MIM capacitor without any plasma treatment on the Cu-surface were also prepared. To ensure good contact in electrical measurements, a 500-nm-thick Al layer was also deposited on the back surface of the Si substrate for all samples.

An HP4145B semiconductor parameter analyzer was used to measure the dielectric leakage current and breakdown field of the Al/α-SiCN/Cu MIM capacitors. Secondary ion mass spectrometry (SIMS) was used to detect the penetration of Cu in the α-SiCN dielectric. Atomic force microscopy (AFM) was used to evaluate the roughness of the Cu-surface. Grazing angle fourier transform infrared spectroscopy (FTIR) was used to analyze the chemical bonding of the Cu-surface.

4-3 Electrical Property

Figure 4-2 shows the room-temperature leakage current density of various Al/α-SiCN/Cu MIM capacitors. The measurements were performed with the MIM capacitors biased with negative polarity on the Al metal-electrode to ensure the p-type Si substrate in the accumulation regime. Apparently, the leakage current of the capacitor is dependent on the plasma treatment of the Cu-surface. The leakage current density of the O_2- and N_2-samples are several orders of magnitude larger than that of the control sample at the same electric field intensity. In each sample, when the applied electric field approaches the breakdown field intensity, the leakage current through the dielectric increases rapidly and jumps to the current limit (20 mA, equivalent to 3.57 A/cm^2) of the HP4145B semiconductor parameter analyzer, similar to the observation in our another work [4], as presented in chapter 3. The dielectric breakdown results in a thermal instability and high-temperature Joule heating [5], leading to the burnout of Al metal-electrode in the Al/α-SiCN/Cu MIM capacitor, as shown in Fig. 4-3. The statistical distribution of breakdown field is illustrated in Fig. 4-4 for the Al/α-SiCN/Cu MIM capacitors, indicating the adverse effect on breakdown field by the plasma treatment of the Cu-surface.

4-4 Physical Property

Possible determining factors for the increased leakage current and decreased breakdown field of the O_2- and N_2-samples may include the diffusion of Cu into the α-SiCN film during the deposition of the dielectric barrier film, plasma treatment induced Cu-surface roughness, and/or the formation of metastable Cu compounds during the plasma treatment. Figure 4-5 shows the SIMS depth profiles of Cu in the α-SiCN film for the control, O_2-, and N_2-sample. Although there is a broadening of SIMS depth profile at the α-SiCN/Cu interface for the O_2-sample, this is believed to be arisen from the rougher Cu-surface in the O_2-sample [6] (to be shown later in Fig. 4-6). Moreover, the surface peak (surface effect) of Cu depth profile at the α-SiCN surface is attributed to the presence of native oxide [7]. Furthermore, we have confirmed in our previous work, as shown in chapters 2 and 3, that the 3MS-based α-SiCN dielectric barrier films are capable of preventing Cu diffusion at temperatures up to 400^{o}C [8]. Thus, we believe that there is no diffusion of Cu into the α-SiCN films in all of the three samples. It was reported that surface-microroughness of Si substrate affects the quality of thin oxide films grown on the Si substrate because increased surface-microroughness of Si substrate leads to a higher defect density in thermal oxide [9] and thus more point discharge at the local peaks. The breakdown electric filed and time-dependent dielectric breakdown (TDDB) of the thin oxide film decrease with an increase of the surface-microroughness of Si substrate [10]. The film density and defect density of chemical vapor deposited (CVD) films are also dependent on the deposition temperature and surface roughness of the substrate [11-13]. Thus, a rough Cu-surface may induce a higher defect density and more point discharge in the α-SiCN film deposited on the rough surface, leading to the increased leakage current and decreased breakdown field. Figure 4-6 shows the AFM images and average surface-roughness of the Cu-surface with and without a plasma treatment. The O_2-plasma treatment significantly roughened the Cu-surface, whereas the N_2-plasma treatment did not obviously change the Cu-surface roughness. Thus, we may also exclude the surface-roughness of the Cu-surface as a dominant factor in determining the leakage current and breakdown field of the Al/α-SiCN/Cu MIM capacitors studied in this chapter. It was reported that Cu-O oxide and Cu-N azide are present, respectively, on the O_2- and NH_3-plasma-treated Cu-surface [14]. In this work, the grazing angle FTIR spectra show that the Cu-O and Cu-N bonds are present, respectively, on the O_2- and N_2-plasma-treated Cu-surface, as shown in Fig. 4-7. The Cu compounds have a low stability, e.g. the formation-heat (ΔH_f) of 157.3 kJ/mol for CuO compound as compared to 910.7 kJ/mol for SiO_2 at the temperature of 298.15 K [15]. Moreover, the Cu-N azides are very unstable and may easily ignite or explode [16]. Consequently, the increased leakage current and decreased breakdown field of the Al/α-SiCN/Cu MIM capacitors with O_2- and N_2-plasma-treated Cu-surface are attributed, respectively, to the presence of metastable Cu-O oxide and Cu-N azide.

4-5 Summary

It is found that both the O_2-plasma and N_2-plasma treatments on the Cu-surface have an adverse effect on the leakage current and breakdown field of the Al/α-SiCN/Cu MIM capacitors. The MIM capacitors with the Cu-surface exposed to O_2- or N_2-plasma treatment prior to the deposition of the α-SiCN dielectric film exhibit a room-temperature leakage current density several orders of magnitude larger than the sample without the plasma treatment at the same applied electric field. The room-temperature breakdown fields of the MIM capacitors with O_2- and N_2-plasma-treated Cu-surface are 3.8 and 3.2 MV/cm, respectively, while that of the control sample without a plasma treatment is 7.8 MV/cm. The increased leakage current and decreased breakdown field of the O_2- and N_2-plasma-treated samples are attributed, respectively, to the presence of metastable Cu-O oxide and Cu-N azide at the Cu-surface.

References

[1] E. Apen, B. R. Rogers, and J. A. Sellers, *J. Vac. Sci. Technol. A*, **16** (1998) p. 1227.

[2] G. P. Beyer, M. Baklanov, T. Conard, and K. Maex, *Mat. Res. Soc. Symp. Proc.*, **612** (2000) p. D9.17.1.

[3] J. Noguchi, N. Ohashi, T. Jimbo, H. Yamaguchi, K. I. Takeda, and K. Hinode, *IEEE Trans. Electron Devices*, **48** (2001) p. 1340.

[4] C. C. Chiang, M. C. Chen, C. C. Ko, S. M. Jang, C. H. Yu, and M. S. Liang, *Jpn. J. Appl. Phys.*, **42** (2003) p. 5246.

[5] D. Brassard and M. A. E. Khakani, *J. Appl. Phys.*, **93** (2003) p. 4066.

[6] R. G. Wilson, F. A. Stevie, and C. W. Magee, *Secondary Ion Mass Spectrometry-A Practical Handbook for Depth Profiling and Bulk Impurity Analysis* (John Wiley & Sons, New York, 1989) p. 4.2-1.

[7] R. G. Wilson, F. A. Stevie, and C. W. Magee, *Secondary Ion Mass Spectrometry-A Practical Handbook for Depth Profiling and Bulk Impurity Analysis* (John Wiley & Sons, New York, 1989) p. 2.4-1.

[8] C. C. Chiang, Z. C. Wu, W. H. Wu, M. C. Chen, C. C. Ko, H. P. Chen, S. M. Jang, C. H. Yu, and M. S. Liang, *Jpn. J. Appl. Phys.*, **42** (2003) p. 4489.

[9] W. M. Huang, Z. J. Ma, M. Racanelli, D. Hughes, S. Ajuria, G. Huffman, T. P. Ong, P. K. Ko, C. Hu, and B. Y. Hwang, *IEEE IEDM Technol. Dig.* (1993) p. 735.

[10] M. Miyashita, M. Itano, T. Imaoka, I. Kawanabe, and T. Ohmi, *IEEE VLSI Technol. Dig.* (1991) p. 45.

[11] S. Wolf and R. N. Tauber, *Silicon Processing for the VLSI Era, Volume 1: Process Technology* (Lattice Press, California, 1986) p. 162.

[12] S. Y. Kang, H. J. Lim, C. S. Hwang, and H. J. Kim, *J. Electrochem. Soc.*, **149** (2002) p. C317.

[13] C. L. Lin, P. S. Chen, and M. C. Chen, *J. Electrochem. Soc.*, **149** (2002) p. C237.

[14] L. J. Li, C. Y. Sheu, B. T. Chen, T. I. Bao, T. L. Lee, R. L. Hwang, S. M. Jang, C. H. Yu, and M. S. Liang, *Symp. AMC Technol. Dig.* (2001) p. 261.

[15] S. P. Murarka, I. V. Verner, and R. J. Gutmann, *Copper-Fundamental Mechanisms for Microelectronic Applications* (John Wiley & Sons, New York, 2000) p. 127.

[16] S. P. Murarka, I. V. Verner, and R. J. Gutmann, *Copper-Fundamental Mechanisms for Microelectronic Applications* (John Wiley & Sons, New York, 2000) p. 129.

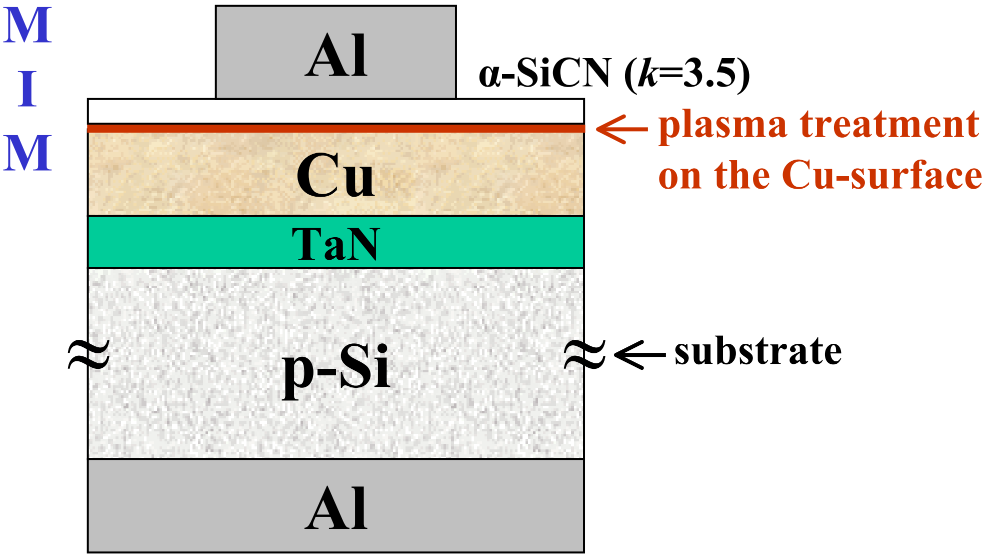

Fig. 4-1 Schematic cross-sectional view of the Al/α-SiCN/Cu MIM capacitor test structure employed in the study of this chapter.

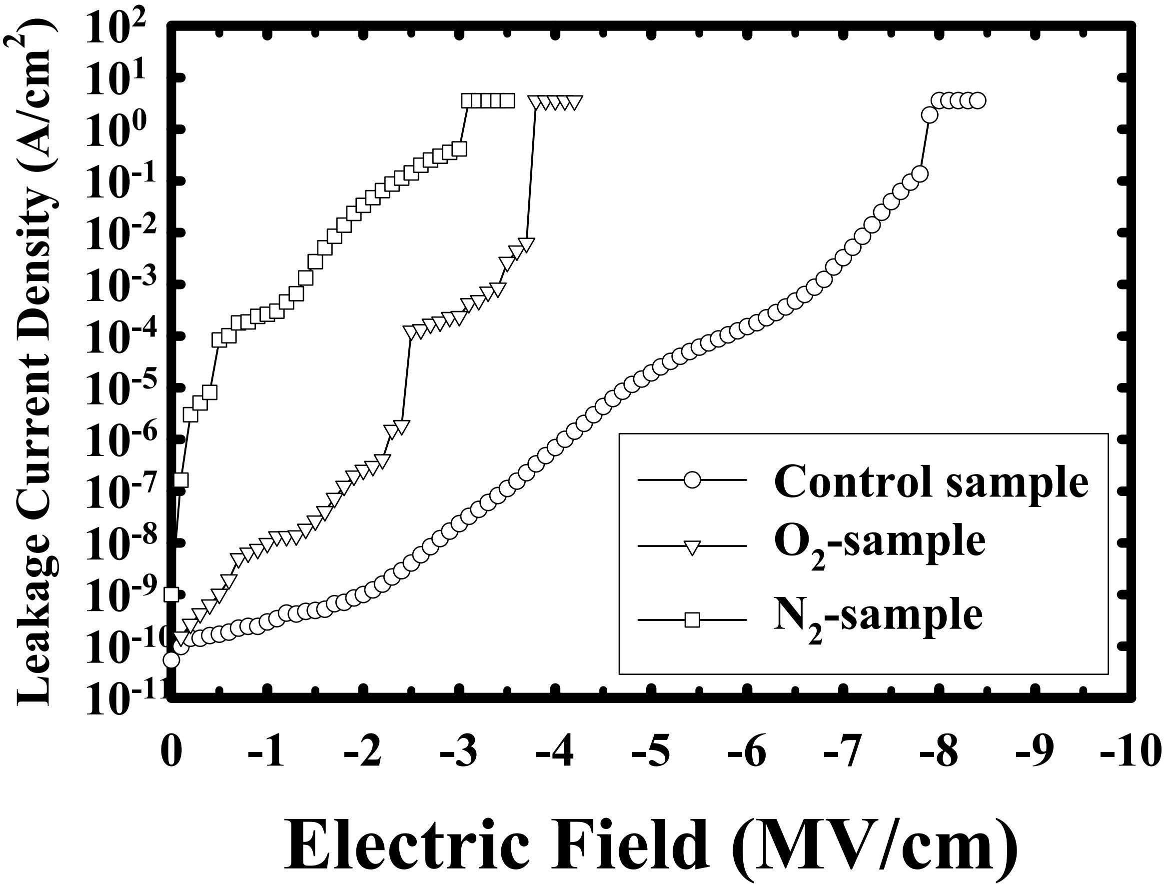

Fig. 4-2 Leakage current density vs. electric field measured at room temperature for the Al/α-SiCN/Cu MIM capaciotrs without and with O_2- or N_2-plasma treatment.

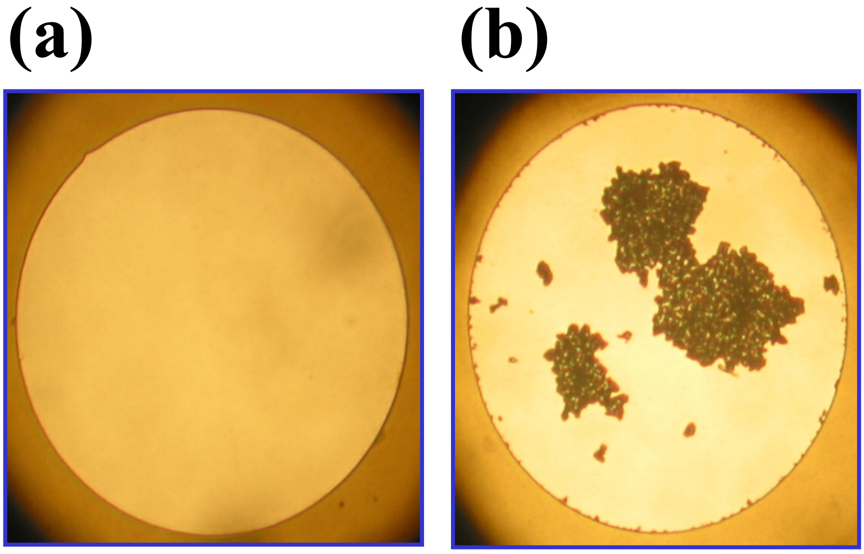

Fig. 4-3 Optical microscope (OM) images for the Al metal-electrode on the Al/α-SiCN/Cu MIM capacitors (a) before and (b) after dielectric breakdown.

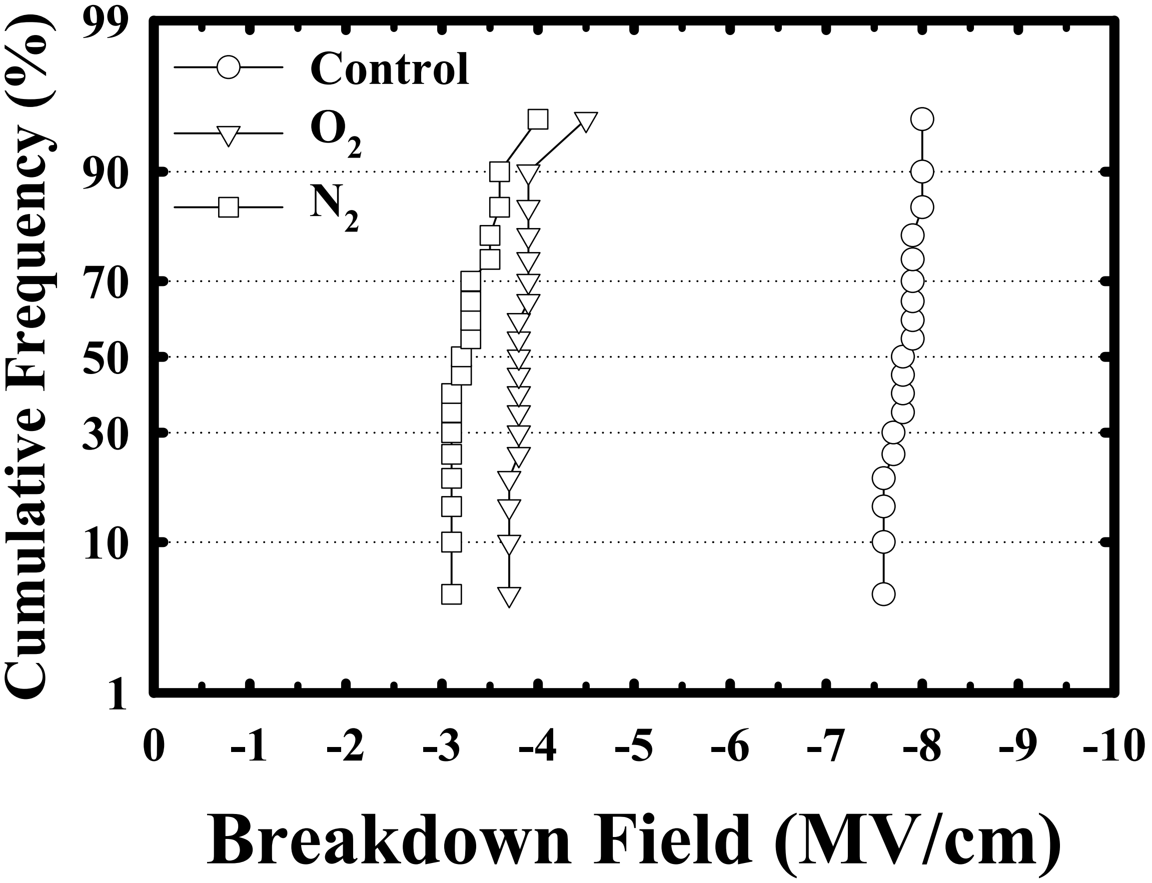

Fig. 4-4 Distributiom of breakdown field measured at room temperature for the Al/α-SiCN/Cu MIM capacitors without and with O_2- or N_2-plasma treatment.

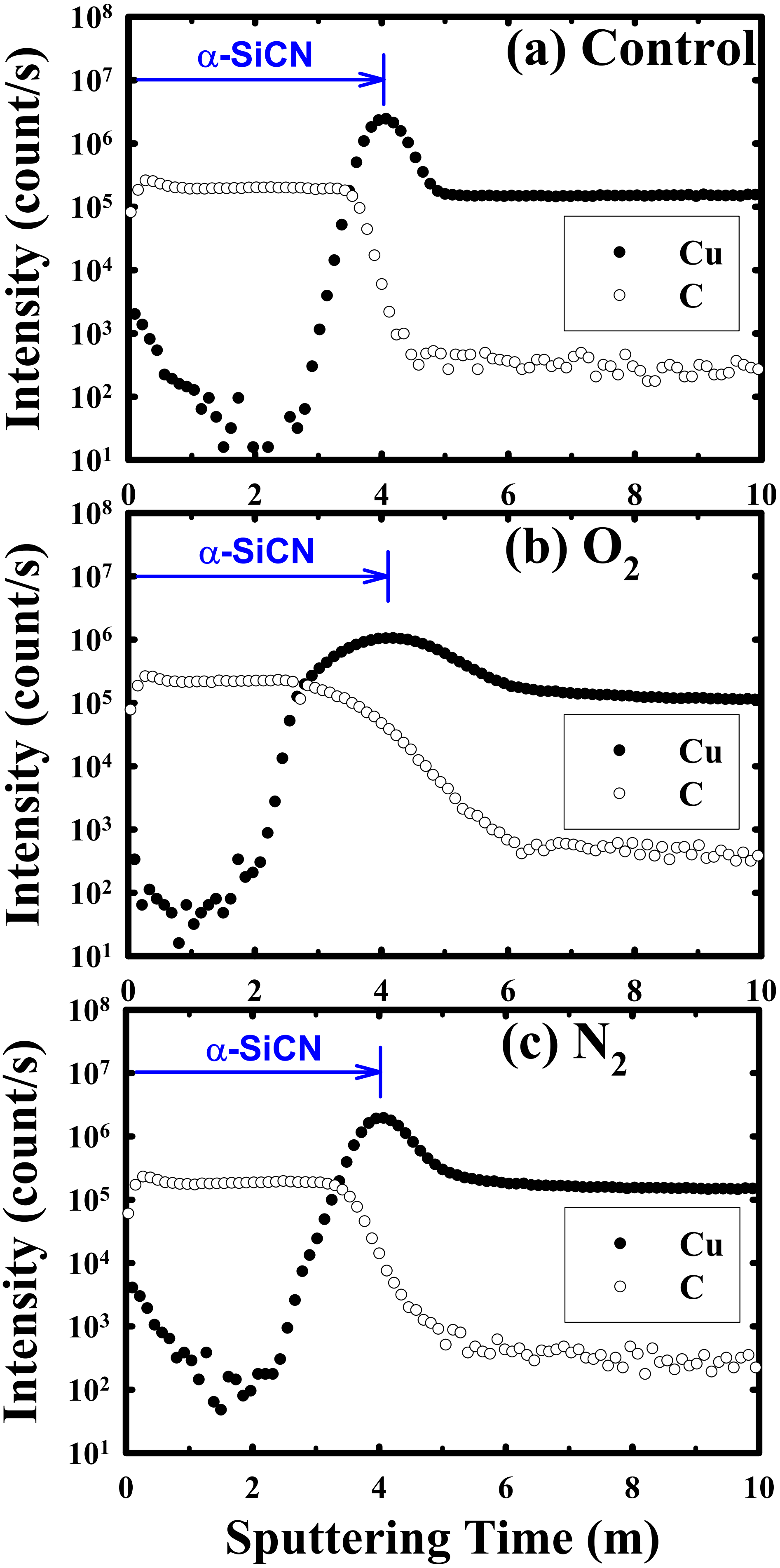

Fig. 4-5 SIMS depth profiles of Cu in the α-SiCN film for (a) control sample, (b) O_2-sample, and (c) N_2-sample.

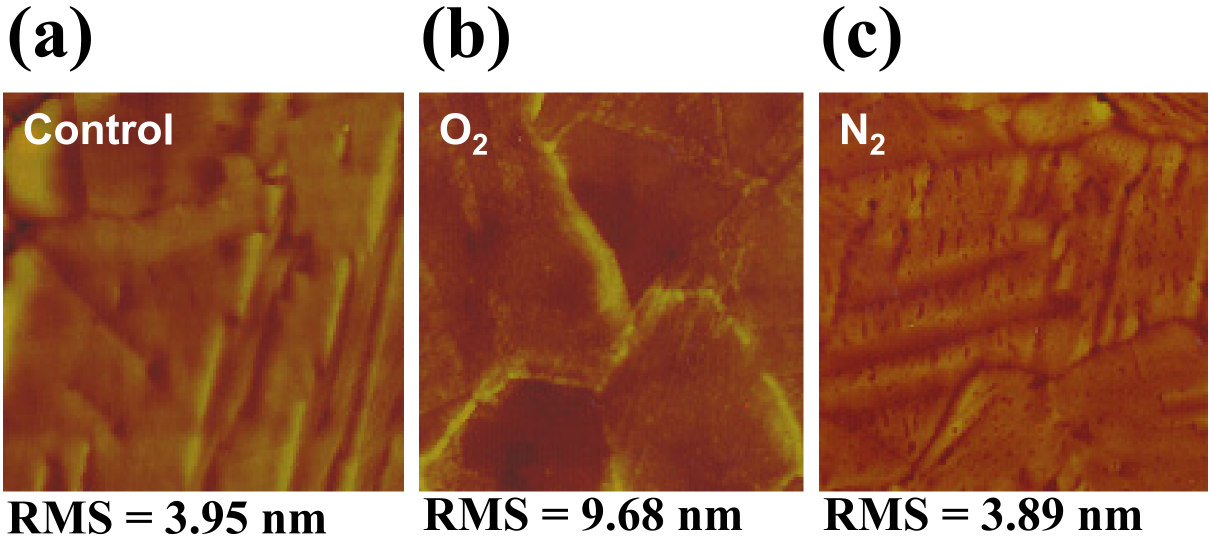

Fig. 4-6 AFM images and average surface-roughness [root-mean square (rms) value] of the Cu-surface (a) without plasma treatment, (b) with O_2-plasma treatment, and (c) with N_2-plasma treatment.

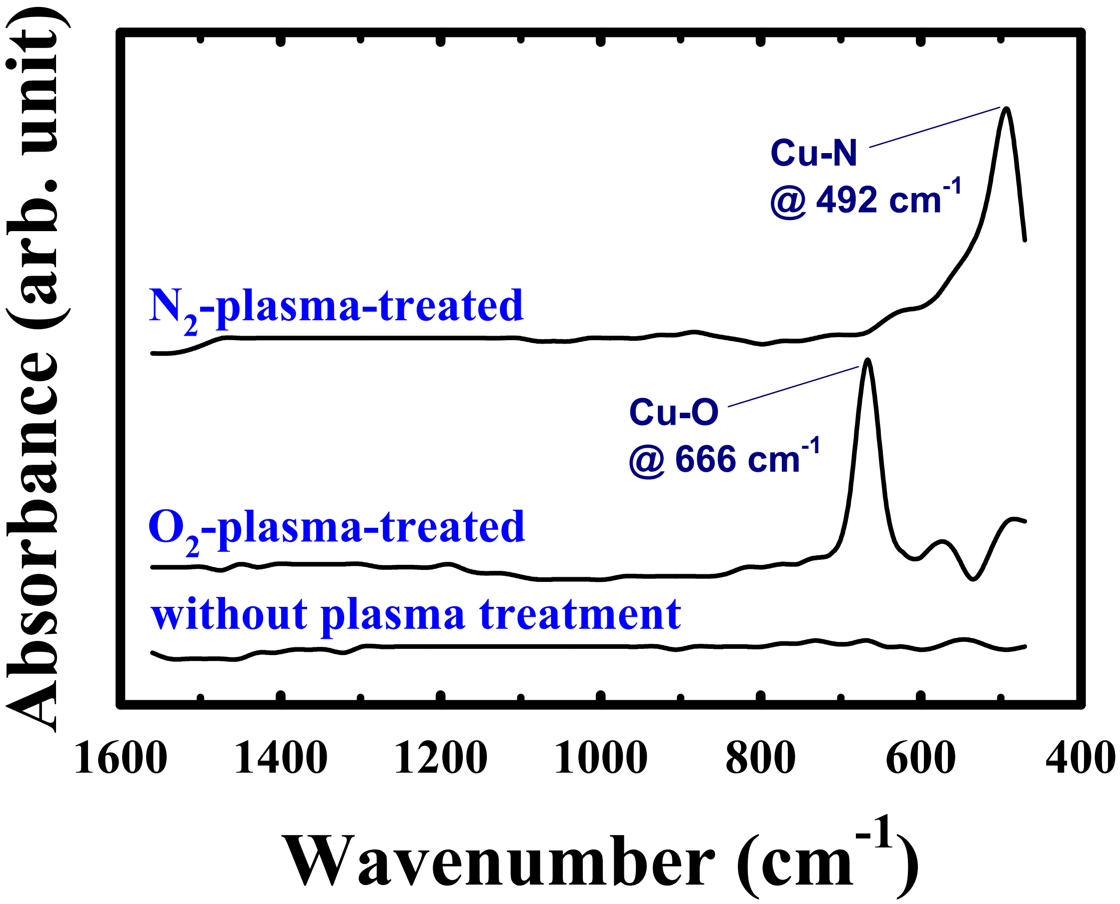

Fig. 4-7 Grazing angle FTIR of the Cu-surface without and with O_2- or N_2-plasma treatment.

Part 2

Chapter 5

Amorphous Silicon-Carbide (α-SiC) Dielectric Barrier

5-1 Introduction

A number of studies have been reported regarding the thermally stable and Cu-diffusion restrained low-*k* SiN-based and SiC-based dielectric films deposited by LPCVD/PECVD using organosilicate gases [1-11]. These dielectrics, such as the PECVD α-SiCN films studied in chapters 2 and 3, tend to have an instable molecular structure because of their higher nitrogen concentration. In this chapter, we investigate the physical and barrier properties of two low-*k* nitrogen-free α-SiC dielectric films (k<5) deposited using trimethylsilane (3MS) and tetramethylsilane (4MS) organosilicate gases.

5-2 Experimental Details

Two PECVD α-SiC films deposited using $(CH_3)_3SiH$ (3MS) and $(CH_3)_4Si$ (4MS) organosilicate gases are investigated with respect to their thermal stability and physical and barrier properties. All films are deposited to a thickness of 50 nm on p-type, (100)-oriented Si wafers using a parallel-plate PECVD system operated at 13.56 MHz. One α-SiC film, designated as SC3M, was deposited at a temperature of 350-400^{o}C using He/$(CH_3)_3SiH$ gases with a flow rate ratio of 3-4, a total gas pressure of 2-4 Torr, and a plasma power of 200-300 W. The other α-SiC film, designated as SC4M, was deposited at a temperature of 350-400^{o}C using He/$(CH_3)_4Si$ gases with a flow rate ratio of 3-5, a total gas pressure of 2-4 Torr, and a plasma power of 400-600 W. All films deposited were annealed at 400^{o}C for 30 min in N_2 ambient to remove moisture possibly absorbed in the dielectrics prior to the investigation of physical properties or the deposition of the electrode (TaN/Cu or Al) to construct the MIS capacitor structure. The TaN/Cu-geted MIS capacitors were constructed by first sputter-depositing a 200-nm-thick Cu layer on the α-SiC films using a dc magnetron sputtering system, followed by the reactive sputter deposition of a 50-nm-thick TaN layer on the Cu surface in the same sputtering system without breaking the vacuum. The TaN film served as a passivation layer to prevent Cu metal from oxidation in the subsequent high-temperature processes. For a comparison, Al-electrode control samples were also prepared by depositing a 500-nm-thick Al layer directly on the α-SiC dielectric surfaces using a thermal evaporation system. All metal electrodes with a circular area of 0.84 mm diameter were defined by a lift-off process in order to prevent unexpected deterioration of the dielectrics by chemical wet etching. To ensure good contact in electrical measurements, a 500-nm-thick Al layer was also thermally evaporated on the back surface of the Si substrate for all samples. Some of the completed MIS samples were thermally annealed at 400^{o}C for 30 min in N_2 ambient. This annealing step eradicates the plasma induced damage during the sputter deposition of the TaN/Cu electrodes and also provides the driving force for Cu diffusion.

Rutherford backscattering spectroscopy (RBS) was used to determine the elemental compositions of the dielectrics. Secondary ion mass spectrometry (SIMS) was also used to evaluate the compositions of the α-SiC films and the penetration of Cu in the dielectrics. The film thickness and refractive index were measured by a well-calibrated n&k analyzer at 633 nm wavelength, and the *k*-value of the dielectrics was evaluated from the maximum capacitance of the Al-gated MIS capacitors measured at 1 MHz using a Keithley 82 C-V measurement system. Thermal desorption spectroscopy (TDS) was used to monitor the outgassing behavior of the dielectrics during the thermal annealing process. Fourier transform infrared spectroscopy (FTIR) was used to analyze the chemical bonding of the dielectrics. An HP4145B semiconductor parameter analyzer was used to measure the dielectric leakage current and provide the bias for the bias-temperature-stress (BTS).

5-3 Physical Property and Thermal Stability

Table 5-1 shows the properties of the two PECVD α-SiC dielectric films studied in this chapter. A higher power is needed for the deposition of the SC4M film than the SC3M film because the tetramethysilane reactant gas has a higher gas-phase dissociation energy and ionization energy [12]. The SC4M film has a lower dielectric constant than the SC3M film, presumably due to the SC4M film's higher carbon content, because carbon is less polarizable than silicon and has no orientational polarizability [13,14]. Moreover, carbon in the silicon matrix generates atomic scale nanopores and results in the enhancement of any pre-existing nanoporosity or microvoids in the low-k films after annealing [14-19]. However, the SC4M film has a higher refractive index at 633 nm (~5×10^{14} Hz) than the SC3M film because the SC4M film is more reflective than the SC3M film at optical frequency [20]. Figure 5-1 shows the thickness shrinkage of the dielectric films thermally annealed at various temperatures for 30 min in N_2 ambient. The thickness of both dielectric films remained nearly constant at temperatures up to 500^{o}C. Both films shrunk slightly after thermal annealing at 550^{o}C; however, the film shrinkage remained less than 5% even after thermal annealing at 600^{o}C. This implies that there is little physical densification and chemical outgassing of the dielectrics at temperatures up to 600^{o}C, the latter of which is further confirmed by the TDS spectra of the dielectric films, as illustrated in Fig. 5-2. The thickness shrinkage and chemical outgassing are closely related to the changes in the chemical bonding and microstructure of the dielectric films, which also result in the variation of refractive indices and dielectric constants of the dielectrics, as shown in Fig. 5-3 and Fig. 5-4, respectively. The refractive indices and dielectric constants of these two α-SiC dielectrics remained nearly constant at temperatures up to 500°C but increased at temperatures above 550°C. Nonetheless, the thermal stability of the 3MS/He α-SiC film is slightly better than that of the 4MS/He α-SiC film, and both films are thermally very stable compared to the α-SiCN films deposited using 3MS/NH_3 gases studied in our previous work [21], as presented in chapters 2 and 3.

5-4 Electrical and Barrier Properties

Figure 5-5 shows the room-temperature leakage current density for the as-fabricated as well as 400°C-annealed (30 min in N_2 ambient) Al-gated and TaN/Cu-gated MIS capacitors of the α-SiC dielectric films. The measurements were performed with the MIS capacitors biased in the accumulation region. For each dielectric film, negligible difference in the leakage current was observed between the Al-gated and TaN/Cu-gated MIS capacitors, whether as-fabricated or 400°C-annealed. This implies that both of the dielectrics are capable of preventing Cu permeation at temperatures up to 400°C. BTS was used to further explore the dielectric barrier capability of the TaN/Cu-gated MIS capacitors. The BTS test was performed at 200°C with an applied electric field of 3 MV/cm on the MIS capacitors which had been annealed at 400°C for 30 min. An N_2 purging was used to prevent oxidation of the Cu electrode and moisture uptake in the dielectric films during the BTS. Figure 5-6 shows the leakage current transient during the BTS and the instantaneous leakage current density versus applied electric field (in accumulation mode) before and immediately after the BTS for the MIS capacitors. The TaN/Cu-gated SC3M sample remained stable up to at least 15 h BTS, whereas the SC4M dielectric sample failed after approximately 40 min BTS. Figure 5-7 shows the SIMS depth profiles of Cu in the

TaN/Cu-gated SC4M film after removal of the TaN/Cu electrode. The depth profile of Cu clearly indicates the permeation of Cu into the SC4M dielectric for the TaN/Cu-gated SC4M sample after 1 h BTS. Thus, we may conclude that the spiking in the leakage current of the TaN/Cu-gated SC4M sample during the BTS (Fig. 5-6a) and the significant increase of leakage current in the TaN/Cu-gated SC4M sample after 1 h BTS (Fig. 5-6b) resulted from the penetration of Cu into the SC4M dielectric.

The inferior barrier property of the SC4M film against Cu penetration is attributed to the film's rich carbon content. The concentrated carbon atoms may generate nanopores and enhance the porosity of carbon-doped oxide and α-SiC films after annealing [14-19,21], resulting in easier penetration of Cu into the film. Figure 5-8 illustrates the Cu ions drift into a porous α-SiC film during BTS and a schematic microstructure of a porous α-SiC film. The open pore is a cavity or a channel that can communicate with the surface of the dielectric film, while the closed pore is a cavity not communicating with the surface [22]. Conceivably, materials with a high density of voids, pores, and other defects have a higher density of silanol (Si-OH) groups and, therefore, a higher density of bound water [23]. After the α-SiC films were immersed in boiling water for 1 h, the signals of H_2O-related bonds (Si-OH) were observed in the FTIR spectrum for the SC4M sample, as shown in Fig. 5-9, indicating that the SC4M film stored a large amount of moisture (H_2O). Moreover, it was reported that water vapor in the ambient or in dielectrics such as oxide-based materials will markedly enhance the Cu penetration into the dielectric film, either by causing deep level electron traps arising from H_2O in the dielectric film, or by hydration-energy induced ionization of metal atoms [24-26]. Thus, these nanopores act as fast diffusion paths via which Cu ions can drift rapidly in the SC4M film during the BTS, and the Cu penetration into the SC4M film may also be enhanced by the uptake of a trace of H_2O even with continuous N_2 purging during the BTS. Presumably due to the nanopores and the extra leakage paths arising from the uptake of a small amount of H_2O [27], the SC4M dielectric film exhibited a higher leakage current density and a lower dielectric breakdown field than the SC3M dielectric film, as shown in Fig. 5-10. The penetration of Cu into the SC4M film in the TaN/Cu/SC4M/Si MIS capacitor during the BTS is attributed to the porosity enrichment caused by an abundant amount of carbon atoms in the SC4M dielectric.

5-5 Summary

Two α-SiC dielectric barriers (k<5) deposited using $(CH_3)_3SiH$ (3MS) and $(CH_3)_4Si$ (4MS) organosilicate gases were investigated with respect to their thermal stability and physical and barrier properties. It is found that the 4MS α-SiC film contains a higher content of carbon and has a lower dielectric constant. Both of the 3MS and 4MS α-SiC films are thermally stable at temperatures up to 500^{o}C (for 30 min in N_2 ambient). However, degraded barrier property and moisture resistance were observed for the 4MS α-SiC film; this is attributed to the porosity enrichment caused by the film's high carbon content. The 3MS α-SiC film, which exhibits a superior Cu-barrier property, is a potential candidate for replacing the higher dielectric constant α-SiN film as a Cu cap-barrier and etching stop layer in the Cu damascene structure.

References

[1] M. Tanaka, S. Saida, and Y. Tsunashima, *J. Electrochem. Soc.*, **147** (2000) p. 2284.

[2] P. Xu, K. Huang, A. Patel, S. Rathi, B. Tang, J. Ferguson, J. Huang, C. Ngai, and M. Loboda, *IEEE IITC Technol. Dig.* (1999) p. 109.

[3] M. J. Loboda, *Microelectronic Engineering*, **50** (2000) p. 15.

[4] M. J. Loboda, J. A. Seifferly, and F. C. Dall, *J. Vac. Sci. & Technol. A*, **12** (1994) p. 90.

[5] C. C. Chiang, M. C. Chen, Z. C. Wu, L. J. Li, S. M. Jang, C. H. Yu, and M. S. Liang, *IEEE IITC Technol. Dig.* (2002) p. 200.

[6] K. Higashi, N. Nakamura, H. Miyajima, S. Satoh, A. Kojima, J. Abe, K. Nagahata, T. Tatsumi, K. Tabuchi, T. Hasegawa, H. Kawashima, S. Arakawa, N. Matsunaga, and H. Shibata, *IEEE IITC Technol. Dig.* (2002) p. 15.

[7] J. Martin, S. Filipiak, T. Stephens, F. Huang, M. Aminpur, J. Mueller, E. Demircan, L. Zhao, J. Werking, C. Goldberg, S. Park, T. Sparks, and C. Esber, *IEEE IITC Technol. Dig.* (2002) p. 42.

[8] S. G. Lee, Y. J. Kim, S. P. Lee, H. S. Oh, S. J. Lee, M. Kim, I. G. Kim, J. H. Kim, H. J. Shin, J. G. Hong, H. D. Lee, and H. K. Kang, *Jpn. J. Appl. Phys.*, **40** (2001) p. 2663.

[9] K. L Fang, B. Y. Tsui, C. C. Yang, and S. D. Lee, *IEEE IITC Technol. Dig.* (2001) p. 250.

[10] K. I. Takeda, D. Ryuzaki, T. Mine, and K. Hinode, *IEEE IITC Technol. Dig.* (2001) p. 244.

[11] T. Ishimaru, Y. Shioya, H. Ikakura, M. Nozawa, Y. Nishimoto, S. Ohgawara, and K. Maeda, *IEEE IITC Technol. Dig.* (2001) p. 36.

[12] S. Wolf and R. N. Tauber, *Silicon Processing for the VLSI Era, Volume 1: Process Technology* (Lattice Press, California, 1986) p. 172.

[13] S. K. Pangrle, S. Nitta, and J. Pellerin, *VMIC Technol. Dig.* (1999) p. 161.

[14] B. K. Hwang, M. J. Loboda, G. A. Cerny, R. F. Schneider, J. A. Seifferly, and T. Washer, *IEEE IITC Technol. Dig.* (2000) p. 52.

[15] A. Grill, L. Perraud, V. Patel, C. Jahnes, and S. Cohen, *Mat. Res. Soc. Symp. Proc.*, **565** (1999) p. 107.

[16] A. Grill and V. Patel, *J. Appl. Phys.*, **85** (1999) p. 3314.

[17] R. P. Mandal, V. Rana, M. Naik, D. Yost, D. Cheung, and W. F. Yau, *VMIC Technol. Dig.* (1999) p. 585.

[18] R. P. Mandal, D. Cheung, W. F. Yau, B. Cohen, S. Rengarajan, and E. Chou, *IEEE/SEMI Adv. Semiconductor Manufacturing Conf.* (1999) p. 299.

[19] Z. C. Wu, Z. W. Shiung, C. C. Chiang, W. H. Wu, M. C. Chen, S. M. Jeng, W. Chang, P. F. Chou, S. M. Jang, C. H. Yu, and M. S. Liang, *J. Electrochem. Soc.*, **148** (2001) p. F127.

[20] C. Kittel, *Introduction to Solid State Physics*, 7th ed. (John Wiley & Sons, New York, 1996) p. 307.

[21] C. C. Chiang, Z. C. Wu, W. H. Wu, M. C. Chen, C. C. Ko, H. P. Chen, S. M. Jeng, S. M. Jang, C. H. Yu, and M. S. Liang, *Jpn. J. Appl. Phys.*, **42** (2003) p. 4489.

[22] S. J. Gregg and K. S. W. Sing, *Adsorption, Surface Area and Porosity*, 2nd ed. (Academic Press, London, 1982) p. 38.

[23] N. Lifshitz and G. Smolinsky, *J. Electrochem. Soc.*, **136** (1989) p. 2335.

[24] Y. S. Diamand, A. Dedhia, D. Hoffstetter, and W. G. Oldham, *J. Electrochem. Soc.*, **140** (1993) p. 2427.

[25] J. D. Mcbrayer, R. M. Swanson, and T. W. Sigmon, *J. Electrochem. Soc.*, **133** (1986) p. 1242.

[26] Z. C. Wu, Z. W. Shiung, C. C. Chiang, W. H. Wu, M. C. Chen, S. M. Jeng, W. Chang,

P. F. Chou, S. M. Jang, C. H. Yu, and M. S. Liang, *J. Electrochem. Soc.*, **148** (2001) p. F115.

[27] C. G. Shirley and S. C. Maston, *IEEE IRPS Technol. Dig.* (1990) p. 72.

Table 5-1 Properties of the α-SiC dielectrics studied in this chapter.

Sample designation	SC3M	SC4M
Deposition gas	3MS/He	4MS/He
Deposition power (W)	200-300	400-600
RBS C/Si ratio	1.022	1.250
SIMS intensity ratio of C/Si $(\times 10^{-2})$	0.595	2.985
Refractive index (at 633 nm)	1.68	1.73
Dielectric constant @ 1 MHz	4.7	4.0

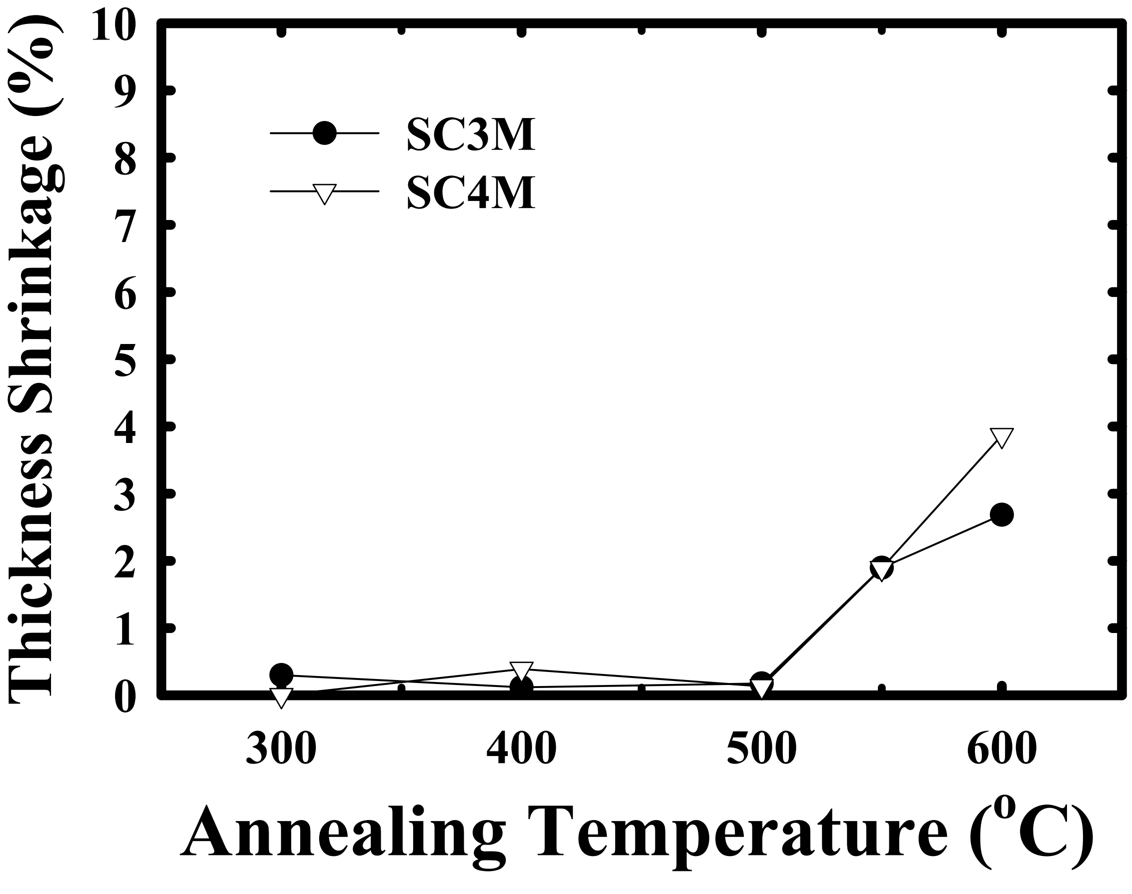

Fig. 5-1 Thickness shrinkage vs. annealing temperature for two PECVD α-SiC dielectrics.

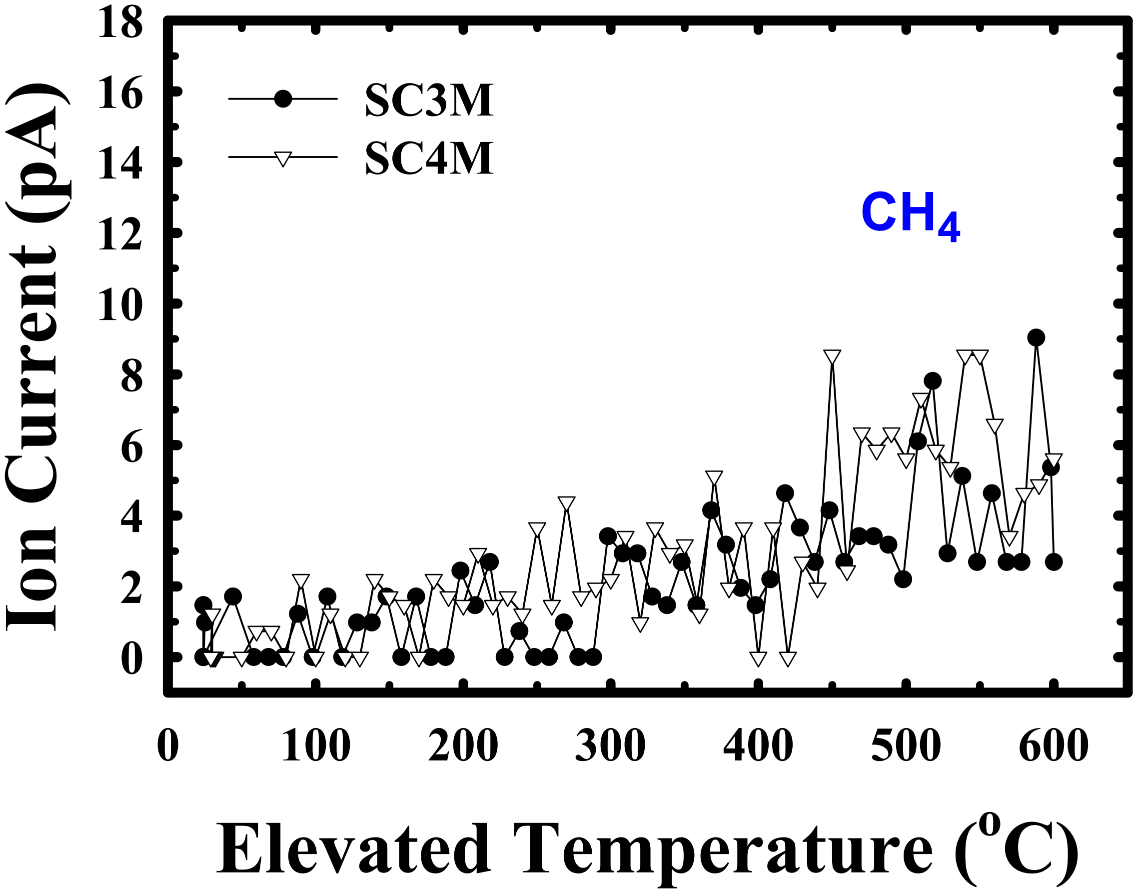

Fig. 5-2 TDS spectra of CH_4 for two PECVD α-SiC dielectrics.

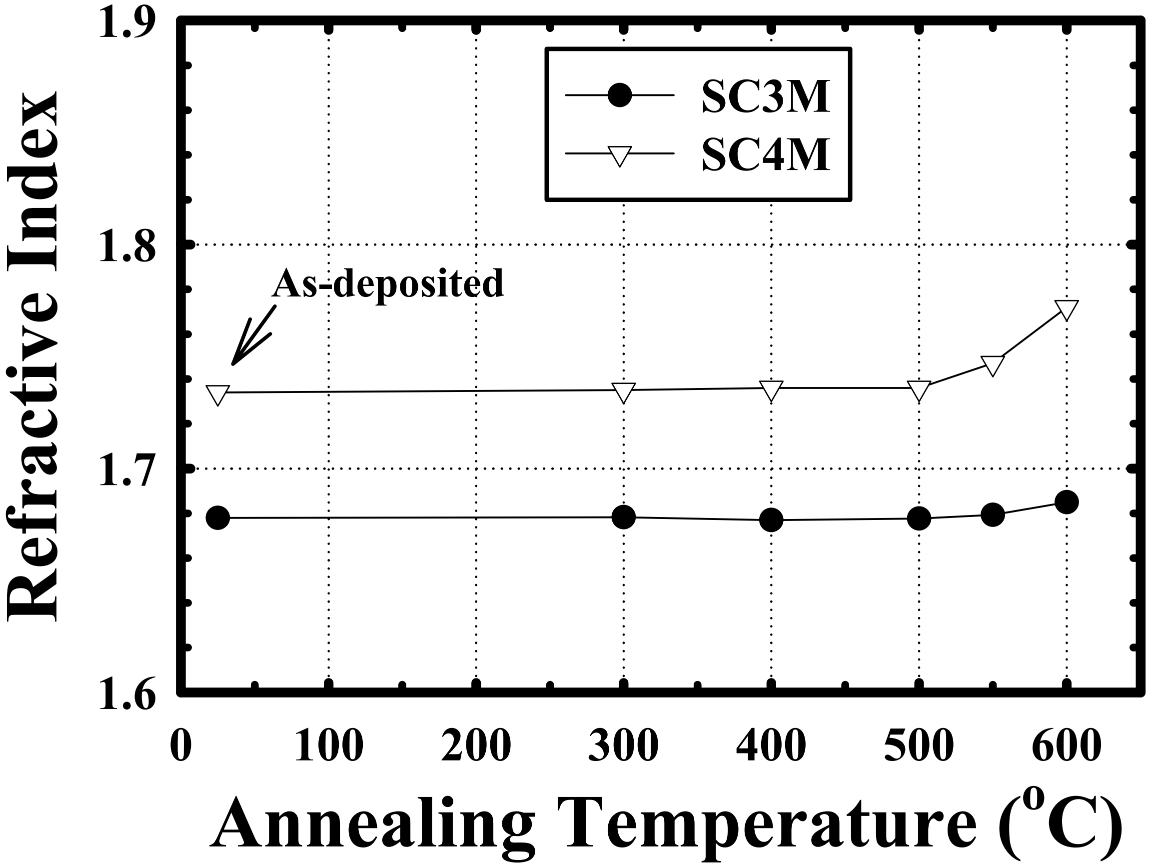

Fig. 5-3 Refractive index vs. annealing temperature for two PECVD α-SiC dielectrics.

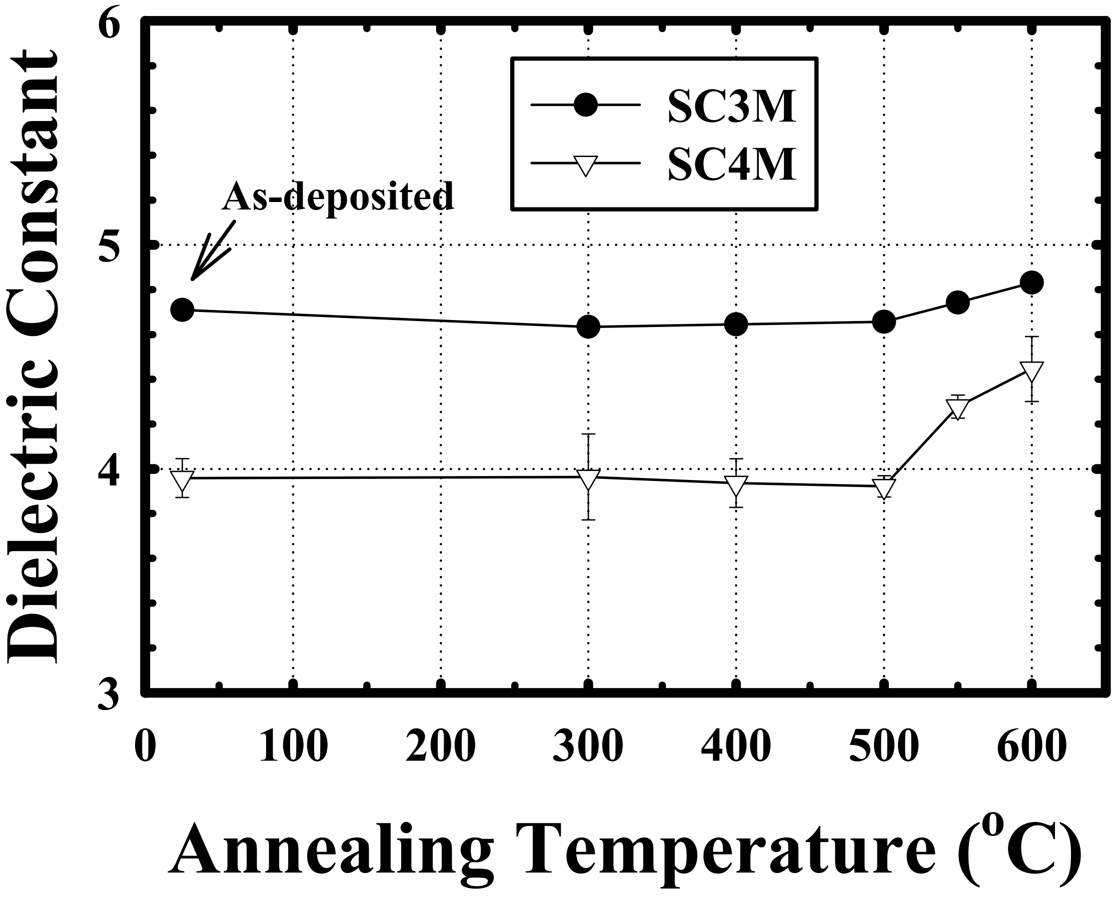

Fig. 5-4 Dielectric constant vs. annealing temperature for two PECVD α-SiC dielectrics.

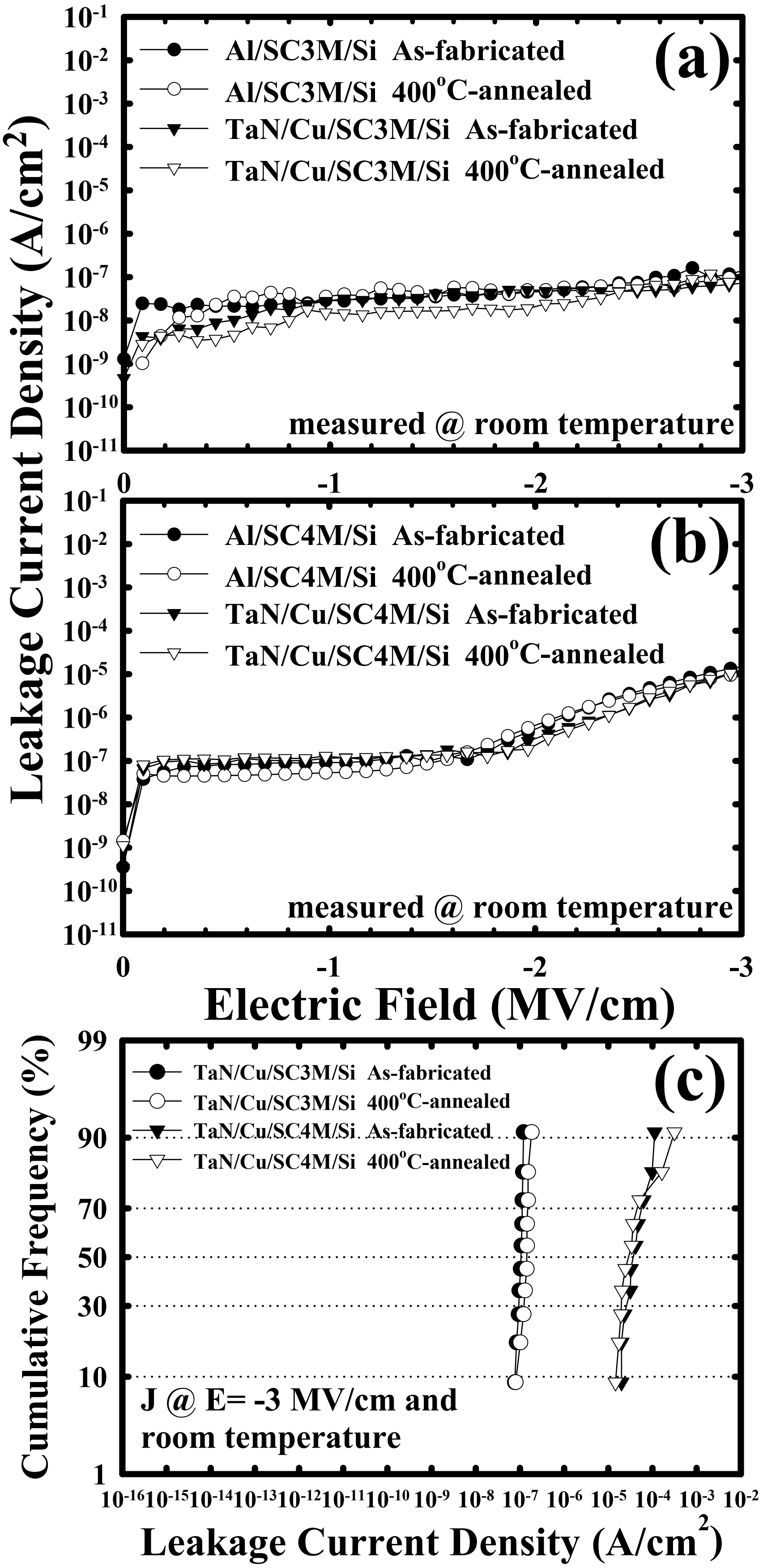

Fig. 5-5 Leakage current density vs. electric field measured at room temperature for the as-fabricated and 400°C-annealed Al- and TaN/Cu-gated MIS capacitors of (a) SC3M and (b) SC4M; (c) statistical distribution of leakage current density for the as-fabricated and 400°C-annealed TaN/Cu/SC3M/Si and TaN/Cu/SC4M/Si MIS capacitors.

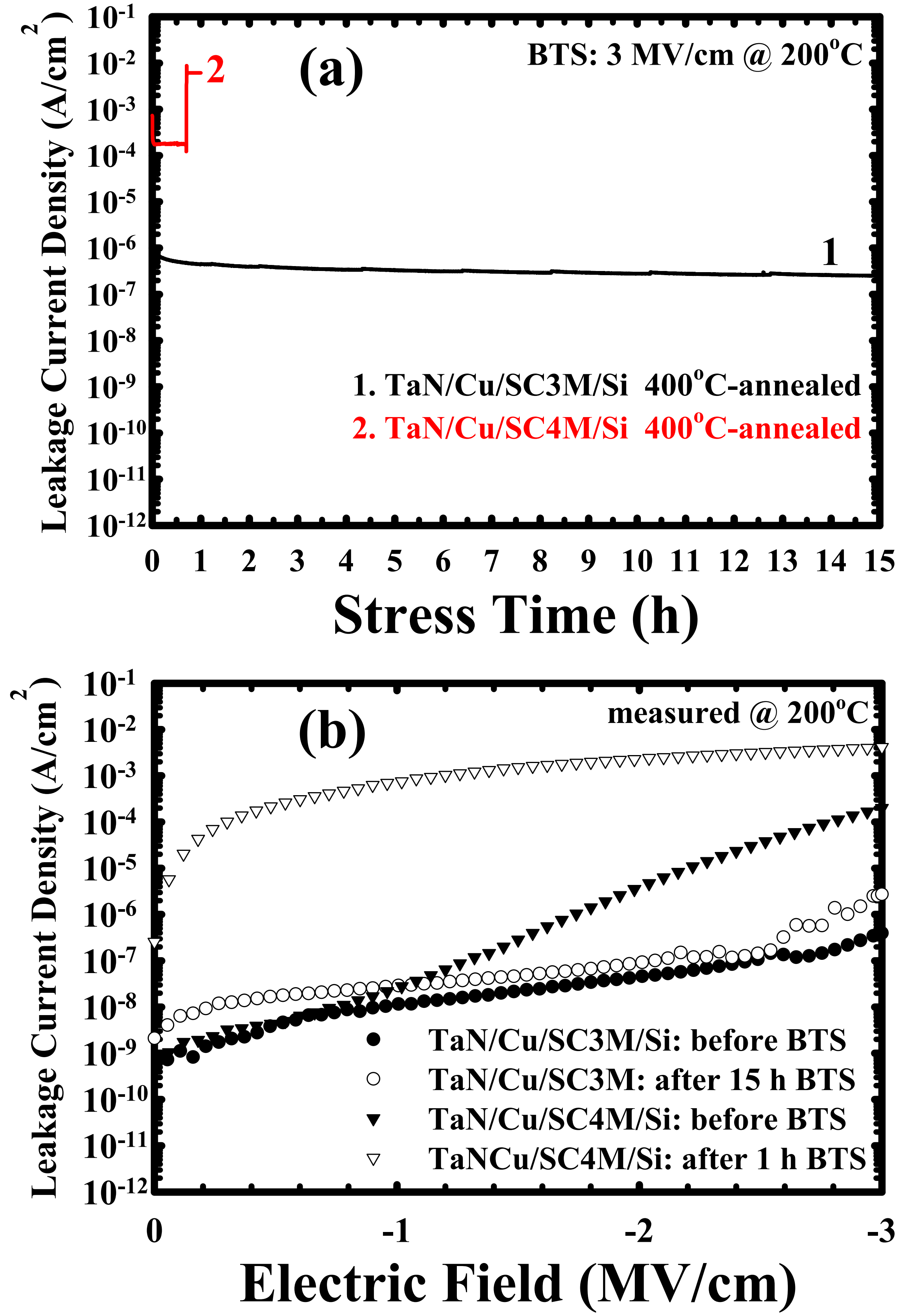

Fig. 5-6 (a) Current transient during the BTS and (b) leakage current density vs. electric field measured before and immediately after BTS (at 200°C with an electric field of 3 MV/cm).

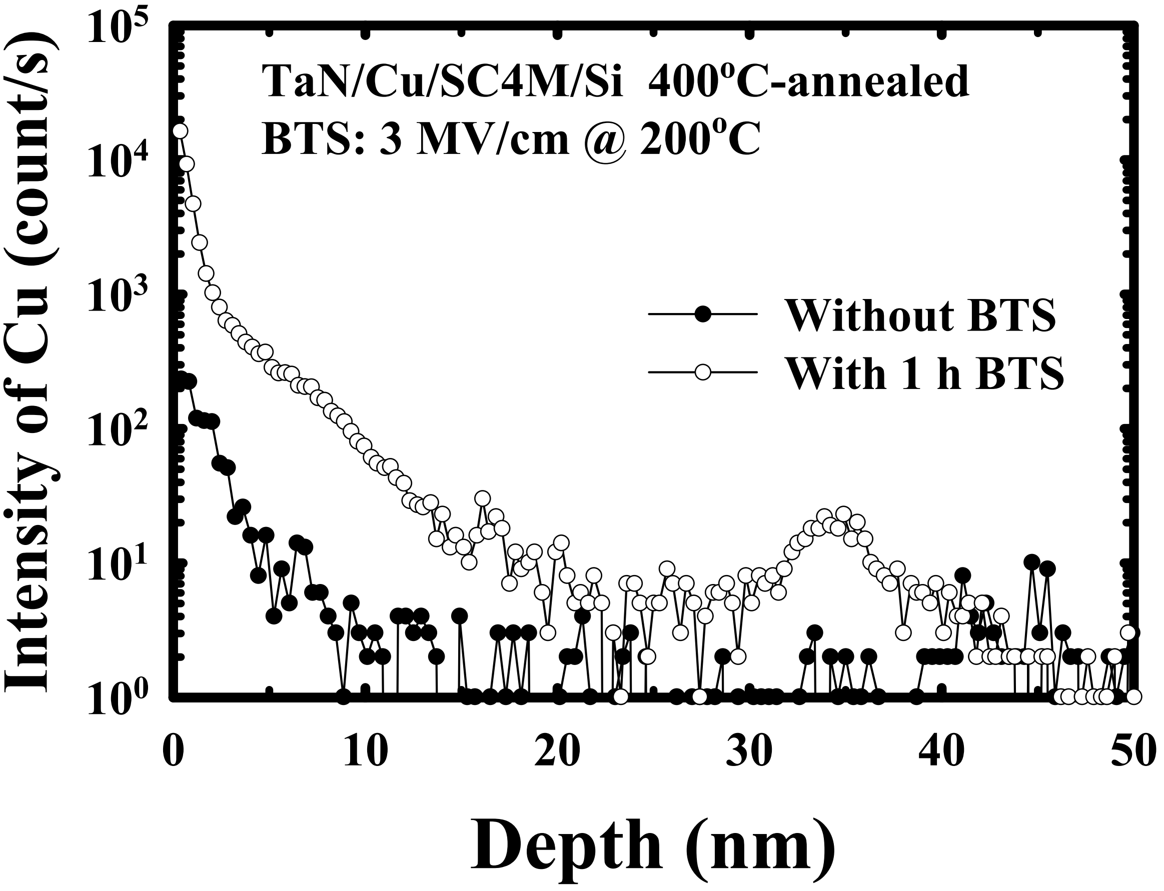

Fig. 5-7 SIMS depth profile of Cu in SC4M film of TaN/Cu/SC4M/Si capacitor before and after 1 h BTS at 200°C with an electric field of 3 MV/cm. The TaN/Cu electrode was removed before the SIMS analysis.

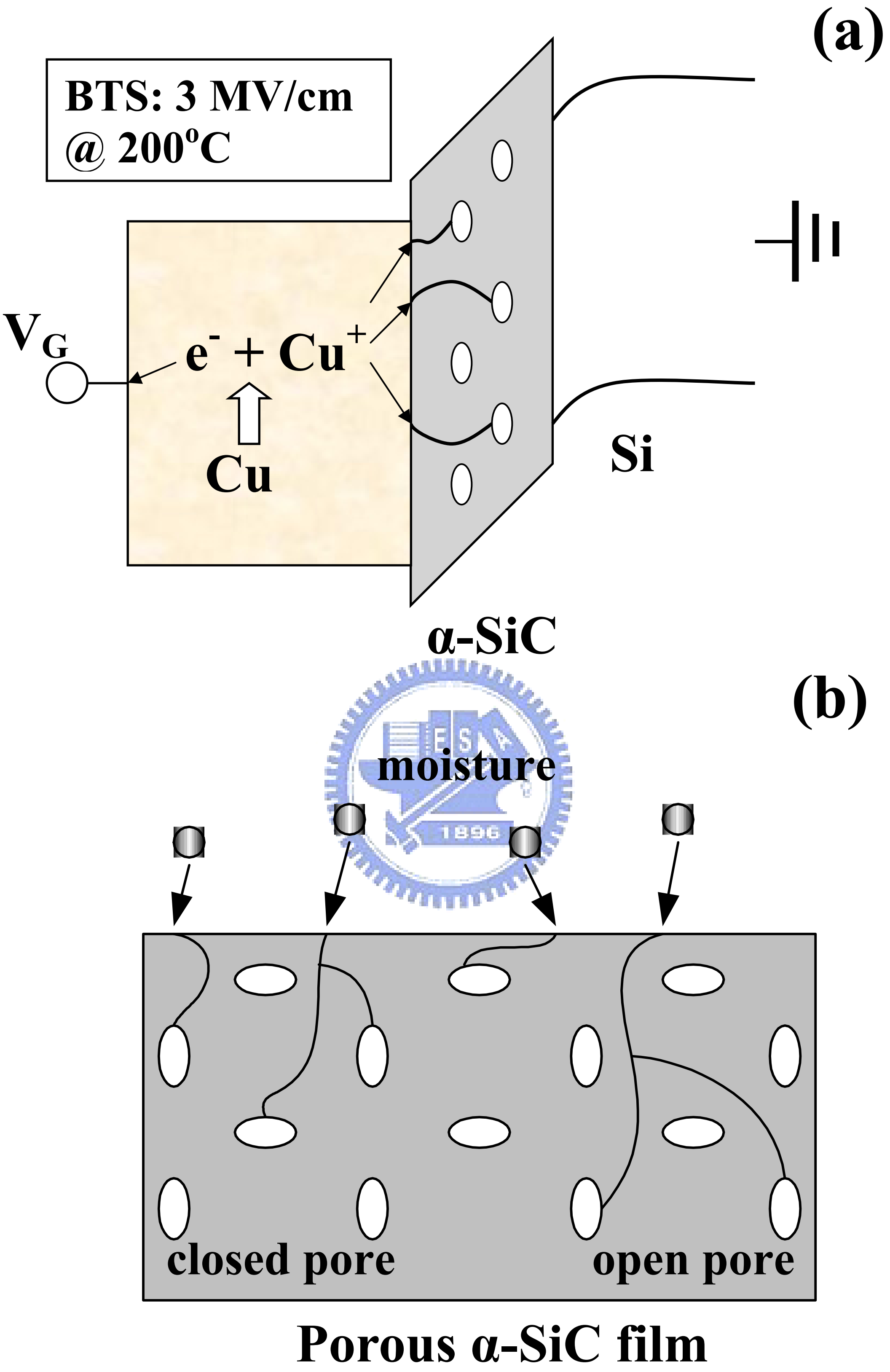

Fig. 5-8 (a) Energy band diagram illustrating the Cu ions drift into a porous α-SiC film during BTS and (b) schematic diagram showing the microstructure of a porous α-SiC film.

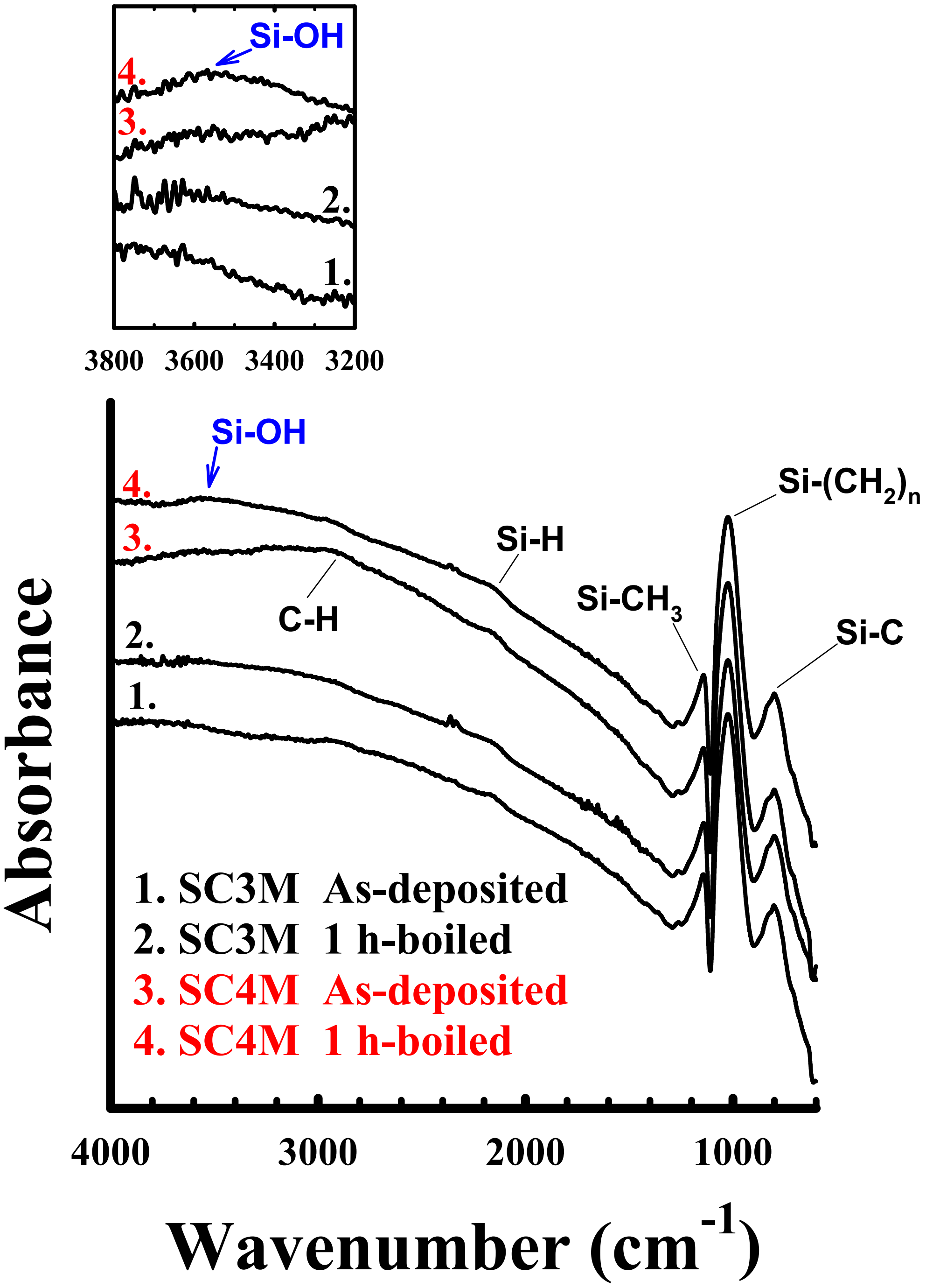

Fig. 5-9 FTIR spectra of two PECVD α-SiC dielectrics before and after immersion in boiling water for 1 h.

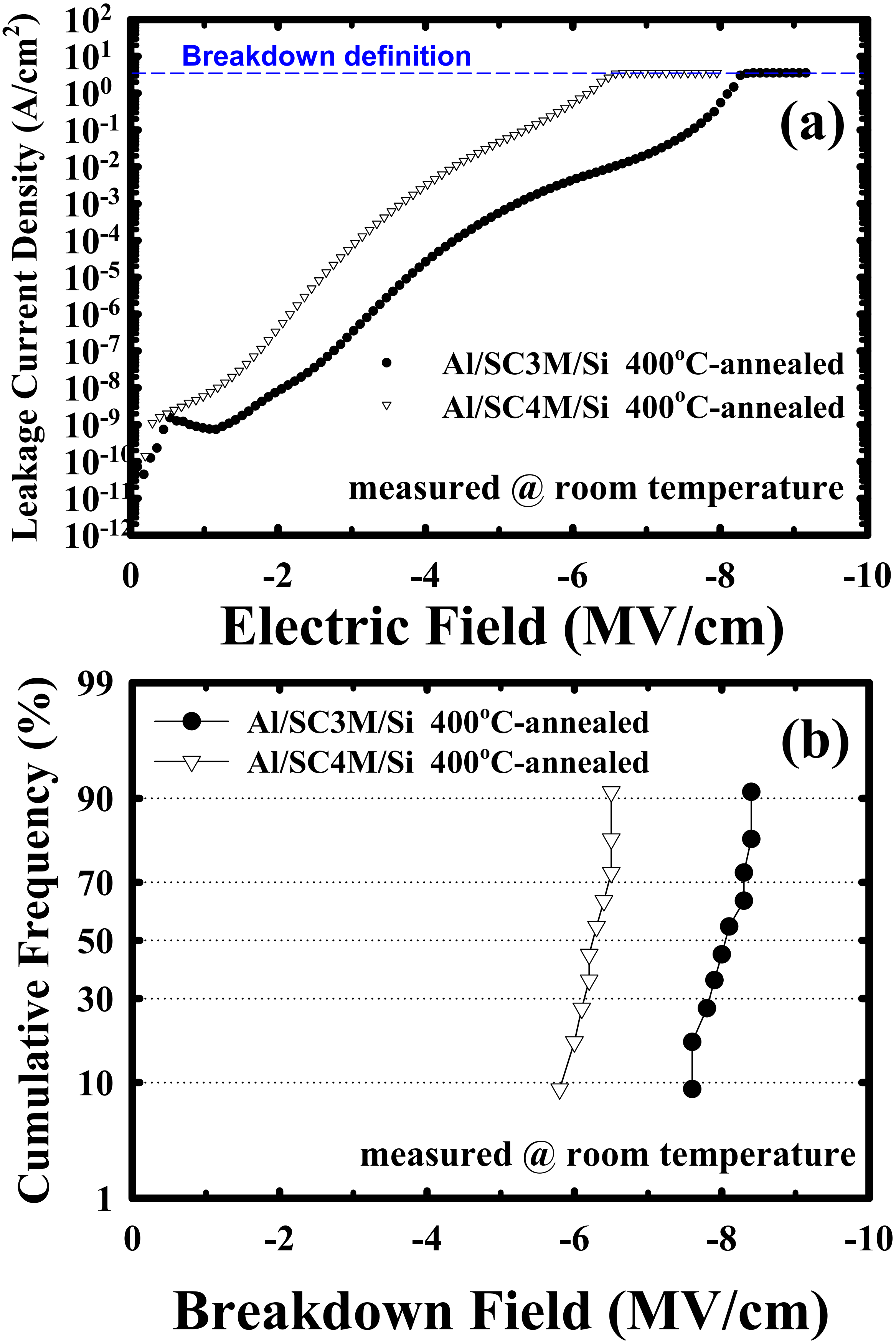

Fig. 5-10 (a) Leakage current density vs. electric field and (b) statistical distribution of breakdown field for the 400°C-annealed Al/SC3M/Si and Al/SC4M/Si MIS capacitors.

Chapter 6

Cu-Comb Capacitor with α-SiCN/α-SiC Bilayer Barrier

6-1 Introduction

Increasing interest has been focused on the study of low stress and thermally stable low-*k* SiC-based films deposited by PECVD using organosilicate gases [1-5], including the α-SiCN and α-SiC dielectric barrier films discussed in chapters 2, 3, and 5. In this chapter, we investigate in the first place, the thermal stability and physical and barrier properties of low-*k* α-SiCN and α-SiC dielectric films ($k<5$) deposited using different process conditions from the previous work. This is followed by investigating the TDDB lifetime of a Cu damascene metallization structure (Cu-comb capacitor) having a bilayer dielectric cap-barrier made up of these low-*k* α-SiCN and α-SiC dielectric films.

6-2 Experimental Details

Two species of PECVD SiC-based dielectric barrier films with *k*-values less than 5 are investigated with respect to the thermal stability and physical and barrier properties. The SiC-based films of α-SiCN and α-SiC, designated as SCN and SC respectively, were deposited on p-type, (100)-oriented Si wafers to a thickness of 50-nm. In addition, a SCN/SC bilayer dielectric film, designated as SCB, was also prepared with a 5 nm SC film deposited on the Si substrate followed by a 45 nm SCN film deposited on top of it. A metal electrode (TaN/Cu or Al) was deposited on the SiC-based films to construct the MIS capacitor structure. For the TaN/Cu-gated MIS capacitors, a Cu layer of 200 nm thickness was sputter deposited on the SiC-based films, followed by a reactive sputter deposition of a 50-nm-thick TaN layer on the Cu surface for the purpose of preventing oxidation of the Cu metal during the subsequent thermal process. Al-gated samples were also prepared by depositing 500-nm-thick Al layers directly on the SiC-based dielectric surfaces. For better electrical measurements, a 500-nm-thick Al layer was also deposited on the backside of the Si substrate for all samples. The TaN/Cu-gated MIS capacitors were then annealed at 400°C for 30 min in N_2 ambient. This annealing step eliminates the plasma induced damage during the sputter deposition of the TaN/Cu electrodes and also provides the driving force for Cu diffusion.

Cu damascene structures (Cu-comb capacitors) were constructed for the TDDB reliability study. Figure 6-1 shows the schematic comb1/serpentine/comb2 test structure and the cross-sectional transmission electron microscopy (TEM) micrograph of the Cu-comb capacitor employed in this study. A PECVD OSG film was first deposited to serve as the IMD. After patterning of 0.20/0.20 μm line-width/space trenches in the OSG dielectric, the damascene Cu features were electrochemically deposited on a 30-nm-thick TaN liner barrier. Following the Cu CMP, either a SCN (50 nm) single layer dielectric or a SCN(45 nm)/SC(5 nm) bilayer dielectric stack (with the thin SC layer deposited first on the Cu-OSG surface), which is designated as SCB, was prepared as the cap-barrier. The Cu-comb capacitor with a SC single layer cap-barrier was not used in this study because the SC dielectric has a very low deposition rate and is susceptible to plasma damage. Finally, the Cu-comb capacitor was passivated with a USG (undoped silicate glass) capping layer of 400 nm thickness.

The dielectric film thickness and refractive index were measured using a well-calibrated n&k analyzer at 633 nm wavelength. The *k*-value of the dielectrics was determined by the maximum capacitance of the Al-gated MIS capacitors measured at 1 MHz using a Keithley 82 C-V measurement system. Fourier transform infrared spectroscopy (FTIR) was used to analyze the chemical bonding of the dielectrics. An HP4145B semiconductor parameter analyzer was used to measure the dielectric leakage current and provide bias for the BTS test. The adhesion of films was measured using a 4-point bending technique [6]. X-ray photoelectron spectroscopy (XPS) was used to analyze the elemental composition of Cu surface.

6-3 Basic Property of Dielectric Barrier

Table 6-1 shows the deposition gas, deposition temperature, deposition rate, and the refractive index and dielectric constant for the two species of PECVD SiC-based films investigated in this chapter. Notably, the deposition rate of SC, which contains no nitrogen at all, is much slower than that of SCN. Figure 6-2 shows the film thickness shrinkage as well as dielectric constant as a function of annealing temperature (for 30 min in N_2 ambient) for the SCN, SC, and SCB films. The SC film has a dielectric constant of about 3.8, while the nitrogen containing SCN film has a higher dielectric constant of about 4.9, presumably due to the polarization contribution from nitrogen. Moreover, higher carbon content would lead to a decrease in dipolar and ionic polarizations, resulting in a lower *k*-value of the dielectrics [7,8]. The effective dielectric constant of the SCB film, which is a bilayer SCN(45 nm)/SC(5 nm) film, should be very close to that of the SCN film. The substantial increase in thickness shrinkage and dielectric constant at temperatures above 500^{o}C is attributed to the outgassing of the methyl group, resulting in a decrease and eventual disappearance of Si-CH_3, C-H, and Si-H peak heights, as shown in the FTIR spectra illustrated in Fig. 6-3. The leakage current density of the Al/SCN/Si, Al/SC/Si, and Al/SCB/Si MIS capacitors measured at various temperatures is illustrated in Fig.

6-4. The TDDB was measured on the TaN/Cu-gated SCN(50 nm), SC(50 nm), and SCB(45 nm SCN/5 nm SC) MIS samples at 200°C under a bias stress of 1 MV/cm. Figure 6-5 illustrates the leakage current transient during the BTS and the instantaneous leakage current density versus applied electric field (in accumulation mode) before and after the BTS. All the samples remained stable under the BTS up to at least 15 hrs. This implies that both SCN and SC dielectric bulk films were capable of preventing Cu permeation.

6-4 Electrical Property of Comb Capacitor

Figures 6-6 and 6-7 illustrate the results of leakage current measurements and breakdown field statistics, respectively, for the Cu-comb capacitors with a cap-barrier layer of SCN(50 nm) as well as SCB(45 nm SCN/5 nm SC). The breakdown field is defined as the field strength such that the leakage current between comb1/comb2 (grounded) and serpentine (positive biased) exceeds 1 mA, and the histogram of the breakdown field was constructed from the data obtained by measuring twenty-nine samples. The Cu-comb capacitor with a SCB bilayer cap-barrier exhibits a much lower leakage current and higher breakdown field than that with a SCN single layer cap-barrier. Figure 6-8 shows the TDDB measurement at 200°C under a bias stress of 2 MV/cm for the Cu-comb capacitor with different cap-barrier of SCN and SCB layer, while Fig. 6-9 shows the measured time-to-breakdown versus BTS stress field. The Cu-comb capacitor with a SCB bilayer cap-barrier has a higher value of TDDB lifetime than the structure using a SCN single layer cap-barrier of the same thickness. All these observations are attributed to the lower leakage current of SC dielectric film (Fig. 6-4) since both dielectric films were capable of preventing Cu permeation (Fig. 6-5). In addition, the adhesion strength of SC/Cu and SC/OSG interfaces is superior to that of

SCN/Cu and SCN/OSG interfaces, as shown in Table 6-2. XPS analysis shows that there is a nitridation layer of CuN_x at the SCN/Cu interface, but not at the SC/Cu interface (not shown). The ionized Cu atoms of CuN_x compound have a lower activation energy for diffusion [9], leading to the degradation of the TDDB reliability of Cu-comb capacitor with a SCN single layer cap-barrier. Since the SC dielectric has a very low deposition rate, we believe that the SCN/SC bilayer dielectric is a favorable combination for the cap-barrier because the nitrogen containing SCN film with the SiN_x compound can protect the SC film from plasma attack, such as O_2 plasma attack during photoresist stripping [10] and organosilicate plasma attack during OSG deposition.

6-5 Summary

The TDDB lifetime of Cu-comb capacitor is greatly improved by using an α-SiCN/α-SiC bilayer dielectric stack as the cap-barrier layer. This improvement is attributed to the lower leakage current of α-SiC, absence of nitridation on Cu surface, and better adhesion of α-SiC on Cu and OSG IMD. Although the α-SiC film has a very low deposition rate, the α-SiCN/α-SiC bilayer dielectric is a favorable combination for the cap-barrier layer because α-SiCN can protect α-SiC from plasma attack, such as O_2 plasma attack during photoresist stripping and organosilicate plasma attack during OSG deposition.

References

[1] M. J. Loboda, J. A. Seifferly, and F. C. Dall, *J. Vac. Sci. Technol. A*, **12** (1994) p. 90.

[2] M. J. Loboda, J. A. Seifferly, C. M. Grove, and R. F. Schneider, *Mat. Res. Soc. Symp. Proc.*, **447** (1997) p. 145.

[3] P. Xu, K. Huang, A. Patel, S. Rathi, B. Tang, J. Ferguson, J. Huang, C. Ngai, and M. Loboda, *IEEE IITC Technol. Dig.* (1999) p. 109.

[4] M. J. Loboda, *Microelectronic Engineering*, **50** (2000) p. 15.

[5] S. G. Lee, Y. J. Kim, S. P. Lee, H. S. Oh, S. J. Lee, M. Kim, I. G. Kim, J. H. Kim, H. J. Shin, J. G. Hong, H. D. Lee, and H. K. Kang, *Jpn. J. Appl. Phys.*, **40** (2001) p. 2663.

[6] T. Scherban, B. Sun, J. Blaine, C. Block, B. Jin, and E. Andideh, *IEEE IITC Technol. Dig.* (2001) p. 257.

[7] B. K. Hwang, M. J. Loboda, G. A. Cerry, R. F. Schneider, J. A. Seifferly, and T. Washer, *IEEE IITC Technol. Dig.* (2000) p. 52.

[8] J. Y. Kim, M. S. Hwang, Y. H. Kim, H. J. Kim, and Y. Lee, *J. Appl. Phys.*, **90** (2001) p. 2469.

[9] J. D. McBrayer, R. M. Swanson, and T. W. Sigmon, *J. Electrochem. Soc.*, **133** (1986) p. 1242.

[10] P. T. Liu, T. C. Chang, H. Su, Y. S Mor, Y. L. Yang, H. Chung, J. Hou, and S. M. Sze, *J. Electrochem. Soc.*, **148** (2001) p. F30.

Table 6-1 Properties of SiC-based dielectric barrier films studied in this chapter.

Sample	**SCN**	**SC**
Structure	**α-SiCN**	**α-SiC**
Deposition gas	**He/$(CH_3)_3SiH/NH_3$**	**$(CH_3)_3SiH$**
Deposition temperature (^oC)	**350**	**350**
Deposition rate (nm/min)	**176**	**2.6**
Refractive index (at 633 nm)	**1.90**	**1.85**
Dielectric constant @ 1 MHz	**4.9**	**3.8**

Table 6-2 Adhesion strength of SiC-based dielectric/Cu and SiC-based dielectric/OSG interfaces.

Film Scheme	**Adhesion Gc (J/m^2)**
SCN/Cu/TaN/PE-OX/Si	**2.76**
SC/Cu/TaN/PE-OX/Si	**8.44**
SCN/OSG/SiN/PE-OX/Si	**4.44**
SC/OSG/SiN/PE-OX/Si	**9.34**

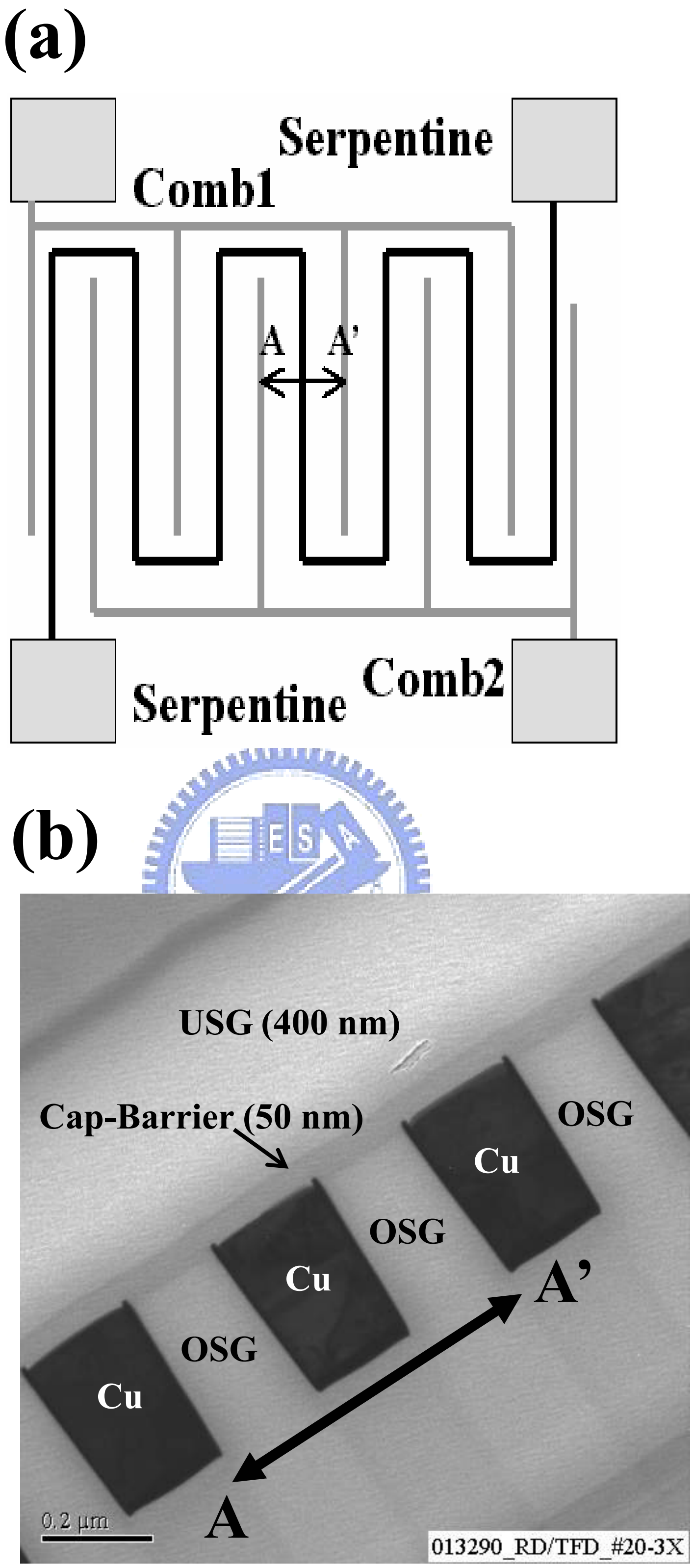

Fig. 6-1 (a) Schematic diagram of comb1/serpentine/comb2 test structure and (b) cross-sectional TEM micrograph of the Cu-comb capacitor.

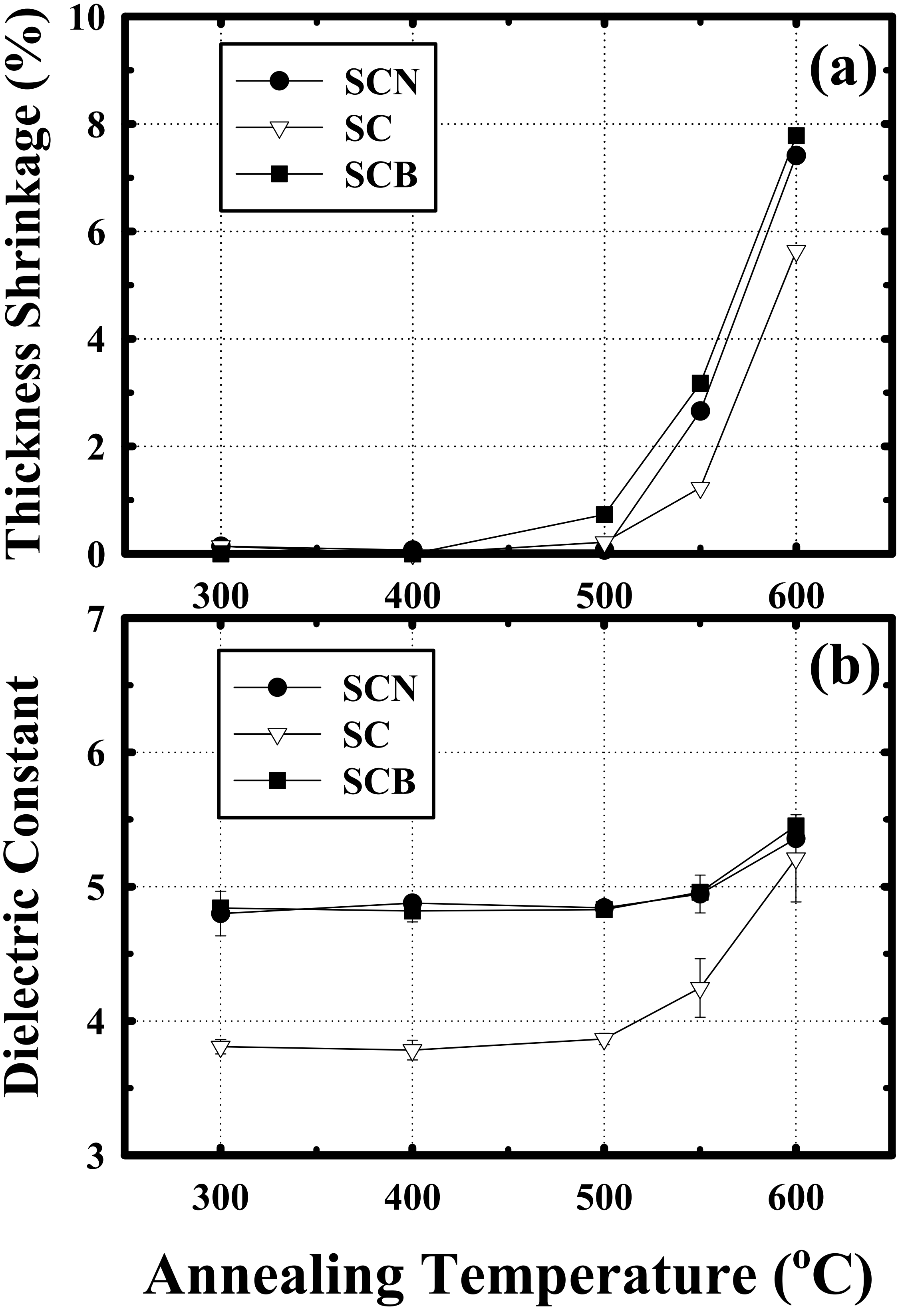

Fig. 6-2 (a) Thickness shrinkage and (b) dielectric constant vs. annealing temperature for three samples of PECVD SiC-based dielectrics.

.

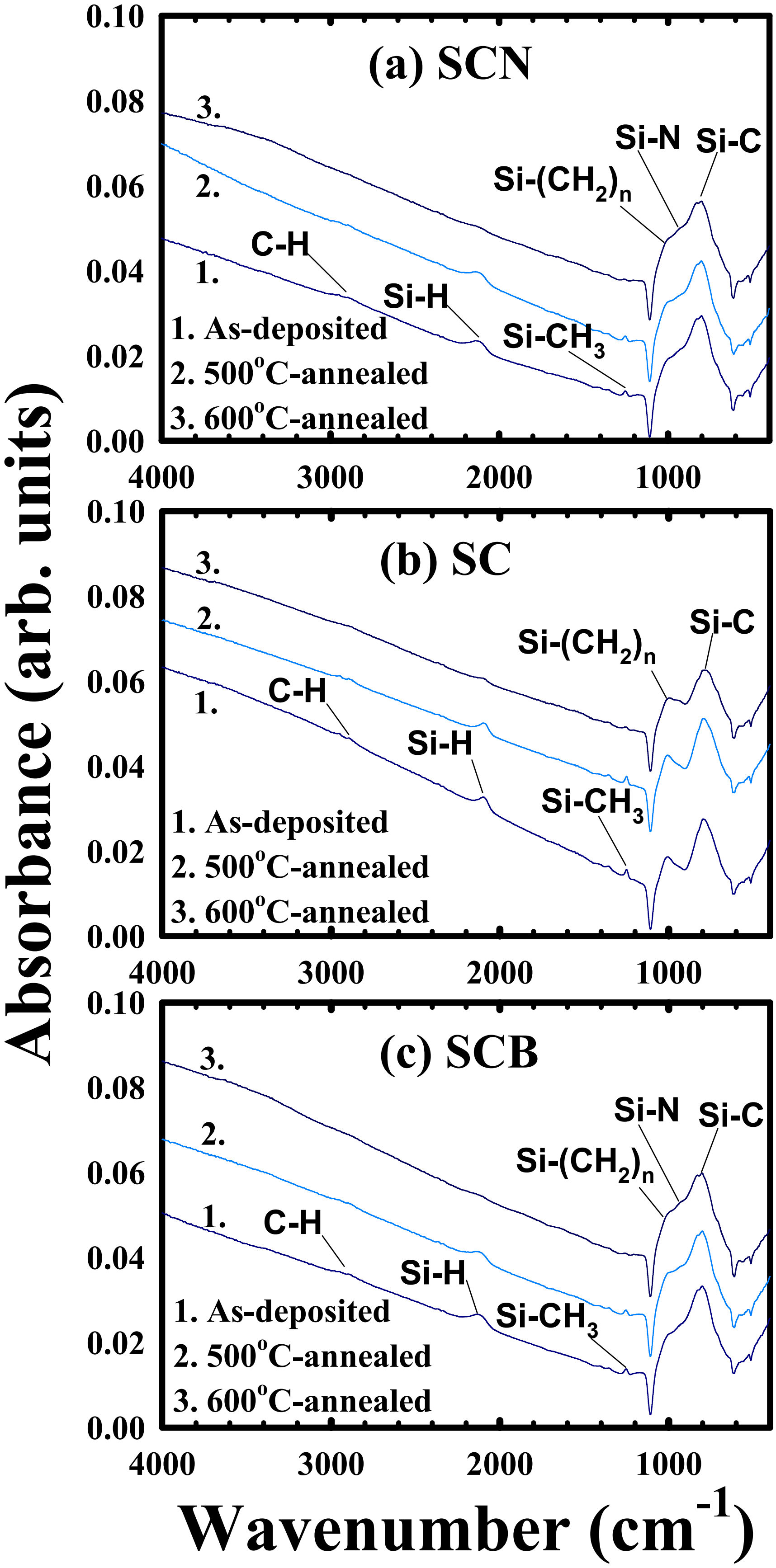

Fig. 6-3 FTIR spectra for three samples of PECVD SiC-based dielectrics (a) SCN, (b) SC, and (c) SCB.

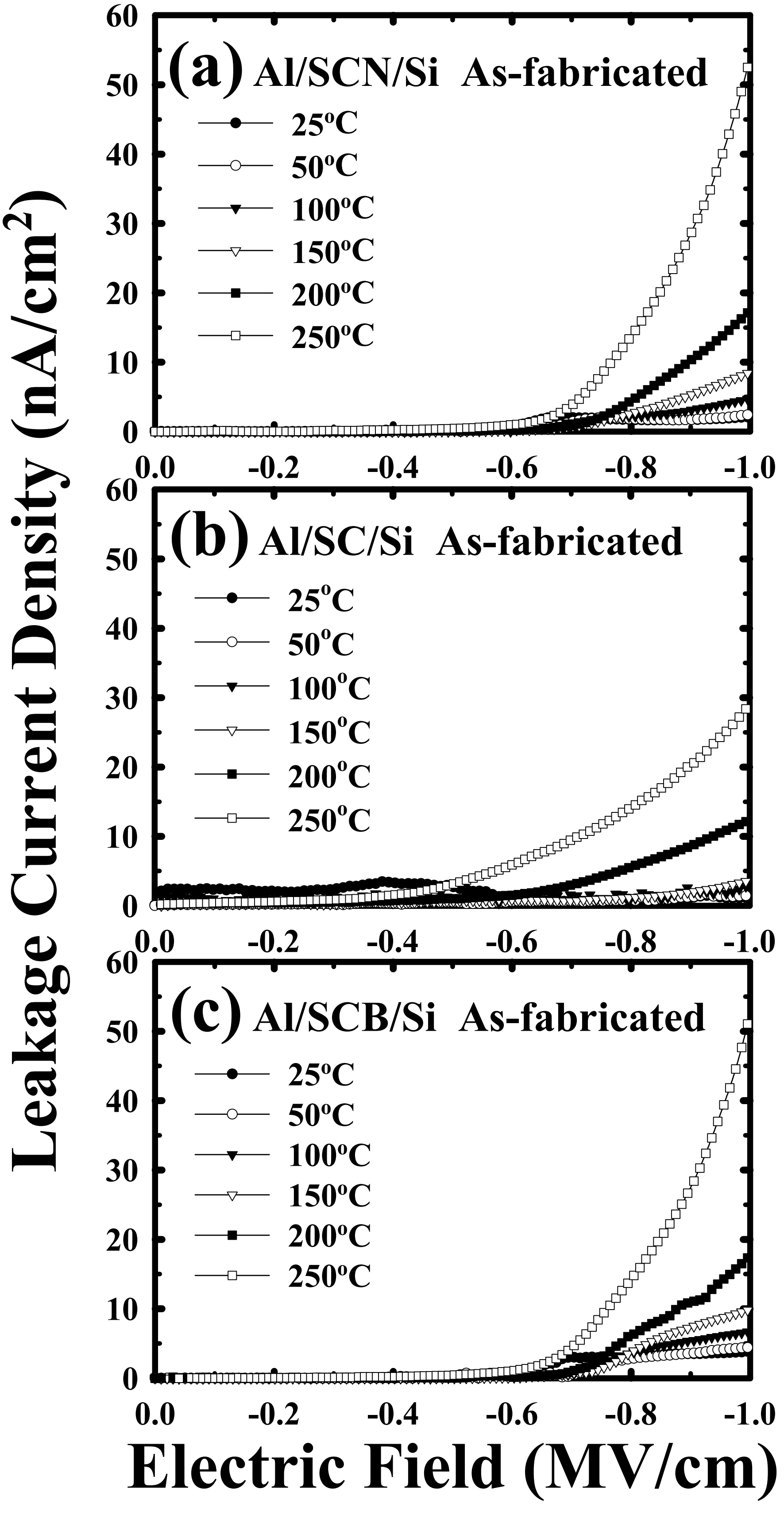

Fig. 6-4 Current density vs. electric field, measured at various temperatures, for (a) Al/SCN/Si, (b) Al/SC/Si, and (c) Al/SCB/Si MIS capacitors.

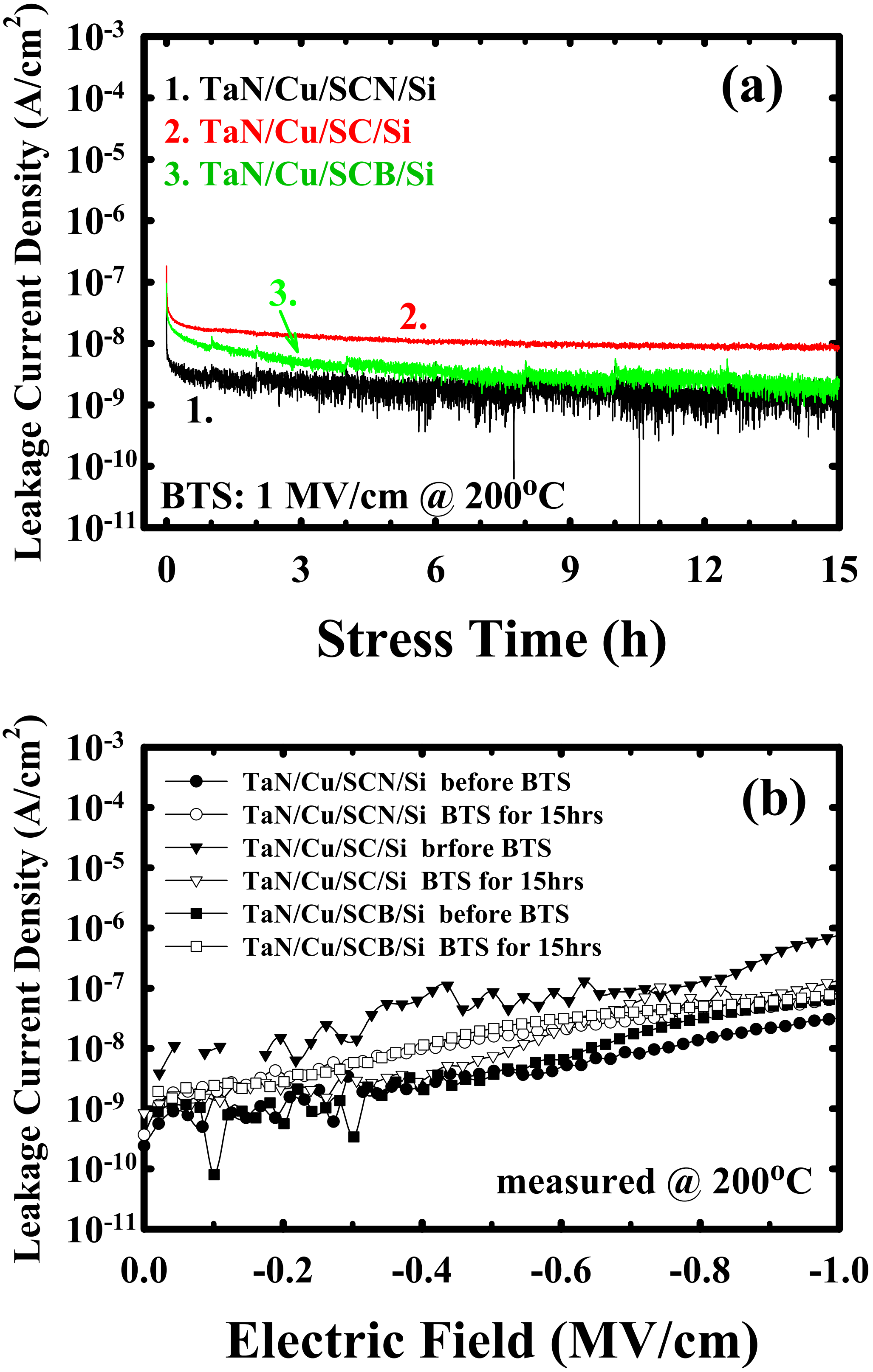

Fig. 6-5 (a) Current transient during BTS (1 MV/cm at 200°C) and (b) instantaneous current density vs. electric field before and after the BTS for the TaN/Cu/SCN/Si, TaN/Cu/SC/Si, and TaN/Cu/SCB/Si MIS capacitors.

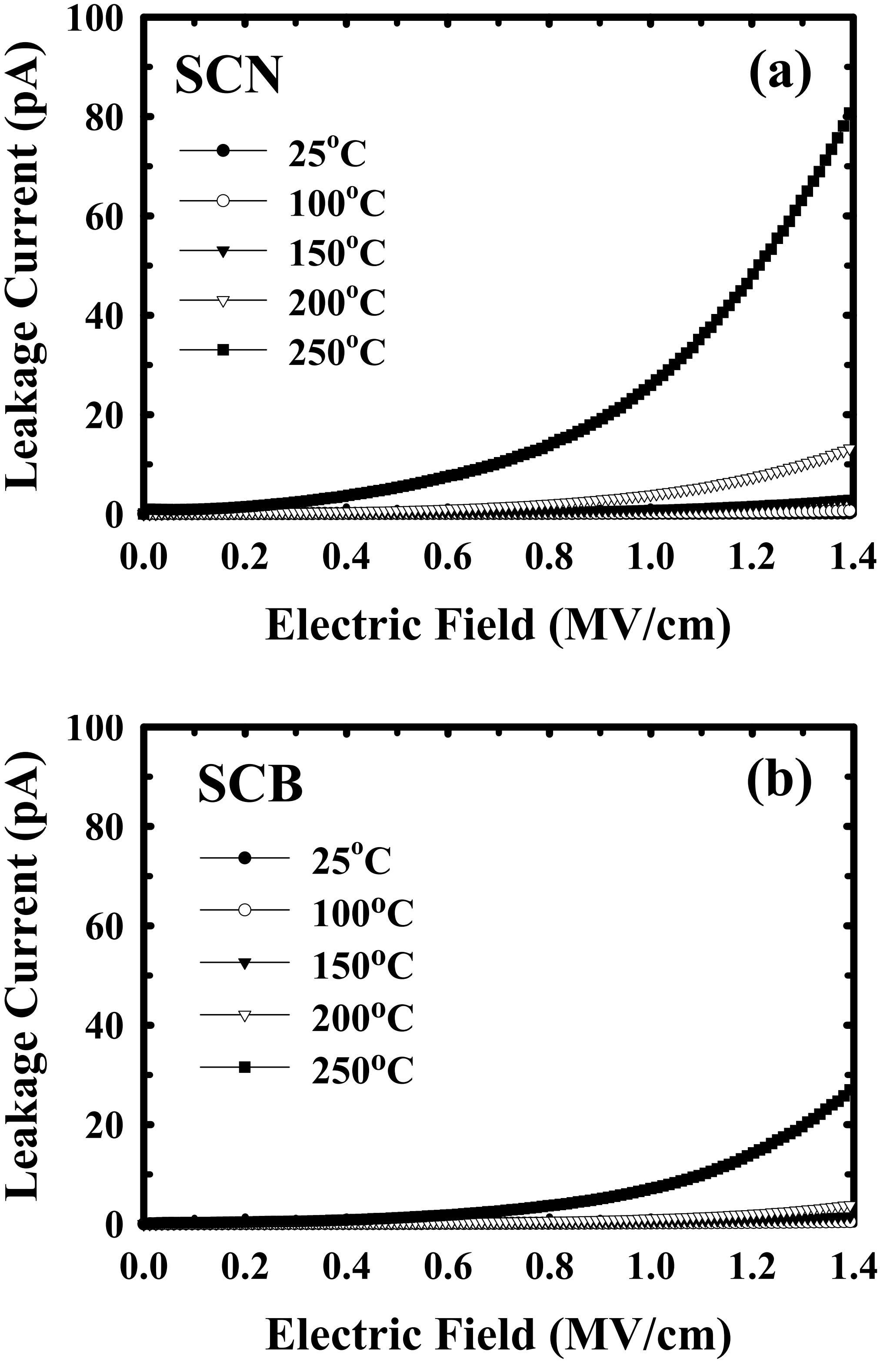

Fig. 6-6 Leakage current vs. electric field, measured at various temperatures, for Cu-comb capacitor with a cap-barrier layer of (a) SCN and (b) SCB.

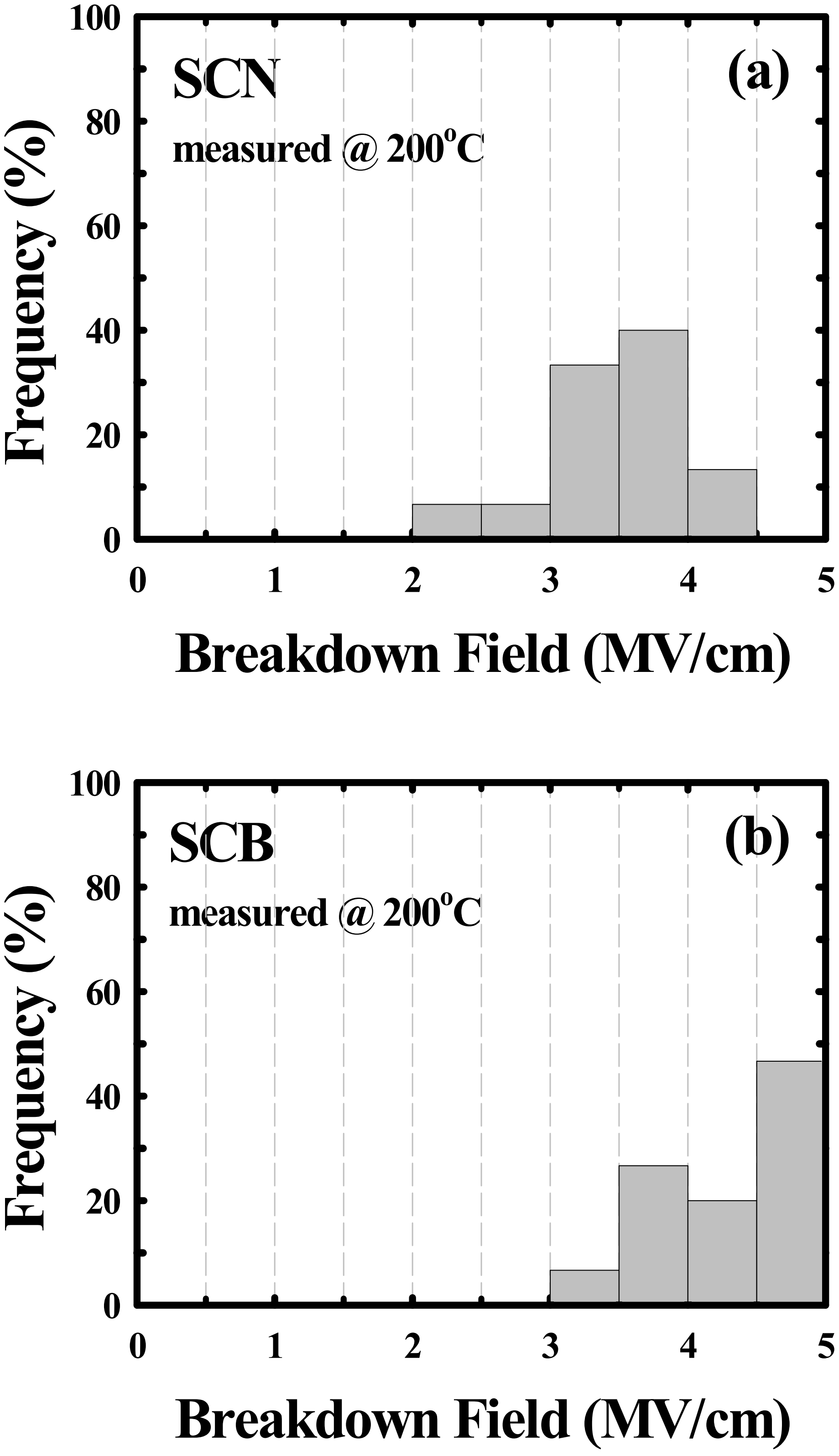

Fig. 6-7 Histogram of breakdown field for the Cu-comb capacitor with a cap-barrier layer of (a) SCN and (b) SCB.

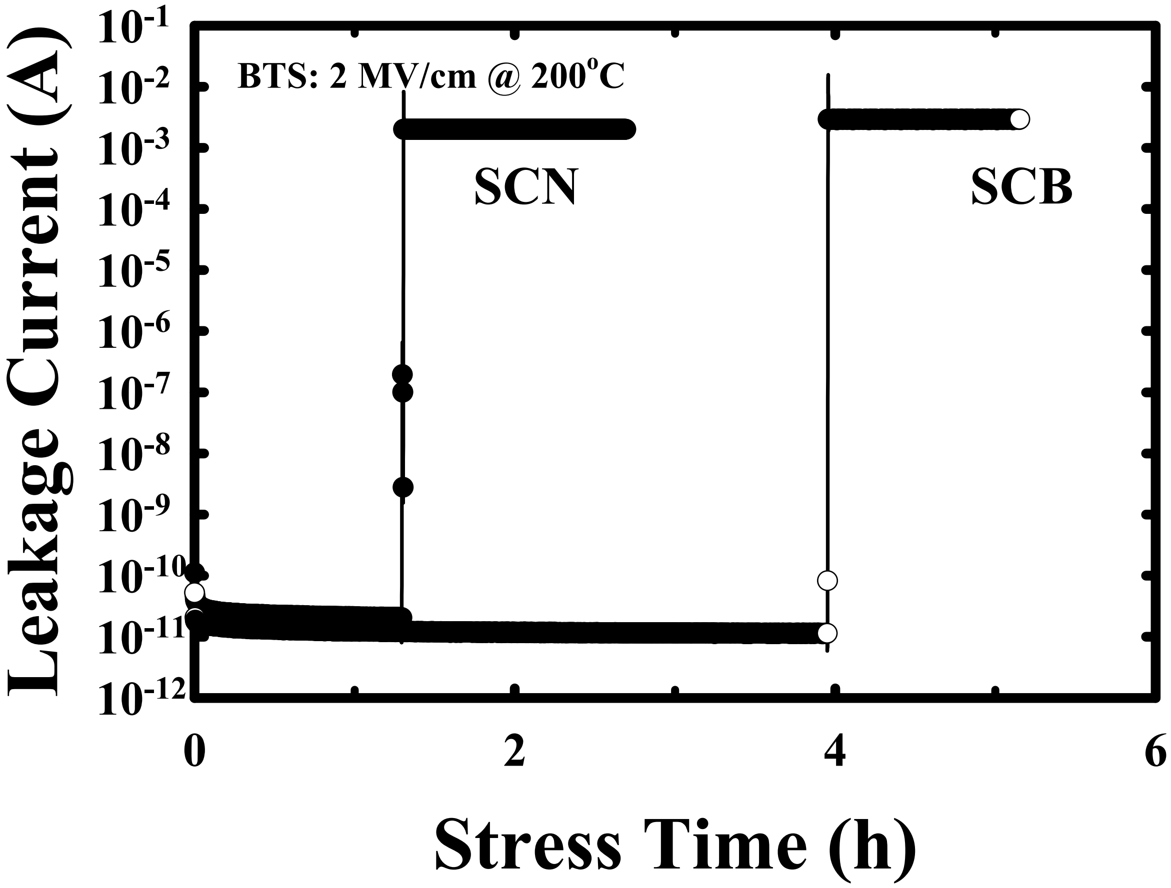

Fig. 6-8 Current transient during BTS (2 MV/cm at 200°C) for Cu-comb capacitor with a cap-barrier layer of SCN and SCB.

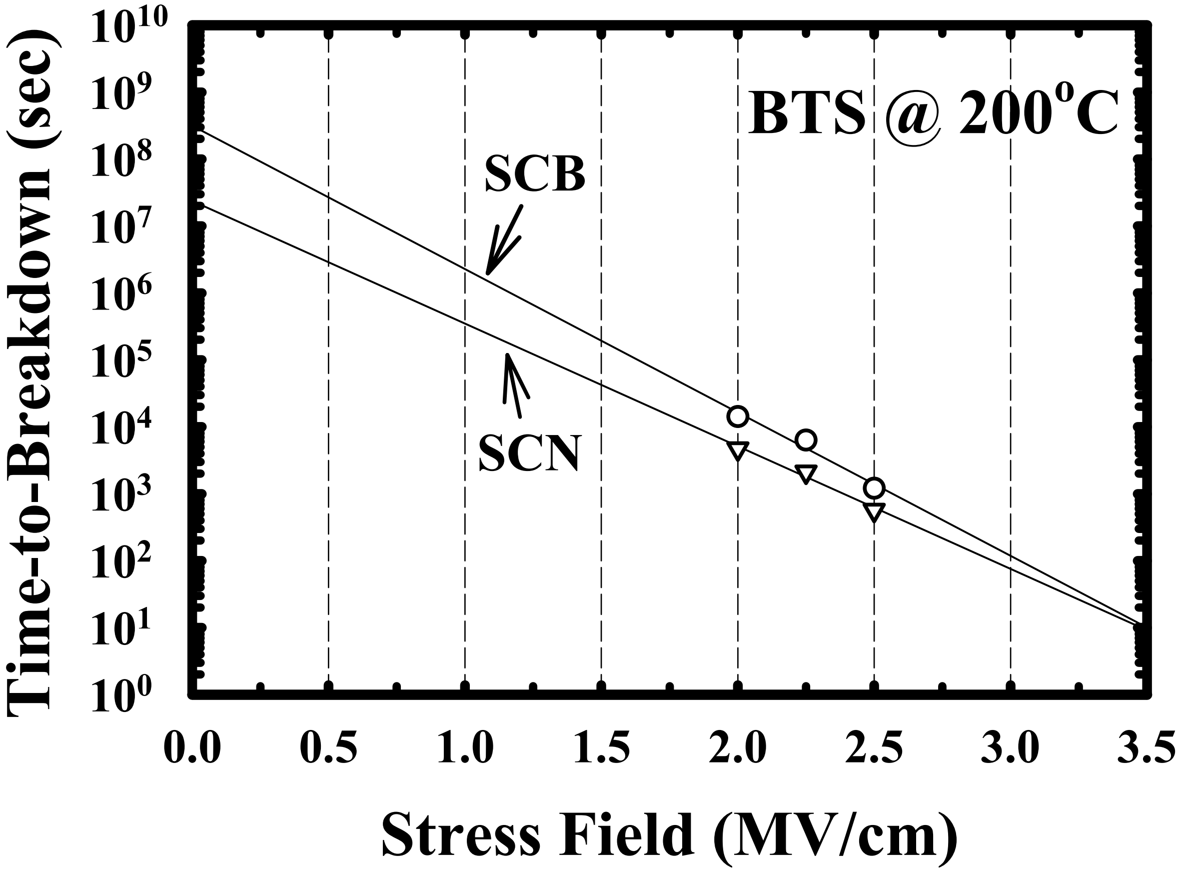

Fig. 6-9 Time-to-breakdown vs. BTS stress field at 200°C for Cu-comb capacitor with a cap-barrier layer of SCN and SCB.

Chapter 7

Leakage and Breakdown Mechanisms of Cu-Comb Capacitor with α-SiCN/α-SiC Bilayer Barrier

7-1 Introduction

There are a number of studies on the electrical reliability of the α-SiC and α-SiCN films with respect to their integration with Cu using planar MIS capacitors [1-6], as also discussed in chapters 2, 3, 5, and 6. In practical applications, however, considerable attention must be focused on the electrical reliability issues of comb capacitors, such as leakage and breakdown mechanisms and potential leakage paths in the bulk of the low-*k* film, the Cu cap-barrier/low-*k* film interface, and the surrounding dielectrics. It was found in chapter 6 that the bilayer-structured α-SiCN/α-SiC dielectric film is a favorable combination to serve as a Cu cap-barrier to improve TDDB reliability of the Cu-comb capacitor [6]. The improvement in TDDB is attributed to the α-SiC film's lower leakage current, better adhesion to Cu and OSG IMD, and absence of nitridation on the Cu surface. The α-SiCN film on top of the α-SiC film serves to protect the α-SiC film from plasma attack, such as O_2 plasma attack during photoresist stripping and organosilicate plasma attack during OSG deposition. In this chapter, we investigate the leakage and breakdown mechanisms in the Cu-comb capacitor with a bilayer-structured α-SiCN/α-SiC Cu cap-barrier.

7-2 Experimental Details

The leakage current of Cu-comb capacitors was measured on a 0.12/0.12 μm (line-width/space) comb capacitor as illustrated in Fig. 7-1. A 40 nm PECVD α-SiCO ESL was deposited on the PECVD oxide ILD. A single level Cu damascene (Metal-1) process with a 250 nm PECVD methylsilane-based low-*k* OSG (*k*=3) as the IMD was employed to fabricate the comb capacitor. After patterning of the 0.12/0.12 μm (line-width/space) trenches in the OSG/ESL/ILD dielectric stack, the damascene Cu feature was electrochemically deposited on a 15 nm physical vapor deposited (PVD) TaN liner barrier. Following the Cu CMP, a bilayer-structured α-SiCN(*k*=5)/α-SiC(*k*=4) Cu cap-barrier with bilayer thicknesses of 50/2, 45/5, 40/10, and 30/20 (nm/nm) was sequentially deposited in a PECVD system at 350°C and a total gas pressure of 1-5 Torr. The α-SiC film was deposited using $(CH_3)_3SiH$ with a flow rate of 100-500 sccm and a plasma power of 100-200 W, while the α-SiCN layer was deposited using $He/(CH_3)_3SiH/NH_3$ with a flow rate ratio of 8/3/6 and a plasma power of 100-500 W. Another layer of PECVD OSG was deposited for the next Cu damascene (Metal-2) process.

An HP4145B semiconductor parameter analyzer was used to measure the leakage current between Cu lines and provide the bias for the bias-temperature-stress (BTS) test. An N_2 purging was used to prevent possible oxidation of the Cu metal and moisture uptake in the dielectric films during the measurement. Raphael modeling [7] was used to obtain the distribution of electric field in the Cu-comb capacitors.

7-3 Leakage Mechanism

Figure 7-2 shows the leakage current of Cu-comb capacitors with an α-SiCN/α-SiC bilayer barrier of different thickness ratios measured at various temperatures. The dominant current conduction mechanisms in the Cu-comb capacitors were identified by fitting slopes for various conduction mechanisms, as shown in Fig. 7-3. Evidently, the fitting slopes vary with the electric field. All comb capacitors exhibit ionic conduction at electric fields below 0.5 MV/cm at all measurement temperatures employed in this study. The ionic current shows a hysteresis effect (Fig. 7-3a), as confirmed by repeatedly sweeping the electric field from –1.25 to +1.25 MV/cm and back down [8,9]. The ionic conduction of Cu-comb capacitors becomes more apparent at low temperatures (e.g. 25°C), whereas a conduction mechanism like ohmic conduction prevails at temperatures above 200°C. Notably, the comb capacitors with an α-SiCN/α-SiC bilayer barrier of 40 nm/10 nm or 30 nm/20 nm thickness exhibit ohmic conduction at electric fileds between 0.25 and 0.5 MV/cm and at temperatures of 200 to 250°C; in this region, the leakage current (I) is linearly correlated with the electric field (E) (Fig. 7-3b), and the current can be expressed by Eq. (7-1) [8]. The comb-capacitor with an α-SiCN/α-SiC bilayer barrier of 50 nm/2 nm thickness exhibits Schottky emission (SE) at electric fields above 0.5 MV/cm, particularly at temperatures above 200°C. The SE conduction shows $\mathrm{Ln}(I/T^2)$ linearly correlated with $E^{1/2}$ (Fig. 3c), and the current can be expressed by Eq. (7-2) [8]. Nevertheless, the comb-capacitor with an α-SiCN/α-SiC bilayer barrier of 45 nm/5 nm thickness exhibits SE conduction only at electric fields of 0.5 to 0.8 MV/cm, and Frenkel-Poole (F-P) emission appears after the kink at 0.8 MV/cm, in particular at temperatures above 200°C. The F-P conduction shows $\mathrm{Ln}(I/E)$ linearly correlated with $E^{1/2}$ (Fig. 7-3d), and the current can be expressed by Eq. (7-3) [8]. As for the comb capacitors with an α-SiCN/α-SiC bilayer barrier of 40 nm/10 nm or 30 nm/20 nm thickness, F-P conduction prevails at electric fields above 0.5 MV/cm.

ohmic $I \sim E \exp(-\Delta E_{ae}/kT)$ (7-1)

SE $I \sim T^2 \exp(\beta E^{1/2}/kT - q\Phi_{SE}/kT)$ (7-2)

F-P $I \sim E \exp(2\beta E^{1/2}/kT - q\Phi_{FP}/kT)$ (7-3) where ΔE_{ae} is the activation energy of electron, β represents $(q^3/4\pi\varepsilon)^{1/2}$ and ε is the dielectric dynamic permittivity, k is the Boltzmann constant, q is an electron-charge, Φ_{SE} is the barrier height of metal/dielectric interface, and Φ_{FP} is the barrier height of trap potential well. Table 7-1 summarizes the leakage mechanisms at various electric fields for the Cu-comb capacitors measured at temperatures of 200 to 250°C. The leakage mechanism between the Cu lines is dependent on the thickness ratio of the α-SiCN/α-SiC bilayer barrier. In contrast to the α-SiCN(50 nm)/α-SiC(2 nm) sample, there is a transition of SE to F-P conduction at 0.8 MV/cm electric field in the α-SiCN(45 nm)/α-SiC(5 nm) sample, while the α-SiCN(40 nm)/α-SiC(10 nm) and α-SiCN(30 nm)/α-SiC(20 nm) samples exhibit the same leakage mechanisms at all electric fields employed in this study. Figure 7-4 shows the leakage current of various Cu-comb capacitors versus measurement temperature. Notably, the leakage current behavior at the low electric field of 0.65 MV/cm can be divided into two groups, with α-SiCN(50 nm)/α-SiC(2 nm) and α-SiCN(45 nm)/α-SiC(5 nm) samples in one group (Fig. 7-4a); at the high electric field of 1.25 MV/cm, however, the leakage current behavior of the α-SiCN(45 nm)/α-SiC(5 nm) sample deviates from that of the α-SiCN(50 nm)/α-SiC(2 nm) sample (Fig. 7-4b). This is due to the transition of SE to F-P conduction in the α-SiCN(45 nm)/α-SiC(5 nm) sample at 0.8 MV/cm electric field at elevated temperatures.

The leakage current density of the bulk OSG is at least 20 times larger than that of the bulk α-SiCN, α-SiC, α-SiCO (ESL) and PECVD oxide (ILD) films studied using MIS capacitors; thus the effective leakage current component through the bulk OSG (250 nm) is expected to be at least two orders of magnitude larger than that through the α-SiCN (≤50 nm), α-SiC (≤20 nm), ESL (40 nm) and ILD (≤10 nm below ESL) dielectric films in the Cu-comb capacitors. However, it has been reported that the localized surface defects at the α-SiC/OSG interface (CMP-surface) can degrade the leakage current and TDDB reliability [10,11]. Since there is no CMP-induced damage at the OSG/ESL and ESL/ILD interfaces, we did not observe the pseudo-breakdown phenomenon, which is supposedly arisen from the defects at the OSG/ESL and ESL/ILD interfaces [12]. This will be further discussed later and illustrated in Fig. 7-8. Therefore, the dominant leakage path in the Cu-comb capacitor could be the electronic current through the bulk of OSG and/or the α-SiC/OSG interface.

Possible determining factors for the dominant leakage path in the Cu-comb capacitor may include the electric field and/or physical stress at the α-SiC/OSG interface and/or in the bulk of OSG. Figure 7-5 shows the electric field at the α-SiC/OSG interface and in the bulk of OSG obtained from the Raphael simulation for various Cu-comb capacitors biased with an electric voltage of 24 V. The higher electric field at the α-SiC/OSG interface than that in the bulk of OSG may be due to a number of factors, such as shorter distance at the top of Cu lines, angular shape at the corner of Cu lines, and higher dielectric constant of the α-SiC layer [10]. Since the behavior of the simulation obtained electric field is contrary to the magnitude of leakage current with respect to the bilayer thickness ratio of the Cu-comb capacitors, we presume that the increased leakage current between Cu lines for the α-SiCN(40 nm)/α-SiC(10 nm) and α-SiCN(30 nm)/α-SiC(20 nm) samples is attributed to the physical stress. Because the OSG film exhibits a tensile stress of 40~60 MPa, a compressive stress should be preferred for the α-SiC film deposited on the top of the OSG layer [2]. However, the α-SiC film has a tensile stress of 10~20 MPa, and a thicker α-SiC film would be subjected to a larger tensile force [13], which may generate a large number of interfacial defects, such as cracks, voids, traps or dangling bonds at the α-SiC/OSG interface, as illustrated in Fig. 7-6. For the Cu-comb capacitors with α-SiCN(40 nm)/α-SiC(10 nm) and α-SiCN(30 nm)/α-SiC(20 nm) bilayer thicknesses, which exhibit a larger leakage current at temperatures above 200°C, the ohmic conduction dominates at an electric field between 0.25~0.5 MV/cm (Table 7-1) and the current is carried by thermally excited electrons hopping from one isolated trap to the next [8]. At an electric field above 0.5 MV/cm, the current is dominated by the F-P emission, which is due to field-enhanced thermal excitation of trapped electrons into conduction band [8]. Both of the ohmic conduction and the F-P emission mechanisms result from a large number of interfacial defects at the α-SiC/OSG interface.

7-4 Breakdown Mechanism

Figure 7-7 shows the breakdown field measured at 200°C for various comb capacitors with the data obtained from 10 randomly chosen samples in each case. All samples exhibit a comparable breakdown field and the breakdown is presumably due to dielectric breakdown in the bulk of OSG rather than that at the α-SiC/OSG interface; the large variation of the breakdown field is possibly resulting from the discordant force of manual probing and/or unfavorable samples at the wafer edge. Figure 7-8 shows the TDDB lifetime of various comb capacitors under different BTS conditions with the data obtained from 6 randomly chosen samples. It is found that all the comb capacitors reveal a comparable TDDB lifetime under a given BTS condition. The fact that the breakdown field (Fig. 7-7) and the TDDB lifetime (Fig. 7-8) of the Cu-comb capacitors show little dependence on the thickness ratio of the α-SiCN/α-SiC bilayer barrier implies that the breakdown is very likely due to dielectric breakdown in the bulk of OSG. Figure 7-9 illustrates the proposed leakage paths of the Cu-comb capacitor studied in this chapter. We may conclude that the leakage and breakdown mechanisms in the Cu-comb capacitor with an α-SiCN/α-SiC bilayer barrier is closely correlated with the quality of the α-SiC/OSG interface and the OSG layer.

7-5 Summary

It is found that the leakage mechanism between Cu lines is dependent on the thickness ratio of the α-SiCN/α-SiC bilayer barrier in the Cu-comb capacitor. Using an α-SiCN(40 nm)/α-SiC(10 nm) or α-SiCN(30 nm)/α-SiC(20 nm) bilayer barrier, the increased leakage (Frenkel-Poole emission) between Cu lines is attributed to the large number of interfacial defects, such as cracks, voids, traps or dangling bonds at the α-SiC/OSG interface, which are generated by the larger tensile force of the thicker α-SiC film. The Cu-comb capacitor with an α-SiCN(50 nm)/α-SiC(2 nm) bilayer barrier exhibits a much smaller leakage current. On the other hand, the breakdown field and TDDB lifetime of the Cu-comb capacitor reveal little dependence on the thickness ratio of the α-SiCN/α-SiC bilayer barrier, and the observed breakdown of the Cu-comb capacitor is presumably due to dielectric breakdown of the bulk OSG layer.

References

[1] J. Martin, S. Filipiak, T. Stephens, F. Huang, M. Aminpur, J. Mueller, E. Demircan, L. Zhao, J. Werking, C. Goldberg, S. Park, T. Sparks, and C. Esber, *IEEE IITC Technol. Dig.* (2002) p. 42.

[2] M. Fayolle, J. Torres, G. Passemard, F. Fusalba, G. Fanget, D. Louis, L. Arnaud, V. Girault, J. Cluzel, H. Feldis, M. Rivoire, O. Louveau, T. Mourier, and L. Broussous, *IEEE IITC Technol. Dig.* (2002) p. 39.

[3] F. Lanckmans, W. D. Gray, B. Brijs, and K. Maex, *Microelectronic Engineering*, **55** (2001) p. 329.

[4] K. L. Fang, B. Y. Tsui, C. C. Yang, and S. D. Lee, *IEEE IITC Technol. Dig.* (2001) p.250.

[5] P. Xu, K. Huang, A. Patel, S. Rathi, B. Tang, J. Ferguson, J. Huang, C. Ngai, and M. Loboda, *IEEE IITC Technol. Dig.* (1999) p. 109.

[6] C. C. Chiang, M. C. Chen, Z. C. Wu, L. J. Li, S. M. Jang, C. H. Yu, and M. S. Liang, *IEEE IITC Technol. Dig.* (2002) p. 200.

[7] Raphael modeling is provided by Avant! business unit.

[8] S. M. Sze, *Physics of Semiconductor Devices*, 2nd Ed. (John Wiley & Sons, 1981) p. 402.

[9] G. Bersuker, V. Blaschke, S. Choi, and D. Wick, *IEEE IRPS Technol. Dig.* (2000) p. 344.

[10] J. Noguchi, T. Saito, N. Ohashi, H. Ashihara, H. Maruyama, M. Kubo, H. Yamaguchi, D. Ryuzaki, K. I. Takeda, and K. Hinode, *IEEE IRPS Technol. Dig.* (2001) p. 355.

[11] S. U. Kim, T. Cho, and P. S. Ho, *IEEE IRPS Technol. Dig.* (1999) p. 277.

[12] W. S. Song, T. J. Kim, D. H. Lee, T. K. Kim, C. S. Lee, J. W. Kim, S. Y. Kim, D. K.

Jeong, K. C. Park, Y. J. Wee, B. S. Suh, S. M. Choi, H. K. Kang, K. P. Suh, and S. U. Kim, *IEEE IRPS Technol. Dig.* (2002) p. 305.

[13] K. N. Tu, J. W. Mayer, and L. C. Feldman, *Electronic Thin Film Science* (Macmillan, 1992) p. 79.

Table 7-1 Leakage mechanisms at various electric fields measured at 200 to 250°C for Cu-comb capacitors with a bilayer-structured Cu cap-barrier of various α-SiCN/α-SiC bilayer thicknesses.

Electric Field (MV/cm)	**α-SiCN/α-SiC Bilayer Thickness (nm/nm)**			
	50/2	**45/5**	**40/10**	**30/20**
0~0.25	**Ionic**	**Ionic**	**Ionic**	**Ionic**
0.25~0.5	**Ionic**	**Ionic**	**Ohmic**	**Ohmic**
0.5~0.8	**SE**	**SE**	**F-P**	**F-P**
0.8~1.25	**SE**	**F-P**	**F-P**	**F-P**

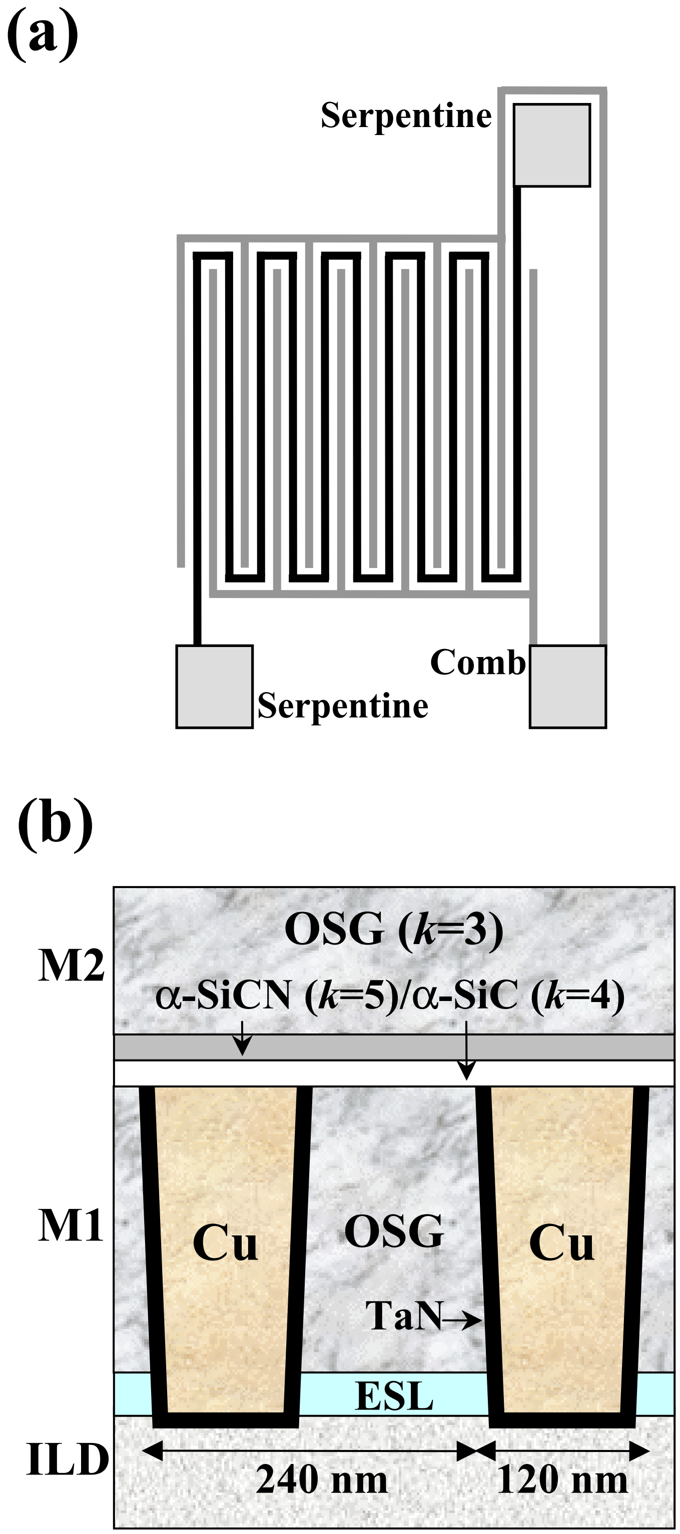

Fig. 7-1 Schematic (a) top-view and (b) cross-sectional view of the Cu-comb capacitor test structure employed in this study.

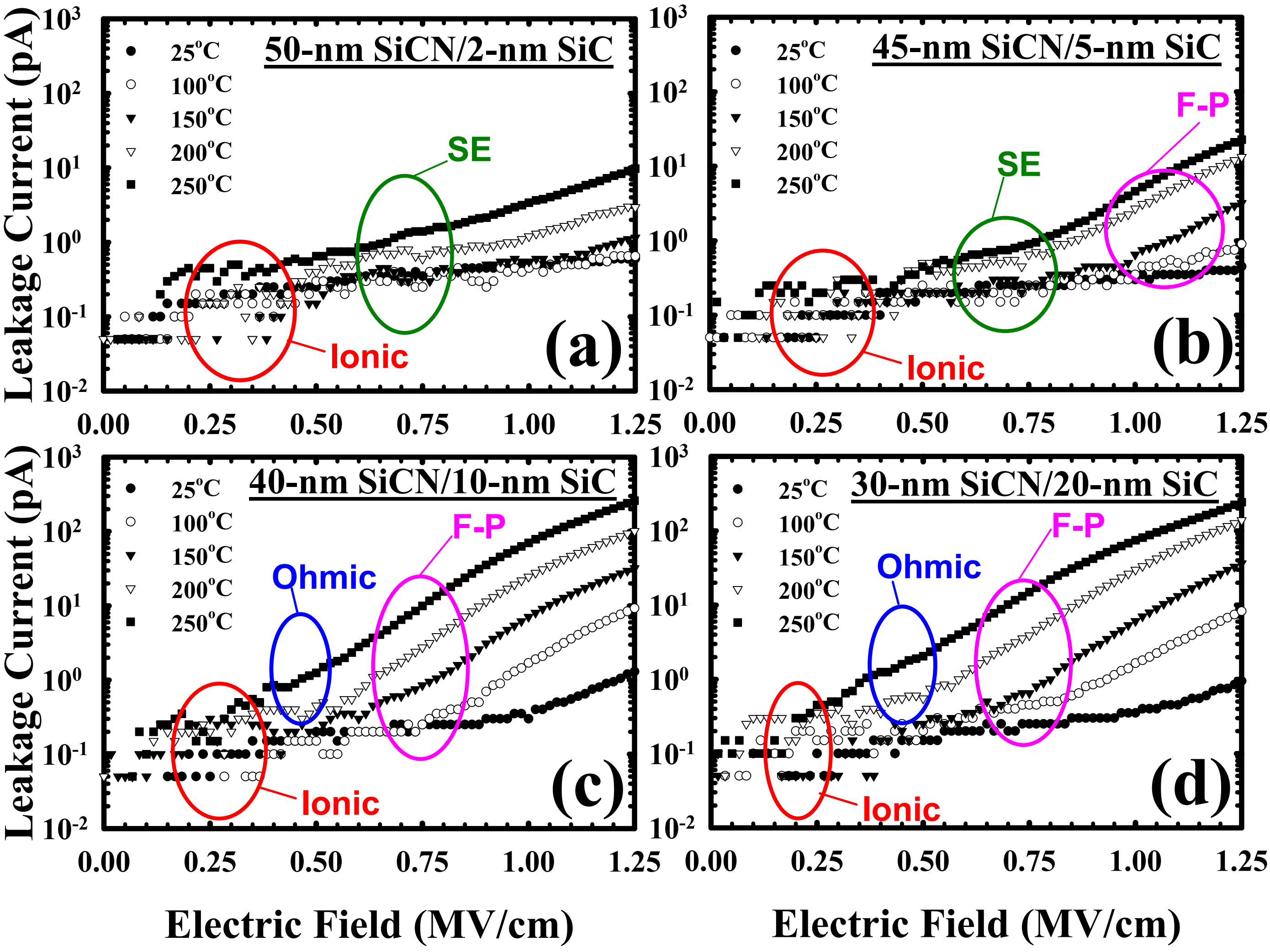

Fig. 7-2 Leakage current vs. electric field, measured at various temperatures, for Cu-comb capacitor using a bilayer-structured Cu cap-barrier with an α-SiCN/α-SiC bilayer thickness of (a) 50/2, (b) 45/5, (c) 40/10, and (d) 30/20 (nm/nm).

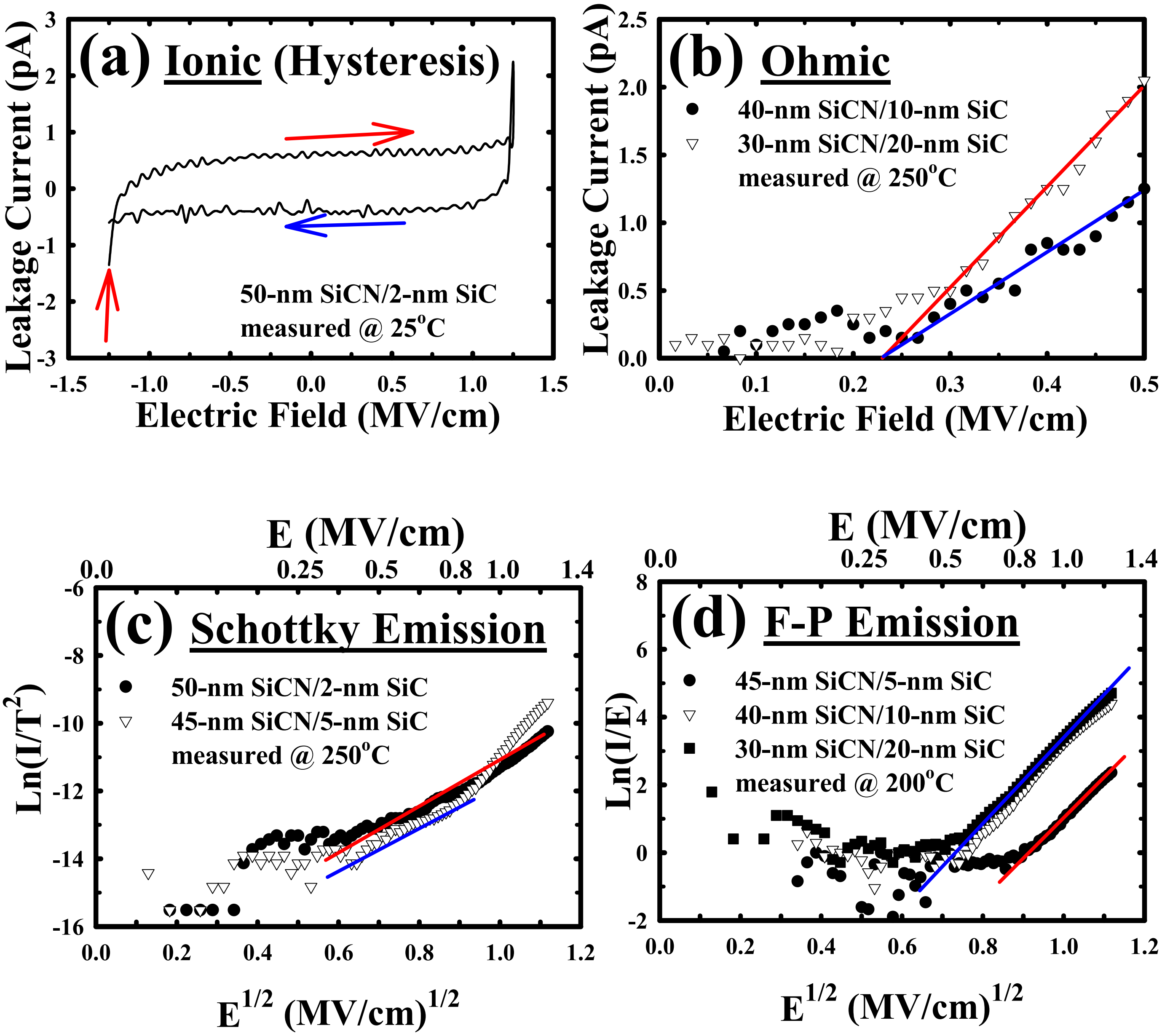

Fig. 7-3 Conduction mechanism of (a) ionic, (b) ohmic, (c) Schottky emission, and (d) Frenkel-Poole emission for the Cu-comb capacitor with a bilayer-structured Cu cap-barrier of various α-SiCN/α-SiC bilayer thicknesses.

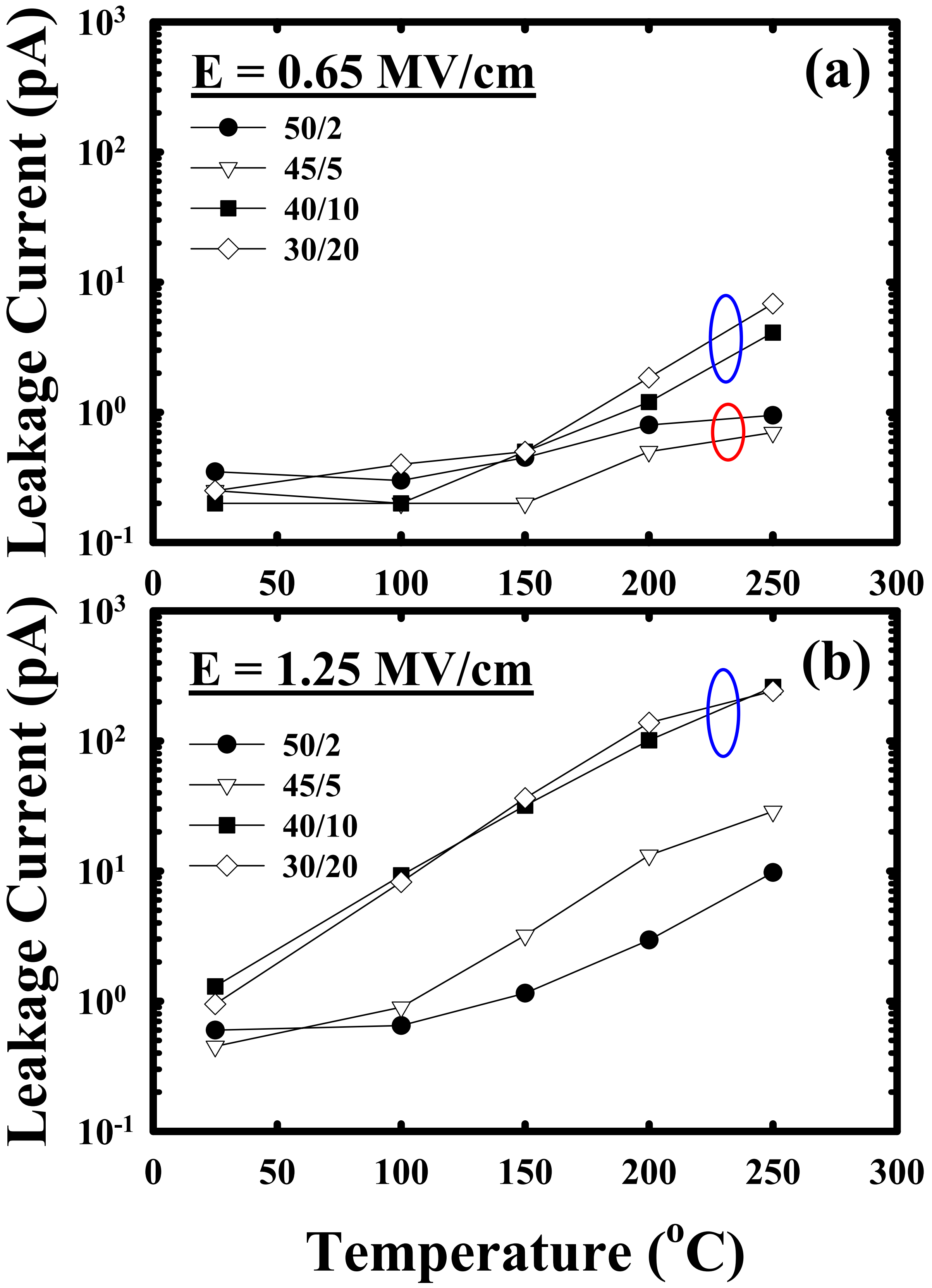

Fig. 7-4 Leakage current as a function of temperature measured at an electric field of (a) 0.65 and (b) 1.25 MV/cm for the Cu-comb capacitor with a bilayer-structured Cu cap-barrier of various α-SiCN/α-SiC bilayer thicknesses.

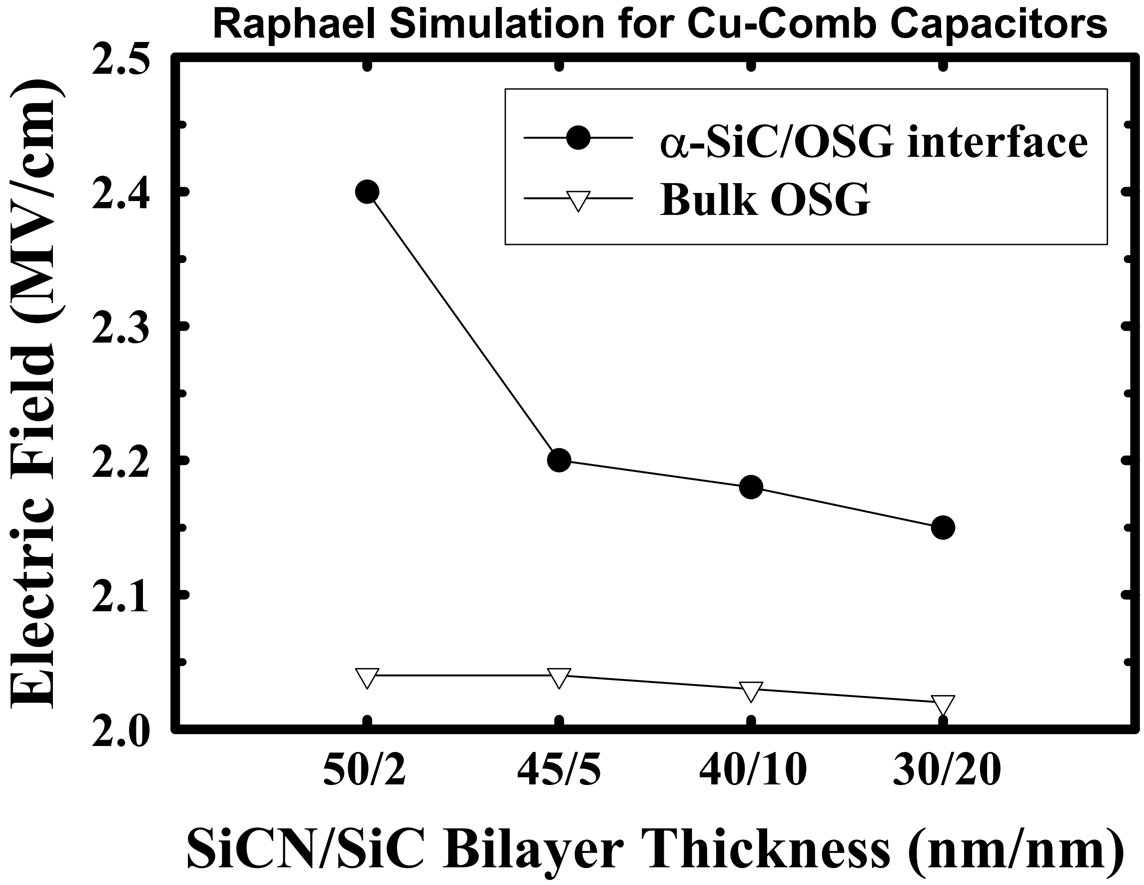

Fig. 7-5 Electric field at the α-SiC/OSG interface and in the bulk of OSG obtained from Raphael simulation for various Cu-comb capacitors biased with an electric voltage of 24 V.

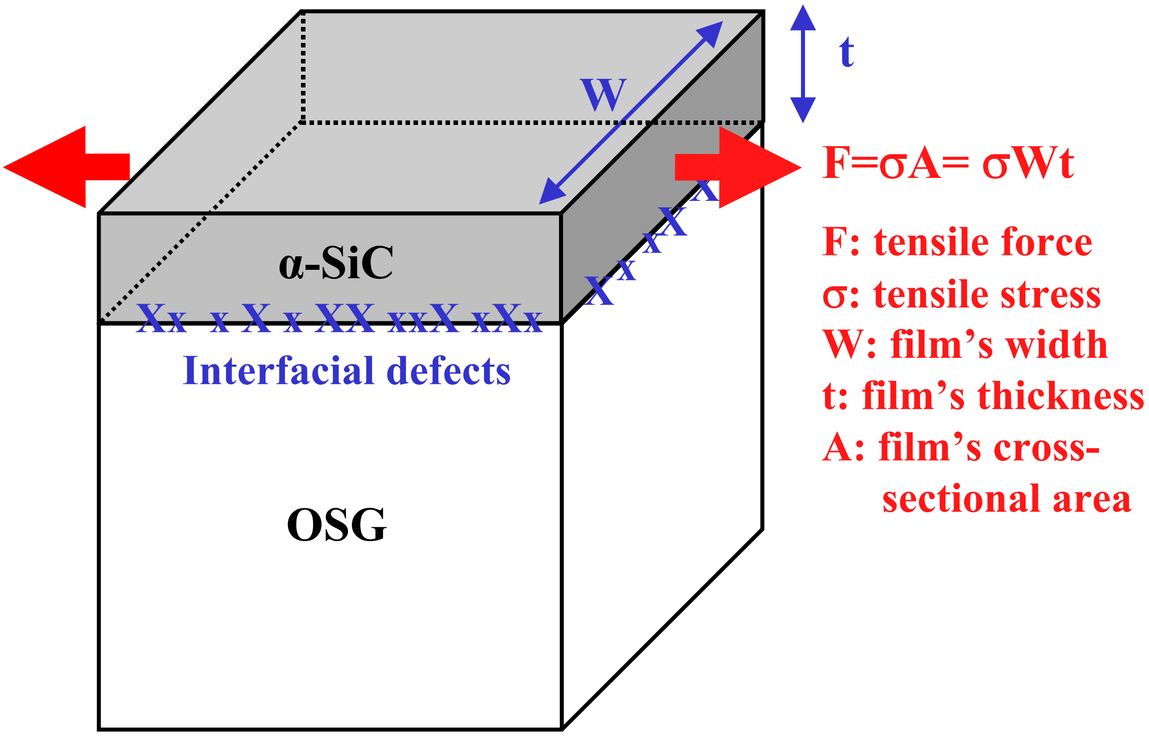

Fig. 7-6 Schematic diagram showing the interfacial defects generated by the tensile force of the α-SiC film.

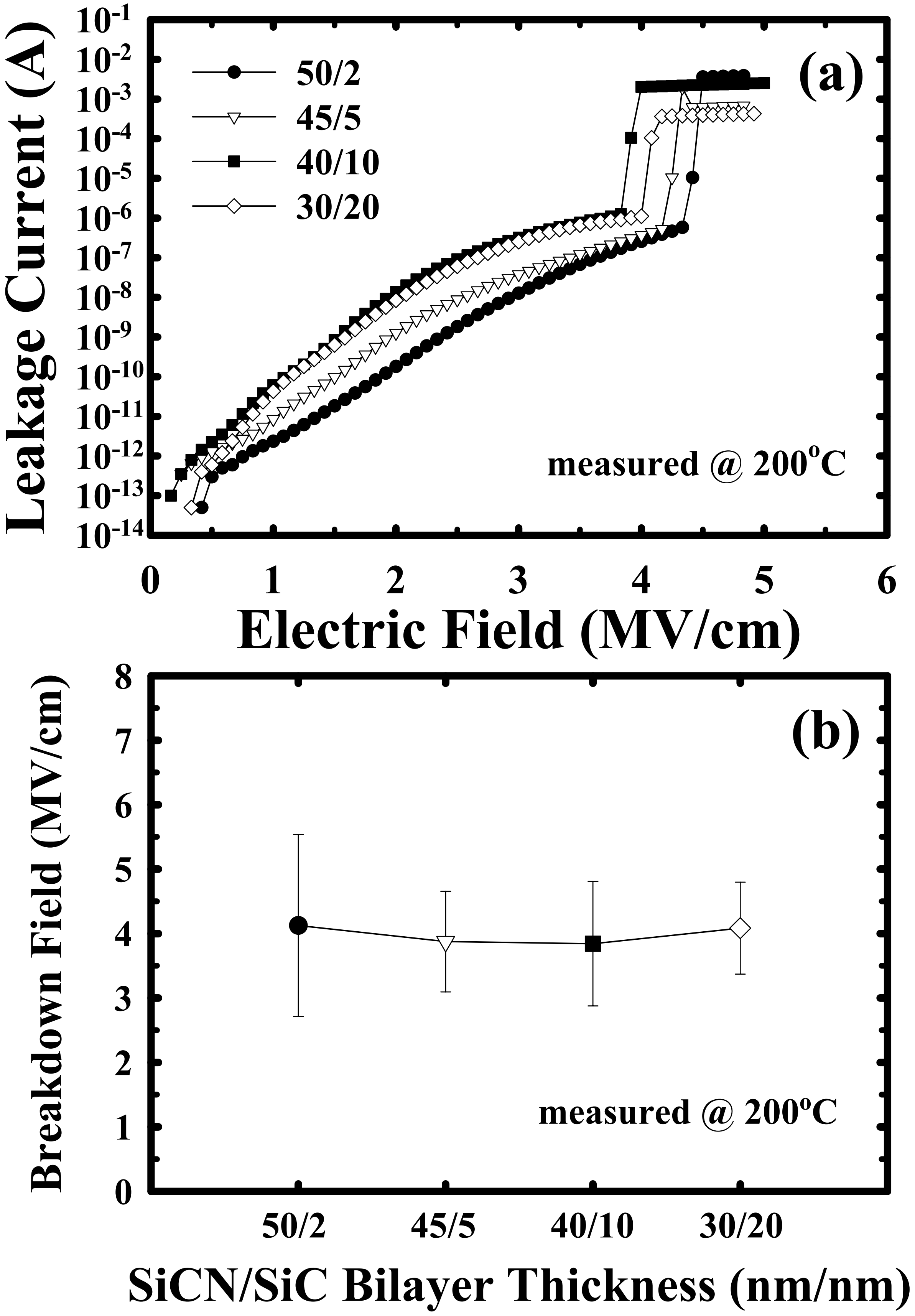

Fig. 7-7 (a) Leakage current vs. electric field and (b) breakdown field for various Cu-comb capacitors.

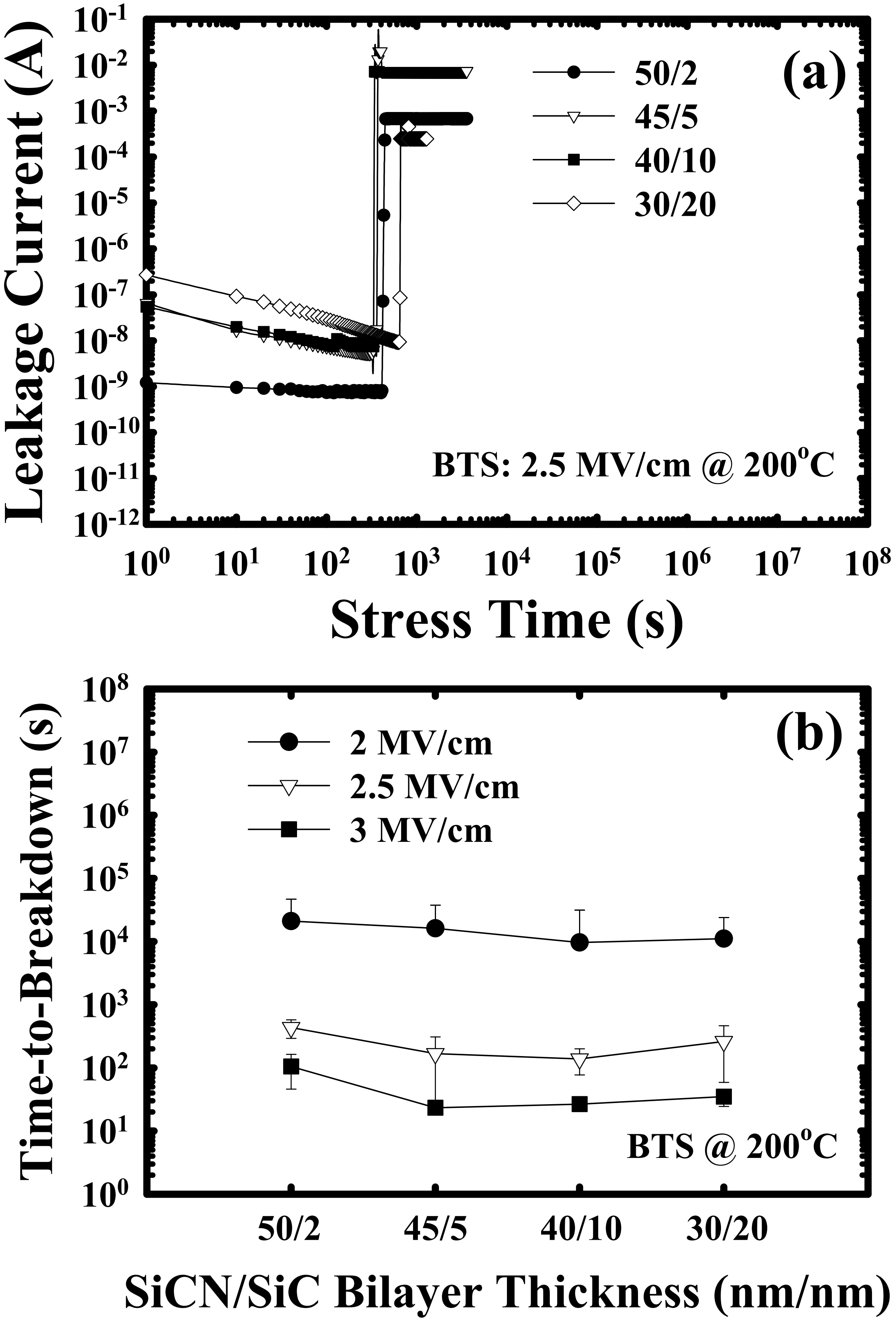

Fig. 7-8 (a) TDDB under a BTS (2.5 MV/cm at 200°C) and (b) time-to-breakdown under different BTS conditions for various Cu-comb capacitors.

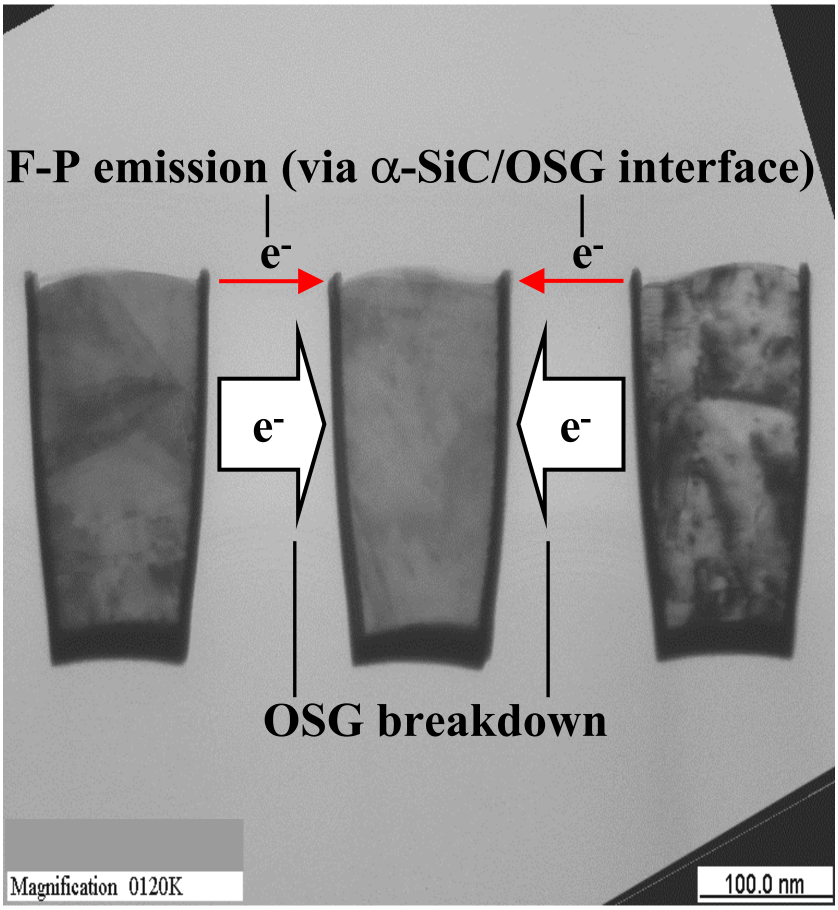

Fig. 7-9. Proposed leakage paths of the Cu-comb capacitor studied in this work.

Part 3

Chapter 8

Amorphous Silicon-Oxycarbide (α-SiCO) Dielectric Barrier

8-1 Introduction

The PECVD α-SiC and α-SiCN dielectric barrier films deposited using organosilicate gases are receiving extensive attention for applications as Cu cap-barrier and etching stop layer in Cu damascene structures because of their lower *k*-value, better etching selectivity with respect to OSG, excellent CMP strength, and superb property as Cu barrier and passivation layer in terms of electromigration resistance and Cu hillock density [1-3]. We also made intensive studies on the PECVD α-SiC and α-SiCN dielectric films in the previous chapters of this thesis [4,5]. The 3MS-based α-SiC and α-SiCN barrier films show *k*-values in the range of 4 to 5 [1-5], while the α-SiCO barrier films deposited using tetramethylsilane (4MS), hexamethydisiloxane (HMDSO) or trimethoxysilane (TMOS) precursor exhibit an even lower *k*-value of 3.9 [6-8]. Moreover, it has been reported that the α-SiCO barrier film deposited using 3MS precursor with He carrier gas and the addition of O_2 exhibits a *k*-value of 3.7 under an optimal process condition [9]. In this chapter, we investigate the thermal stability and physical and barrier properties for four α-SiC and α-SiCO dielectric barrier films, with dielectric constants between 3.7 and 4.4, deposited using trimethylsilane (3MS) precursor with He carrier gas and the addition of CO_2 reaction gas.

8-2 Experimental Details

Four α-SiC(O) dielectric barrier films were deposited using 3MS [$(CH_3)_3SiH$] precursor with He carrier gas and the addition of CO_2 reaction gas with various flow rates. The resulting films were investigated with respect to their thermal stability and physical and barrier properties. In this study, all of the α-SiC(O) films were deposited to a thickness of 50 nm on p-type, (100)-oriented Si wafers at a temperature of 300~400^{o}C, a gas pressure of 1~5 Torr, and a plasma power of 100~300 W using a parallel-plate PECVD system operated at 13.56 MHz. The flow rate ratio of 3MS/He gases was maintained at 2/5, while the flow rate of CO_2 was separately controlled at 0, 300, 600, and 1200 sccm, which resulted in four α-SiC(O) films with different elemental compositions. All films were thermally annealed at 400^{o}C for 30 min in N_2 ambient to remove moisture possibly absorbed in the dielectric prior to the investigation of the films' physical properties or the deposition of the electrode (TaN/Cu or Al) to construct the metal-insulator-semiconductor (MIS) capacitor structure. The TaN/Cu-gated MIS capacitors were constructed by first sputter-depositing a 200-nm-thick Cu layer on the α-SiC(O) dielectric films using a dc magnetron sputtering system; this was followed by the reactive sputter deposition of a 50-nm-thick TaN layer on the Cu surface in the same sputtering system without breaking the vacuum. The TaN film served as a passivation layer to prevent the Cu electrode from oxidation in the subsequent high-temperature processes. For a comparison, Al-gated control samples were also prepared by depositing a 500-nm-thick Al layer directly on the α-SiC(O) dielectric surfaces using a thermal evaporation system. All metal electrodes with a circular area of 0.84 mm diameter were defined by a lift-off process in order to prevent unexpected deterioration of the dielectric films by wet chemical etching. To ensure good contact in electrical measurements, a 500-nm-thick Al layer was also thermally evaporated on the back surface of the Si substrate for all samples. Some of the completed MIS samples were thermally annealed at 400°C for 30 min in N_2 ambient. This annealing step eliminates the plasma-induced damage during the sputter deposition of the TaN/Cu electrodes and also provides the driving force for Cu diffusion.

Auger electron spectroscopy (AES) was used to detect the elemental compositions of the dielectric barrier films. The film thickness and refractive index were measured using a well-calibrated n&k analyzer at 633 nm wavelength, and the *k*-value of the dielectrics was determined by the maximum capacitance of the Al-gated MIS capacitors measured at 1 MHz using a Keithley 82 C-V measurement system. The film density was directly calculated by the ratio of mass to volume of the film, whereas the film mass was measured by an electronic microbalance and the film volume was calculated from the film thickness and the area of the substrate wafer. Fourier transform infrared spectroscopy (FTIR, ASTeX PDS-17 System) was used to analyze the chemical bonding of the dielectrics from 600 to 2300 cm^{-1} wavenumber. An HP4145B semiconductor parameter analyzer was used to measure the dielectric leakage current and provide the bias for the bias-temperature-stress (BTS) test.

8-3 Physical Property and Thermal Stability

Table 8-1 shows the properties of the four 3MS-based α-SiC(O) dielectric barrier films studied in this work. It is found that the oxygen content of the dielectrics, as determined by AES, increases with increasing CO_2 flow rate. Notably, the C/Si concentration ratio remains nearly constant at 0.92 to 0.97 for all four films. However, the refractive index of the dielectrics decreases with increasing CO_2 flow rate, and thus with increasing oxygen content. This is consistent with the results reported in the literature for the α-SiC(O) films deposited using O_2/3MS, N_2O/HMDSO, O_2/4MS, and N_2O/4MS gases [9-12]. The k-value at 1 MHz consists of three components arising from the contribution of electronic, ionic, and dipolar k-value [9,10,13,14],

$$k \text{ (at 1 MHz)} = k_e + k_{ion} + k_{dipolar} \qquad (8\text{-}1)$$

The electronic contribution arises from the displacement of the electrons relative to a nucleus. The ionic contribution comes from the displacement of the charged ion cores of the atoms with respect to other ions, and the dipolar contribution arises from the change of orientation for the molecules with a permanent electric dipole moment in an applied electric field. The electronic k-value (k_e), which equals the square of refractive index [9,10,13,14], and the k-value (@ 1 MHz) of the film both decrease with increasing CO_2 flow rate. However, the ionic and dipolar k-value, which is obtained by subtracting k_e from the k-value at 1 MHz [9,10,13], increases with increasing CO_2 flow rate. The reduction in the electronic contribution to k-value with increasing CO_2 flow rate is attributed to the increase in the density of the Si-O bonds in the film [9,10], which is more ionic and polarizable than the Si-C bond [9,10,14,15]. Thus, k-value for an α-SiC(O) film (@ 1 MHz), which is dominated by the electronic polarization, would decrease with increasing incorporation of oxygen [9,12]. The higher electronegativity of the oxygen atom also decreases the polarizability of the bonds and results in a lower k-value of the film [9]. The change of oxygen concentration, refractive index, and k-value (@ 1 MHz) for the α-SiC(O) dielectric films with increasing CO_2 flow rate appear to saturate when the CO_2 flow rate was increased from 600 to 1200 sccm. Table 8-2 shows the chemical composition, density, and porosity of the four films. The chemical composition was determined from the AES analysis, while the porosity was calculated from the film density and molecular weight of each film [15]. It is conceivable that the α-SiC(O) dielectric films with a less dense and highly porous structure may exhibit poor thermal stability and poor electrical and barrier properties [16].

Figure 8-1 shows the FTIR spectra of the α-SiC(O) dielectric films before and after thermal annealing at various temperatures (30 min in N_2 ambient). It is notable that the decreasing peak at 1100 cm^{-1} (i.e., going below the background) resulted from the bare Si reference wafer calibrated by the FTIR measurement system. By introducing the CO_2 gas in the deposition process, we found that the absorbance of the Si-C stretching mode (800 cm^{-1}) and the Si-H stretching mode (2100 cm^{-1}) decreased, whereas the absorbance near 1000 cm^{-1} significantly increased (Figs. 8-1a and 8-1b). The peak near 1000 cm^{-1} represents the Si-$(CH_2)_n$ bending/wagging (995 cm^{-1}) for the α-SiC films or Si-O stretching (1006 cm^{-1}) for the α-SiCO films [9]; moreover, the Si-$(CH_2)_n$ absorption for the α-SiC films vanishes after thermal annealing at 600°C. Specifically, the FTIR spectra of the SCO6 and SCO12 films are similar in every respect; this implies that the CO_2 gas flow rates larger than 1200 sccm would produce little change in the film properties.

The Si-H stretching (2100 cm^{-1}) and Si-CH_3 bending (1250 cm^{-1}) absorptions in the films decrease after thermal annealing at temperatures above 500°C, as shown in Fig. 8-2, where the spectra have been shifted for clarity. Chemical desorption of carbon- and hydrogen-related groups were detected at temperatures above 550°C for the SCO0 and SCO3 films and at 600°C for the SCO6 and SCO12 films. Figure 8-3 shows the thickness shrinkage, refractive index, and dielectric constant as a function of annealing temperature for the α-SiC(O) barrier films. The film thickness remained nearly constant for all films at temperatures up to 450°C. However, all films started to show shrinkage at 500°C. The SCO0 and SCO3 films shrank more than 5% at 550°C and more than 10% at 600°C, presumably due to desorption of hydrocarbon groups (Fig. 8-2). Similarly, shrinkage of more than 5% was observed at 600°C for the SCO6 and SCO12 films. The outgassing implies the occurrence of changes in chemical bonding structure and physical microstructure of the dielectric film, resulting in the variation of refractive index and dielectric constant (Figs. 8-3b and 8-3c). In summary, the 3MS-based α-SiCO dielectric barrier films deposited with a higher CO_2 flow rate (≥600 sccm) are stable up to 550°C, while the films deposited without or with lower CO_2 flow rates (≤300 sccm) are stable up to 500°C. Interestingly, the α-SiC(O) dielectric barrier film with a lower dielectric constant exhibits a higher thermal stability-temperature in this study, which is contrary to the α-SiC and α-SiCN dielectric barrier films investigated in the previous chapters of this thesis [17,18].

8-3 Electrical and Barrier Properties

Figure 8-4 shows the room temperature leakage current density and the statistical distribution of breakdown field for the 400°C-annealed MIS capacitors with Al gates made using α-SiC(O) films deposited with different CO_2 flow rates. The measurements were performed with the MIS capacitors biased in the accumulation region. The breakdown field is defined as the field strength such that the leakage current of the MIS capacitor reaches 20 mA (equivalent to 3.57 A/cm^2). The breakdown field of the α-SiC(O) films increases with increasing CO_2 flow rate. Similar result was observed in the α-SiC(O) dielectric films deposited using O_2/3MS gases of various flow ratios and the breakdown field increased with increasing O_2 flow rate [9]. Figure 8-5 shows the room temperature leakage current density for the as-fabricated as well as the 400°C-annealed (30 min in N_2 ambient) TaN/Cu-gated MIS capacitors with α-SiC(O) dielectric barrier films. For each dielectric barrier film, negligible difference in leakage current was observed between the as-fabricated and the 400°C-annealed MIS capacitors. This implies that all the dielectric barrier films are capable of preventing Cu penetration at temperatures up to 400°C. The fact that the breakdown field and the leakage current density of the α-SiC(O) dielectric films depend on the CO_2 flow rate (Figs. 8-4b and 8-5b) is apparently due to the CO_2 flow rate dependence of the film's density and porosity (Table 8-2).

BTS test was used to further explore the dielectric barrier property of the α-SiC(O) films. In these tests, the TaN/Cu-gated MIS capacitor structure annealed at 400°C was used. The BTS was performed at 200°C with an applied electric field of 2.5 MV/cm on the MIS capacitors. N_2 purging was used to prevent the oxidation of the Cu electrode and moisture uptake in the dielectric barriers during the BTS. Figure 8-6 shows the leakage current transient during the BTS. Current-spiking occurred for the SCO0 and SCO3 dielectric MIS samples after 1 and 5 h, respectively, whereas the SCO6 and SCO12 dielectric MIS samples remained stable up to at least 15 h. Figure 8-7 shows the instantaneous leakage current density versus applied electric field (in accumulation mode) before and after the BTS for the MIS capacitors. Significant leakage current increase was detected for the TaN/Cu-gated MIS capacitors made from SCO0 and SCO3 films after 2 and 6 h BTS, respectively. Figure 8-8 shows the time-to-breakdown, under different BTS conditions, for the 400°C-annealed TaN/Cu-gated MIS capacitors with α-SiC(O) dielectric films deposited with various CO_2 flow rates. All BTS tests were stopped at 15 h, and all the 400°C-annealed Al-gated MIS capacitors with α-SiC(O) dielectrics remained stable up to at least 15 h under the BTS of 3 MV/cm at 200°C (not shown). This further confirms that the current-spiking during the BTS (Fig. 8-6) and the significant leakage current increase after the BTS (Fig. 8-7) in the 400°C-annealed TaN/Cu-gated MIS capacitors made from SCO0 and SCO3 films are due to the penetration of Cu into the dielectric barriers rather than the BTS-induced dielectric breakdown.

The improved barrier property of the α-SiC(O) dielectric films deposited with high CO_2 flow rates is attributed to the denser and more crosslinked film structure; thus, the Cu ions may be less mobile in the dense film [16,19-23]. However, it was reported that the Cu barrier property of the α-SiC(O) dielectric films degrades with high O_2 flow rates [9].

Since abundant oxygen in dielectric films will possibly enhance the penetration of Cu into the dielectric film by Cu-O reactions [10,24], ability for the film to prevent Cu diffusion is expected to degrade with higher flow rates of oxygen-containing gas during the film's deposition process [9,10]. Nonetheless, the α-SiCO film deposited in this work using PECVD with a CO_2 flow rate of 1200 sccm still exhibits a superb barrier property. This might be due to the fact that the SCO12 film's chemical composition is SiC-based rather than SiO-based (Table 8-2).

8-5 Summary

Four α-SiC(O) films were deposited using PECVD from 3MS precursor without and with three different CO_2 flow rates. The resulting films were investigated with respect to their thermal stability and physical and barrier properties. With the addition of CO_2 during the dielectric deposition process, the dielectric constant of the α-SiCO dielectric films decreases with increasing CO_2 flow rate. Increasing CO_2 flow rate also results in dielectric films of better thermal stability, higher breakdown field, lower leakage current, and superior resistance to Cu diffusion. The improved barrier property is attributed to the denser and less porous structure of the α-SiCO dielectric barrier film. The α-SiCO dielectric barrier film deposited with a large (1200 sccm) CO_2 flow rate exhibits a low *k*-value of 3.7, thermal stability up to 550°C, room-temperature breakdown field of 8 MV/cm, leakage current densities of 10^{-7} to 10^{-6} A/cm^2 at 3 MV/cm, and a superb Cu barrier property.

References

[1] F. Lanckmans, W. D. Gray, B. Brijs, and K. Maex, *Microelectronic Engineering*, **55** (2001) p. 329.

[2] J. Martin, S. Filipiak, T. Stephens, F. Huang, M. Aminpur, J. Mueller, E. Demircan, L. Zhao, J. Werking, C. Goldberg, S. Park, T. Sparks, and C. Esber, *IEEE IITC Technol. Dig.* (2002) p. 42.

[3] S. G. Lee, Y. J. Kim, S. P. Lee, H. Y. Oh, S. J. Lee, M. Kim, I. G. Kim, J. H. Kim, H. J. Shin, J. G. Hong, H. D. Lee, and H. K. Kang, *Jpn. J. Appl. Phys.*, **40** (2001) p. 2663.

[4] C. C. Chiang, M. C. Chen, Z. C. Wu, L. J. Li, S. M. Jang, C. H. Yu, and M. S. Liang, *IEEE IITC Technol. Dig.* (2002) p. 200.

[5] C. C. Chiang, I. H. Ko, M. C. Chen, Z. C. Wu, Y. C. Lu, S. M. Jang, and M. S. Liang, *IEEE IITC Technol. Dig.* (2003) p. 201.

[6] K. Goto, H. Yuasa, A. Andatsu, and M. Matsuura, *IEEE IITC Technol. Dig.* (2003) p. 6.

[7] T. Ishimaru, Y. Shioya, H. Ikakura, M. Nozawa, Y. Nishimoto, S. Ohgawara, and K. Maeda, *IEEE IITC Technol. Dig.* (2001) p. 36.

[8] K. I. Takeda, D. Ryuzaki, T. Mine, and K. Hinode, *IEEE IITC Technol. Dig.* (2001) p. 244.

[9] Y. W. Koh, K. P. Loh, L. Rong, A. T. S. Wee, L. Huang, and J. Sudijono, *J. Appl. Phys.*, **93** (2003) p. 1241.

[10] T. Ishimaru, Y. Shioya, H. Ikakura, M. Nozawa, S. Ohgawara, T. Ohdaira, R. Suzuki, and K. Maeda, *J. Electrochem. Soc.*, **150** (2003) p. F83.

[11] A. Grill and V. Patel, *J. Appl. Phys.*, **85** (1999) p. 3314.

[12] L. M. Han, J. S. Pan, S. M. Chen, N. Balasubramanian, J. Shi, L. S. Wong, and P. D. Foo, *J. Electrochem. Soc.*, **148** (2001) p. F148.

[13] C. Kittel, *Introduction to Solid State Physics*, 7th ed. (John Wiley & Sons, New York, 1996) p. 390.

[14] S. M. Han and E. S. Aydil, *J. Appl. Phys.*, **83** (1998) p. 2172.

[15] J. Y. Kim, M. S. Hwang, Y. H. Kim, H. J. Kim, and Y. Lee, *J. Appl. Phys.*, **90** (2001) p. 2469.

[16] Z. C. Wu, Z. W. Shiung, C. C. Chiang, W. H. Wu, M. C. Chen, S. M. Jeng, W. Chang, P. F. Chou, S. M. Jang, C. H. Yu, and M. S. Liang, *J. Electrochem. Soc.*, **148** (2001) p. F127.

[17] C. C. Chiang, M. C. Chen, C. C. Ko, Z. C. Wu, S. M. Jang, and M. S. Liang, *Jpn. J. Appl. Phys.*, **42** (2003) p. 4273.

[18] C. C. Chiang, Z. C. Wu, W. H. Wu, M. C. Chen, C. C. Ko, H. P. Chen, S. M. Jang, C. H. Yu, and M. S. Liang, *Jpn. J. Appl. Phys.*, **42** (2003) p. 4489.

[19] A. L. S. Loke, J. T. Wetzel, P. H. Townsend, T. Tanabe, R. N. Vrtis, M. P. Zussman, D. Kumar, C. Ryu, and S. S. Wong, *IEEE Trans. Electron Devices*, **46** (1999) p. 2178.

[20] D. Gupta, *Materials Chemistry and Physics*, **41** (1995) p. 199.

[21] J. D. Mcbrayer, R. M. Swanson, and T. W. Sigmon, *J. Electrochem. Soc.*, **133** (1986) p. 1242.

[22] J. L. Duda and N. Faridi, *Diffusion in Amorphous Materials*, edited by H. Jain and D. Gupta, The Minerals, Metals and Materials Society (Warrendale, PA, 1994) p. 55.

[23] D. Gupta, F. Faupel, and R. Willecke, *Diffusion in Amorphous Materials*, edited by H. Jain and D. Gupta, The Minerals, Metals and Materials Society (Warrendale, PA, 1994) p. 189.

[24] Y. S. Diamand, A. Dedhia, D. Hoffstetter, and W. G. Oldham, *J. Electrochem. Soc.*, **140** (1993) p. 2427.

Table 8-1 Properties of 3MS-based α-SiC(O) dielectric films studied in this work.

Sample ID	**SCO0**	**SCO3**	**SCO6**	**SCO12**
CO_2 flow rate (sccm)	**0**	**300**	**600**	**1200**
Elemental composition				
Si (%)	**51**	**45**	**40**	**38**
C (%)	**47**	**42**	**38**	**37**
O (%)	**2**	**13**	**22**	**25**
Structure	**α-SiC**	**α-SiCO**	**α-SiCO**	**α-SiCO**
Refractive index @ 633 nm	**2.04**	**1.94**	**1.76**	**1.72**
Electronic *k*-value	**4.16**	**3.76**	**3.09**	**2.95**
***k*-value @ 1 MHz**	**4.41**	**4.06**	**3.81**	**3.73**
Ionic and dipolar *k*-value	**0.25**	**0.30**	**0.72**	**0.78**

Table 8-2 Chemical composition, density, and porosity of 3MS-based α-SiC(O) dielectrics and SiO_2 films.

Sample ID	**SCO0**	**SCO3**	**SCO6**	**SCO12**	**oxide**
Chemical composition	$\mathbf{SiC_{0.92}O_{0.04}}$	$\mathbf{SiC_{0.93}O_{0.29}}$	$\mathbf{SiC_{0.95}O_{0.55}}$	$\mathbf{SiC_{0.97}O_{0.66}}$	$\mathbf{SiO_2}$
Density (g/cm^3)	**1.24**	**1.43**	**1.65**	**1.80**	**2.20**
Porosity (%)[a]	**14.77**	**10.96**	**6.64**	**2.21**	**0**

[a] Porosity (%) is calculated from the film density (ρ) and molecular weight (M) of α-SiC(O) dielectric, based on the assumption that the oxide (SiO_2) has no porosity; thus $(1-\text{porosity})M_{SCO}/M_{oxide}=\rho_{SCO}/\rho_{oxide}$.

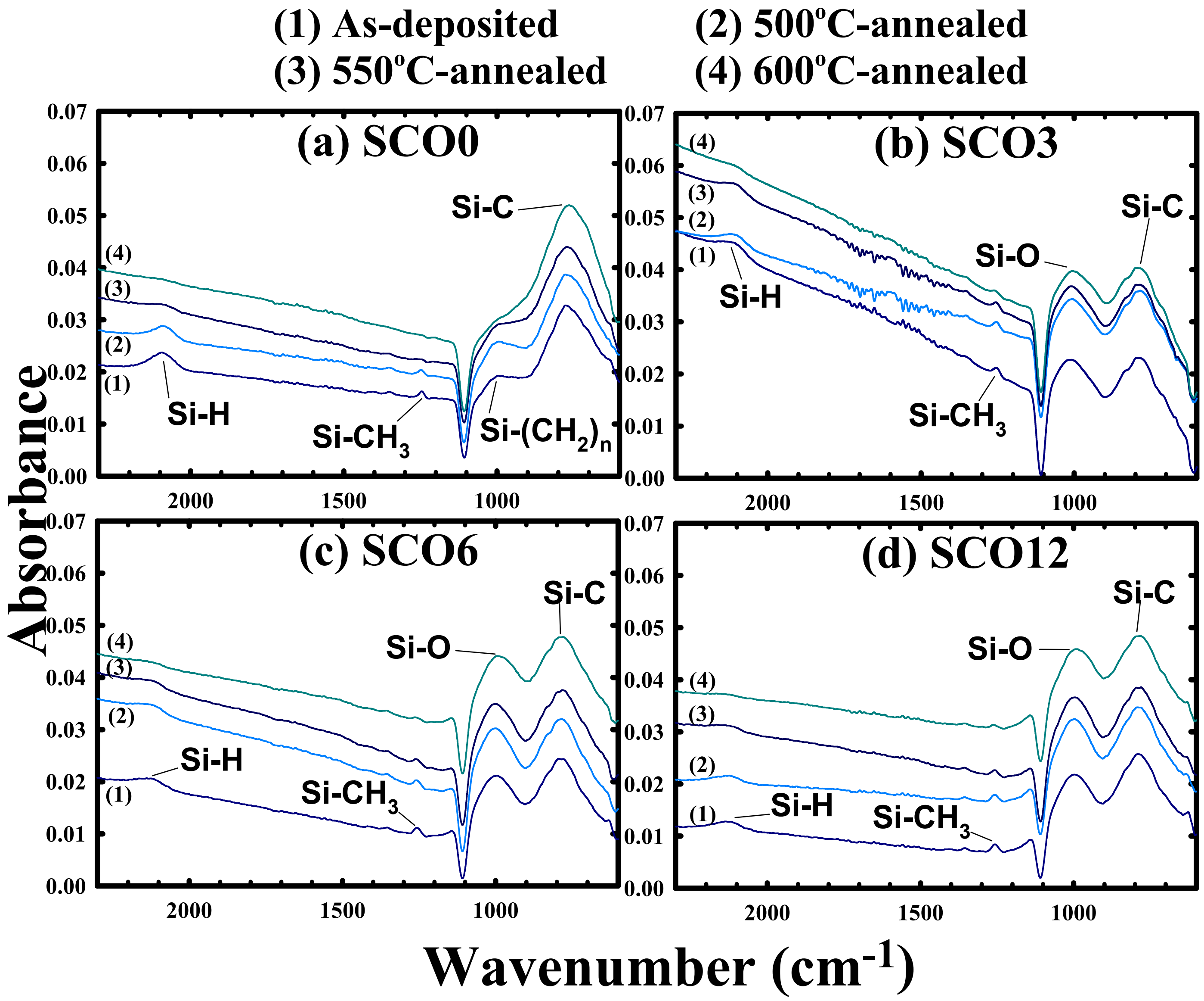

Fig. 8-1 FTIR spectra of (a) SCO0, (b) SCO3, (c) SCO6, and (d) SCO12 dielectric films before and after thermal annealing at various temperatures (30 min in N_2 ambient).

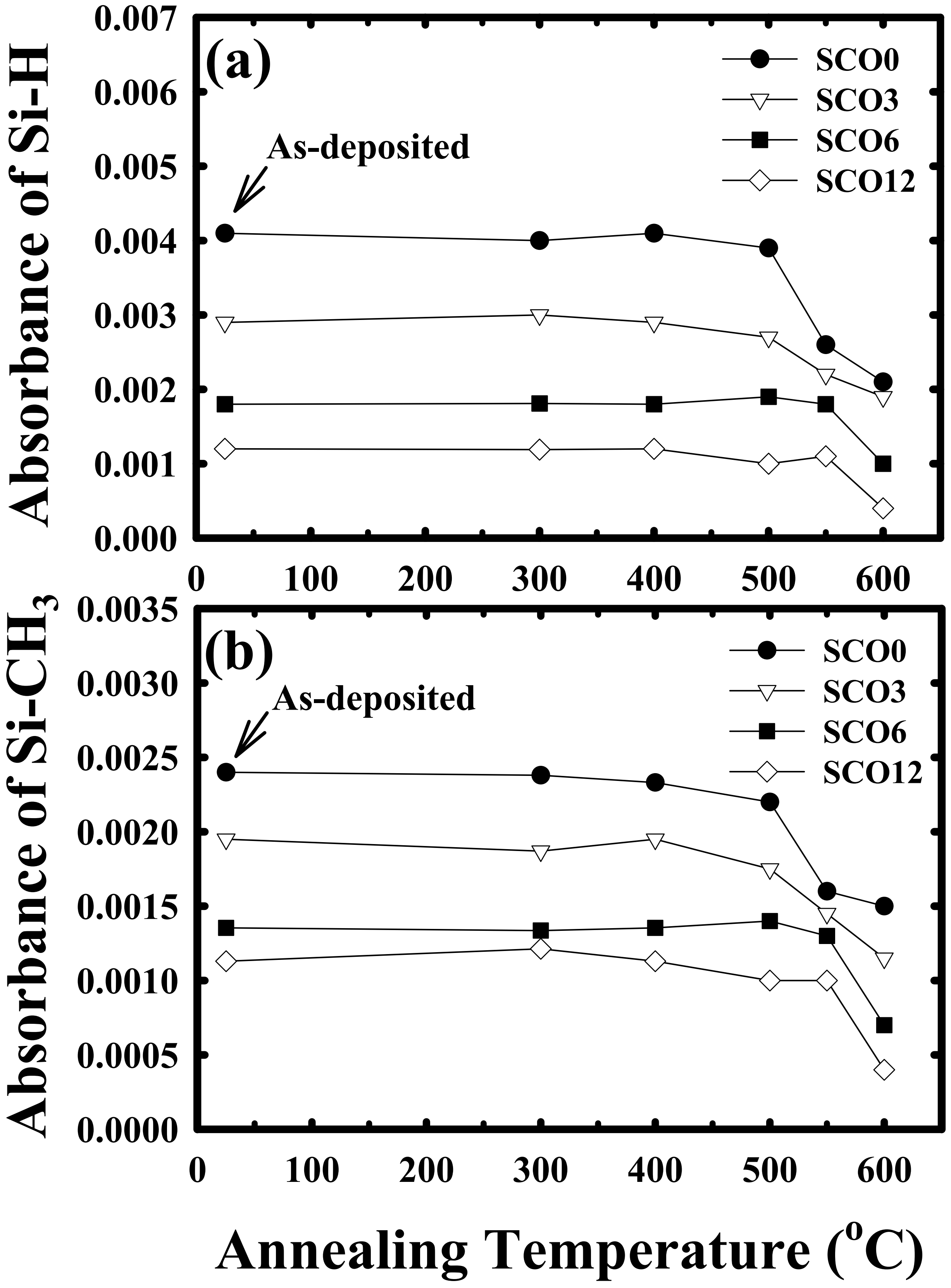

Fig. 8-2 Annealing temperature dependence of FTIR absorbance peak height for (a) Si-H stretching (2100 cm^{-1}) absorbance and (b) Si-CH_3 bending (1250 cm^{-1}) absorbance for various 3MS-based α-SiC(O) dielectric films.

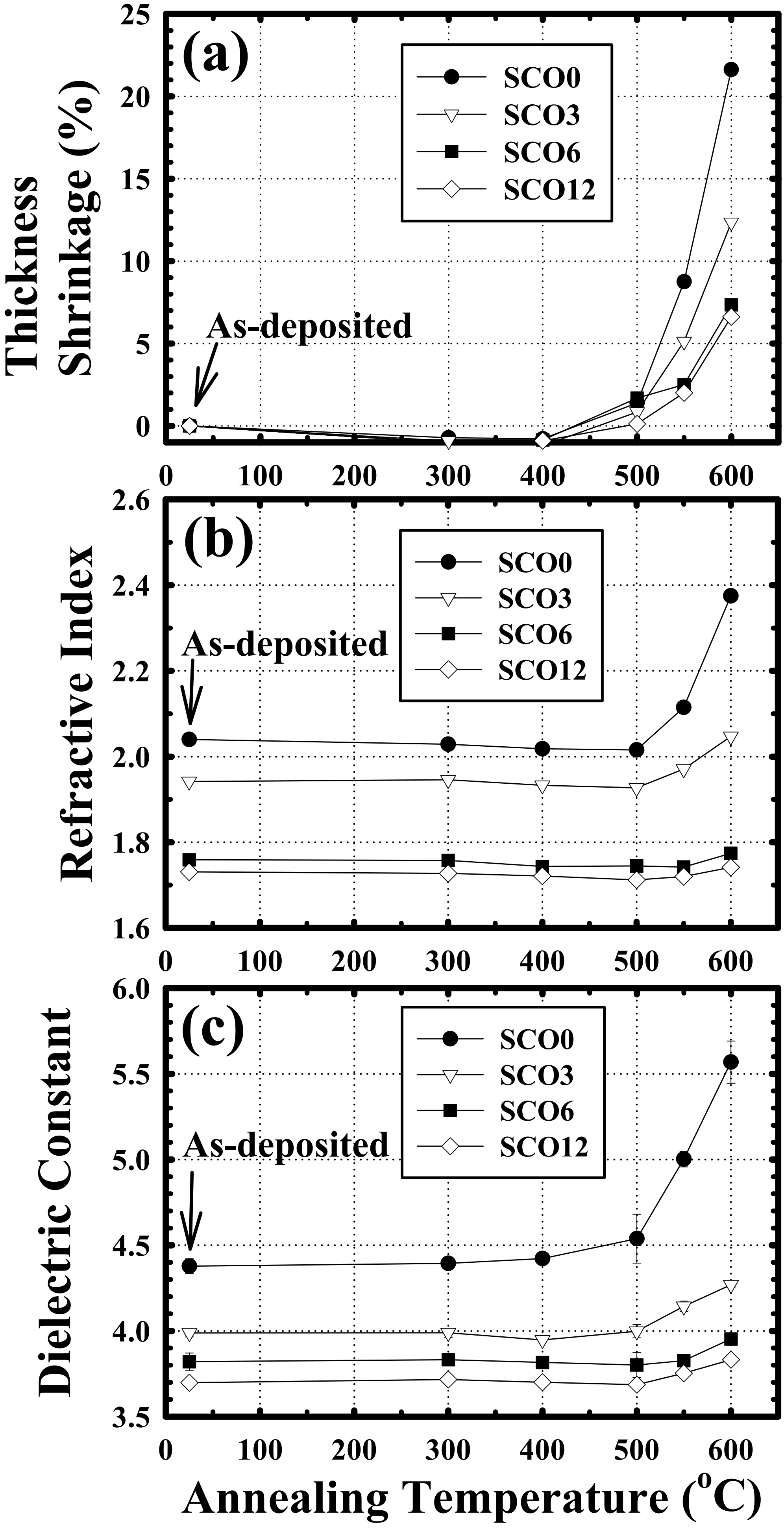

Fig. 8-3 (a) Thickness shrinkage, (b) refractive index, and (c) dielectric constant vs. annealing temperature for various 3MS-based α-SiC(O) dielectric films.

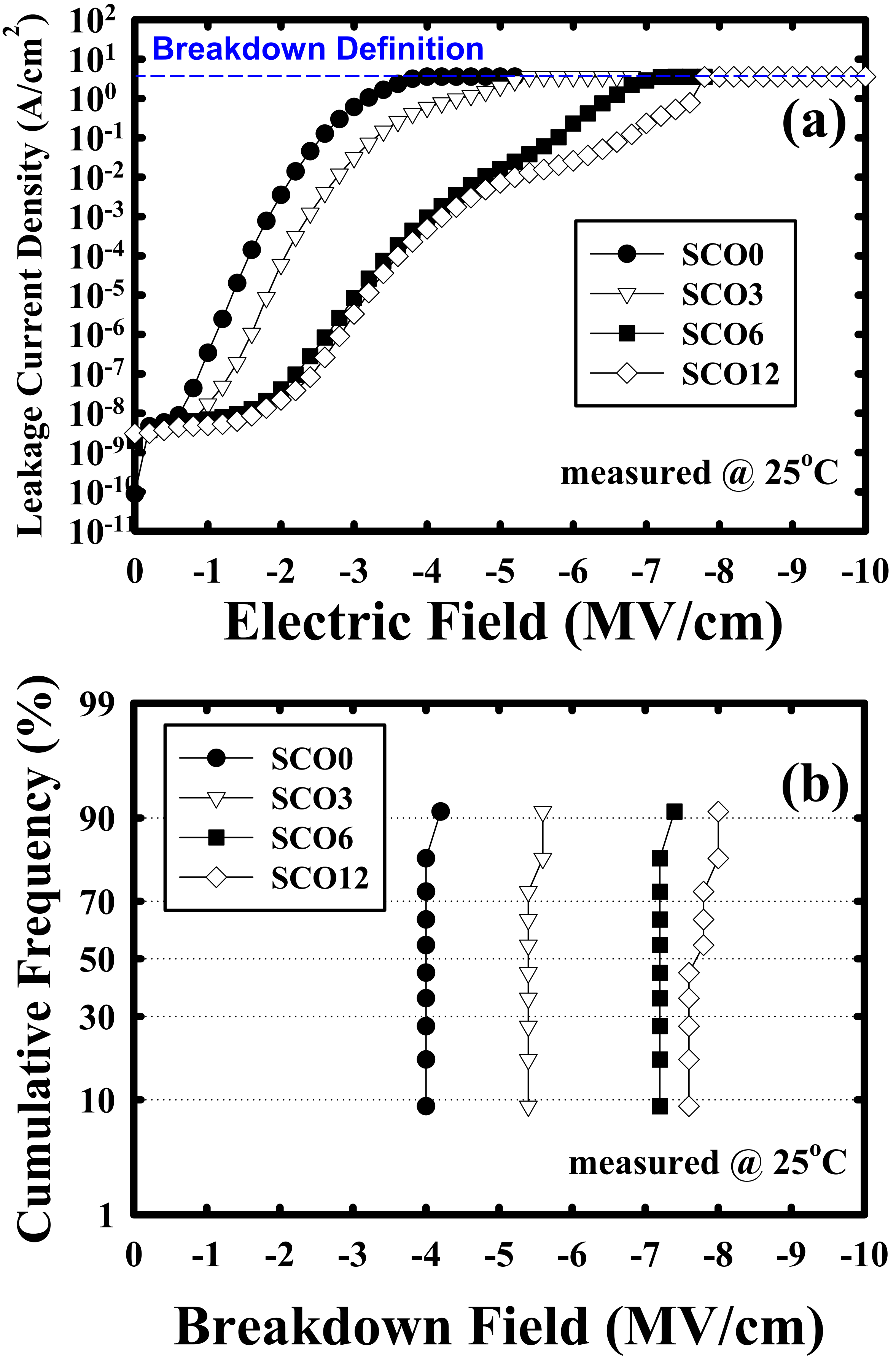

Fig. 8-4 (a) Leakage current density vs. electric field and (b) statistical distribution of breakdown field for the 400°C-annealed Al-gated MIS capacitors.

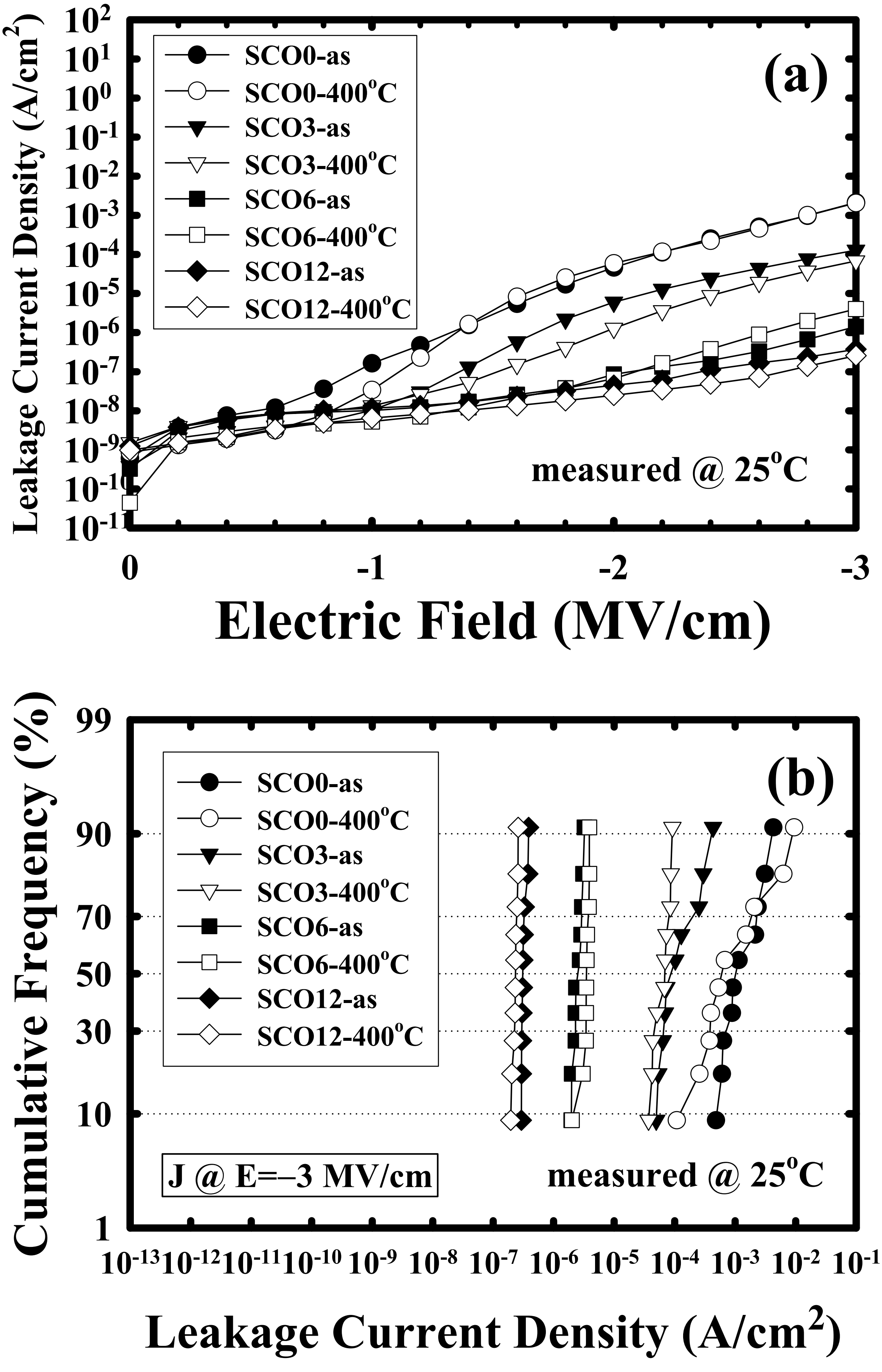

Fig. 8-5 (a) Leakage current density vs. electric field and (b) statistical distribution of leakage current density at an applied electric field of 3 MV/cm for the as-fabricated and 400°C-annealed TaN/Cu-gated MIS capacitors.

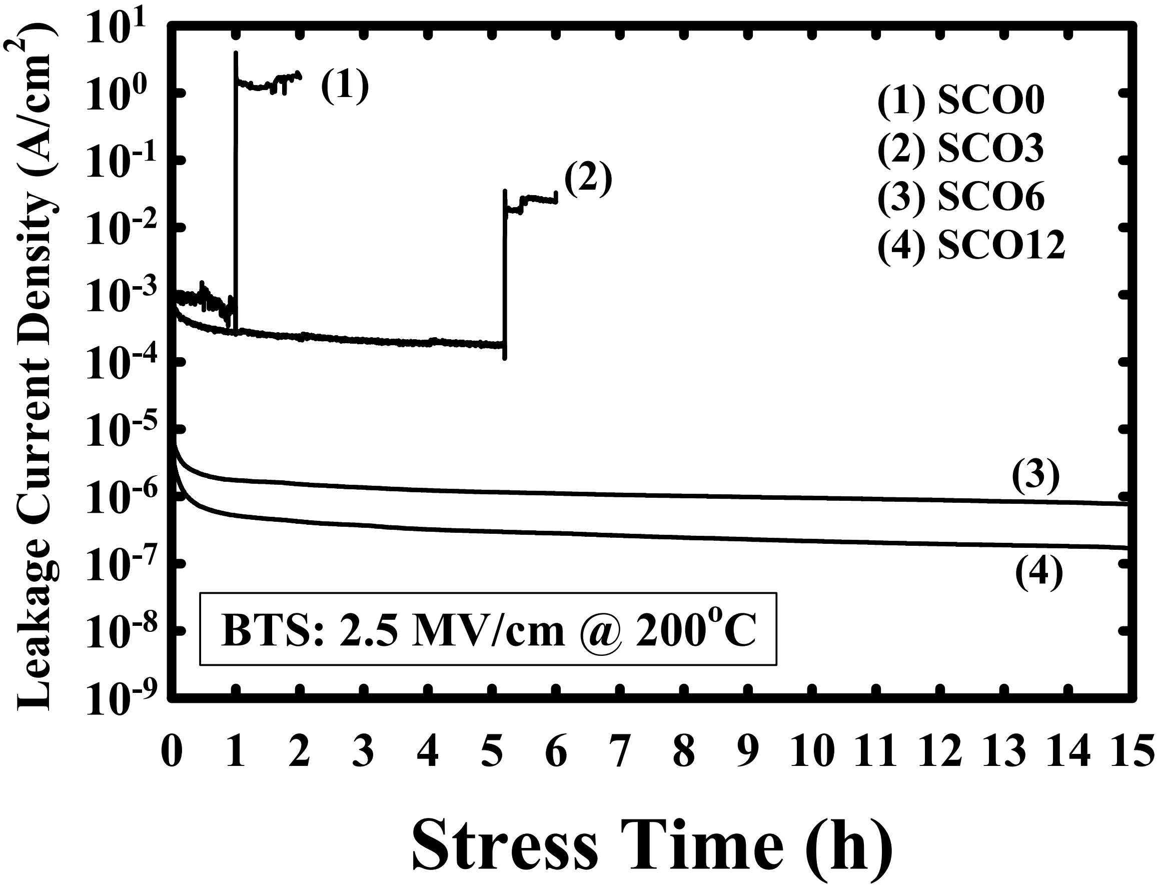

Fig. 8-6 Current transient during the BTS at 200°C with an electric field of 2.5 MV/cm for the 400°C-annealed TaN/Cu-gated MIS capacitors.

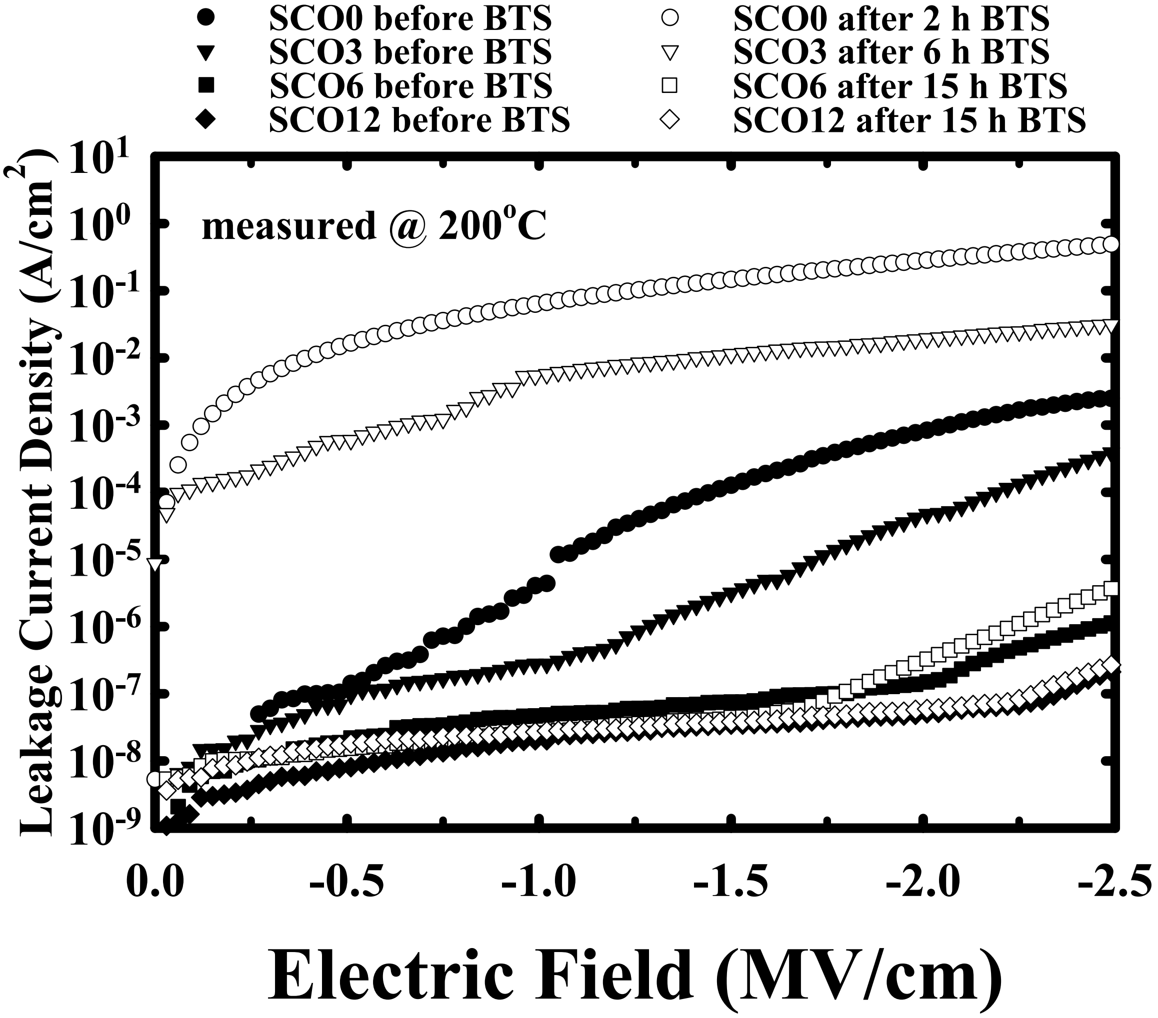

Fig. 8-7 Instantaneous leakage current density vs. applied electric field before and after the BTS (2.5 MV/cm at 200°C) for the 400°C-annealed TaN/Cu-gated MIS capacitors.

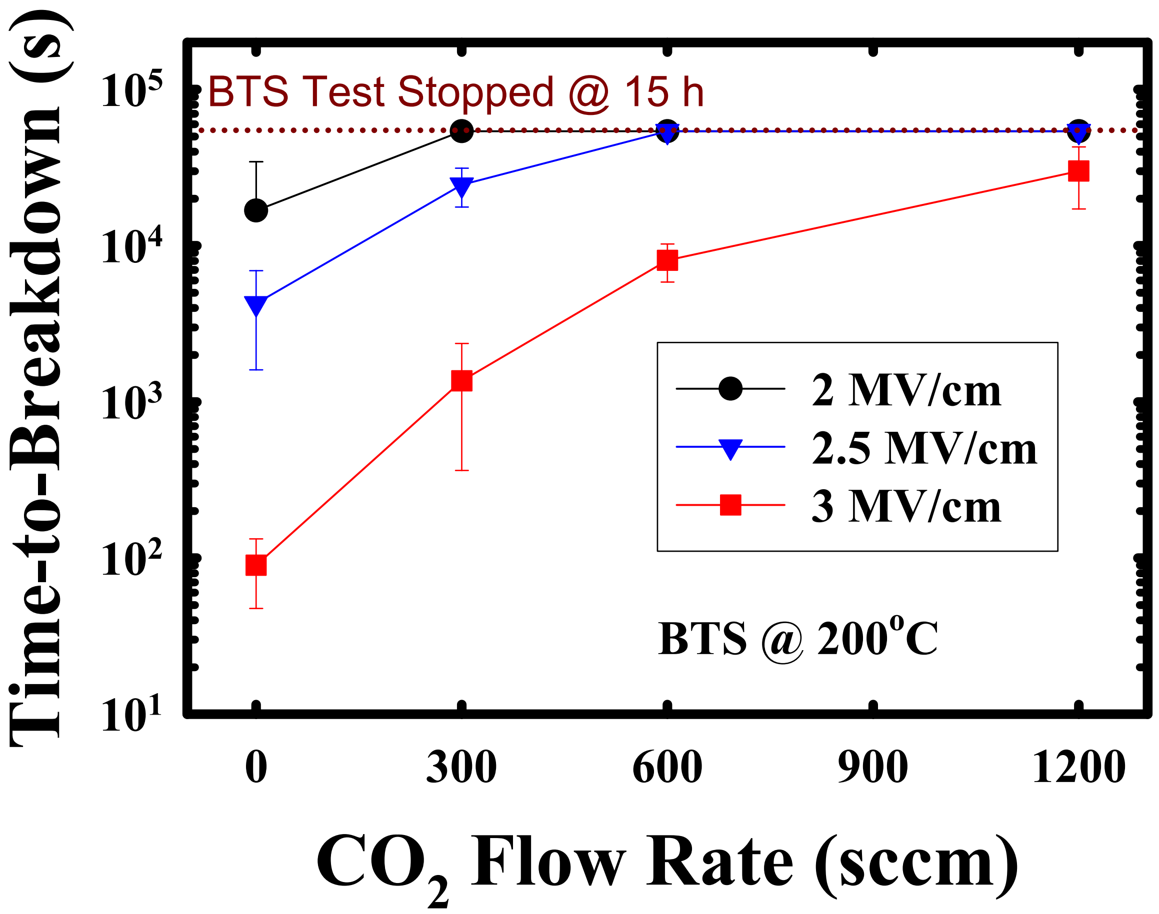

Fig. 8-8 Time-to-breakdown under different BTS conditions for the 400°C-annealed TaN/Cu-gated MIS capacitors with α-SiC(O) dielectric films deposited with various CO_2 flow rates.

Chapter 9

Cu-Comb Capacitor with α-SiCO Cap-Barrier

9-1 Introduction

The PECVD α-SiC, α-SiCN, and α-SiCO dielectric barrier films deposited using organosilicate gases have received extensive attention for applications as Cu cap-barrier and ESL in Cu interconnection scheme [1-6], and were also studied in the previous chapters of this thesis [7,8]. The fine-tuned α-SiC is better than α-SiCN and α-SiCO in the aspects of *k*-value, etching selectivity, photoresist poisoning, anti-reflective coating lithography behavior, adhesion strength to Cu and OSG IMD, electrical property, and reliability performance [2,3,7]. However, the film stress of the fine-tuned α-SiC is tensile or less compressive as compared with that of α-SiCN and α-SiCO, which results in a poor stack-stability of Cu-OSG interconnect system and a degraded interface quality of α-SiC/OSG [2,3,8]. In this work, we investigate the improvement in leakage current and breakdown field of the Cu-MIS and Cu-comb capacitors with an α-SiCO dielectric barrier over those with an α-SiC dielectric barrier having a comparable compressive film stress.

9-2 Experimental Details

The leakage current and breakdown field of Cu-MIS and Cu-comb capacitors were measured on the TaN/Cu-gated MIS structure and 0.12/0.12 μm (line-width/space) Cu-OSG single damascene structure, respectively. For the fabrication of Cu-MIS capacitor, 50-nm-thick PECVD dielectric films were deposited on p-type, (100)-oriented Si wafers at a temperature of 300~400$^{\mathrm{o}}$C, a gas pressure of 1~5

Torr, and a plasma power of 100~300 W using a parallel-plate system operated at 13.56 MHz. The flow rate ratio of 3MS [$(CH_3)_3SiH$] precursor to He carrier gas was maintained at 2/5, while the flow rate of CO_2 reaction gas was separately controlled at 0 and 1200 sccm, which resulted in the 3MS-based α-SiC and α-SiCO films, respectively, with different elemental compositions. The 3MS-based α-SiC and α-SiCO films are, in fact, the SCO0 and SCO12 samples, respectively, studied in chapter 8. A Cu layer of 200 nm thickness was sputter-deposited on the α-SiC and α-SiCO dielectric films using a dc magnetron sputtering system; this was followed by the reactive sputter deposition of a 50-nm-thick TaN layer on the Cu surface in the same sputtering system without breaking the vacuum. The TaN film served as a passivation layer to prevent the Cu electrode from oxidation in the subsequent high-temperature processes or measurements. The metal electrodes with a circular area of 0.84 mm diameter were defined by a lift-off process in order to prevent unexpected deterioration of the dielectric films by chemical wet etching. To ensure good contact in electrical measurements, a 500-nm-thick Al layer was thermally evaporated on the back surface of the Si substrate for all samples. The completed Cu-MIS capacitors were thermally annealed at 400°C for 30 min in N_2 ambient. This annealing step eliminates the plasma-induced damage during the sputter deposition of the TaN/Cu electrodes.

Figure 9-1 shows the schematic top and cross-sectional views of the Cu-comb capacitor test structure. A 40 nm PECVD 3MS-based α-SiCO (k=4.5) ESL was deposited on the PECVD oxide ILD. A single level Cu damascene (Metal-1) process with a 250 nm PECVD methylsilane-based carbon-doped low-k OSG as the IMD was employed to fabricate the Cu-comb capacitor. After patterning of 0.12/0.12 μm (line-width/space) trenches in the OSG/ESL/ILD dielectric stack, the damascene Cu feature was electrochemically deposited on a 15 nm physical vapor deposited (PVD) TaN liner barrier. Following the Cu CMP, the 3MS-based α-SiC or α-SiCO cap-barrier was deposited in a PECVD system. Another layer of PECVD OSG was deposited for the next Cu damascene (Metal-2) process.

Auger electron spectroscopy (AES) was used to obtain the chemical composition of the dielectric barrier films. The film thickness and refractive index were measured using an n&k analyzer at 633 nm wavelength, and the *k*-value of the dielectrics was determined by the maximum capacitance of the Al-gated MIS capacitors measured at 1 MHz using a Keithley 82 C-V measurement system. The film density was directly calculated by the ratio of mass to volume of the film, whereas the film mass was measured by an electronic microbalance and the film volume was calculated by the film thickness and the area of the substrate wafer. The film stress was measured using a well-calibrated thin-film stress analyzer. An HP4145B semiconductor parameter analyzer was used to measure the leakage current and breakdown field of the Cu-MIS and Cu-comb capacitors. During the measurement, N_2 purging was used to prevent possible oxidation of the Cu metal and moisture uptake in the dielectric films. Raphael modeling [9] was used to obtain the distribution of electric field in the Cu-MIS and Cu-comb capacitors.

9-3 Electrical Property of MIS Capacitor

Table 9-1 shows the basic film properties for the 3MS-based α-SiC and α-SiCO dielectrics studied in this work. Although the chemical composition indicates that the oxygen content in SiCO is much higher than that in SiC, both dielectrics have nearly the same deposition rate and compressive film stress. The compressive stress of about -200 MPa in the SiC and SiCO dielectric films is high enough to achieve a robust stack-stability [2,3]. However, it is conceivable that the SiC may exhibit inferior thermal stability and electrical and barrier properties because of its lower density (i.e., higher degree of porosity) [10,11]. Nonetheless, the refractive index of SiCO is lower than that of SiC; this results in lower electronic-dielectric constant, and thus lower dielectric constant (at 1 MHz) of the SiCO film because of the replacement of Si-C with Si-O bond and the higher electronegativity of oxygen atom [12].

Figure 9-2 shows the leakage current of Cu-MIS capacitors with SiC and SiCO dielectrics measured at various temperatures. The leakage current of the SiCO sample is generally three orders of magnitude smaller than that of the SiC sample at the electric field of 1.6 MV/cm and at temperatures ranging from 25 to 250°C, presumably due to the higher density of the SiCO film (Table 9-1). The higher density (i.e., lower degree of porosity) of film prohibited the diffusion/drift of Cu owing to the miniature free volume [11,13-17]. Higher oxygen content in the α-SiCO dielectric film would also effectively reduce the film's leakage current [18]. Since single-crystal SiC is a semiconductor having a bandgap of 2.3 to 3.0 eV, the polycrystalline or amorphous SiC possibly also has a semiconductor nature of high conductivity. Therefore, it is natural to reduce the leakage current of SiC just by doping with oxygen and making SiCO. From the log-log plot of the leakage current vs. electric field data, two different electric-field-dependent conduction mechanisms are observed in the Cu-MIS capacitors. First, all Cu-MIS capacitors exhibit ohmic conduction at low electric fields (<0.3 and <1 MV/cm for SiC and SiCO, respectively) since the leakage current (I) is linearly correlated with the electric field (E) [19], and the current can be expressed by Eq. (9-1) [20]. The ohmic conduction is carried by thermally excited electrons hopping from one isolated state to the next [19,20]. However, at high electric fields (>0.3 and >1 MV/cm for SiC and SiCO, respectively), the Cu-MIS capacitors with SiC and SiCO dielectrics exhibit different slopes in their I-E plot, particularly at temperatures above 200°C. This implies that the SiC and SiCO samples have different conduction mechanisms at high electric fields. By curve fitting with various known conduction mechanisms in dielectrics [19,20], we found that the SiC sample exhibits Frenkel-Poole (F-P) emission, while the SiCO sample reveals Schottky emission (SE), as shown in Fig. 9-3. The F-P emission shows Ln(I/E) linearly correlated with $E^{1/2}$ (Fig. 9-3a), and the current can be expressed by Eq. (9-2) [19,20]. The SE conduction shows Ln(I/T^2) linearly correlated with $E^{1/2}$ (Fig. 9-3b), and the current can be expressed by Eq. (9-3) [20]. The F-P emission is due to field-enhanced thermal excitation of trapped electrons in dielectrics into the conduction band, while the SE conduction is derived from the thermionic emission across the metal-dielectric interface or the dielectric-semiconductor interface [19-21].

ohmic $I \sim E \exp(-\Delta E_{ae}/kT)$ (9-1)

F-P $I \sim E \exp(2\beta E^{1/2}/kT - q\Phi_{FP}/kT)$ (9-2)

SE $I \sim T^2 \exp(\beta E^{1/2}/kT - q\Phi_{SE}/kT)$ (9-3)

where ΔE_{ae} is the activation energy of electron, β represents $(q^3/4\pi\varepsilon)^{1/2}$ and ε is the dielectric dynamic permittivity, k is the Boltzmann constant, q is an electron-charge, Φ_{FP} is the barrier height of trap potential well, and Φ_{SE} is the barrier height of metal/dielectric interface [20]. The F-P emission and higher leakage current of the SiC sample are presumably due to the presence of defects and/or traps [19-21] possibly resulting from the film's lower density. Clearly, temperature enhances the F-P emission and SE conduction in the SiC and SiCO samples, respectively (Fig. 9-3). Figure 9-4 shows the leakage current and breakdown field for the SiC and SiCO Cu-gated MIS capacitors measured at 200°C. The measurements were performed with the MIS capacitors biased in the accumulation region. The breakdown field is defined as the field strength such that the leakage current of the MIS capacitor reaches the current limit (20 mA, equivalent to 3.57 A/cm^2) of the HP4145B semiconductor parameter analyzer. Notably, the breakdown field of the SiCO sample is about 60% higher than that of the SiC sample. This increase in breakdown field is presumably due to the enhanced Si-O bond that has a high thermochemical energy [22]. Moreover, the oxygen atoms and the higher density of the SiCO dielectric film would also effectively increase the breakdown field [12,19]. In addition, the lower *k*-value of the SiCO film would induce lower fringe-electric field at the edge of metal-gate, as illustrated in the model shown in Fig. 9-5, which is derived from the high-*k* gate dielectrics used in the front-end-of-line (FEOL) technology [23]. It is conceivable that the lower fringe-electric field in the SiCO film would result in lower leakage current and higher breakdown field for the SiCO sample. Figure 9-6 shows the fringe-electric field obtained from Raphael simulation for the Cu-gated MIS capacitors of SiC as well as SiCO dielectric biased with an electric voltage of 10 V, which would produce an electric field of 2 MV/cm in the dielectric layer of the Cu-MIS capacitor. Notably, the SiC sample exhibits about 10% higher fringe-electric field near the Cu electrode as compared with the SiCO sample.

9-4 Electrical Property of Comb Capacitor

Figure 9-7 shows the leakage current, measured at various temperatures, for the Cu-comb capacitors with SiC as well as SiCO dielectric cap-barriers. Notably, the dependence of leakage current on the cap-barrier dielectric material implies that the dominant leakage paths are not in the bulk OSG but in the bulk cap-barrier and along the cap-barrier/OSG interface (CMP-surface) [24,25]. The fact that the leakage current of the SiCO sample at a field of 1.6 MV/cm between 25 and 250°C is at least three orders of magnitude smaller than that of the SiC sample, can be attributed to the semiconductor nature of SiC and the better electrical property of the SiCO film, as studied in the previous paragraph using the MIS capacitors. Moreover, the CMP-surface leak-path may be efficiently eliminated in the SiCO sample since both the SiCO cap-barrier and the OSG layer are similar materials of Si-C-O compounds, while the SiC cap-barrier is an oxygen-absent Si-C compound. Similar presumption was reported for the CMP-surface at the α-SiCN(cap-barrier)/α-SiCN(hard-mask) interface of the same material in the Cu damascene interconnect [24]. Two different electric-field-dependent conduction mechanisms were also observed in the Cu-comb capacitors. First, all Cu-comb capacitors exhibit ohmic conduction at low electric fields (<0.3 and <0.4 MV/cm for SiC and SiCO cap-barriers, respectively) since the leakage current (I) is linearly correlated with the electric field (E) [19,20]. Nevertheless, at high electric fields (>0.3 and >0.4 MV/cm for SiC and SiCO cap-barriers, respectively), the Cu-comb capacitors with SiC and SiCO cap-barriers exhibit quite different nonlinear I-E relation, particularly at temperatures above 200°C. This implies that the SiC and SiCO samples have different conduction mechanisms at high electric fields. From the best fitting of the known conduction mechanisms in dielectrics [19,20], we found that the SiC sample exhibits F-P emission, while the SiCO sample reveals SE conduction, as shown in Fig. 9-8. It is interesting to observe that the Cu-comb capacitors and the Cu-MIS capacitors exhibit the same electric-field-dependent conduction mechanisms. This further confirms that the dominant leakage paths are not only along the cap-barrier/OSG interface (CMP-surface) but also in the bulk cap-barrier. Furthermore, it was found in our previous work that the more leaked CMP-surface of Cu-comb capacitor would also enhance the leakage current and F-P emission [8]. Thus, the semiconductor nature of the conductive bulk SiC and the more leaked CMP-surface at the SiC/OSG interface resulted in the increased leakage current and F-P emission for the Cu-comb capacitor with a SiC cap-barrier. Figure 9-9 shows the leakage current and breakdown field for the Cu-comb capacitors with SiC and SiCO dielectric cap-barriers measured at 200°C. Notably, the breakdown field of the SiCO sample is about 25% higher than that of the SiC sample. This increase in breakdown field is presumably due to the better electrical property of bulk SiCO and the diminution of CMP-surface leak-path. In addition, the lower *k*-value of the SiCO film would also reduce the surface-electric field at the cap-barrier/OSG interface (CMP-surface), as illustrated in Fig. 9-10 [25,26]. The lower surface-electric field at the CMP-surface would result in a lower leakage current and higher breakdown field for the SiCO sample. Figure 9-11 shows the surface-electric field obtained from Raphael simulation for the Cu-comb capacitors biased with an electric voltage of 24 V, which would produce an electric field of 2 MV/cm in the dielectric layer of the Cu-comb capacitor. Notably, the surface-electric field near the Cu-line of the SiCO sample is about 6% lower than that of the SiC sample.

9-5 Summary

The leakage current and breakdown field of the Cu-MIS and Cu-comb capacitors are dependent on the dielectrics (α-SiC and α-SiCO) used as insulator and dielectric cap-barrier, respectively. The Cu-MIS and Cu-comb capacitors with an α-SiCO (*k*=3.7) dielectric barrier film exhibit a leakage current at least three orders of magnitude smaller than those with an α-SiC (*k*=4.4) dielectric film at an applied electric field of 1.6 MV/cm between 25 and 250°C. Moreover, the breakdown field of the Cu-MIS and Cu-comb capacitors with an α-SiCO dielectric barrier, measured at 200°C, are 60% and 25% respectively, higher than that of the capacitors with an α-SiC dielectric barrier. The decreased leakage current and increased breakdown field of the Cu-MIS and Cu-comb capacitors with an α-SiCO dielectric barrier are attributed to the higher density, oxygen-improved film's property, non-semiconductor behavior, and lower fringe- or surface-electric field of the α-SiCO dielectric film.

References

[1] F. Lanckmans, W. D. Gray, B. Brijs, and K. Maex, *Microelectronic Engineering*, **55** (2001) p. 329.

[2] K. Goto, H. Yuasa, A. Andatsu, and M. Matsuura, *IEEE IITC Technol. Dig.* (2003) p. 6.

[3] M. Fayolle, J. Torres, G. Passemard, F. Fusalba, G. Fanget, D. Louis, L. Arnaud, V. Girault, J. Cluzel, H. Feldis, M. Rivoire, O. Louveau, T. Mourier, and L. Broussous, *IEEE IITC Technol. Dig.* (2002) p. 39.

[4] J. Martin, S. Filipiak, T. Stephens, F. Huang, M. Aminpur, J. Mueller, E. Demircan, L. Zhao, J. Werking, C. Goldberg, S. Park, T. Sparks, and C. Esber, *IEEE IITC Technol. Dig.* (2002) p. 42.

[5] T. Ishimaru, Y. Shioya, H. Ikakura, M. Nozawa, Y. Nishimoto, S. Ohgawara, and K. Maeda, *IEEE IITC Technol. Dig.* (2001) p. 36.

[6] K. I. Takeda, D. Ryuzaki, T. Mine, and K. Hinode, *IEEE IITC Technol. Dig.* (2001) p. 244.

[7] C. C. Chiang, M. C. Chen, Z. C. Wu, L. J. Li, S. M. Jang, C. H. Yu, and M. S. Liang, *IEEE IITC Technol. Dig.* (2002) p. 200.

[8] C. C. Chiang, I. H. Ko, M. C. Chen, Z. C. Wu, Y. C. Lu, S. M. Jang, and M. S. Liang, *IEEE IITC Technol. Dig.* (2003) p. 201.

[9] Raphael modeling is provided by Avant! business unit.

[10] J. Y. Kim, M. S. Hwang, Y. H. Kim, H. J. Kim, and Y. Lee, *J. Appl. Phys.*, **90** (2001) p. 2469.

[11] Z. C. Wu, Z. W. Shiung, C. C. Chiang, W. H. Wu, M. C. Chen, S. M. Jeng, W. Chang, P. F. Chou, S. M. Jang, C. H. Yu, and M. S. Liang, *J. Electrochem. Soc.*, **148** (2001) p. F127.

[12] Y. W. Koh, K. P. Loh, L. Rong, A. T. S. Wee, L. Huang, and J. Sudijono, *J. Appl. Phys.*, **93** (2003) p. 1241.

[13] A. L. S. Loke, J. T. Wetzel, P. H. Townsend, T. Tanabe, R. N. Vrtis, M. P. Zussman, D. Kumar, C. Ryu, and S. S. Wong, *IEEE Trans. Electron Devices*, **46** (1999) p. 2178.

[14] D. Gupta, *Materials Chemistry and Physics*, **41** (1995) p. 199.

[15] J. D. Mcbrayer, R. M. Swanson, and T. W. Sigmon, *J. Electrochem. Soc.*, **133** (1986) p. 1242.

[16] J. L. Duda and N. Faridi, *Diffusion in Amorphous Materials*, edited by H. Jain and D. Gupta, The Minerals, Metals and Materials Society (Warrendale, PA, 1994) p. 55.

[17] D. Gupta, F. Faupel, and R. Willecke, *Diffusion in Amorphous Materials*, edited by H. Jain and D. Gupta, The Minerals, Metals and Materials Society (Warrendale, PA, 1994) p. 189.

[18] T. Ishimaru, Y. Shioya, H. Ikakura, M. Nozawa, S. Ohgawara, T. Ohdaira, R. Suzuki, and K. Maeda, *J. Electrochem. Soc.*, **150** (2003) p. F83.

[19] D. Brassard and M. A. E. Khakani, *J. Appl. Phys.*, **93** (2003) p. 4066.

[20] S. M. Sze, *Physics of Semiconductor Devices*, 2nd Ed. (John Wiley & Sons, 1981) p. 403.

[21] P. T. Liu, T. C. Chang, Y. L. Yang, Y. F. Cheng, and S. M. Sze, *IEEE Trans. Electron Devices*, **47** (2000) p. 1733.

[22] J. R. Bowser, *Inorganic Chemistry* (Brooks/Cole Publishing Co., California, 1993) p. 401.

[23] G. C. F. Yeap, S. Krishnan, and M. R. Lin, *IEE Electronics Lett.*, **34** (1998) p. 1150.

[24] M. Tada, Y. Harada, H. Ohtake, S. Saito, T. Onodera, and Y. Hayashi, *IEEE IITC Technol. Dig.* (2003) p. 256.

[25] J. Noguchi, T. Saito, N. Ohashi, H. Ashihara, H. Maruyama, M. Kubo, H.

Yamaguchi, D. Ryuzaki, K. I. Takeda, and K. Hinode, *IEEE IRPS Technol. Dig.* (2001) p. 355.

[26] Z. C. Wu, T. J. Chou, S. H. Lin, Y. L. Huang, Y. L. Yang, L. P. Li, B. T. Chen, Y. C. Lu, C. C. Chiang, M. C. Chen, W. Chang, S. M. Jang, and M. S. Liang, *IEEE IEDM Technol. Dig.* (2003) p. 849.

Table 9-1 Basic film properties for 3MS-based α-SiC and α-SiCO dielectric barrier films with a thickness of 50 nm used in this study.

Sample ID	SiC	SiCO
Structure	α-SiC	α-SiCO
Chemical composition	$SiC_{0.92}O_{0.04}$	$SiC_{0.97}O_{0.66}$
Deposition rate (nm/min)	100.4	102.6
Film stress (MPa)	-200	-210
Film density (g/cm^3)	1.24	1.80
Refractive index @ 633 nm	2.04	1.72
Dielectric constant @ 1 MHz	4.41	3.73

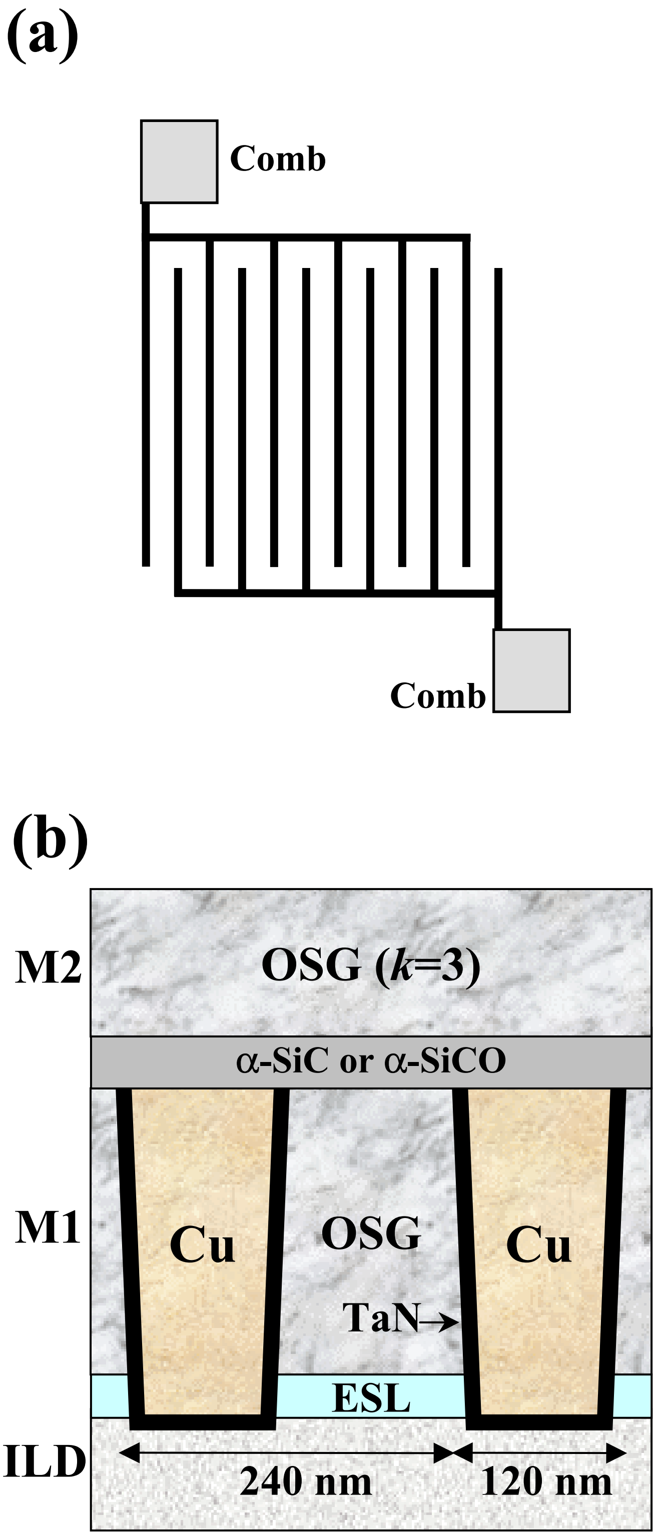

Fig. 9-1 Schematic (a) top view and (b) cross-sectional view of the Cu-comb capacitor test structure employed in this study.

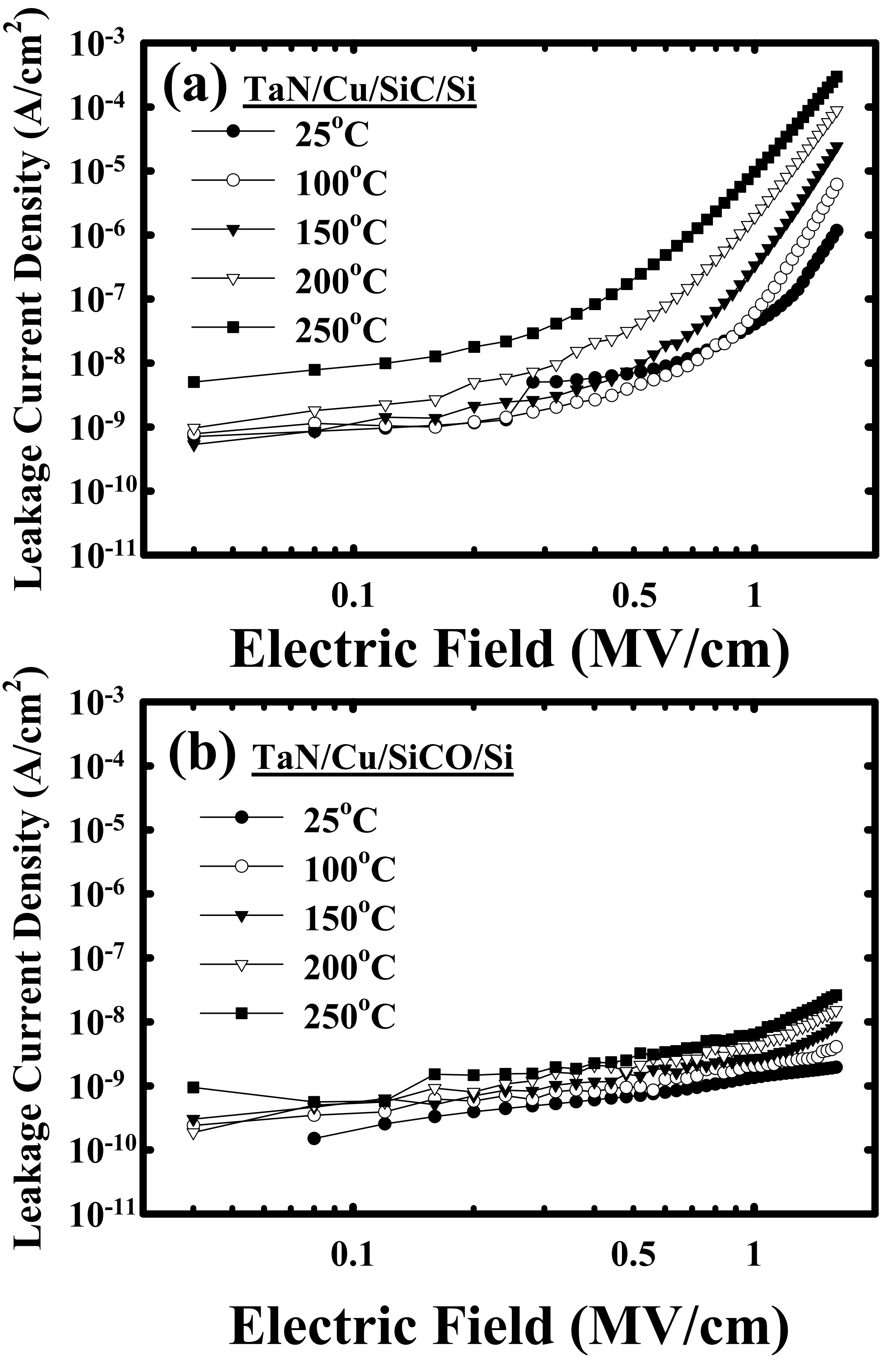

Fig. 9-2 Leakage current density vs. electric field in a log-log plot, measured at various temperatures, for Cu-MIS capacitors with (a) α-SiC and (b) α-SiCO dielectric films.

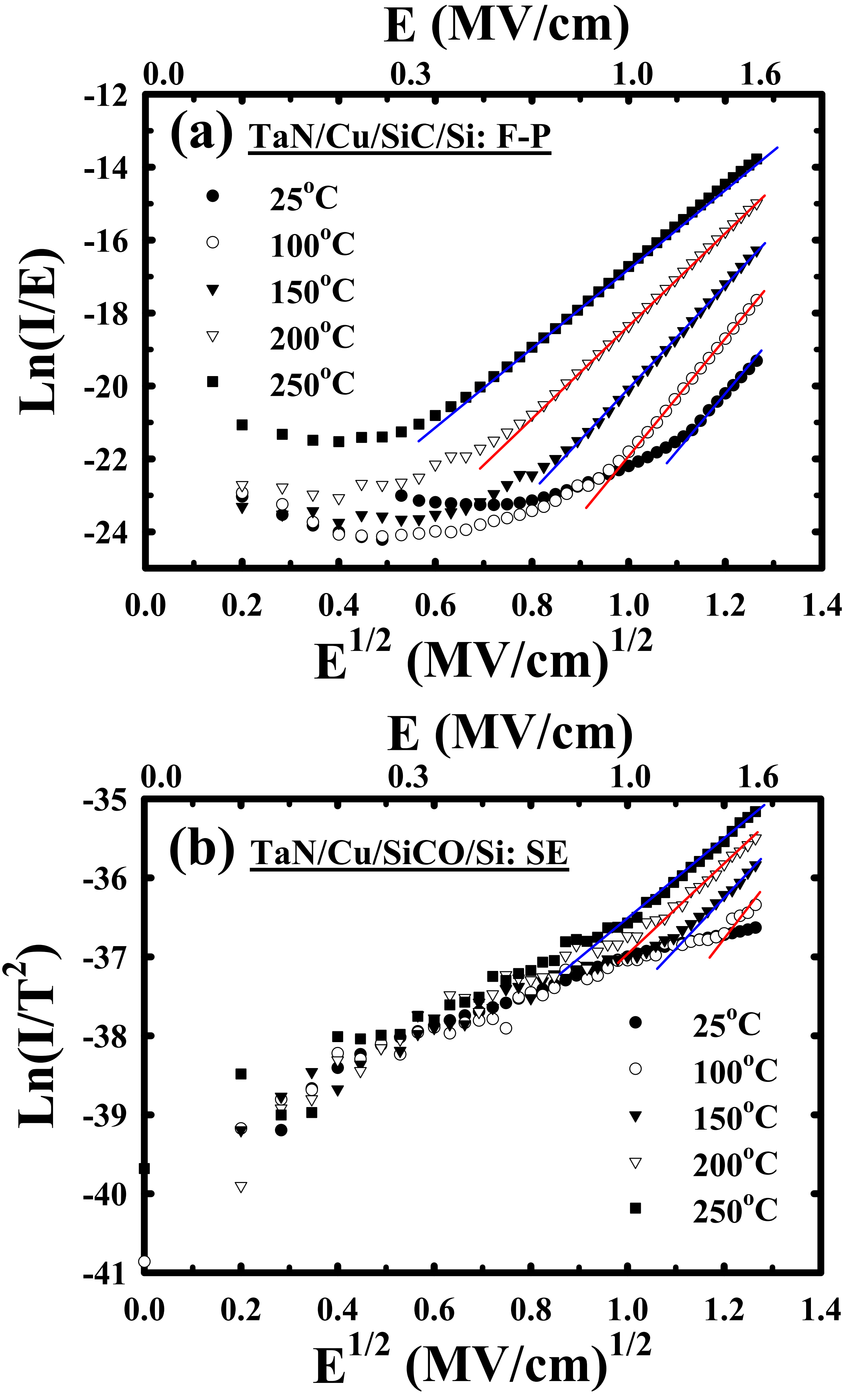

Fig. 9-3 Conduction mechanism of (a) Frenkel-Poole emission in TaN/Cu/α-SiC/Si and (b) Schottky emission in TaN/Cu/α-SiCO/Si samples.

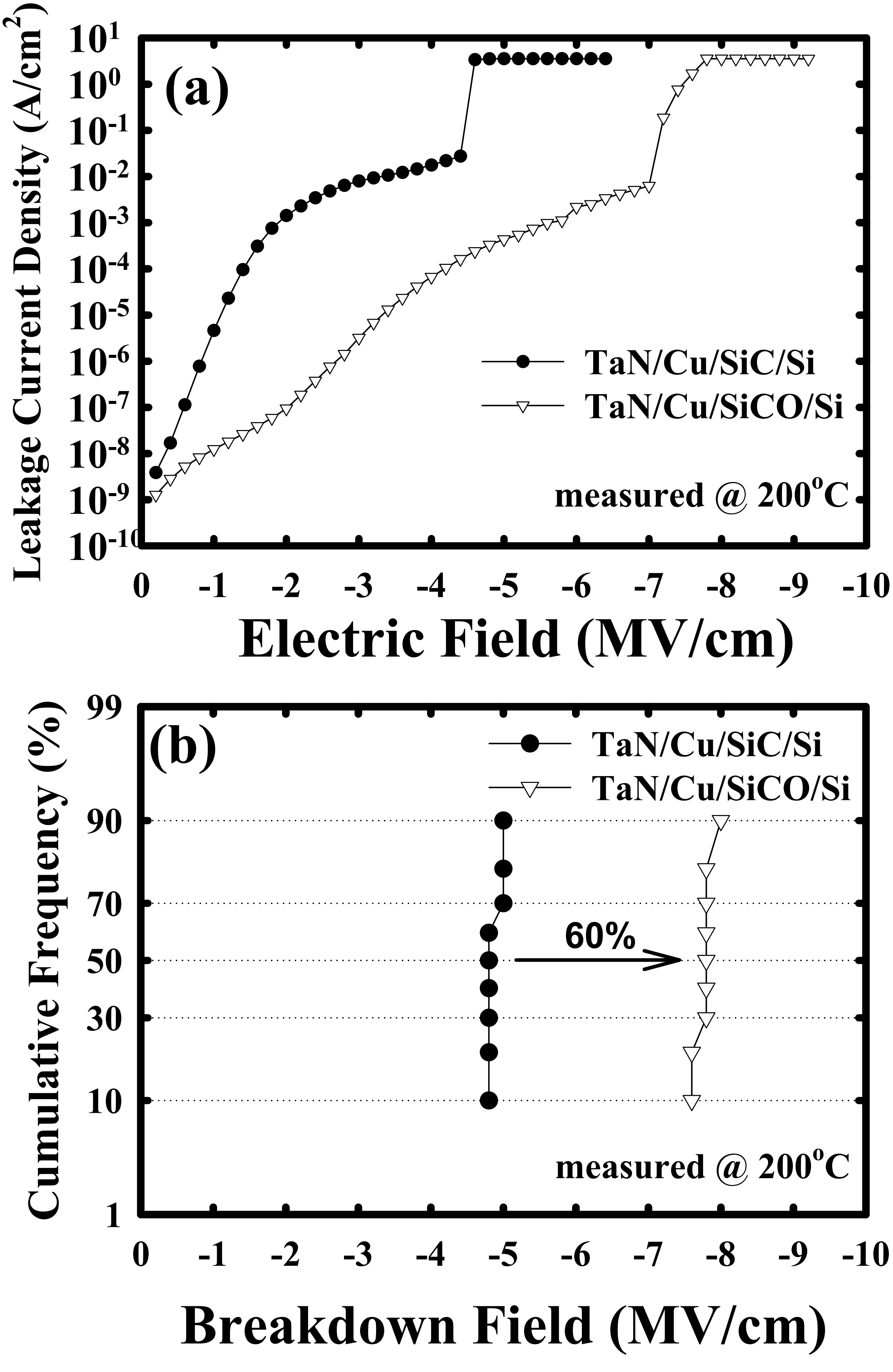

Fig. 9-4 (a) Leakage current density vs. electric field and (b) distribution of breakdown field for the α-SiC and α-SiCO Cu-gated MIS capacitors measured at 200°C.

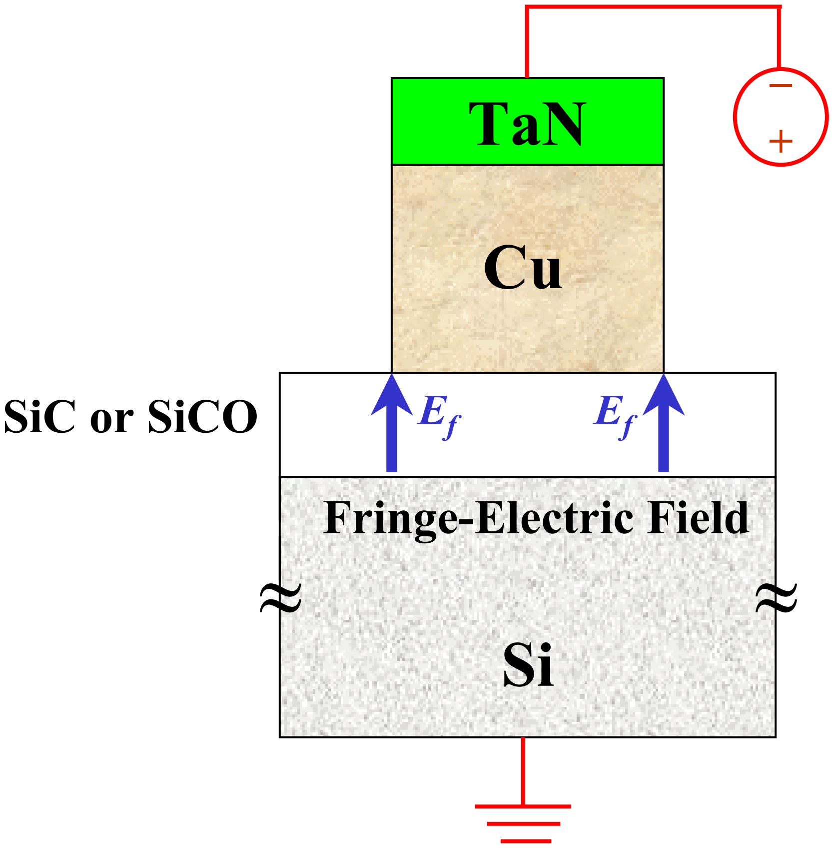

Fig. 9-5 Proposed fringe-electric field in the MIS capacitor studied in this work.

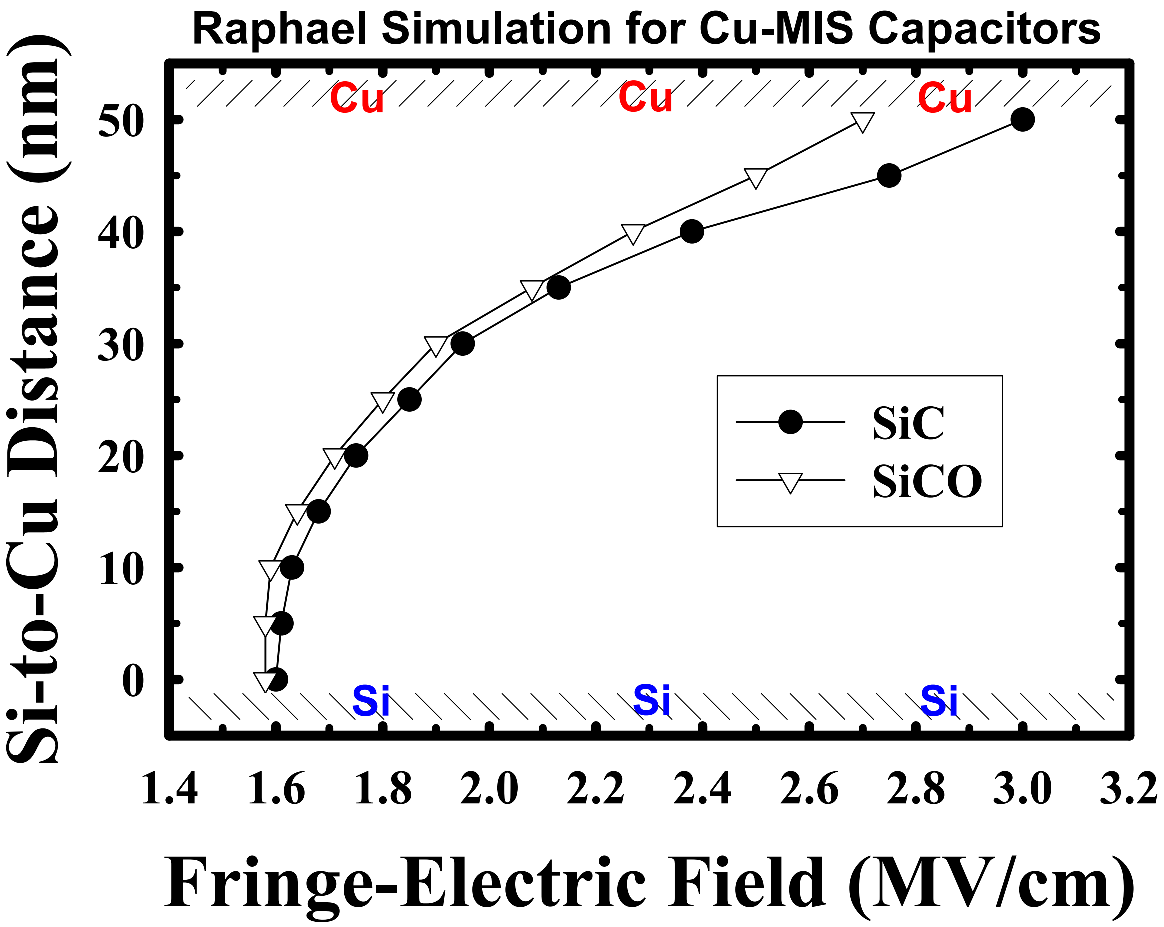

Fig. 9-6 Fringe-electric field obtained from Raphael simulation for the Cu-gated MIS capacitors of α-SiC as well as α-SiCO dielectric biased with an electric voltage of 10 V (equivalent to an electric field of 2 MV/cm).

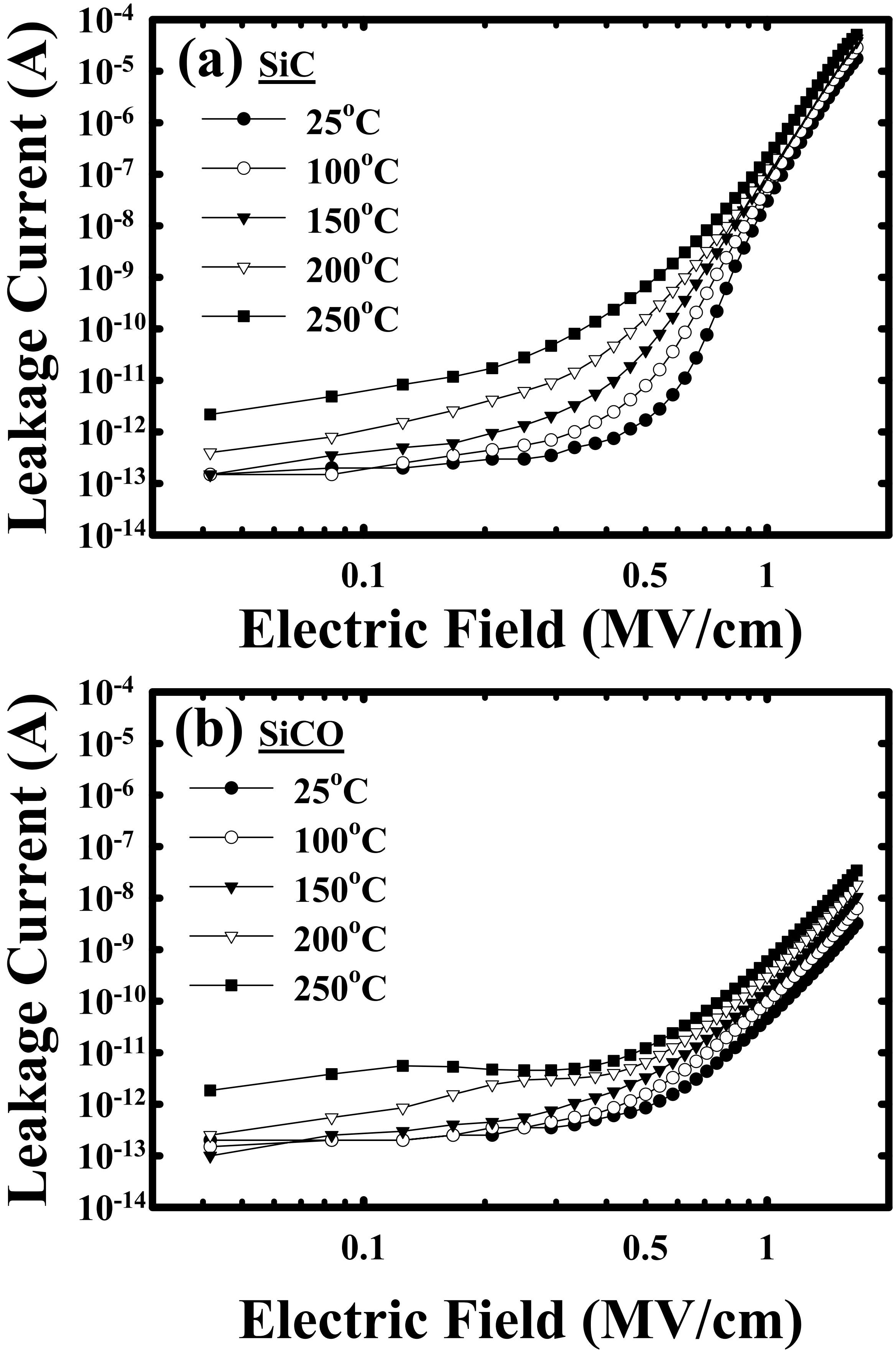

Fig. 9-7 Leakage current vs. electric field in a log-log plot, measured at various temperatures, for Cu-comb capacitors with (a) α-SiC and (b) α-SiCO cap-barriers.

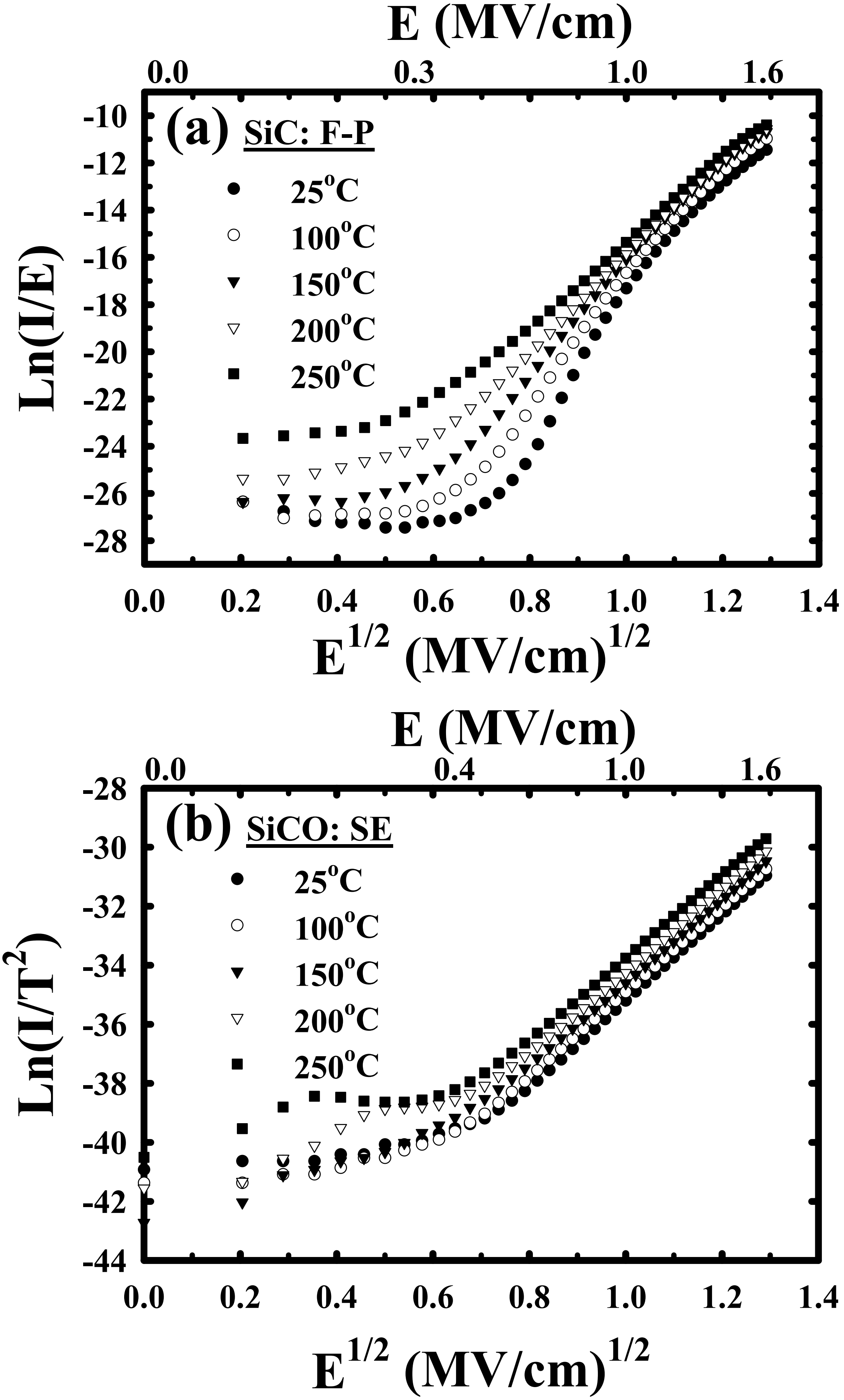

Fig. 9-8 Conduction mechanism of (a) Frenkel-Poole emission in Cu-comb capacitor with α-SiC cap-barrier and (b) Schottky emission in Cu-comb capacitor with α-SiCO cap-barrier.

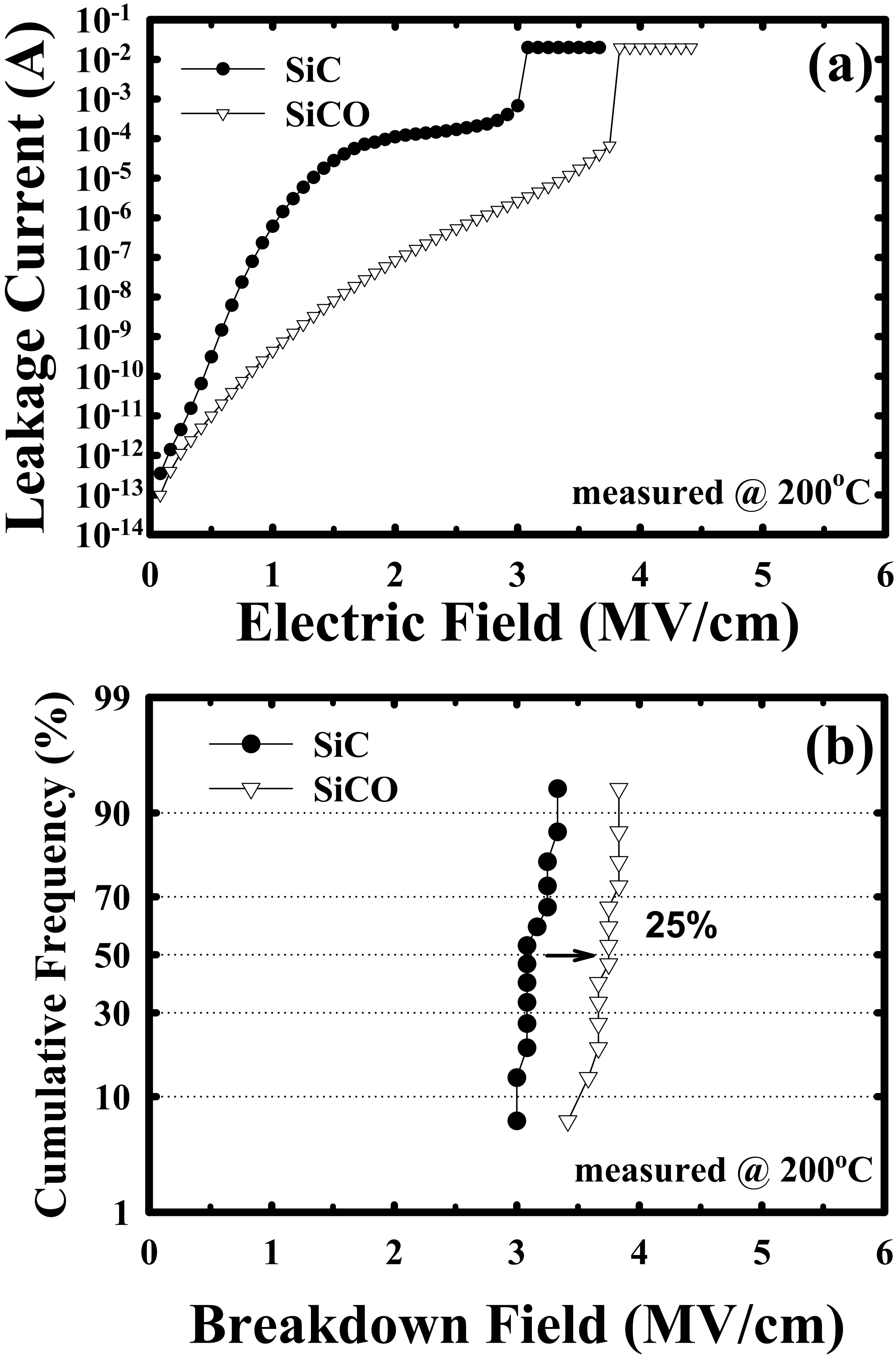

Fig. 9-9 (a) Leakage current vs. electric field and (b) distribution of breakdown field for the α-SiC and α-SiCO Cu-comb capacitors measured at 200°C.

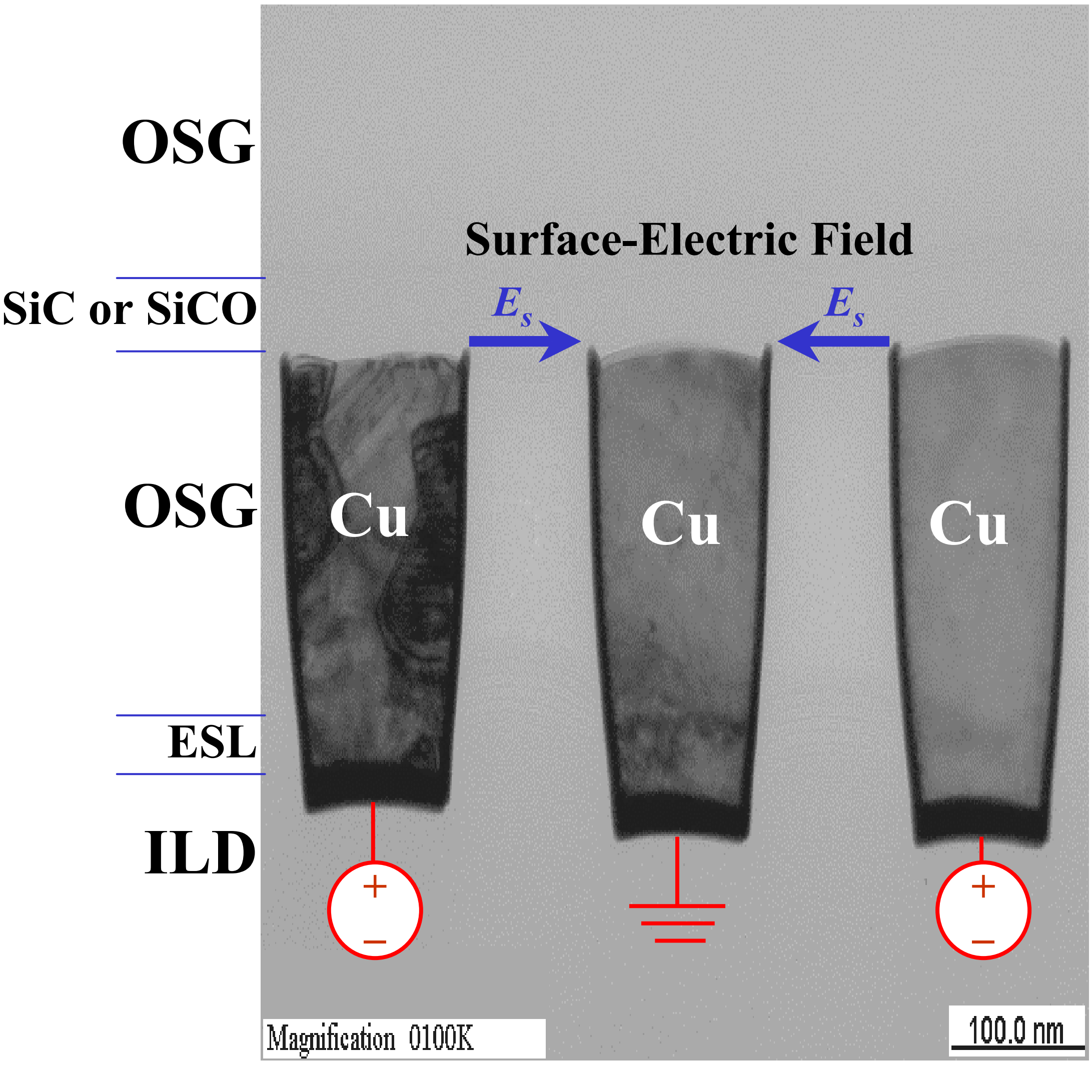

Fig. 9-10 Proposed surface-electric field in the Cu-comb capacitor studied in this work.

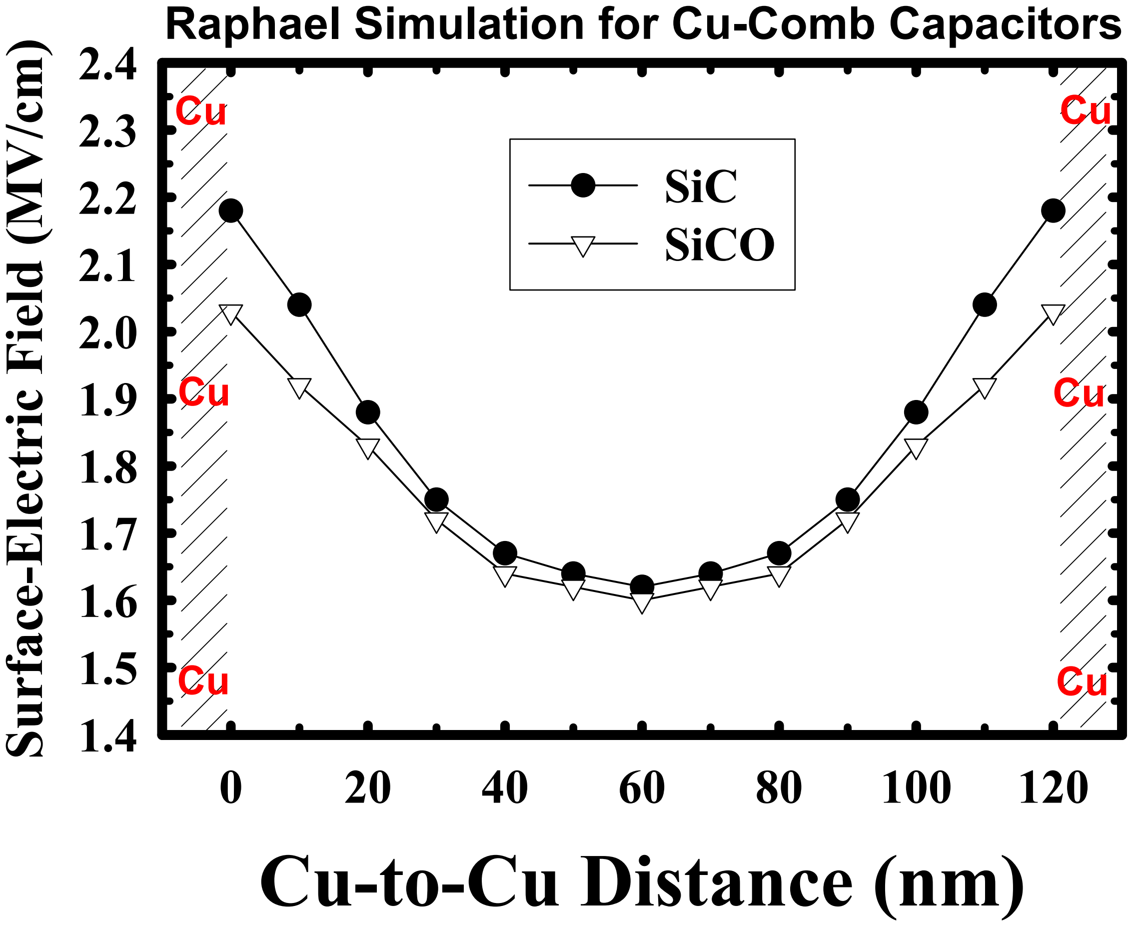

Fig. 9-11 Surface-electric field obtained from Raphael simulation for the Cu-comb capacitors with α-SiC and α-SiCO cap-barriers biased with an electric voltage of 24 V (equivalent to an electric field of 2 MV/cm).

Chapter 10

Octamethylcyclotetrasiloxane-Based α-SiCO Dielectric Barrier

10-1 Introduction

The PECVD α-SiC, α-SiCN, and α-SiCO dielectric barrier films deposited using organosilicate gases are receiving extensive attention for applications as Cu cap-barrier and etching stop layer in Cu damascene structures [1-3], and were also studied in the previous chapters of this thesis [4]. The 3MS- or 4MS-based α-SiC and α-SiCN dielectric barrier films show *k*-values in the range of 4 to 5 [1-4], while the α-SiCO dielectric barrier films deposited using hexamethydisiloxane (HMDSO) or trimethoxysilane (TMOS) precursor exhibit a lower *k*-value of 3.9 [5,6]. In chapters 8 and 9, we found that the α-SiCO dielectric barrier film deposited using 3MS precursor with He carrier gas and 1200 sccm CO_2 reaction gas exhibits a *k*-value of 3.7. Moreover, it has been reported that the α-SiCO dielectric barrier film deposited using 3MS precursor with He carrier gas and O_2 reaction gas exhibits an even lower *k*-value of 3.3 [7]. In this work, we investigate the thermal stability and physical and barrier properties for three α-SiCO dielectric barrier films, with dielectric constants between 2.8 and 6.3, deposited using octamethylcyclotetrasiloxane (OMCTS) precursor and He carrier gas with and without O_2 reaction gas.

10-2 Experimental Details

Three α-SiCO dielectric barrier films deposited using OMCTS $\{[(CH_3)_2SiO]_4\}$ precursor and He carrier gas with and without O_2 reaction gas are investigated with respect to their thermal stability and physical and barrier properties. OMCTS is a cyclic structured silicone compound with low water solubility and high vapor pressure. It is a highly safe compound because it converts into SiO_2, H_2O, and CO_2 in the ambient of atmosphere. In this study, all of the α-SiCO films were deposited to a thickness of 50 nm on p-type, (100)-oriented Si wafers (8~12 Ω-cm resistivity) at a temperature of 350°C, a total gas pressure of 7 Torr, and a plasma power of 600 W using a parallel-plate PECVD system operated at 13.56 MHz. The flow rate of OMCTS precursor was maintained at 800 sccm, while the flow rate of O_2 reaction gas was separately controlled at 0, 200, and 300 sccm, which resulted in three α-SiCO films with different elemental compositions. All deposited films were thermally annealed at 400°C for 30 min in N_2 ambient to remove moisture possibly absorbed in the dielectric barrier films prior to the investigation of the films' physical property or the deposition of electrode (TaN/Cu or Al) to construct the metal-insulator-semiconductor (MIS) capacitor structure. The TaN/Cu-gated MIS capacitors were constructed by first sputter-depositing a 200-nm-thick Cu layer on the α-SiCO dielectric barrier film using a dc magnetron sputtering system, followed by a reactive sputter deposition of a 50-nm-thick TaN layer on the Cu surface in the same sputtering system without breaking the vacuum. The TaN film served as a passivation layer to prevent the Cu electrode from oxidization during the subsequent high-temperature processes. For a comparison, Al-gated control samples were also prepared by depositing a 500-nm-thick Al layer directly on the α-SiCO dielectric surfaces using a thermal evaporation system. All metal electrodes with a circular area of 0.84 mm diameter were defined by a lift-off process in order to prevent unexpected deterioration of the dielectric barrier films due to chemical wet etching. For better electrical measurements, a 500-nm-thick Al layer was also deposited on the back surface of the Si substrate for all samples. Some of the completed MIS samples were thermally annealed at 400°C for 30 min in N_2 ambient. This annealing step eliminates the plasma-induced damage that may have occurred during the sputter deposition of the TaN/Cu electrodes and also provides the driving force for Cu diffusion.

Fourier transform infrared spectroscopy (FTIR, ASTeX PDS-17 System) was used to analyze the chemical bonding of the dielectric barrier films. The film thickness and refractive index were measured using a well-calibrated measurement system (n&k analyzer 1200) at 633 nm wavelength, and the *k*-value of the dielectric barrier films was determined by the maximum capacitance of the Al-gated MIS capacitors measured at 1 MHz using a C-V measurement system (Keithley 82). A semiconductor parameter analyzer (HP4145B) was used to measure the dielectric leakage current and provide the bias for the bias-temperature-stress (BTS) test. Secondary ion mass spectrometry (SIMS) was used to detect the penetration of Cu in the dielectric barrier films.

10-3 Physical Property and Thermal Stability

Table 10-1 shows the basic data of the three OMCTS-based α-SiCO dielectric barrier films studied in this work. The α-SiCO dielectric barrier films deposited with O_2 flow rate of 0, 200, and 300 sccm are designated as SiCO-0, SiCO-2, and SiCO-3, respectively. It is found that the FTIR Si-O(1020 cm^{-1})/Si-C(800 cm^{-1}) absorbance peak ratio increases with increasing flow rate of O_2 reaction gas during the deposition of the α-SiCO dielectric barrier films. However, the refractive index of the α-SiCO dielectric barrier films decreases with the addition of O_2 reaction gas. This result of observation is consistent with those reported in the literature regarding various α-SiCO dielectric films deposited using O_2/3MS, N_2O/HMDSO, O_2/4MS, and N_2O/4MS gases [7-10]. Dielectric constant at 1 MHz consists of three components arising from the contribution of electronic, ionic, and dipolar dielectric constant [7,8], as shown in Eq. (10-1):

$$k(\text{at 1 MHz}) = k_e(n^2) + k_{ion} + k_{dipolar} \qquad (10\text{-}1)$$

The electronic contribution arises from the displacement of the electron shell relative to a nucleus. The ionic contribution comes from the displacement of a charged ion with respect to other ions, and the dipolar contribution arises from the change of orientation for the molecules with a permanent electric dipole moment in an applied electric field. Although the electronic dielectric constant, which equals the square of refractive index [7,8], decreases with the addition of O_2 reaction gas, the dielectric constant (@ 1 MHz) of the α-SiCO dielectric barrier films increases with increasing flow rate of O_2 reaction gas during the film's deposition process. Moreover, the ionic and dipolar dielectric constants, which are obtained by subtracting the electronic dielectric constant from the dielectric constant at 1 MHz [7,8], increase with increasing flow rate of O_2 reaction gas. The reduction in the electronic dielectric constant of the α-SiCO dielectric barrier films is attributed to the increase of Si-O bond, which is more ionic- and dipolar-polarizable than the Si-C bond [7,8,11,12]. Thus, an α-SiCO film's dielectric constant, which is dominated by the electronic polarization, would decrease with increasing incorporation of oxygen [7]. Nevertheless, when the strong ionic and dipolar polarizations of the Si-O bonds become predominant in the dielectric constant of an α-SiCO film, the film's dielectric constant is expected to increase with increasing flow rate of oxygen-containing reaction gas during the film's deposition process [8-10].

The lower refractive index of the α-SiCO dielectric film implies a lower film density and vice versa [10], and refractive indices below 1.46 have been proposed to indicate less dense or porous materials such as the α-SiCO dielectric films with a porosity of 14~39% [12,13]. It is conceivable that dielectric films with a high density of pores, voids, and other defects tend to contain a high density of bound water because of the film's larger effective surface area [13-15], e.g. the as-deposited SiCO-2 and SiCO-3 dielectric barrier films whose FTIR spectra reveal a broad peak of H-OH bond at 3480 cm^{-1}, and a clear Si-OH peak at 975 cm^{-1} observed in the SiCO-3 film, as shown in Fig. 10-1. Such a susceptibility to moisture may significantly increase the dielectric constant because of the incorporation of H_2O (k=80) and adversely affect the electrical reliability of the dielectric film. The bound moisture (H-OH at 3480 cm^{-1} and Si-OH at 975 cm^{-1}) disappeared completely after the films were thermally annealed at 600°C for 30 min in N_2 ambient. The absorbance of Si-C (800 cm^{-1}) and Si-CH_3 (1265 cm^{-1}) peaks decrease, whereas that of the Si-O (1020 cm^{-1}) peak increases for the films with increased flow rate of O_2 reaction gas during the films' deposition. Notably, all films show a tiny Si-O shoulder at 1100 cm^{-1}, indicating the existence of the caged Si-O structure in the dielectric films [10,13], which may result from the OMCTS cyclic precursor. The slight Si-H (2102 cm^{-1}) peak appeared only in the SiCO-0 film, and the small C-H (2962 cm^{-1}) peak was detected only in the SiCO-0 and SiCO-2 films, whereas a distinguishable C-O shoulder at 1200 cm^{-1} was observed only in the SiCO-3 film. Figure 10-2 shows the FTIR absorbance peak ratios of Si-CH_3(1265 cm^{-1})/Si-O(1020 cm^{-1}) and H-OH(3480 cm^{-1})/Si-O(1020 cm^{-1}) and the thickness shrinkage for the α-SiCO dielectric barrier films thermally annealed at various temperatures for 30 min in N_2 ambient. Notably, only the SiCO-0 film exhibits chemical outgassing of the CH_3 group above 550°C, whereas only the SiCO-2 and SiCO-3 films exhibit desorption of moisture at temperatures above 400°C. With regard to the film thickness, the thickness of all films remained nearly constant at temperatures up to 400°C. Upon annealing at 550°C, the shrinkage of the SiCO-0 film remained below 1%; at 600°C, however, the film shrank for more than 2%, presumably due to chemical outgassing, leading to partial removal of the CH_3 group (Fig. 10-2a). For the SiCO-2 and SiCO-3 films, severer shrinkage (>2%) was observed at and above 550°C, presumably due to the desorption of moisture (Fig. 10-2b), leading to a denser film structure. The chemical outgassing of the CH_3 group and the desorption of moisture imply the changes in chemical bonding structure and physical microstructure of the dielectric film, resulting in the variation of refractive index and dielectric constant, as shown in Fig. 10-3. In summary, the OMCTS-based α-SiCO dielectric barrier film deposited without O_2 reaction gas has a thermally stable temperature of 550°C, while the films deposited with an addition of O_2 reaction gas have a lower thermal stability temperature, which is about 400°C for the films studied in this work.

10-4 Electrical and Barrier Properties

Figure 10-4 shows the room temperature leakage current density and the distribution of dielectric breakdown field for the as-fabricated Al-gated MIS capacitors of various α-SiCO dielectric barrier films. The measurements were performed with the MIS capacitors biased in the accumulation region. The leakage current characteristics indicate the existence of two breakdown mechanisms: electric breakdown and dielectric breakdown. The electric breakdown, which has been referred to as a soft, quasi, or non-destructive breakdown and is associated with the creation of a temporary conducting path between the cathode and anode [16], occurs at an electric field of 4 to 6 MV/cm. After the electric breakdown, the leakage current reached a saturated value until the occurrence of dielectric breakdown, which has been referred to as a hard, thermal, or destructive breakdown and is associated with the creation of a permanent conducting path between the cathode and anode [16], at an electric field of 8 to 11 MV/cm. Similar dual breakdown was observed elsewhere in the metal-insulator-metal (MIM) capacitors of low-*k* dielectric materials [17]. Notably, the α-SiCO films deposited with the addition of O_2 reaction gas exhibit a higher dielectric breakdown field. This increase of dielectric breakdown field is presumably due to the enhanced Si-O bond that has a high thermochemical energy [18]. Similar result was observed in the α-SiCO dielectric films deposited using O_2/3MS gases of various flow ratios that the dielectric breakdown field increased with increasing O_2 flow rate [7]. On the other hand, the lower electric breakdown fields of the α-SiCO dielectric barrier films deposited with the addition of O_2 reaction gas might result from a larger number of communicating traps [16] such as moisture, voids, pores or other defects. Figure 10-5 shows the room temperature leakage current density for the as-fabricated as well as 400°C-annealed (30 min in N_2 ambient) Al-gated and TaN/Cu-gated MIS capacitors of the α-SiCO dielectric barrier films. For each dielectric barrier film, negligible difference in leakage current was observed between the Al-gated and TaN/Cu-gated MIS capacitors, whether as-fabricated or 400°C-annealed. This implies that all the dielectrics are capable of preventing Cu penetration at temperatures up to 400°C. The increased leakage current density for the α-SiCO dielectric barrier films deposited with the addition of O_2 reaction gas (Fig. 10-5d) might result from the defect and/or moisture induced extra leakage paths [19].

BTS test was used to further explore the dielectric barrier property of the α-SiCO films using the TaN/Cu-gated MIS capacitor structure. The BTS was performed at 125°C with an applied electric field of 1 MV/cm on the MIS capacitors that had been annealed at 400°C for 30 min. An N_2 purging was used to prevent oxidation of the Cu electrode and moisture uptake in the dielectric barrier films during the BTS. Figure 10-6 shows the leakage current transient during the BTS. Current-spiking occurred for the SiCO-2 and SiCO-3 dielectric MIS samples after BTS for about 2 and 1 h, respectively, whereas the SiCO-0 dielectric MIS sample remained stable up to at least 15 h. Figure 10-7 shows the SIMS depth profiles of Cu in the TaN/Cu-gated α-SiCO dielectric barrier films after removal of the TaN/Cu electrodes. The depth profiles of Cu clearly indicate the penetration of Cu into the SiCO-2 and SiCO-3 dielectric barrier films for the TaN/Cu-gated SiCO-2 and SiCO-3

MIS samples after 3 and 2 h BTS, respectively. Thus, we may conclude that the current-spiking in the leakage current of the TaN/Cu-gated SiCO-2 and SiCO-3 MIS samples during the BTS is due to the penetration of Cu into the dielectric barrier films, not the BTS-induced dielectric breakdown. This conclusion is consistent with the results of BTS test on the Al-gated α-SiCO dielectric MIS samples that all of them remained stable up to at least 15 h stress (not shown). The inferior barrier property of the α-SiCO dielectric barrier films deposited with the addition of O_2 reaction gas is attributed to the film's microporous Si-O structure [7]. It has been reported that water vapor in the ambient or in dielectric film will markedly enhance the penetration of Cu into the dielectric film, either by hydration-energy induced ionization of metal atoms, or by the creation of deep level electron traps arising from H_2O in the dielectric film [13,20,21]. Moreover, the abundant oxygen in dielectric films might also enhance the penetration of Cu into the dielectric film by Cu-O reacting [8,20]. Thus, nanopores, moisture, and the abundant oxygen may all enhance the penetration of Cu into the SiCO-2 and SiCO-3 dielectric barrier films and the rapid drift of Cu ions across the barrier layer during the BTS test.

10-5 Summary

Three PECVD OMCTS-based α-SiCO dielectric barrier films deposited with and without O_2 reaction gas were investigated with respect to their thermal stability and physical and barrier properties. It is found that the α-SiCO dielectric barrier film deposited without O_2 reaction gas exhibits a low *k*-value of 2.8, thermal stability at temperatures up to 550^{o}C, excellent moisture resistance, and superb Cu barrier property up to 400^{o}C. With the addition of O_2 reaction gas during the dielectric deposition process, the dielectric constant of the α-SiCO films increases with increasing flow rate of O_2 reaction gas. Increasing flow rate of O_2 reaction gas during the deposition of the α-SiCO films also degrades the thermal stability and moisture resistance of the dielectric barrier films. Moreover, an addition of O_2 reaction gas also results in degraded Cu barrier property of the dielectric films.

References

[1] F. Lanckmans, W. D. Gray, B. Brijs, and K. Maex, *Microelectronic Engineering*, **55** (2001) p. 329.

[2] J. Martin, S. Filipiak, T. Stephens, F. Huang, M. Aminpur, J. Mueller, E. Demircan, L. Zhao, J. Werking, C. Goldberg, S. Park, T. Sparks, and C. Esber, *IEEE IITC Technol. Dig.* (2002) p. 42.

[3] S. G. Lee, Y. J. Kim, S. P. Lee, H. Y. Oh, S. J. Lee, M. Kim, I. G. Kim, J. H. Kim, H. J. Shin, J. G. Hong, H. D. Lee, and H. K. Kang, *Jpn. J. Appl. Phys.*, **40** (2001) p. 2663.

[4] C. C. Chiang, M. C. Chen, Z. C. Wu, L. J. Li, S. M. Jang, C. H. Yu, and M. S. Liang, *IEEE IITC Technol. Dig.* (2002) p. 200.

[5] T. Ishimaru, Y. Shioya, H. Ikakura, M. Nozawa, Y. Nishimoto, S. Ohgawara, and K. Maeda, *IEEE IITC Technol. Dig.* (2001) p. 36.

[6] K. I. Takeda, D. Ryuzaki, T. Mine, and K. Hinode, *IEEE IITC Technol. Dig.* (2001) p. 244.

[7] Y. W. Koh, K. P. Loh, L. Rong, A. T. S. Wee, L. Huang, and J. Sudijono, *J. Appl. Phys.*, **93** (2003) p. 1241.

[8] T. Ishimaru, Y. Shioya, H. Ikakura, M. Nozawa, S. Ohgawara, T. Ohdaira, R. Suzuki, and K. Maeda, *J. Electrochem. Soc.*, **150** (2003) p. F83.

[9] A. Grill and V. Patel, *J. Appl. Phys.*, **85** (1999) p. 3314.

[10] L. M. Han, J. S. Pan, S. M. Chen, N. Balasubramanian, J. Shi, L. S. Wong, and P. D. Foo, *J. Electrochem. Soc.*, **148** (2001) p. F148.

[11] S. M. Han and E. S. Aydil, *J. Appl. Phys.*, **83** (1998) p. 2172.

[12] J. Y. Kim, M. S. Hwang, Y. H. Kim, H. J. Kim, and Y. Lee, *J. Appl. Phys.*, **90** (2001) p. 2469.

[13] Z. C. Wu, Z. W. Shiung, C. C. Chiang, W. H. Wu, M. C. Chen, S. M. Jeng, W. Chang,

P. F. Chou, S. M. Jang, C. H. Yu, and M. S. Liang, *J. Electrochem. Soc.*, **148** (2001) p. F127.

[14] N. Lifshitz and G. Smolinsky, *J. Electrochem. Soc.*, **136** (1989) p. 2335.

[15] A. Jain, S. Rogojevic, S. V. Nitta, V. Pisupatti, W. N. Gill, P. C. Wayner Jr., and J. L. Plawsky, *Mat. Res. Soc. Symp. Proc.*, **565** (1999) p. 29.

[16] J. C. Jackson, Ö Oralkan, D. J. Dumin, and G. A. Brown, *Microelectronics Reliability*, **39** (1999) p. 171.

[17] R. Tsu, J. W. McPherson, and W. R. Mckee, *IEEE IRPS Technol. Dig.* (2000) p. 348.

[18] J. R. Bowser, *Inorganic Chemistry* (Brooks/Cole Publishing Co., California, 1993) p. 401.

[19] C. G. Shirley and S. C. Maston, *IEEE IRPS Technol. Dig.* (1990) p. 72.

[20] Y. S. Diamand, A. Dedhia, D. Hoffstetter, and W. G. Oldham, *J. Electrochem. Soc.*, **140** (1993) p. 2427.

[21] J. D. Mcbrayer, R. M. Swanson, and T. W. Sigmon, *J. Electrochem. Soc.*, **133** (1986) p. 1242.

Table 10-1 Basic data of OMCTS-based α-SiCO dielectric barrier films studied in this work.

Sample ID	SiCO-0	SiCO-2	SiCO-3
O_2/OMCTS flow rate (sccm/sccm)	0/800	200/800	300/800
FTIR Si-O/Si-C absorbance peak ratio	1.83	5.07	10.52
Refractive index @ 633 nm	1.507	1.439	1.434
Electronic dielectric constant	2.27	2.07	2.05
Dielectric constant @ 1 MHz	2.78	4.60	6.30
Ionic and dipolar dielectric constant	0.51	2.53	4.25

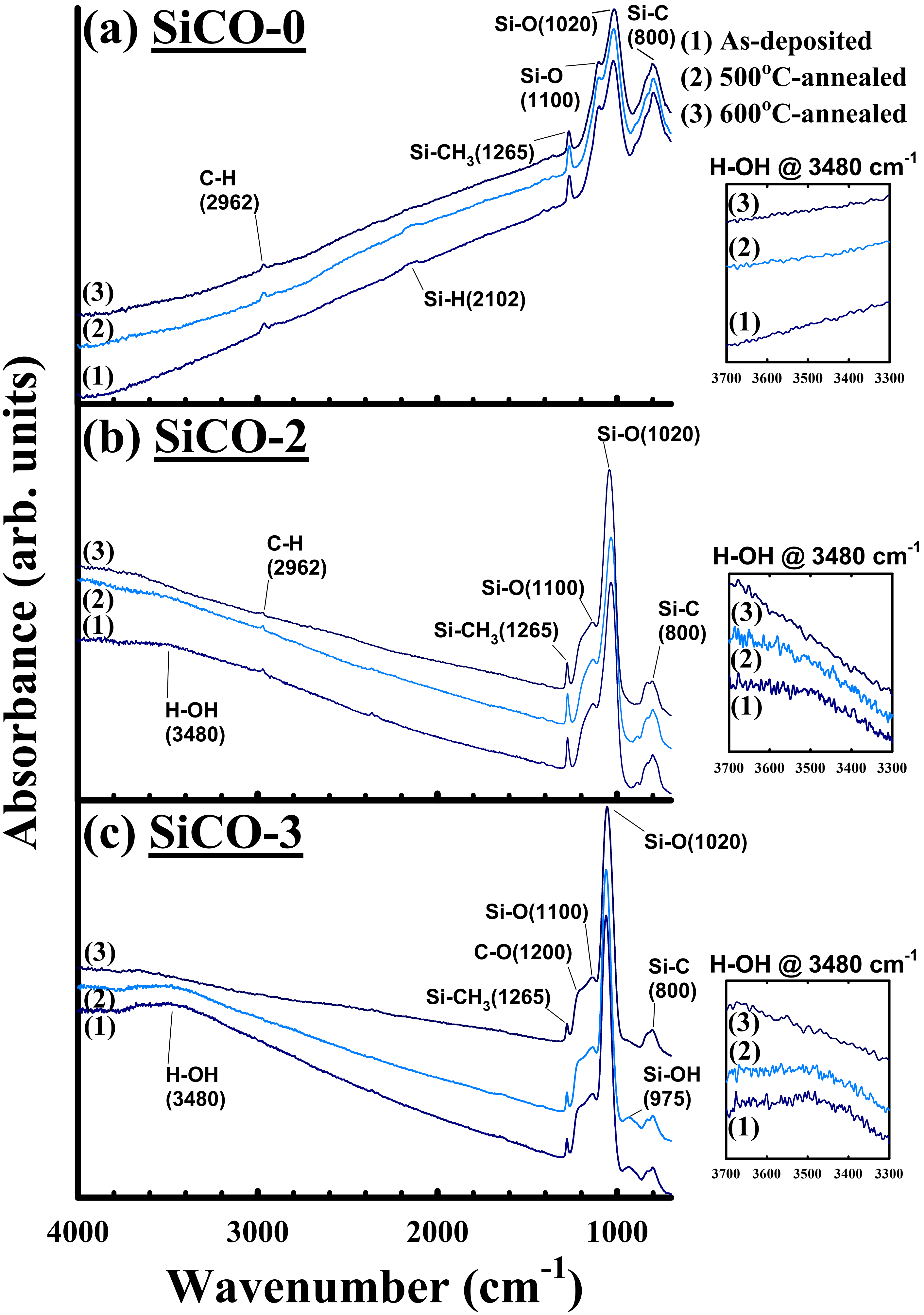

Fig. 10-1 FTIR spectra of (a) SiCO-0, (b) SiCO-2, and (c) SiCO-3 dielectric barrier film with and without thermal anneal.

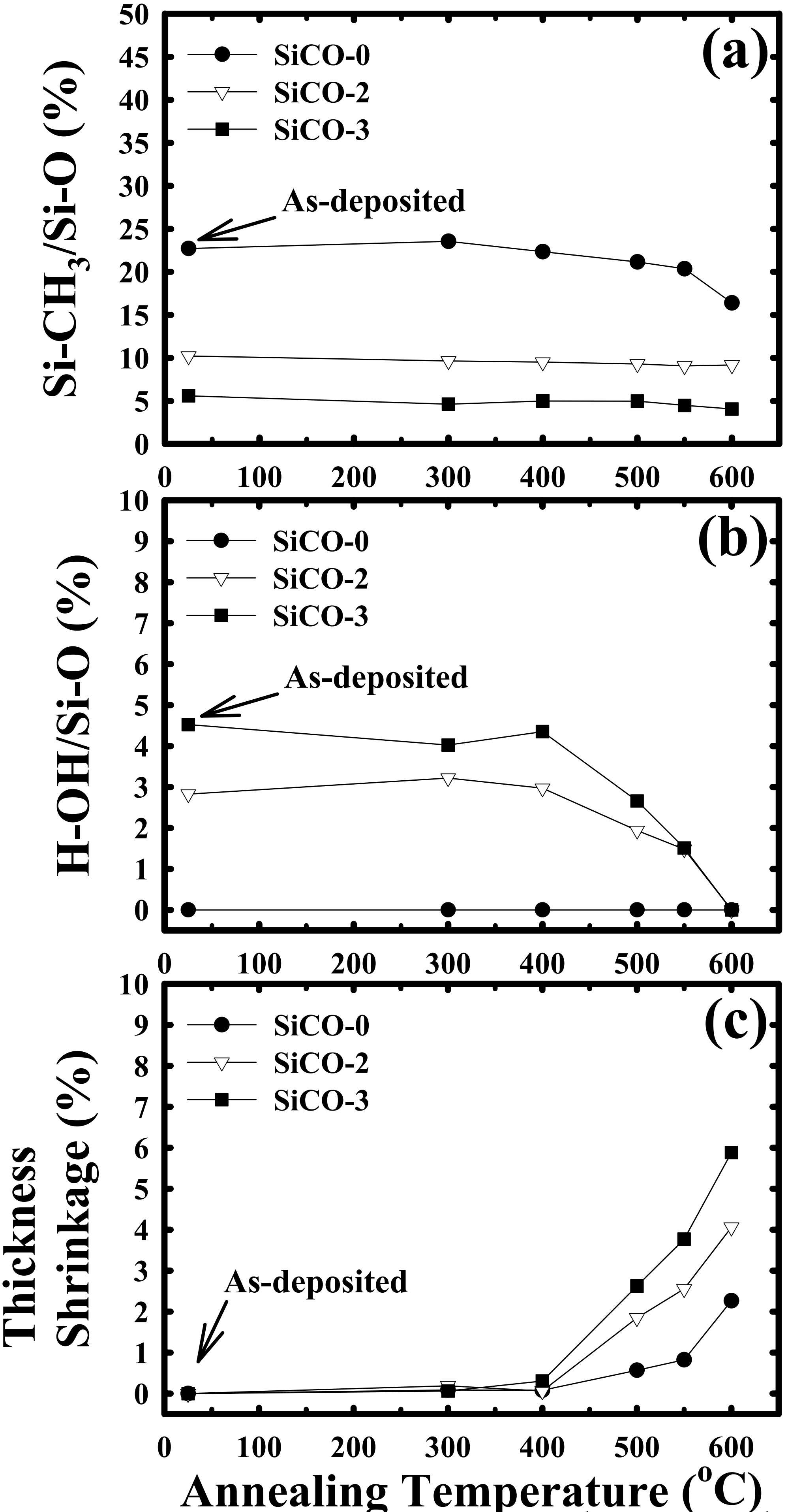

Fig. 10-2 FTIR absorbance peak ratio of (a) Si-CH_3 (1265 cm^{-1})/Si-O (1020 cm^{-1}) and (b) H-OH (3480 cm^{-1})/Si-O (1020 cm^{-1}) vs. annealing temperature, and (c) thickness shrinkage vs. annealing temperature for three OMCTS-based α-SiCO dielectric barrier fims.

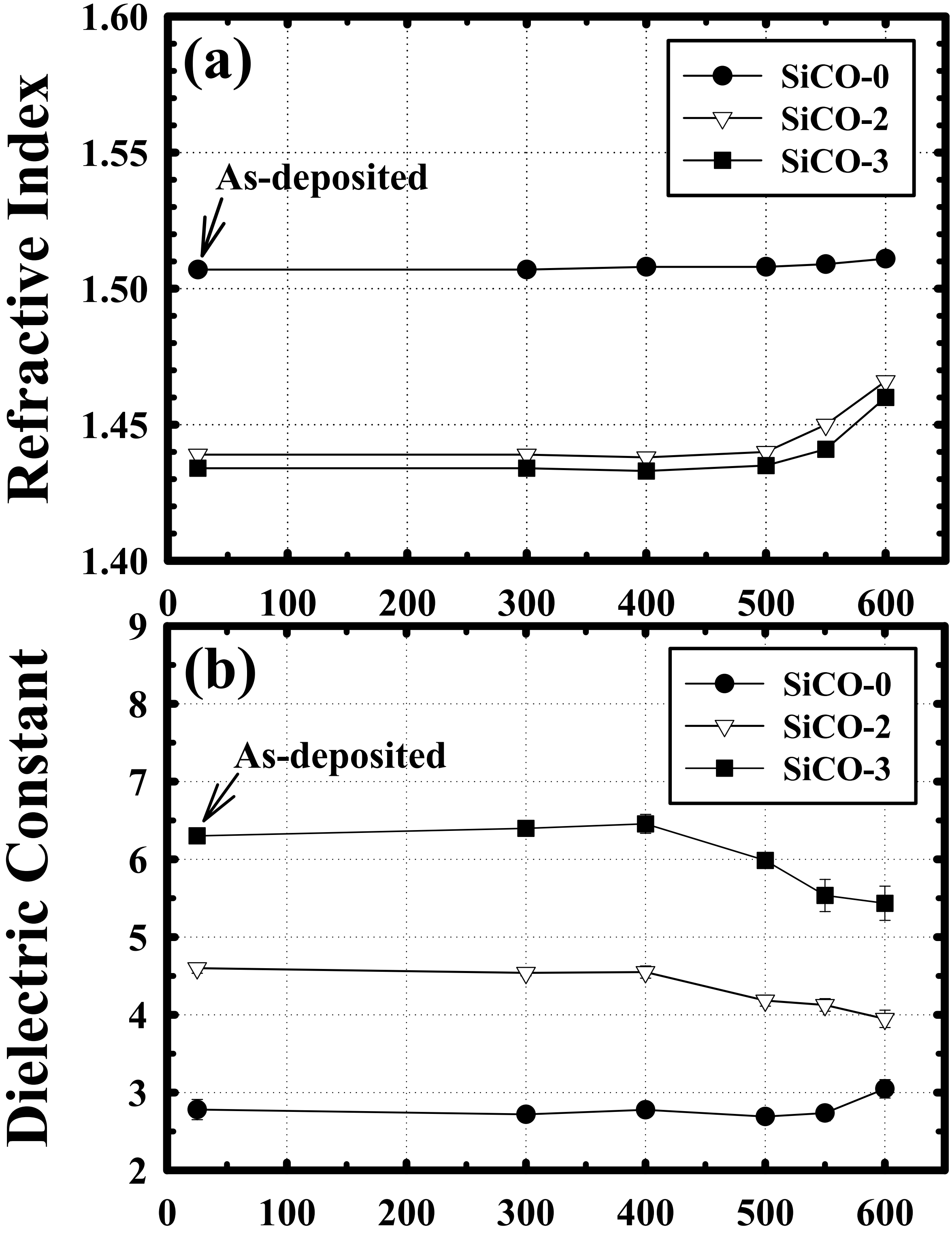

Fig. 10-3 (a) Refractive index and (b) dielectric constant vs. annealing temperature for three OMCTS-based α-SiCO dielectric barrier films.

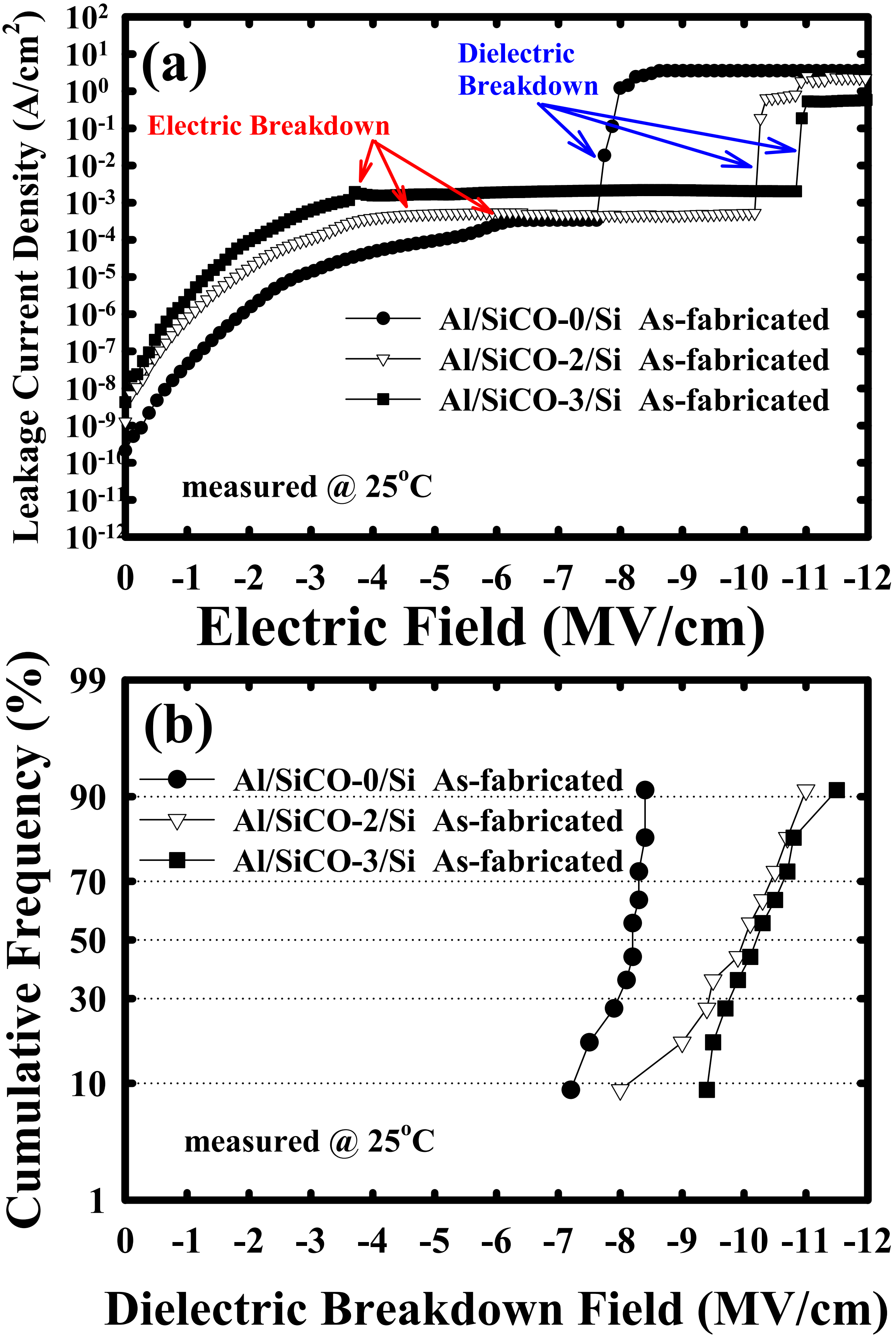

Fig. 10-4 (a) Leakage current density vs. electric field and (b) statistical distribution of dielectric breakdown field for the as-fabricated Al-gated MIS capacitors.

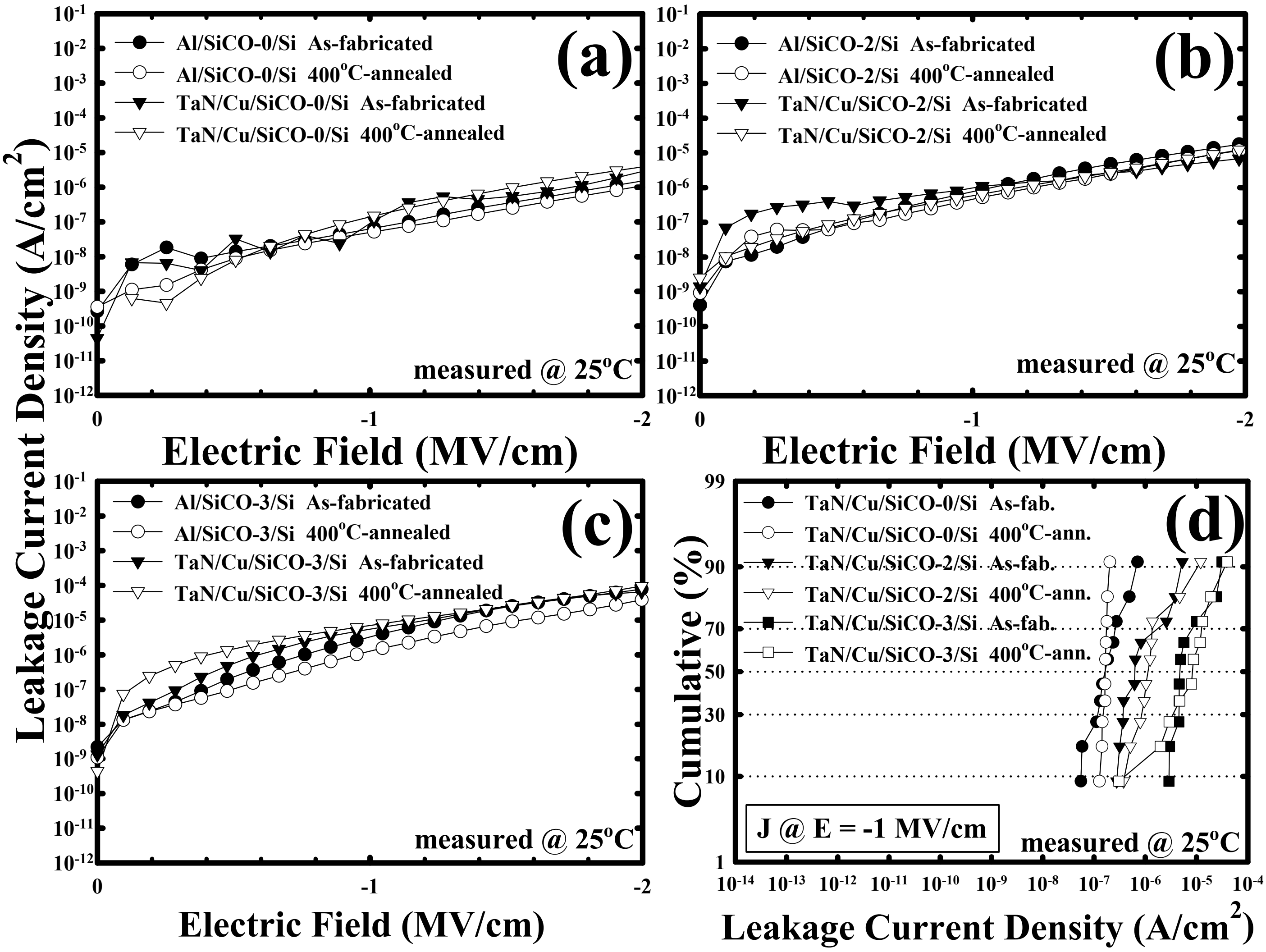

Fig. 10-5 Room temperature leakage current density vs. electric field for the as-fabricated and 400°C-annealed Al-gated and TaN/Cu-gated MIS capacitors of (a) SiCO-0, (b) SiCO-2, and (c) SiCO-3 dielectric barrier films; (d) statistical distribution of leakage current density for the as-fabricated and 400°C-annealed TaN/Cu-gated MIS capacitors.

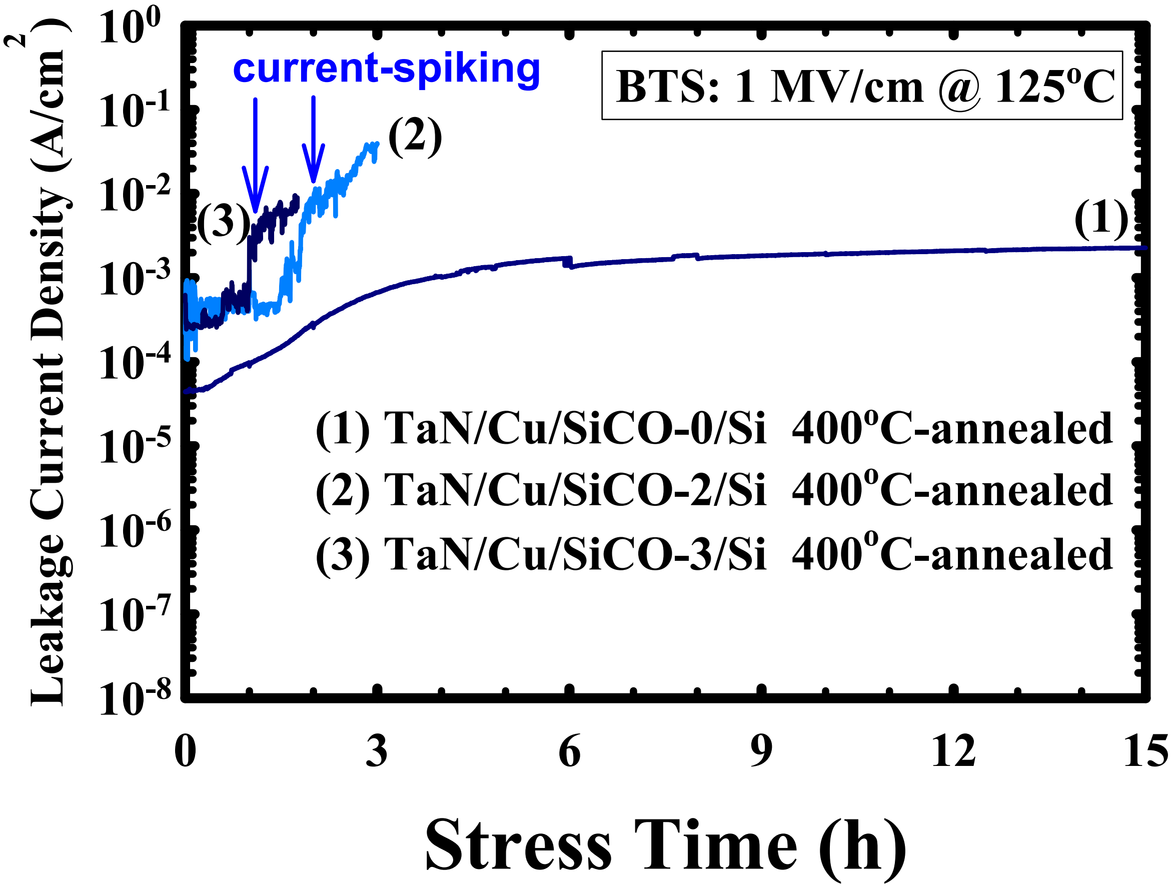

Fig. 10-6 Current transient during BTS test at 125°C with an electric field of 1 MV/cm for TaN/Cu-gated MIS capacitors.

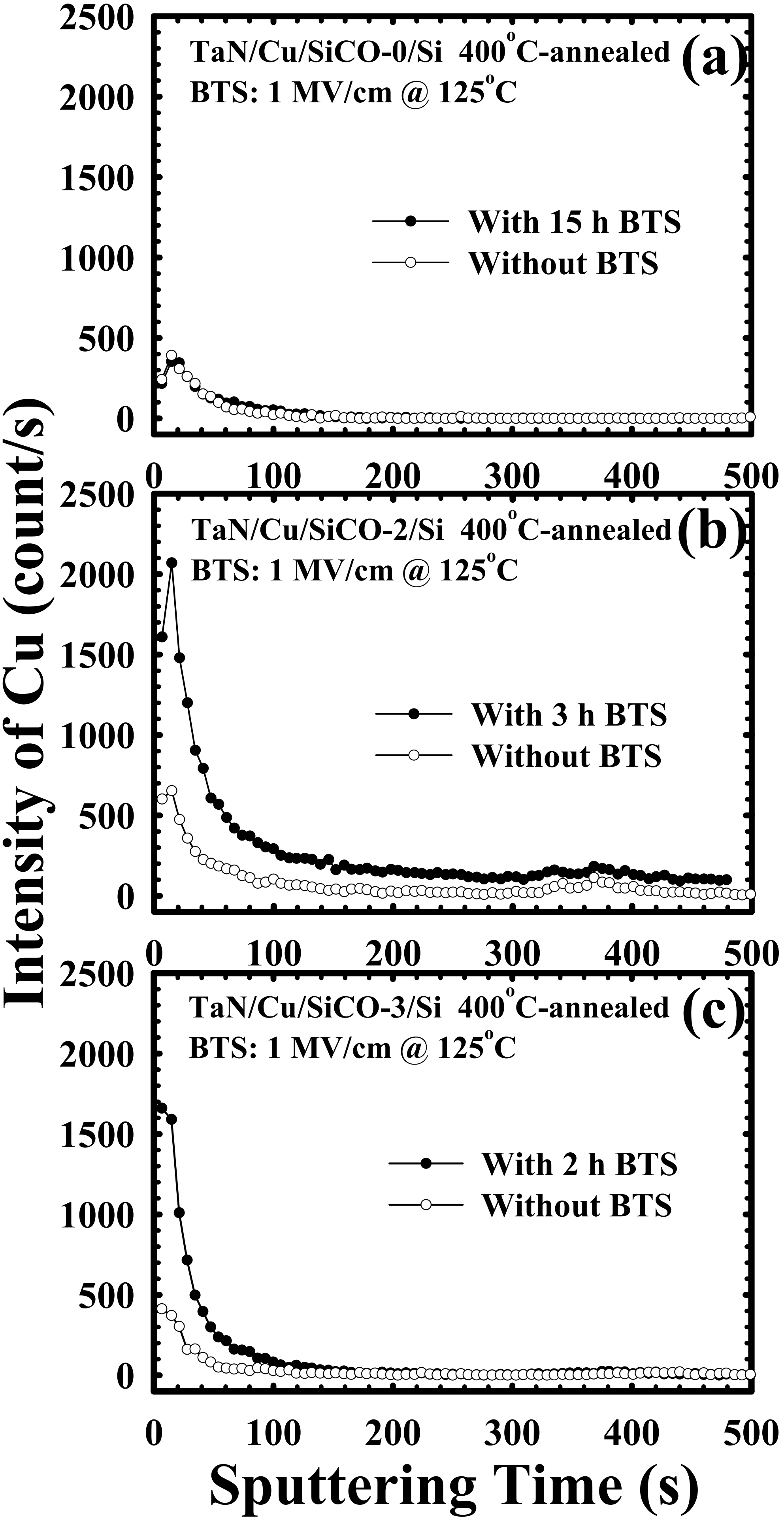

Fig. 10-7 SIMS depth profiles of Cu in (a) SiCO-0, (b) SiCO-2, and (c) SiCO-3 dielectric barrier films for the TaN/Cu-gated MIS capacitors with and without BTS at 125°C with an electric field of 1 MV/cm. The TaN/Cu electrode was removed before the SIMS analysis.

Chapter 11

Conclusions and Suggestions for Future Work

11-1 Conclusions

There are three major parts of studies in this thesis. The first part studies the thermal stability and physical and barrier properties of various 3MS-based α-SiCN dielectric films deposited with NH_3 reaction gas (chapters 2 and 3). The effects of O_2- and N_2-plasma treatments on the Cu-surface are also studied using the Al/α-SiCN/Cu MIM capacitor (chapter 4). The second part deals with the thermal stability and physical and barrier properties of 3MS- and 4MS-based α-SiC dielectric films (chapter 5). The TDDB improvement and leakage and breakdown mechanisms are also investigated using Cu-comb capacitors with 3MS-based α-SiCN/α-SiC bilayer-structured Cu cap-barrier films (chapters 6 and 7). The third part explores the thermal stability and physical and barrier properties of various 3MS-based α-SiCO dielectric films deposited with CO_2 reaction gas (chapter 8) as well as their electrical performance using Cu-comb capacitors (chapter 9). The thermal stability and physical and barrier properties of various OMCTS-based α-SiCO dielectric films deposited with O_2 reaction gas are also studied (chapter 10).

The first part concludes that the dielectric constant and thermal stability of the 3MS-based α-SiCN films decrease with increasing carbon and hydrogen contents and decreasing nitrogen content in the films. The reduced dielectric constant is attributed to the lower dipolar and ionic polarizations of carbon atoms and the lower electronic polarization of hydrogen atoms, while the decreased thermal stability is due to massive outgassing of hydrocarbon groups at elevated temperatures. The α-SiCN films with abundant carbon and hydrogen contents exhibit degraded barrier property and dielectric strength. This can be attributed to the poorly crosslinked molecular structure and the porosity enrichment caused by carbon atoms as well as the hydrogen-related defects, such as Si-H$^+$-Si hydrogen bridges, and the numerous Si-H weak bonds arisen from the hydrogen atoms in the film. Moreover, the Al/α-SiCN/Cu MIM capacitors with the Cu-surface exposed to O_2- or N_2-plasma treatment prior to the deposition of the 3MS-based α-SiCN film exhibit higher leakage current and lower breakdown field. The increased leakage current and decreased breakdown field of the O_2- and N_2-plasma-treated samples are attributed, respectively, to the presence of metastable Cu-O oxide and Cu-N azide at the Cu-surface.

The second part concludes that the 4MS-based α-SiC film contains a higher carbon content and thus has a lower dielectric constant and thermal stability than the 3MS-based α-SiC film. The 4MS-based α-SiC film also exhibits degraded barrier property and moisture resistance. The TDDB lifetime of Cu-comb capacitor is greatly improved by using a 3MS-based α-SiCN/α-SiC bilayer dielectric stack instead of the 3MS-based α-SiCN single film as a Cu cap-barrier layer. This improvement is attributed to the lower leakage current of α-SiC, absence of nitridation on Cu surface, and better adhesion of α-SiC to Cu and OSG IMD. The leakage current between Cu lines in the Cu-comb capacitor is dependent on the thickness ratio of the α-SiCN/α-SiC bilayer barrier. The Cu-comb capacitor with an α-SiCN(50 nm)/α-SiC(2 nm) bilayer barrier exhibits a much smaller leakage current than that with a bilayer barrier of thicker α-SiC film, such as α-SiCN(40 nm)/α-SiC(10 nm) or α-SiCN(30 nm)/α-SiC(20 nm). The increased leakage (Frenkel-Poole emission) between Cu lines is attributed to the large number of interfacial defects, such as cracks, voids, traps or dangling bonds at the α-SiC/OSG interface, which are generated by the larger tensile force of the thicker α-SiC film. On the other hand, the breakdown field and TDDB lifetime of the Cu-comb capacitor reveal little dependence on the thickness ratio of the α-SiCN/α-SiC bilayer barrier, and the observed breakdown of the Cu-comb capacitor is due to dielectric breakdown of the bulk OSG layer.

The third part concludes that the dielectric constant of the 3MS-based α-SiCO dielectric films decreases with increasing CO_2 flow rate during the dielectric deposition process. The decreased dielectric constant is attributed to the lower electronic polarization and higher electronegativity of oxygen atoms in the α-SiCO dielectric film. Increasing CO_2 flow rate also leads to an α-SiCO dielectric film of better thermal stability, higher breakdown field, lower leakage current, and superior resistance to Cu diffusion. The improved barrier property is attributed to the denser and less porous structure of the 3MS-based α-SiCO dielectric film deposited with a higher CO_2 flow rate. The Cu-MIS and Cu-comb capacitors with a 3MS-based α-SiCO dielectric barrier film exhibit much smaller leakage current and higher breakdown field than those with a 3MS-based α-SiC dielectric film. This is attributed to the higher density, oxygen-improved film's property, non-semiconductor behavior, and lower fringe- or surface-electric field of the 3MS-based α-SiCO dielectric film. The dielectric constant of the OMCTS-based α-SiCO films increases with increasing O_2 flow rate during the dielectric deposition process, presumably due to the increasing content of the higher dipolar and ionic polarized oxygen atoms in the dielectric film. Increasing O_2 flow rate also degrades the thermal stability, moisture resistance, and Cu barrier property of the OMCTS-based α-SiCO dielectric film. Notably, the 3MS-based α-SiCO dielectric barrier films exhibit superior Cu barrier property than the OMCTS-based α-SiCO films. This is due to the fact that the 3MS α-SiCO films have a SiC-based molecular structure, while the molecular structure of the

OMCTS α-SiCO films is SiO-based.

Table 11-1 summarizes the properties of α-SiCN, α-SiC, and α-SiCO dielectric barrier films studied in this thesis. The Cu barrier lifetime is defined as the time-to-breakdown of the TaN/Cu-gated MIS capacitors by the specified BTS test. The 3MS-based α-SiCO film (SCO12) deposited with an addition of CO_2 reaction gas is a very potential candidate as the Cu cap-barrier and etching stop layer in the Cu damascene structure of future BEOL technology.

11-2 Suggestions for Future Work

Some topics relevant to this thesis work are suggested for the follow-up study as follows.

(1) Hydrogen forward scattering spectroscopy (HFS) [1] or forward recoil elastic scattering spectroscopy (FRES) [2] may be used to determine quantitatively the hydrogen content of the dielectric barrier film.

(2) Specular X-ray reflectivity (SXR), small angle neutron scattering (SANS), traditional N_2 porosimetry (BET, Brunauer-Emmett-Teller), ellipsometric porosimetry (EP) [3], or positronium annihilation lifetime spectroscopy (PALS) [1,3,4] may be used to determine the porosity, pore size, and pore distribution in the dielectric barrier film.

(3) Some simulation tools may be used to estimate the three-dimensional molecular structure of the dielectric barrier film.

(4) The 3MS-based α-SiCO dielectric barrier film deposited with other oxygen-containing reaction gas may be worthy of further exploration. Moreover, the 3MS precursor may be replaced with other advanced new precursor materials for the deposition of dielectric barrier films, such as

hexamethydisiloxane (HMDSO) or trimethoxysilane (TMOS) [1,5].

(5) Advanced low-k ($k \leq 3$) dielectric barrier films, such as plasma-polymerized divinyl siloxane bis-benzocyclobutene (p-BCB, $k=2.7$) [6] or oxygen-doped carbide (α-SiCO, $k=3$) [7], may be worthy of further study. When the low-k dielectric barrier films can be successfully integrated with the BEOL technology, the low-k IMDs with poor Cu barrier property must be replaced. Moreover, the metallic barrier films as shown in Fig. 1-3 become unnecessary.

(6) The improvement of interface property at the cap-barrier/Cu and cap-barrier/OSG interfaces by plasma treatment [8] or chemical soaking without side effects is worthy of further exploration.

References

[1] T. Ishimaru, Y. Shioya, H. Ikakura, M. Nozawa, S. Ohgawara, T. Ohdaira, R. Suzuki, and K. Maeda, *J. Electrochem. Soc.*, **150** (2003) p. F83.

[2] A. Grill and V. Patel, *J. Appl. Phys.*, **85** (1999) p. 3314.

[3] J. N. Sun, D. W. Gidley, Y. F. Hu, W. E. Frieze, and S. Yang, *Mat. Res. Soc. Symp. Proc.*, **726** (2002) p. Q10.5.1.

[4] J. N. Sun, Y. F. Hu, W. E. Frieze, and D. W. Gidley, *Radiation Physics and Chemistry*, **68** (2003) p. 345.

[5] K. I. Takeda, D. Ryuzaki, T. Mine, and K. Hinode, *IEEE IITC Technol. Dig.* (2001) p. 244.

[6] M. Tade, Y. Harada, K. Hijioka, H. Ohtake, T. Takeuchi, S. Saito, T. Onodera, M. Hiroi, N. Furutake, and Y. Hayashi, *IEEE IITC Technol. Dig.* (2002) p. 12.

[7] Z. C. Wu, T. J. Chou, S. H. Lin, Y. L. Huang, Y. L. Yang, L. P. Li, B. T. Chen, Y. C. Lu, C. C. Chiang, M. C. Chen, W. Chang, S. M. Jang, and M. S. Liang, *IEEE IEDM Technol. Dig.* (2003) p. 849.

[8] L. J. Li, C. Y. Sheu, B. T. Chen, T. I. Bao, T. L. Lee, R. L. Hwang, S. M. Jang, C. H. Yu, and M. S. Liang, *AMC Technol. Dig.* (2001) p. 261.

Table 11-1 Properties of α-SiCN, α-SiC, and α-SiCO dielectric barrier films.

Chap	**Sample ID**	**Deposition gas**	***k*-value**	**Thermal Stability (°C)**	**J@1 MV/cm, 25°C (A/cm^2)**	**Cu barrier lifetime (sec)**
2	**SC3**	**$3MS/NH_3$**	**3.5**	**500**	**8.2×10^{-10}**	**1.8×10^{3} (1 MV/cm, 200°C)**
2	**SC2**	**$3MS/NH_3$**	**4.5**	**500**	**3.2×10^{-8}**	**$>5.4\times10^{4}$ (1 MV/cm, 200°C)**
2	**SC1**	**$3MS/NH_3$**	**5.4**	**550**	**3.1×10^{-9}**	**$>5.4\times10^{4}$ (1 MV/cm, 200°C)**
3	**SCH1**	**$3MS/NH_3$**	**4.0**	**500**	**5.8×10^{-10}**	**2.1×10^{3} (1 MV/cm, 200°C)**
3	**SCH0**	**$3MS/NH_3$**	**4.8**	**550**	**5.2×10^{-10}**	**$>5.4\times10^{4}$ (1 MV/cm, 200°C)**
5	**SC3M**	**He/3MS**	**4.7**	**550**	**1.5×10^{-8}**	**$>5.4\times10^{4}$ (3 MV/cm, 200°C)**
5	**SC4M**	**He/4MS**	**4.0**	**500**	**1.3×10^{-7}**	**2.5×10^{3} (3 MV/cm, 200°C)**
6	**SCN**	**$He/3MS/NH_3$**	**4.9**	**550**	**2.1×10^{-9}**	**$>5.4\times10^{4}$ (1 MV/cm, 200°C)**
6	**SC**	**3MS**	**3.8**	**500**	**9.6×10^{-10}**	**$>5.4\times10^{4}$ (1 MV/cm, 200°C)**
8	**SCO0**	**He/3MS**	**4.4**	**500**	**3.4×10^{-8}**	**1.7×10^{4} (2 MV/cm, 200°C)**
8	**SCO3**	**$He/3MS/CO_2$**	**4.1**	**500**	**1.3×10^{-8}**	**$>5.4\times10^{4}$ (2 MV/cm, 200°C)**
8	**SCO6**	**$He/3MS/CO_2$**	**3.8**	**550**	**5.3×10^{-9}**	**$>5.4\times10^{4}$ (2 MV/cm, 200°C)**
8	**SCO12**	**$He/3MS/CO_2$**	**3.7**	**550**	**4.5×10^{-9}**	**$>5.4\times10^{4}$ (2 MV/cm, 200°C)**
10	**SiCO-0**	**He/OMCTS**	**2.8**	**550**	**1.5×10^{-7}**	**$>5.4\times10^{4}$ (1 MV/cm, 125°C)**
10	**SiCO-2**	**$He/OMCTS/O_2$**	**4.6**	**400**	**6.5×10^{-7}**	**7.2×10^{3} (1 MV/cm, 125°C)**
10	**SiCO-3**	**$He/OMCTS/O_2$**	**6.3**	**400**	**7.9×10^{-6}**	**3.8×10^{3} (1 MV/cm, 125°C)**

Vita

姓名：蔣秋志（Chiu-Chih Chiang）

性別：男

出生年月日：民國六十六年七月三十日

戶籍：高雄縣

學歷：國立交通大學電子工程系

（民國 84 年 9 月----88 年 6 月）

國立交通大學電子研究所碩士與博士班

（民國 88 年 9 月----93 年 6 月）

博士論文題目：碳化矽基介電層與銅金屬整合之電性和阻障特性

Electrical and Barrier Properties of Silicon-Carbide-Based Dielectrics Integrated with Cu Metallization

經歷：以建教合作方式與台積電研發部門（AMTD/TSMC）從事碳化矽基介電層與銅製程整合之電性可靠度分析研究（89 年 9 月----93 年 6 月）

Publication List

Journal Paper

1. [新--2 點，長文] **Chiu-Chih Chiang**, Mao-Chieh Chen, Chung-Chi Ko, Syun-Ming Jang, and Mong-Song Liang, "Physical and Barrier Properties of Plasma-Enhanced Chemical Vapor Deposited α-SiC:H Films from Trimethylsilane and Tetramethylsilane", *Jpn. J. Appl. Phys.*, **42**, pp. 4273-4277 (2003).
2. [新--2 點，長文] **Chiu-Chih Chiang**, Zhen-Cheng Wu, Wei-Hao Wu, Mao-Chieh Chen, Chung-Chi Ko, Hsi-Ping Chen, Syun-Ming Jang, Chen-Hua Yu, and Mong-Song Liang, "Physical and Barrier Properties of Plasma Enhanced Chemical Vapor Deposition α-SiC:N:H Films", *Jpn. J. Appl. Phys.*, **42**, pp. 4489-4494 (2003).
3. [新--2 點，長文] **Chiu-Chih Chiang**, Mao-Chieh Chen, Chung-Chi Ko, Syun-Ming Jang, Chen-Hua Yu, and Mong-Song Liang, "Physical and Barrier Properties of Plasma-Enhanced Chemical Vapor Deposited α-SiCN:H Films with Different Hydrogen Contents", *Jpn. J. Appl. Phys.*, **42**, pp. 5246-5250 (2003).
4. [新--3 點，長文] **Chiu-Chih Chiang**, Mao-Chieh Chen, Zhen-Cheng Wu, Lain-Jong Li, Syun-Ming Jang, Chen-Hua Yu, and Mong-Song Liang, "TDDB Reliability Improvement of Cu Damascene with a Bilayer-Structured α-SiC:H Dielectric Barrier", *J. Electrochem. Soc.*, **151**, pp. G89-G92 (2004).
5. [新--3 點，長文] **Chiu-Chih Chiang**, I-Hsiu Ko, Mao-Chieh Chen, Zhen-Cheng Wu, Yung-Cheng Lu, Syun-Ming Jang, and Mong-Song Liang, "Leakage and Breakdown Mechanisms of Cu Comb-Capacitor with a Bilayer-Structured α-SiCN/α-SiC Cu-Cap Barrier", *J. Electrochem. Soc.*, **151**, pp. G93-G97 (2004).
6. [新--3 點，長文] **Chiu-Chih Chiang**, I-Hsiu Ko, Mao-Chieh Chen, Zhen-Cheng Wu, Yung-Cheng Lu, Syun-Ming Jang, and Mong-Song Liang, "Improvement in Leakage Current and Breakdown Field of Cu-Comb Capacitor by Using a Silicon-Oxycarbide Dielectric Barrier", to appear in *J. Electrochem. Soc.*
7. [新--3 點，長文] **Chiu-Chih Chiang**, Mao-Chieh Chen, Lain-Jong Li, Zhen-Cheng Wu, Syun-Ming Jang, and Mong-Song Liang, "Physical and Barrier Properties of Plasma-Enhanced Chemical Vapor Deposited Amorphous Silicon-Oxycarbide from Octamethylcyclotetrasiloxane", to appear in *J.*

Electrochem. Soc.

8. [新--3 點，長文] **Chiu-Chih Chiang**, I-Hsiu Ko, Mao-Chieh Chen, Zhen-Cheng Wu, Yung-Cheng Lu, Syun-Ming Jang, and Mong-Song Liang, “Physical and Barrier Properties of Plasma-Enhanced Chemical Vapor Deposited Amorphous Silicon-Oxycarbide from Trimethylsilane and CO_2”, to appear in *J. Electrochem. Soc.*
9. [新--2 點，長文] **Chiu-Chih Chiang**, Mao-Chieh Chen, Lain-Jong Li, Zhen-Cheng Wu, Syun-Ming Jang, and Mong-Song Liang, “Effects of O_2- and N_2-Plasma Treatments on Copper-Surface”, to appear in *Jpn. J. Appl. Phys.*

Conference Paper

1. **Chiu-Chih Chiang**, Zhen-Cheng Wu, Wei-Hao Wu, Mao-Chieh Chen, Chung-Chi Ko, His-Ping Chen, Shwang-Ming Jeng, Syun-Ming Jang, Chen-Hua Yu, and Mong-Song Liang, “Barrier Characteristics of PECVD α-SiC:H Dielectrics”, in *Proceedings of 2001 AMC*, pp. 603-607 (2001).
2. **Chiu-Chih Chiang**, Mao-Chieh Chen, Zhen-Cheng Wu, Lain-Jong Li, Syun-Ming Jang, Chen-Hua Yu, and Mong-Song Liang, “TDDB Reliability Improvement in Cu Damascene by using a Bilayer-Structured PECVD SiC Dielectric Barrier”, in *Proceedings of IEEE 2002 IITC*, pp. 200-202 (2002).
3. [新--1 點，短文] **Chiu-Chih Chiang**, I-Hsiu Ko, Mao-Chieh Chen, Zhen-Cheng Wu, Yung-Cheng Lu, Syun-Ming Jang, and Mong-Song Liang, “Leakage and Breakdown Mechanisms in Cu Damascene with a Bilayer-Structured α-SiCN/α-SiC Dielectric Barrier”, in *Proceedings of IEEE 2003 IITC*, pp. 201-203 (2003).

總發表點數: 新--24 點